Searching for new forces of Nature

New neutral gauge bosons in dimuon final states with the ATLAS detector at the LHC

Vanja Morisbak

December 16, 2020

Thesis submitted for the degree of Philosophiæ Doctor

Abstract

Today we use the Standard Model of particle physics to describe Nature, and it is one of the most successful theories in history, being able to both predict the discovery of new particles and withstanding every scrutinizing test we have examined it with. Still we know that the Standard Model is not the Final Theory, as it fails to describe several observed phenomena, most noticeably maybe gravity and dark matter.

High energy collisions between some of the smallest units of Nature provide us with a unique possibility to probe the fabric of reality. It enables us to measure the properties of apparent pointlike particles, like their mass, their spin and their decay modes, and it allows us to test the many possible models we have constructed to explain Nature. This thesis is about testing a small handful of these models, by searching through the vast amount of 13 TeV proton-proton collision data, corresponding to 139 fb^{-1}, collected by the ATLAS detector at the Large Hadron Collider between the years 2015 and 2018.

The hypothetical new, electrically neutral, spin 1 gauge boson Z' appears in quite a few of the many Beyond the Standard Model theories. In general, many models that propose to extend the gauge group of Nature beyond the SM gauge group feature additional U(1) symmetries with corresponding Z' bosons. Some of these theories are inspired by Grand Unified Theories, in which the electroweak and strong strong forces are united at some higher energy, like the E_6-motivated theories which we will encounter throughout this thesis. In the analysis presented in this thesis, we search for a Z' boson that decays to a muon and an antimuon, resulting in a resonance in the dimuon invariant mass distribution. This is a clean search channel, without the extra complications that channels with jets or missing energy provide.

The data analyzed in this thesis did not provide us with any sign of physics beyond the Standard Model. We therefore set upper exclusion limits on the production cross-sections and lower exclusion limits on the mass of the Z' in three scenarios - Z'_ψ, Z'_χ and Z'_{SSM} - at 3.8 TeV, 4.1 TeV and 4.4 TeV respectively. The results are found to be comparable to the most recent published results from both the ATLAS Collaboration and the CMS Collaboration.

Acknowledgements

I remember meeting Farid Ould-Saada and Alexander L. Read at two separate points in history, during my bachelor's degree. Farid was teaching a course in modern physics, and I remember clearly his passion for physics, and how it inspired me enormously. Some time later, during a laboratory course, I met Alex. I remember realizing he worked with particle physics, and asked him nervously if he thought they would accept me as a master student. He smiled warmly at me and said they happily welcomed all newcomers. I met them again some time later, after being accepted into the high-energy experimental particle physics group to take my master's degree. Farid became my supervisor and Alex my subsidiary supervisor, and they both continued in those roles during my Ph.D. work. They both have my deepest gratitude. I especially thank Farid for the invaluable guidance during all these years.

The whole experimental particle physics group, with all the people that have started and left, and the few that have been there since I started in 2008, all deserve words of praise. You are too many to mention explicitely, but I trust you know who you are if you are reading this. Should I attempt to mention a few, I would send a special thanks to Maiken Pedersen, Lillian Smestad, Silje H. Raddum, Kyrre N. Sjøbæk and Knut Oddvar Høie Vadla.

One person in the group would turn out to play a leading role in the rest of my life - my husband Magnar K. Bugge. I thank you for your love and patience, and your support in my seemingly everlasting Ph.D. work. I am forever grateful for the fact that a set of strange events prevented me from completing the course I needed to start my master's degree in astrophysics, which led me to apply to the experimental particle physics group, which led me to you.

Outside of the academic society there are several people that deserve my gratitude. I would like to thank my two children, Ragnhild and Tord, for giving me a completely different perspective on life, and for enriching my life in ways that were previously unfathomable to me. I thank my mom, for her continuous support and love, my grandmother for always believing in me, and my father for his creativity and his interest in the mystery of the Universe. Lastly I thank my cousin Bill “BillBall” Makatowicz for our shared philosophical interests and uncountable transcendental conversations.

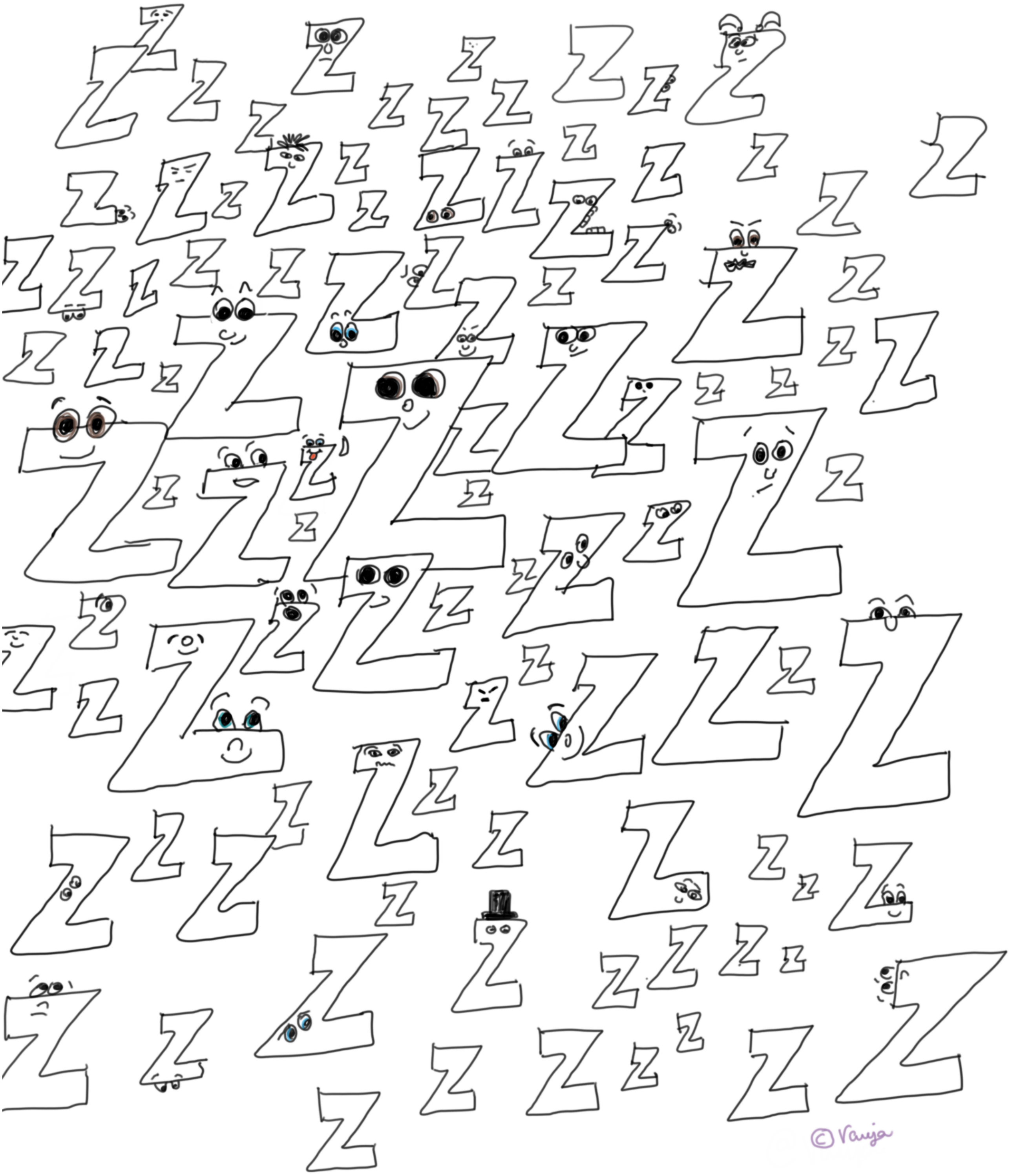
©Vanja

Contents

Introduction

In the year 2008, the very first proton-proton bunches at the Large Hadron Collider (LHC), located on the border between Switzerland and France near the city of Geneva, collided together. The goal was to reach center-of-mass energies many times higher than any other experiment had ever achieved, reproducing the conditions that prevailed in the very early Universe.

In the time leading up to this first collision, some physicists were worried that the LHC could create ever-growing micro black holes that could devour the whole Earth, and even tried to hinder the start up of LHC in the court of law. The newspapers were writing frantically about it. The world was watching, holding its breath. A collective wave of fear traversed the globe. In an office in Oslo, however, I was watching together with many of my colleagues. The air was buzzing with excitement as the time of the first collisions drew nearer. We knew that micro black holes could very well be created that day, but we also knew that they would evaporate within a tiny fraction of a second. The world did not come to an end, and the collective fear slowly died away. To this day, some people remember this event, but most have forgotten.

Today we understand the most basic of the building blocks of Nature and the forces they communicate with via the Standard Model of particle physics, often referred to only as the SM. The first building blocks of the model started developing in the 1920s with Paul Dirac's first attempt at quantizing the electromagnetic field. The Standard Model emerged in an incomplete form in the 1950s, reaching its current form late in the 1960s. The development of particle detectors meant that several of the theorized particles in the SM could be detected. The last missing piece, the Higgs boson, was discovered at the LHC in 2012, realizing one of the main goals of the LHC.

Even though the SM is a hugely successful theory, tested to an extremely high precision, it does not describe everything we have observed in Nature. There are, in fact, many unexplained phenomena. Most noticeably among these are, in my opinion, the fact that Gravity cannot be explained within the SM framework, and that ordinary matter described by the SM account for a mere 5% of the energy content of the Universe. This means, in all simplicity, that the SM is not the Final Theory of Nature. There will most probably be a paradigm shift at some point in the future. We will, or so I hope and believe, at some point discover a better model of Nature. My guess is that it will somehow contain the SM as a low-energy special case. How this new Theory will evolve, is hard to guess, but it is certainly true that it must come with testable predictions. This might include e.g. looking deep into the observable Universe and making a very precise measurement, or it might be colliding particles together at center-of-mass energies that are high enough to allow for the creation of previously unobserved particles. This thesis concerns the latter.

There are two general-purpose particle detectors at the LHC, the ATLAS detector and the CMS detector. They are designed independently, which means that they can make individual measurements which can be statistically combined. In this thesis, I use data collected with the ATLAS detector in the four years from 2015 to 2018 at a center-of-mass energy of 13 TeV to search for hypothetical electrically neutral gauge bosons, referred to in general as Z'. These hypothesized gauge bosons appear in a variety of Beyond the Standard Model (BSM) theories, usually in the context of extending the Standard Model symmetry group.

The work presented in this thesis has partly been in close cooperation with the dilepton resonant search working group within the ATLAS Collaboration, and partly on my own continuing the analysis as performed within the dilepton working group on a larger dataset than what was used for the published result. The structure of the thesis is as follows. In Chapter 1 the Standard Model is presented, with a short historical account, a brief review of the particle content, followed by a brief mathematical description of the main concepts. Chapter 2 concerns the shortcomings of the SM and also looks into some possible BSM theories containing Z'. A description of the LHC and the ATLAS detector follows in Chapter 3, also covering important physics concepts needed to understand the physics at hadron colliders. In Chapter 4 we review the tools we need to perform the dimuon high-mass resonant search, which follows directly after in Chapter 5. This chapter contains the main analysis, with a detailed description of the treatment of simulated data (Monte Carlo data, or MC data), the event selection, data to MC comparisons, systematic uncertainties and the statistical analysis with observed significances and excluded Z' hypotheses. In addition, the results are compared to the published ATLAS results and to the published CMS results. Chapter 6 briefly discussed the results of four previous ATLAS publications, all of which I have worked on, with additional details about my contribution. In Chapter 7 we look at a separate study aimed at confirming the negligibility of the fake background in the dimuon channel. Chapter 8 concerns outreach, in particular The International hands-on particle physics Masterclasses. The focus of this chapter is on the OPloT, a result display and result combination program which I have written. There are two appendices, the first one, Appendix A, concerns my qualification work, which I performed within the Monte Carlo Production Group. The last one, Appendix B, contains tables with additional information on the MC samples in use.

A personal historical account

I started on my Ph.D. work in the fall of the year 2011, and am finishing the thesis now in July 2020, almost 9 years after I started. This is rather uncommon here at the University of Oslo, as the stipulated length is three years' full-time work, and one year dedicated to performing duty work at the University, e.g. teaching. Therefore I think it is worth commenting on both the reasons for and the consequences of this.

When I first started my work in the fall 2011, I was pregnant with my first child, and I was prescribed a 50% sick leave shortly after I started working that lasted until my maternity leave. As a consequence, I could not finish the work I was performing at the time, a data-driven estimate of the dimuon fake background using the co-called Matrix Method. I did however program the tool that has been in use in the yearly particle physics Masterclasses ever since (described in Chapter 8).

I was then on maternity leave until the fall 2012, when I returned partly to work (40%), partly staying at home with my daughter (60%) until she started day care in the fall 2013. I never returned to full-time work after that, always keeping it a maximum 80% to be able to pick up my children in day care before closing time.

In the fall 2015 I was pregnant with my second child, and again partly on sick leave. At that point in time I had finished my duty work (teaching) at the University and had performed the qualification work that ensured I became an ATLAS author, and was working on one of the main results of my thesis work, the minimal Z' models, as described in Section 6.4.2. Again I could not complete my work before starting maternity leave. Luckily someone else in the dilepton working group had also started working on the minimal models, and they were able to finish the work (mainly adding the systematic uncertainties to the framework) in time for the publication [1].

I returned to work in the fall 2017. The dilepton working group had at that point decided to completely change their analysis strategy, from the traditional MC based analysis to a data-driven analysis. I decided, together with my supervisor, that I would keep on the traditional path, which also would serve as a cross-check for the new analysis strategy. As I was the only person working on this analysis, I really started appreciate the collaboration I once had with the dilepton group, and also how much easier it is to discover bugs and keep up-to-date with all the ATLAS physics recommendations and tools and programming tweaks when working in a group.

An obvious consequence of this long history is that my work has stretched out in time, covering five different ATLAS publications. My work has been abruptly aborted at several points in time, not enabling me to finish my contributions to the publications. In addition, I have also had many short and some long absences from work battling periodic chronic illnesses. However, the readers of this thesis are not asked to pity me as I am merely accounting for historical facts. I submit this thesis with a feeling of great pride and accomplishment, and am filled with a sense of having contributed to the search for the Final Theory of Nature.

Chapter 1

Knowledge about the Universe – The Standard Model of particle physics

Our world consists of objects, like the people you know, the trees that reach for the sky and the ocean that covers most of the Earth's surface. Objects consist of molecules. The molecules consist of atoms. Atoms consist of electrons and protons and neutrons. Protons and neutrons consist of quarks. This is the bottom line, as far as we know. Quarks and electrons are pointlike particles without substructure that cannot be divided further.[1] In addition to the particles that make up most of the world we see, there are other, heavier versions of these in the Universe, as well as some very light, ghostly particles, the neutrinos. All the particles communicate with each other via one or more of the four fundamental forces – the strong and the weak force, the electromagnetic force and the gravitational force. Still there is something missing from our understanding, as we will look briefly into in Chapter 2, and these missing pieces fuel our search for new particles, new forces and new theories, hoping to find the Final Theory that describes everything in one beautiful, consistent framework.

1.1 A short introduction to the Standard Model of particle physics

The standard theory of particle physics, or the Standard Model (SM) for short, is a mathematical theory describing all the known fundamental particles in Nature. The theoretical framework is known as Quantum Field Theory (QFT), combining classical field theory with special relativity and quantum mechanics. In QFT we think of the Universe as being permeated by various fields, and the ripples in these field as the observed elementary particles.

1.1.1 A very brief history of the Standard Model

The first successful Quantum Field Theory was Quantum ElectroDynamics (QED). It was developed between the 1920s and the 1940s. It was Paul Dirac who first formulated a quantum theory in the 1920s, describing the interaction between radiation and matter [2].

---

[1] Of course, there is no guarantee that these particles are the bottom line. Quark and/or electron substituents might be discovered in the future.

In 1965 Richard Feynman [3] [4], Sin-Itiro Tomonaga [5] and Julian Schwinger [6] [7] were awarded the Nobel Prize in physics for their work in this area. QED is the relativistic QFT of electrodynamics, describing how light (photons) and matter interact.

In the 1950s so many new particles were discovered that the ensemble of them were referred to as the "particle zoo". One wondered if they could all be elementary particles. In 1963 George Zweig and Murray Gell-Mann independently proposed the existence of a new set of elementary particles called "aces" or "quarks" respectively. It was the name "quark" that caught on and it has been in use ever since. A new quantum number – color – was proposed by Oscar W. Greenberg in 1964 after the discovery of Ω^-, a particle consisting of three strange quarks all with parallel spins. At least three colors had to exist because the three identical quarks of the newly discovered Ω^- cannot be in the same quantum state according to the Pauli exclusion principle stating that two identical fermions cannot occupy the same quantum state.

The asymptotic freedom of QCD, i.e. the apparent freedom of the quarks and gluons at very short distances, was discovered in 1973 by David Gross, Frank Wilczek and David Politzer. They shared the 2004 Nobel Prize in Physics "for the discovery of asymptotic freedom in the theory of the strong interaction" [8].

In 1959, Sheldon Glashow [9], Abdus Salam and John Clive Ward [10] discovered how to combine the electromagnetic and weak interactions, called electroweak interactions, in one framework. Then in 1967 Steven Weinberg [11] and Abdus Salam [12] incorporated the Brout-Englert-Higgs (BEH) mechanism into this theory, giving mass to the mediators of the weak force (the W and Z bosons) while keeping the photon massless. The 1979 Nobel Prize in physics [13] was awarded jointly to Sheldon Lee Glashow, Abdus Salam and Steven Weinberg "for their contributions to the theory of the unified weak and electromagnetic interaction between elementary particles, including, inter alia, the prediction of the weak neutral current." In 1972 Gerardus ’t Hooft and Martinus J. G. Veltman showed that the electroweak theory was indeed renormalizeable (finite) and consistent [14]. The 1999 Nobel Prize in Physics was awarded to ’t Hooft and Veltman for "for elucidating the quantum structure of electroweak interactions in physics" [15].

1.1.2 The particles of the Standard Model

1.1.2.1 Fermions

There are twenty four matter particles – six quarks and six leptons, each with its corresponding antiparticle. The antiparticles have the same properties as their respective particles, except with additive quantum numbers (e.g. electric charge and color) reversed. The matter particles are fermions, with spin ½, obeying Fermi-Dirac statistics, which means they obey the Pauli exclusion principle that forbids two identical particles to be in the same state. Pairs of quarks and leptons are grouped in three generations with increasing mass. Only the first generation of leptons are stable. The origin of the three generations has been and still is a mystery. Figure 1.1 offers a schematic illustration of the particles of the Standard Model, with masses, electric charge, spin and lifetimes included wherever applicable. The five lightest quarks have no mean life, as they hadronize rather than decay.

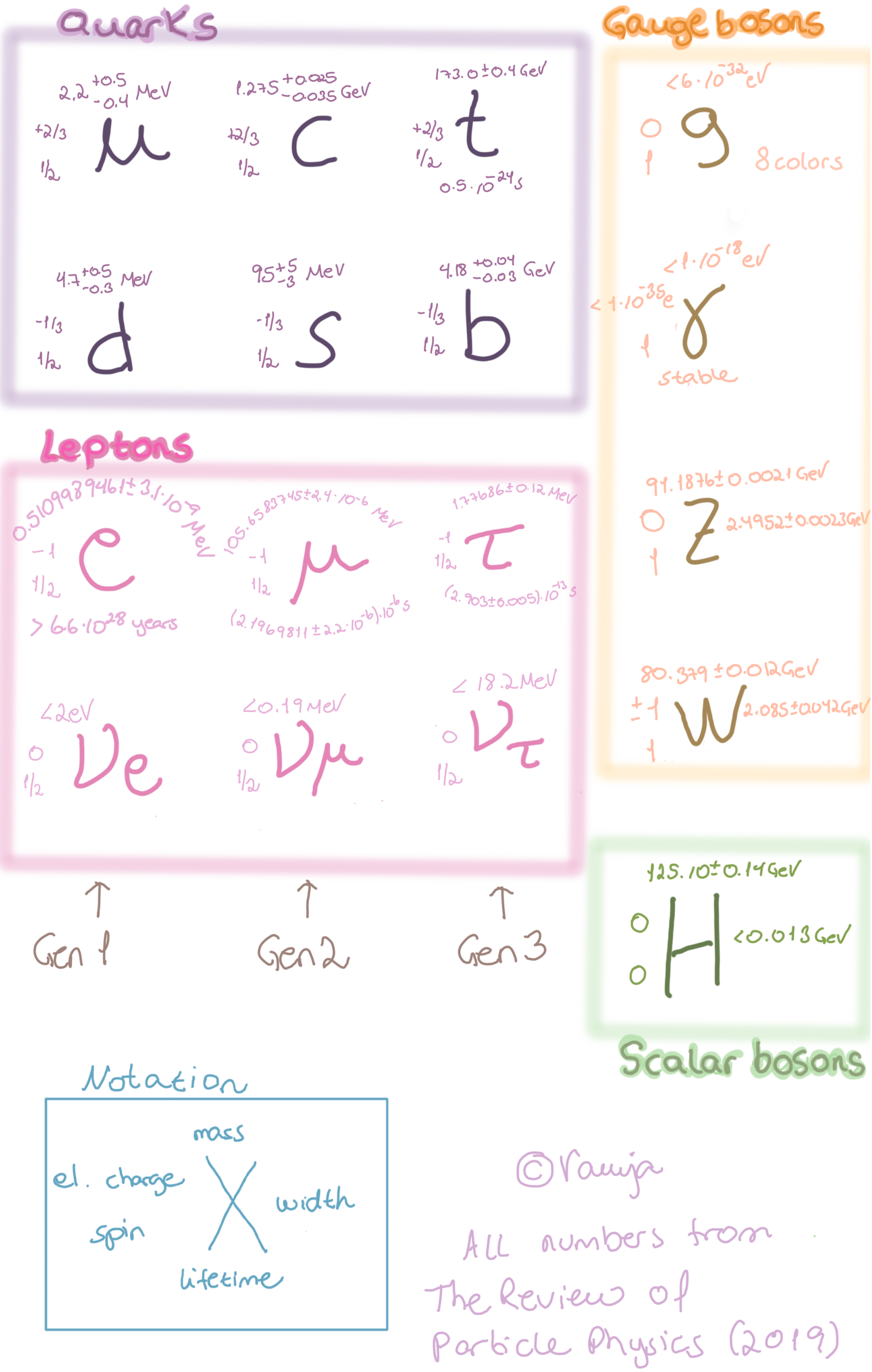

Figure 1.1: The fundamental particles of the Standard Model [16]. The notation of the drawing is shown as a blue mock particle X.

Of the six leptons, three (electron e, muon μ, tau τ) have electric charge and thus feel the electromagnetic force and three (electron neutrino ν_e, muon neutrino ν_μ and tau neutrino ν_τ) do not. All six leptons interact weakly. The three neutrinos were long suspected to be massless, but today they are believed to have a very small mass due to the fact that they oscillate between the three flavors. In the SM the neutrinos are massless [16].

The six quarks – up, down, charm, strange, top, bottom – carry color charge (red, green or blue) and thus interact via the strong force. They also carry fractional electric charge and weak isospin, which means they interact electromagnetically and weakly. The quarks are forever[2] doomed to be confined in colorless combinations creating what is known as hadrons. Possible colorless combinations are one of each color or anticolor, or color/anticolor combinations.

1.1.2.2 Gauge bosons

In the Standard Model we find 12 spin 1 gauge bosons that mediate the strong, weak and electromagnetic forces, as drawn in Figure 1.1. Because they are bosons they do not obey the Pauli exclusion principle like fermions do, and therefore there is no limit on the number of bosons that can occupy the same state.

The mediator of the electromagnetic force is called the photon. The photon is massless and the range of the electromagnetic force is infinite. It is well described by QED.

The three gauge bosons of the weak interactions are called $W^{\pm}$ and Z^0, or simply W and Z bosons. They are all massive, with masses of approximately 80 and 91 GeV respectively. While the relevant charge in QED is the electric charge, the relevant charge in weak interactions is the third component of the weak isospin, I_3. Only left-handed particles and right-handed antiparticles carry non-zero weak isospin. W bosons couple *only* to left-handed particles and right-handed antiparticles, while the Z boson couples *predominantly* to left-handed particles and right-handed antiparticles.

There are eight massless mediators of the strong force, called gluons. They carry color charge and therefore take part in strong interactions themselves. As a result, the effective range of the strong interaction is not infinite, it has an effective limit of the order of 1 fm. No quark or gluon has ever been observed as a free particle. They exist only in colorless hadrons because the strong coupling constant grows with increasing distance between colored objects, until there is enough energy stored to create new objects which then forms new colorless hadrons. This is known as color confinement or just confinement, and is illustrated in Figure 1.2. Curiously, at distances less than about 0.2 fm, when looking inside hadrons or at very high energies, the gluons and quarks behave as free particles. This is what is known as asymptotic freedom.

1.1.2.3 Higgs boson

The Brout-Englert-Higgs (BEH) field pervades the Universe, ensuring that quarks, leptons and W and Z bosons are massive while keeping the photon massless. The more a particle interacts with this field, the heavier it is.

---

[2] This is not quite true. It *is* true at non-extreme densities and temperatures. Under extreme conditions asymptotically free quarks and gluons create a quark-gluon plasma (QGP), or quark-gluon soup.

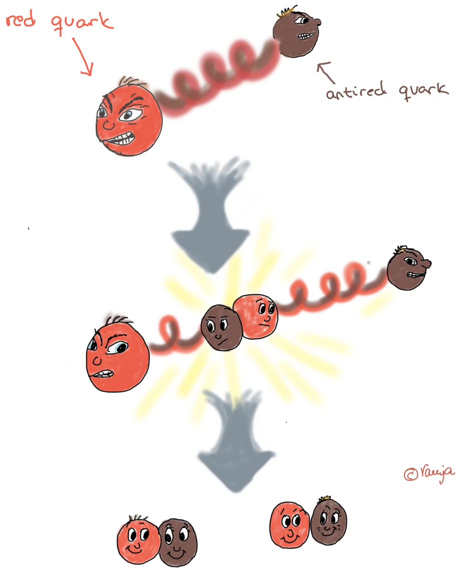

Figure 1.2: Drawing that illustrates color confinement - from the top: the red and the antired quark try to get away from each other, then as the energy in the field between them increases a new quark-antiquark pair is created and two new colorless hadrons are formed.

The Higgs boson is the observable manifestation of the BEH field. It is itself quite massive, weighing in at 125.18 ± 0.16 GeV [16]. The Higgs boson is the only scalar (spin 0) particle in the Standard Model. It carries no electric or color charge.

1.2 A short mathematical description of the Standard Model

We now briefly and superficially describe the mathematics behind the SM, starting with the simplest theory, namely QED, which describes the interaction of photons with matter.[3] The reader is assumed familiar with the background for Quantum Field Theory, and we jump straight into the mathematics of the SM. Note that this section does *not* aim to be a fully detailed textbook description, merely a short summary of the most important aspects of the theory.

1.2.1 Quantum electrodynamics

1.2.1.1 The QED Lagrangian density

The free-fermion Lagrangian density (often referred to as only “the Lagrangian” for brevity) $\mathcal{L}_0$ is given by

$$\mathcal{L}_0(x) \equiv \mathcal{L}_0 = \bar{\psi}(x) \left(i\gamma^\mu \partial_\mu - m\right) \psi(x), \tag{1.1}$$

where m is the rest mass of the fermion.

---

[3] Unless stated otherwise, this section is based on reference [17].

The Lagrangian density is invariant under the *global phase transformations*

$$\begin{aligned}\psi(x) \rightarrow& \psi'(x) = \psi(x)e^{-i\alpha} \\ \bar{\psi}(x) \rightarrow& \bar{\psi}'(x) = \bar{\psi}(x)e^{i\alpha},\end{aligned} \tag{1.2}$$

where α is a real number. This can be shown to ensure that the electromagnetic current

$$s^{\mu}(x) \equiv -q\bar{\psi}(x)\gamma^{\mu}\psi(x) \tag{1.3}$$

satisfies $\partial_{\mu}s^{\mu}(x) = 0$ and thus is conserved, so that the charge

$$Q = -q\int \mathrm{d}^3\mathbf{x}\psi^{\dagger}(x)\psi(x) \tag{1.4}$$

is conserved. Invariance of the Lagrangian density under some transformation always implies a conserved quantity, summarized in what is known as Noether's theorem.

The electromagnetic interaction is introduced by means of minimal substitution,

$$\partial_{\mu} \rightarrow D_{\mu} = [\partial_{\mu} + iqA_{\mu}(x)], \tag{1.5}$$

where q is the electromagnetic charge of the fermion. This transforms the Lagrangian density to

$$\begin{aligned}\mathcal{L} &= \bar{\psi}(x)(i\gamma^{\mu}D_{\mu} - m)\psi(x) \\ &= \mathcal{L}_0 - q\bar{\psi}(x)\gamma^{\mu}\psi(x)A_{\mu}(x) \\ &= \mathcal{L}_0 - s^{\mu}(x)A_{\mu}(x) \\ &\equiv \mathcal{L}_0 + \mathcal{L}_1\end{aligned} \tag{1.6}$$

The theory has to be invariant under a local gauge transformation of the potentials

$$A_{\mu}(x) \rightarrow A'_{\mu}(x) = A_{\mu}(x) + \partial_{\mu}f(x), \tag{1.7}$$

with $f(x)$ as an arbitrary real, differentiable function. The Lagrangian density is invariant under this transformation if and only if the Dirac fields themselves $\psi(x)$ and $\bar{\psi}(x)$ undergo the local transformations

$$\begin{aligned}\psi(x) \rightarrow& \psi'(x) = \psi(x)e^{-iqf(x)} \\ \bar{\psi}(x) \rightarrow& \bar{\psi}'(x) = \bar{\psi}(x)e^{iqf(x)}\end{aligned} \tag{1.8}$$

Any theory that is invariant under such local gauge transformations is said to be a *gauge theory*. This set of arguments also works the other way around – we can derive the QED Lagrangian density in Equation (1.6) from the free-fermion Lagrangian $\mathcal{L}_0$ density in Equation (1.1) by demanding that it is invariant under the local gauge transformations (1.8). We will encounter this in the next section about electroweak interactions.

$\mathcal{L}_0$ in Equation (1.6) is the Lagrangian density of the free Dirac field, while $\mathcal{L}_1$ is interpreted as the *interaction* Lagrangian density. $\mathcal{L}_1$ couples the conserved electromagnetic current $s_\mu(x)$ in Equation (1.3) to the electromagnetic potential $A_\mu(x)$ of the electromagnetic field, and thus describes the interaction between an electrically charged particle and the electromagnetic field.

Lastly we add to the Lagrangian a term that describes the free electromagnetic field and obtain the complete QED Lagrangian,

$$\begin{aligned}\mathcal{L} &= \bar{\psi}(x)\left(i\gamma^\mu\partial_\mu - m\right)\psi(x) - \frac{1}{4}F_{\mu\nu}(x)F^{\mu\nu}(x) - q\bar{\psi}(x)\gamma^\mu\psi(x)A_\mu(x) \\ &= \mathcal{L}_0 + \mathcal{L}_1\end{aligned} \tag{1.9}$$

where

$$F^{\mu\nu}(x) = \partial^\nu A^\mu(x) - \partial^\mu A^\nu(x). \tag{1.10}$$

is the electromagnetic field tensor, and enters in the redefined $\mathcal{L}_0$. $\mathcal{L}_1$ is defined as previously in Equation (1.6).

1.2.1.2 The S-matrix

We are interested in QED in the context of a collider experiment. Using the theory, we can predict the probabilities a final state particle configuration when knowing the initial state particle configuration, e.g the beam particles' 4-momenta and species, and calculate the differential cross-section of a particle scattering event. The system is in an initial state $|i\rangle$ at an initial time $t_i = -\infty$ long before the scattering, where the particles are too far apart to interact. The *S-matrix* is defined as the time evolution operator that relates the initial state at time $t_i = -\infty$ to the final state $|f\rangle$ at time $t_f = +\infty$:

$$S|i(t_i = -\infty)\rangle = |f(t_f = \infty)\rangle.$$

The S-matrix is the solution to the equations of motions for the fields given the initial and final states. After the collision, the probability density to measure certain particles with certain momenta, spins, etc. is

$$|\langle f|(S|i\rangle)|^2 = |\langle f|S|i\rangle|^2 \equiv S_{fi}.$$

We skip the exact form of the S-matrix here, but the interested reader is referred to page 101 of reference [17]. The S-matrix can be calculated to an arbitrary order of perturbation theory.

From the S-matrix expansion we can calculate experimentally observable properties, like the cross-sections, decay widths and lifetimes. This calculation is quite complicated. Luckily, Richard Feynman discovered a set of rules that lead to the result in an easier way.

1.2.1.3 Feynman rules

In Figure 1.3 we see a *Feynman diagram* for a basic QED scattering process, including the basic QED vertex (marked in red) coupling a fermion to a photon. All particle interactions in QED can be constructed by combining these basic vertices. Feynman discovered that the results of the complicated calculations involving the S-matrix expansion could be anticipated

Figure 1.3: A Feynman diagram for a basic QED scattering process. The basic QED vertices are written in red.

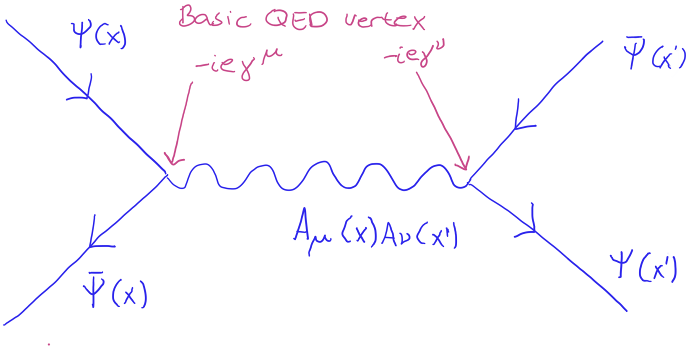

by drawing these diagrams and writing down factors corresponding to the different parts of the diagram. The allowed vertices in a given theory are found by inspecting the interaction Lagrangian density. The exact Feynman rules for QED can be found in Appendix B of reference [17]. All the information about the dynamics of the process, related to the physical theory, is contained in the so-called *Feynman amplitude* $\mathcal{M}$ within the S-matrix, whose absolute square is proportional to the cross-section of the process.

1.2.2 Electroweak interactions

To formulate a theory of weak interactions, we require gauge invariance of the Lagrangian density. Within the description in this section, fermion and boson masses are all zero. This is not what we observe in Nature, and in Section 1.2.4 these particles will acquire mass through the BEH mechanism.

1.2.2.1 Lepton sector

Experiments have shown that the weak charged current mediated by $W^{\pm}$ acts on left-handed particles only. This "handedness" is directly related to the chirality of a particle. For *massless* particles, the chirality of the particle is the same as the helicity of the particle, where helicity is the projection of the spin onto the direction of motion.[4] Because of this fundamental difference between right- and left-handed fields, we group the left-handed fields in doublets,

$$\Psi_l^{\mathrm{L}}(x) = \begin{pmatrix} \psi_{\nu_l}^{\mathrm{L}}(x) \\ \psi_l^{\mathrm{L}}(x) \end{pmatrix} \tag{1.11}$$

---

[4] Meaning the helicity is left-handed if the direction of the spin is in the opposite direction of the motion of the particle.

and we leave the right-handed fields in singlets $\psi_l^{\mathrm{R}}(x)$ and $\psi_{\nu_l}^{\mathrm{R}}(x)$. The left- and right-handed lepton fields are obtained by applying the projection operators $\mathrm{P_L}$ and $\mathrm{P_R}$,

$$\begin{aligned}\psi^{\mathrm{L}}(x) &= \mathrm{P_L}\psi(x), \quad \mathrm{P_L} \equiv \frac{1}{2}(1-\gamma_5), \\ \psi^{\mathrm{R}}(x) &= \mathrm{P_R}\psi(x), \quad \mathrm{P_R} \equiv \frac{1}{2}(1+\gamma_5),\end{aligned} \tag{1.12}$$

with the "fifth γ matrix" defined as $\gamma_5 = i\gamma_0\gamma_1\gamma_2\gamma_3$. Using the definitions above and neglecting the masses at this point, it can be shown that the free-fermion Lagrangian density in Equation 1.1 can be written as

$$\mathcal{L}_0 = i\left[\bar{\Psi}_l^{\mathrm{L}}(x)\gamma^\mu\partial_\mu\Psi_l^{\mathrm{L}}(x) + \bar{\psi}_l^{\mathrm{R}}(x)\gamma^\mu\partial_\mu\psi_l^{\mathrm{R}}(x) + \bar{\psi}_{\nu_l}^{\mathrm{R}}(x)\gamma^\mu\partial_\mu\psi_{\nu_l}^{\mathrm{R}}(x)\right]. \tag{1.13}$$

Summation over all different kind of leptons, $l = e, \mu, \tau$, is implied in this equation and in the following.

We follow the procedure as described in the last section and find a set of global phase transformations leaving the free-lepton Lagrangian density invariant, finally leading to conserved currents and quantities.

The Pauli matrices

$$\tau_1 = \begin{pmatrix} 0 & 1 \\ 1 & 0 \end{pmatrix}, \quad \tau_2 = \begin{pmatrix} 0 & -i \\ i & 0 \end{pmatrix}, \quad \tau_3 = \begin{pmatrix} 1 & 0 \\ 0 & -1 \end{pmatrix}, \tag{1.14}$$

satisfy the commutation relations $[\tau_i, \tau_j] = 2i\epsilon_{ijk}\tau_k$ with ϵ_{ijk} being the antisymmetric tensor. The global phase transformations

$$\begin{aligned}\Psi_l^{\mathrm{L}}(x) &\to \Psi_l^{L\prime}(x) = e^{\frac{1}{2}i\omega_j\tau_j}\Psi_l^{\mathrm{L}}(x) \\ \bar{\Psi}_l^{\mathrm{L}}(x) &\to \bar{\Psi}_l^{L\prime}(x) = \bar{\Psi}_l^{\mathrm{L}}(x)e^{-\frac{1}{2}i\omega_j\tau_j}\end{aligned} \tag{1.15}$$

leave the term $i\bar{\Psi}_l^{\mathrm{L}}(x)\gamma^\mu\partial_\mu\Psi_l^{\mathrm{L}}(x)$ in Equation (1.13) invariant. The right-handed lepton fields are *defined* as invariant under any $\mathrm{SU}(2)$ transformation. This ensures that the whole free-lepton Lagrangian density $\mathcal{L}_0$ is invariant and the corresponding conserved quantities are called the weak isospin currents,

$$J_i^\mu(x) = \frac{1}{2}\bar{\Psi}_l^{\mathrm{L}}(x)\gamma^\mu\tau_i\Psi_l^{\mathrm{L}}(x), \quad i = 1, 2, 3. \tag{1.16}$$

Conserved currents imply conserved quantities according to Noether's theorem, and the three conserved quantities are called weak isospin charges I_i^W,

$$I_i^W = \int d^3\mathbf{x} J_i^0(x) = \frac{1}{2}\int \mathrm{d}^3\mathbf{x}\Psi_l^{L\dagger}(x)\tau_i\Psi_l^{\mathrm{L}}(x), \quad i = 1, 2, 3. \tag{1.17}$$

Using Equation (1.12) and the Pauli matrices (Equation (1.14)) we can rewrite the two first components of the weak isospin currents in Equation (1.16) as

$$
\begin{aligned}
J^{\alpha}(x) &= \bar{\psi}_l(x)\gamma^{\alpha}(1-\gamma_5)\psi_{\nu_l}(x), && (1.18)\\
J^{\alpha\dagger} &= \bar{\psi}_{\nu_l}\gamma^{\alpha}(1-\gamma_5)\psi_l(x). && (1.19)
\end{aligned}
$$

These are charged currents, coupling the electrically neutral neutrinos to the charged leptons. The third component of the weak isospin current,

$$
J_3^{\mu}(x) = \frac{1}{2}\bar{\psi}_{\nu_l}^{\mathrm{L}}(x)\gamma^{\mu}\psi_{\nu_l}^{\mathrm{L}}(x) - \frac{1}{2}\bar{\psi}_l^{\mathrm{L}}(x)\gamma^{\mu}\psi_l^{\mathrm{L}}(x), \tag{1.20}
$$

is an electrically neutral current, it couples either electrically charged leptons or neutral neutrinos. The last term of J_3^{μ} is equal to the electromagnetic current in Equation (1.3) except for a constant factor, hinting at an interconnection between electromagnetic and weak interactions. Based on this we define a new current, the weak hypercharge current J_Y^{μ},

$$
J_Y^{\mu}(x) = \frac{1}{e}s^{\mu}(x) - J_3^{\mu}(x) = -\frac{1}{2}\bar{\Psi}_l^{\mathrm{L}}(x)\gamma^{\mu}\Psi_l^{\mathrm{L}}(x) - \bar{\psi}_l^{\mathrm{R}}(x)\gamma^{\mu}\psi_l^{\mathrm{R}}(x). \tag{1.21}
$$

We call the conserved quantity corresponding to this conserved current the weak hypercharge

$$
Y = \int d^3\mathbf{x} J_Y^0(x). \tag{1.22}
$$

From Equation (1.21) we see that the electric charge Q, the weak isocharge I_3^W and the weak hypercharge Y are linked via the equation

$$
Y = \frac{1}{e}Q - I_3^W. \tag{1.23}
$$

We can now find the weak isospin charge I_3^W and the weak hypercharge Y of the various leptons. From Equation (1.11) and the Pauli matrices defined in Equation (1.14) we find that

$$
\tau_3\Psi_l^{\mathrm{L}}(x) = \begin{pmatrix} 1 & 0 \\ 0 & -1 \end{pmatrix}\begin{pmatrix} \psi_{\nu_l}^{\mathrm{L}}(x) \\ \psi_l^{\mathrm{L}}(x) \end{pmatrix} = \begin{pmatrix} \psi_{\nu_l}^{\mathrm{L}}(x) \\ -\psi_l^{\mathrm{L}}(x) \end{pmatrix}, \tag{1.24}
$$

meaning that the left-handed ν_l neutrino has weak isospin charge $I_3^W = +\frac{1}{2}$ and the left-handed l^- lepton has weak isospin charge $I_3^W = -\frac{1}{2}$. The right-handed lepton fields are isoscalars which means the right-handed neutrino ν_l and lepton l^- have weak isospin charge 0. The right-handed antiparticles have weak isospin with the same value, but opposite sign, while the left-handed antiparticles have weak isospin charge 0. The values of the weak hypercharge follow from Equation (1.23).

The conservation of weak hypercharge also follows directly from the invariance of the free-lepton Lagrangian density (1.13) under the global $\mathrm{U}(1)$ phase transformations

$$
\begin{aligned}
\psi(x) &\rightarrow \psi'(x) = e^{i\beta Y}\psi(x), && (1.25)\\
\bar{\psi}(x) &\rightarrow \bar{\psi}'(x) = e^{-i\beta Y}\bar{\psi}(x),
\end{aligned}
$$

where β is a real number and Y is the weak hypercharge.

We now require $\mathcal{L}_0$ to be invariant under *local* $\mathrm{SU}(2)_\mathrm{L}$ and $\mathrm{U}(1)_\mathrm{Y}$ transformations. The local $\mathrm{SU}(2)_\mathrm{L}$ transformations are

$$\begin{aligned}
&\Psi_l^\mathrm{L}(x) \to \Psi_l^{L\prime}(x) = e^{\frac{1}{2}ig\tau_j\omega_j(x)}\Psi_l^\mathrm{L}(x) \\
&\bar{\Psi}_l^\mathrm{L}(x) \to \bar{\Psi}_l^{L\prime}(x) = \bar{\Psi}_l^\mathrm{L}(x)e^{-\frac{1}{2}ig\tau_j\omega_j(x)} \\
&\psi_l^\mathrm{R}(x) \to \psi_l^{R\prime}(x) = \psi_l^\mathrm{R}(x), \quad \psi_{\nu_l}^\mathrm{R}(x) \to \psi_{\nu_l}^{R\prime}(x) = \psi_{\nu_l}^\mathrm{R}(x) \\
&\bar{\psi}_l^\mathrm{R}(x) \to \bar{\psi}_l^{R\prime}(x) = \bar{\psi}_l^\mathrm{R}(x), \quad \bar{\psi}_{\nu_l}^\mathrm{R}(x) \to \bar{\psi}_{\nu_l}^{R\prime}(x) = \bar{\psi}_{\nu_l}^\mathrm{R}(x)
\end{aligned} \tag{1.26}$$

where $\omega_j(x),\ j = 1, 2, 3$ are three arbitrary real differentiable functions of x and g is a real constant which will be revealed as a coupling constant later. The free-lepton Lagrangian density in Equation (1.13) is not invariant under these transformations, and we must exchange the ordinary derivatives $\partial^\mu\Psi_l^\mathrm{L}(x)$ by covariant derivatives $D^\mu\Psi_l^\mathrm{L}(x)$,

$$\partial^\mu\Psi_l^\mathrm{L}(x) \to D^\mu\Psi_l^\mathrm{L}(x) = \left[\partial^\mu + ig\tau_j W_j^\mu(x)/2\right]\Psi_l^\mathrm{L}(x). \tag{1.27}$$

Note that we introduce three real gauge fields $W_j^\mu(x)$, in analogy to the one gauge field $A^\mu(x)$ introduced in QED, one for each $\mathrm{SU}(2)_\mathrm{L}$ generator. This leaves us with a new expression for the Lagrangian density

$$\tilde{\mathcal{L}}_0 = i\left[\bar{\Psi}_l^\mathrm{L}(x)\gamma^\mu D_\mu\bar{\Psi}_l^\mathrm{L}(x) + \bar{\psi}_l^\mathrm{R}(x)\gamma^\mu\partial_\mu\psi_l^\mathrm{R}(x) + \bar{\psi}_{\nu_l}^R(x)\gamma^\mu\partial_\mu\psi_{\nu_l}^\mathrm{R}(x)\right].$$

We also need the covariant derivatives $D^\mu\Psi_l^\mathrm{L}(x)$ to transform in the same way as the fields $\Psi_l^\mathrm{L}(x)$, i.e.

$$D^\mu\Psi_l^\mathrm{L}(x) \to e^{ig\tau_j\omega_j(x)/2}D^\mu\Psi_l^\mathrm{L}(x) \tag{1.28}$$

This is a complicated matter, but it can be shown that infinitesimal transformations

$$\begin{aligned}
W_i^\mu(x) \to W_i^{\mu\prime}(x) &= W_i^\mu(x) + \delta W_i^\mu(x) \\
&\equiv W_i^\mu(x) - \partial^\mu\omega_i(x) - g\epsilon_{ijk}(x)W_k^\mu(x), \quad \text{small}\,\omega_j(x)
\end{aligned} \tag{1.29}$$

are sufficient to consider. We now require local $\mathrm{U}(1)_\mathrm{Y}$ invariance. The local phase transformations are

$$\begin{aligned}
\psi(x) &\to \psi'(x) = e^{ig'Yf(x)}\psi(x) \\
\bar{\psi}(x) &\to \bar{\psi}'(x) = \bar{\psi}(x)e^{-ig'Yf(x)}.
\end{aligned} \tag{1.30}$$

Y is the weak hypercharge defined in Equation (1.22), g' is a real number (a coupling constant) to be determined later, and $f(x)$ is an arbitrary real differentiable function. As before we replace the ordinary derivatives by covariant derivatives,

$$\partial^\mu\psi(x) \to D^\mu\psi(x) = \left[\partial^\mu + ig'YB^\mu(x)\right]\psi(x), \tag{1.31}$$

where $B^\mu(x)$ is a real gauge field that transforms like

$$B^\mu(x) \to B^{\mu\prime}(x) = B^\mu(x) - \partial^\mu f(x) \tag{1.32}$$

and ψ is any one of the four lepton fields ψ_l^{L}, $\psi_{\nu_l}^{\mathrm{L}}$, ψ_l^{R} or $\psi_{\nu_l}^{\mathrm{R}}$. This ensures local $\mathrm{U}(1)_{\mathrm{Y}}$ invariance.

We now use the local $SU(2)_{\mathrm{L}}$ *and* $U(1)_{\mathrm{Y}}$ transformations at the same time and obtain the leptonic Lagrangian density[5]

$$\begin{aligned}
\mathcal{L}_{\mathrm{L}} &= i\left[\bar{\Psi}_l^{\mathrm{L}}(x)\gamma^\mu D_\mu \Psi_l^{\mathrm{L}}(x) + \bar{\psi}_l^{\mathrm{R}}(x)\gamma^\mu D_\mu \psi_l^{\mathrm{R}}(x) + \bar{\psi}_{\nu_l}^{\mathrm{R}}(x)\gamma^\mu D_\mu \psi_{\nu_l}^{\mathrm{R}}(x)\right] \qquad (1.33)\\
D^\mu \Psi_l^{\mathrm{L}}(x) &= \left[\partial^\mu + \frac{1}{2} i g \tau_j W_j^\mu(x) - \frac{1}{2} i g' B^\mu(x)\right] \Psi_l^{\mathrm{L}}(x)\\
D^\mu \psi_l^{\mathrm{R}}(x) &= \left[\partial^\mu - i g' B^\mu(x)\right] \psi_l^{\mathrm{R}}(x)\\
D^\mu \psi_{\nu_l}^{\mathrm{R}}(x) &= \partial^\mu \psi_{\nu_l}^{\mathrm{R}}(x).
\end{aligned}$$

We *define* the fields $W_i^\mu(x)$ to be invariant under local $\mathrm{U}(1)_{\mathrm{Y}}$ transformations and $B^\mu(x)$ to be invariant under local $\mathrm{SU}(2)_{\mathrm{L}}$ transformations, and the Lagrangian density $\mathcal{L}_{\mathrm{L}}$ is then invariant under both and is said to be $\mathrm{SU}(2)_{\mathrm{L}} \times \mathrm{U}(1)_{\mathrm{Y}}$ gauge-invariant.

Next, we rewrite the leptonic Lagrangian density (1.33) in terms of the weak isospin currents defined in Equation (1.16),

$$\mathcal{L}_{\mathrm{L}} = \mathcal{L}_0 - g J_i^\mu(x) W_{i\mu}(x) - g' J_Y^\mu(x) B_\mu(x) \equiv \mathcal{L}_0 + \mathcal{L}_I, \qquad (1.34)$$

where $\mathcal{L}_I$ represents the interaction of the weak isospin and weak hypercharge currents with the gauge fields $W_{i\mu}(x)$ and $B_\mu(x)$.

We rewrite $\mathcal{L}_I$ in terms of the charged leptonic currents $J^\mu(x)$ and $J^{\mu\dagger}(x)$,

$$\begin{aligned}
J_\mu(x) &= 2[J_{1\mu}(x) - i J_{2\mu}(x)] = \bar{\psi}_l(x)\gamma_\mu(1-\gamma_5)\psi_{\nu_l}(x) \qquad (1.35)\\
J_\mu^\dagger(x) &= 2[J_{1\mu}(x) + i J_{2\mu}(x)] = \bar{\psi}_{\nu_l}(x)\gamma_\mu(1-\gamma_5)\psi_l(x),
\end{aligned}$$

and a new gauge field $W_\mu(x)$ and its adjoint $W_\mu^\dagger(x)$,

$$\begin{aligned}
W_\mu(x) &= \frac{1}{\sqrt{2}}\left[W_{1\mu} - i W_{2\mu}(x)\right] \qquad (1.36)\\
W_\mu^\dagger(x) &= \frac{1}{\sqrt{2}}\left[W_{1\mu} + i W_{2\mu}(x)\right].
\end{aligned}$$

The first two terms of $\mathcal{L}_I$ can be written as

$$-g\sum_{i=1}^{2} J_i^\mu(x) W_{i\mu}(x) = -\frac{g}{2\sqrt{2}}\left[J^{\mu\dagger}(x) W_\mu(x) + J^\mu(x) W_\mu^\dagger(x)\right]. \qquad (1.37)$$

From Equations (1.37) and (1.35) we get the basic vertices for the charged electroweak interactions, drawn in Figure 1.4(a). The quanta of the two fields W^μ and $W^{\mu\dagger}$ are interpreted as the physical, yet still massless, $W^\pm$ bosons.

We return to Equation (1.34) and concentrate on the last two terms of $\mathcal{L}_I$, rewriting

---

[5] We urge the reader to take care not to be confused here. The notation follows what is done in reference [17]. The three D_μ's are not defined by themselves, but rather the three combinations of the D_μ's and the spinors are uniquely defined as written.

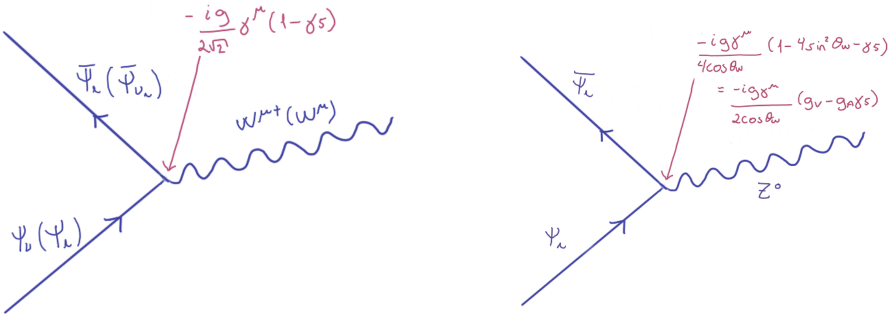

(a) $Wl\nu$ vertex (b) Zl^+l^- vertex

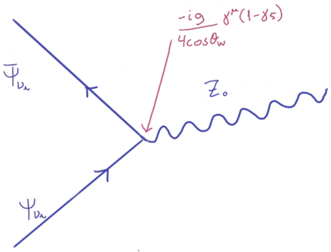

(c) $Z\nu\bar{\nu}$ vertex

Figure 1.4: Basic vertices involving the weak gauge bosons.

$W_{3\mu}(x)$ and $B_\mu(x)$ as linear combinations of two new Hermitian fields $A_\mu(x)$ and $Z_\mu(x)$, and also introducing the weak mixing angle θ_W (also known as the Weinberg angle),

$$\begin{aligned} W_{3\mu}(x) &= \cos\theta_W Z_\mu(x) + \sin\theta_W A_\mu(x) \\ B_\mu(x) &= -\sin\theta_W Z_\mu(x) + \cos\theta_W A_\mu(x). \end{aligned} \tag{1.38}$$

The weak mixing angle is a quantitative measure of the mixture of weak and electromagnetic interactions. A value $\theta_W = 0$ totally decouples the two interactions. θ_W must be measured in experiments. The current and precise measurements yield a value of $\sin^2\theta_W = 0.23129$ [16].

Combining (1.38) with the expression (1.21) we rewrite the two last terms of Equation (1.34) as

$$\begin{aligned} &-J_3^\mu(x)W_{3\mu}(x) - g'J_Y^\mu(x)B_\mu(x) \\ &\quad= -\frac{g'}{e}s^\mu(x)\big[-\sin\theta_W Z_\mu(x) + \cos\theta_W A_\mu(x)]\big] \\ &\quad- J_3^\mu(x)\big(g[\cos\theta_W Z_\mu(x) + \sin\theta_W A_\mu(x)] \\ &\quad- g'[-\sin\theta_W Z_\mu(x) + \cos\theta_W A_\mu(x)]\big). \end{aligned} \tag{1.39}$$

We now demand that $A_\mu(x)$ is the electromagnetic field and that it couples to electric charges in the usual way, i.e. through the term $s^\mu(x)A_\mu(x)$ in the interaction Lagrangian in Equation (1.6). Then we see that the term $J_3^\mu(x)A_\mu(x)$ must vanish. This means we require $g'\cos\theta_W = g\sin\theta_W$, and then $g'\cos\theta_W = g\sin\theta_W = e$. With this final step we arrive at the $\mathrm{SU(2)_L} \times \mathrm{U(1)_Y}$ gauge-invariant interaction Lagrangian density that Sheldon Glashow proposed in 1961,

$$\begin{aligned}\mathcal{L}_I = &- s^{\mu}(x)A_{\mu}(x) - \frac{g}{2\sqrt{2}}\big[J^{\mu\dagger}(x)W_{\mu}(x) + J^{\mu}(x)W_{\mu}^{\dagger}(x)\big] \\ &- \frac{g}{\cos\theta_W}\big[J_3^{\mu}(x) - \frac{1}{e}\sin^2\theta_W s^{\mu}(x)\big]Z_{\mu}(x) \end{aligned} \tag{1.40}$$

We easily recognize the first term from QED, the electromagnetic current is coupled to the photon field. The second and third term we saw earlier in Equation (1.37). The last two terms represent weak neutral currents, and we can get the basic vertices for the neutral electroweak currents. This is illustrated in Figures 1.4(b) and 1.4(c). The quantum of the $Z_{\mu}(x)$ field is the physical, yet massless, Z^0 boson.

1.2.2.2 Quark sector

The description of quarks in electroweak theory very much resembles the one for leptons. The six left-handed quarks are placed in doublets,

$$\begin{pmatrix} u \\ d \end{pmatrix}_L, \quad \begin{pmatrix} c \\ s \end{pmatrix}_L, \quad \begin{pmatrix} t \\ b \end{pmatrix}_L$$

with weak isospin $I_3^W = +\frac{1}{2}$ for up-type quarks and $I_3^W = -\frac{1}{2}$ for down-type quarks, and the six right-handed quarks, u_R, d_R, c_R, s_R, t_R and b_R, are singlets. However, unlike the leptons, the three generations of quarks have the ability to transform between the three generations through charged current interactions mediated by $W^{\pm}$ bosons. The vertex factors involving quarks in electroweak reactions are equal to the ones involving leptons, except that they carry an extra factor representing the probability of the quark to transition between different generations. This probability is given by the Cabibboo-Kobayashi-Maskawa (CKM) mixing matrix. The current values of these elements are [16],

$$\begin{aligned} V_{\text{CKM}} &= \begin{pmatrix} |V_{ud}| & |V_{us}| & |V_{ub}| \\ |V_{cd}| & |V_{cs}| & |V_{cb}| \\ |V_{td}| & |V_{ts}| & |V_{tb}| \end{pmatrix} \\ &= \begin{pmatrix} 0.97434^{+0.00011}_{-0.00012} & 0.22506 \pm 0.00050 & 0.00357 \pm 0.00015 \\ 0.22492 \pm 0.0050 & 0.97351 \pm 0.00013 & 0.0411 \pm 0.0013 \\ 0.00875^{+0.00032}_{-0.00033} & 0.0403 \pm 0.0013 & 0.99915 \pm 0.00005 \end{pmatrix} \end{aligned}$$

The probability for a quark transition from flavor i to flavor j is $|V_{ij}|^2$. Only transitions between up quarks and down quarks are allowed, i.e. an up (down) quark can never transform into a different flavor up (down) quark. The largest values are on the diagonal, meaning that the transitions between the same generation quarks (u↔d, c↔s, t↔b) are more common than jumping generations (e.g. u↔s or s↔t).

1.2.2.3 Vector boson self-interaction

The vector bosons $W^{\pm}$ and Z^0 carry a weak charge, and therefore have self-interactions, meaning they interact also when no leptons or quarks are present. As for the photon fields, we need terms that are $\mathrm{SU}(2)_\mathrm{L} \times \mathrm{U}(1)_\mathrm{Y}$ invariant. For $B^\mu(x)$ we construct an expression in analogy with $A^\mu(x)$ in QED, as defined in Equation (1.10),

$$-\frac{1}{4}B_{\mu\nu}(x)B^{\mu\nu}(x), \quad B^{\mu\nu}(x) \equiv \partial^\nu B^\mu(x) - \partial^\mu B^\nu(x)$$

The case for the $W_i^\mu(x)$ fields is more complex. The interested reader is referred to a book on Quantum Field Theory, e.g. [17], the end result is quoted here:

$$-\frac{1}{4}G_{i,\mu\nu}(x)G_i^{\mu\nu}(x), \quad G_i^{\mu\nu} \equiv F_i^{\mu\nu}(x) + g\epsilon_{ijk}W_j^\mu(x)W_k^\nu(x)$$

where ϵ_{ijk} is the antisymmetric tensor and

$$F_i^{\mu\nu} \equiv \partial^\nu W_i^\mu(x) - \partial^\mu W_i^\nu(x).$$

Combining everything, we get

$$\begin{aligned}
\mathcal{L}^B &= -\frac{1}{4}B_{\mu\nu}(x)B^{\mu\nu}(x) - \frac{1}{4}G_{i,\mu\nu}(x)G_i^{\mu\nu}(x) \\
&= -\frac{1}{4}B_{\mu\nu}(x)B^{\mu\nu}(x) - \frac{1}{4}F_{i,\mu\nu}(x)F_i^{\mu\nu}(x) \\
&+ g\epsilon_{ijk}W_{i,\mu}(x)W_{j,\nu}(x)\partial^\mu W_k^\nu(x) \\
&- \frac{1}{4}g^2\epsilon_{ijk}\epsilon_{ilm}W_j^\mu(x)W_k^\nu(x)W_{l,\mu}(x)W_{m,\nu}(x)
\end{aligned} \tag{1.41}$$

The first two terms of Equation (1.41) represent the free gauge fields, while the two last terms represent self-interaction of the gauge bosons. The basic vertices of this theory are shown in Figure 1.5. No other combination (such as $\gamma\gamma\gamma$ or $Z^0Z^0Z^0$) is allowed within the SM.

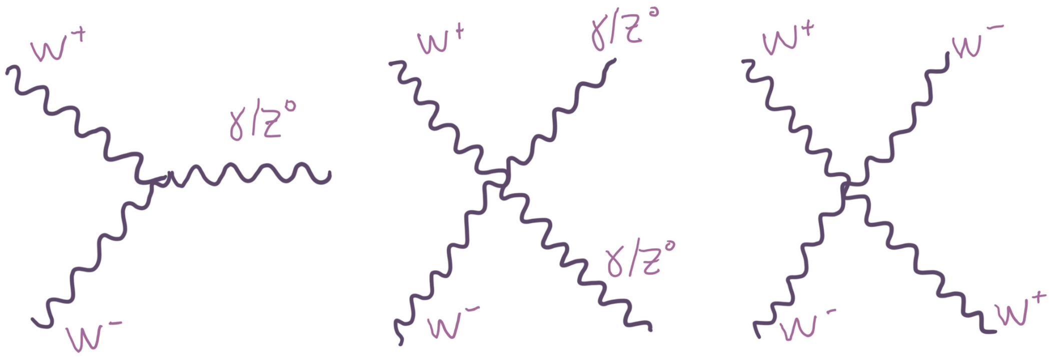

Figure 1.5: Additional basic vertices of the electroweak theory, representing the self-interaction of gauge bosons.

1.2.3 Quantum Chromodynamics

Quarks carry the quantum number color, also known as color charge. The different flavors of quarks carry different mass, as noted in Figure 1.1, but the three different colors of any given quark flavor carry equal mass.

In analogy with QED, we claim that the free-quark Lagrangian density is

$$\mathcal{L}_0 = \bar{\Psi}_q(x)(\gamma^\mu i\partial_\mu - m_q)\Psi_q(x), \tag{1.42}$$

with the quarks in color triplets

$$\Psi_q(x) = \begin{pmatrix} \psi_{q_r}(x) \\ \psi_{q_g}(x) \\ \psi_{q_b}(x) \end{pmatrix}.$$

The QCD Lagrangian density is invariant under the *global* $\mathrm{SU}(3)_\mathrm{C}$ transformations

$$\begin{aligned} \Psi_q(x) &\to \Psi'_q(x) = U(\alpha)\Psi_q(x) \equiv e^{\frac{1}{2}i\alpha_i\lambda_i}\Psi_q(x) \\ \bar{\Psi}_q(x) &\to \bar{\Psi}'_q(x) = \bar{\Psi}_q(x)U^\dagger(\alpha) \equiv \bar{\Psi}_q(x)e^{-\frac{1}{2}i\alpha_i\lambda_i} \end{aligned} \tag{1.43}$$

$\lambda_i,\ i = 1, 2, \ldots 8$ are the eight Gell-Mann matrices that act as the generators of $\mathrm{SU}(3)_\mathrm{C}$ and α_i are eight real constants and $\alpha \equiv (\alpha_1, \alpha_2, \ldots, \alpha_8)$. The invariance follows from the unitarity of the $\mathrm{SU}(3)_\mathrm{C}$ transformations $U^\dagger U = 1$, yielding eight conserved currents,

$$S_i^\mu(x) = \frac{1}{2}\bar{\Psi}_q(x)\gamma^\mu\lambda_i\Psi_q(x). \tag{1.44}$$

This color-octet current conserves the color. Quarks carry color charge (red, green, blue), antiquarks carry anticolor (antired, antigreen, antiblue) and gluons carry a color and an anticolor. A quark can change color for example from blue (b) to red (r) by radiating a gluon (b$\bar{\mathrm{r}}$), and the gluon compensates for this by carrying the colors blue and antired, as illustrated in Figure 1.6. Note that the *flavor* does not change, e.g. an up quark stays an up quark, only the charged currents of the weak interactions are flavor-changing.

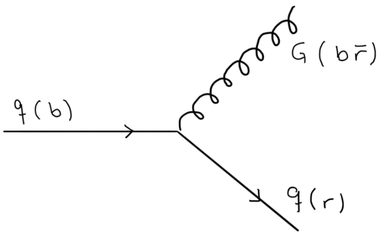

Figure 1.6: An example of the color-octet current conserving color. An incoming blue quark radiates a blue+antired gluon and transitions into a red quark. There are 8 gluons in the SM with different color-anti color combinations that accounts for all possible color transitions.

We now consider local $\mathrm{SU}(3)_\mathrm{C}$ transformations

$$\begin{aligned} \Psi_q(x) &\to \Psi'_q(x) = e^{\frac{1}{2}ig_s\lambda_j\omega_j(x)}\Psi_q(x) \\ \bar{\Psi}_q(x) &\to \Psi'_q(x) = \bar{\Psi}_q(x)e^{-\frac{1}{2}ig_s\lambda_j\omega_j(x)}, \end{aligned} \tag{1.45}$$

with $\omega_j(x),\ j = 1, 2, \ldots, 8$ are real differentiable functions and g_s is a real constant which later will be identified as the strong coupling constant. To ensure invariance under these local $\mathrm{SU}(3)_\mathrm{C}$ transformations, we exchange the ordinary derivatives ∂_μ for covariant derivatives D_μ,

$$\partial^\mu \Psi_q(x) \to D^\mu \Psi_q(x) = \left(\partial^\mu + \frac{1}{2} i g_s \lambda_j A_j^\mu\right) \Psi_q(x) \tag{1.46}$$

The eight new real gauge fields $A_j^\mu(x)$ are called gluon fields. Combining the free-quark Lagrangian density in Equation (1.42) and the covariant derivatives we get

$$\mathcal{L}_q = \bar{\Psi}_q(x)\left(i\gamma^\mu D_\mu - m_q\right) = \bar{\Psi}_q(x)\left(i\gamma^\mu \partial_\mu - m_q\right)\Psi_q(x) - g_s S_\mu^j A_j^\mu = \mathcal{L}_0 + \mathcal{L}_\mathrm{I}, \tag{1.47}$$

with S_μ^j defined in Equation (1.44). $\mathcal{L}_\mathrm{I}$ generates a three-point quark-gluon vertex, as illustrated in Figure 1.7(a).

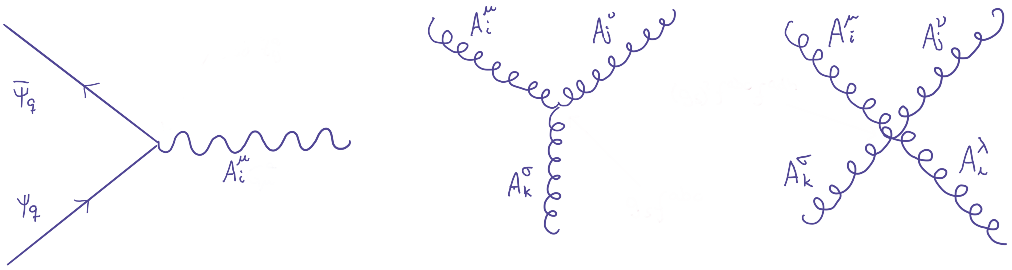

(a) Basic vertex for quark-gluon interaction.

(b) Basic vertices for gluon self-interaction.

Figure 1.7: Feynman diagrams of the basic vertices of QCD.

To ensure that the Lagrangian density $\mathcal{L}_q$ is invariant under the local $\mathrm{SU}(3)_\mathrm{C}$ transformations in Equation (1.45), the transformation of the gluon fields $A_j^\mu(x)$ are chosen carefully such that the covariant derivatives $D^\mu \Psi_q(x)$ transform in the same way as the fields $\Psi_q(x)$ themselves,

$$D^\mu \Psi_q(x) \to e^{\frac{1}{2} i g_s \lambda_j \omega_j(x)} D^\mu \Psi_q(x).$$

As for electroweak interactions this is a complicated matter, but it can be shown [17] that it suffices to consider infinitesimal transformations given by

$$A_i^\mu(x) \to A_i^{\mu\prime}(x) \equiv A_i^\mu(x) - \partial^\mu \omega_i(x) - g_s f_{ijk} \omega_j(x) A_k^\mu(x)$$

for small $\omega_j(x)$, where f_{ijk} are the structure constants defined by the commutation relation $[\hat{F}_i, \hat{F}_j] = i f_{ijk} \hat{F}_k$ with summing over repeated color indices $k = 1, 2, \ldots,\ 8$, and $\hat{F}_i = \frac{1}{2}\lambda_i,\ i = 1, 2, \ldots 8$.

In addition to the terms in $\mathcal{L}_q$ describing quark fields and the interactions between quark and gluon fields, the complete QCD Lagrangian density contains terms which describe the gluons in the absence of quarks. These terms also need to be $\mathrm{SU}(3)_\mathrm{C}$ gauge invariant. In analogy with QED and the term added in Equation (1.9) describing the free electromagnetic field, we examine the following expression describing free gluon fields,

$$-\frac{1}{4}F_{i\mu\nu}(x)F_i^{\mu\nu}(x), \quad F_i^{\mu\nu} \equiv \partial^\nu A_i^\mu(x) - \partial^\mu A_i^\nu(x). \tag{1.48}$$

This expression is not $\mathrm{SU}(3)_\mathrm{C}$ gauge invariant. To restore the invariance, the free gluon fields are replaced by $G_i^{\mu\nu}(x)$,

$$G_i^{\mu\nu}(x) \equiv F_i^{\mu\nu}(x) + g_s f_{ijk} A_j^\mu(x) A_k^\nu(x), \tag{1.49}$$

obtaining the Lagrangian density for the free gluon fields,

$$\mathcal{L}_G = -\frac{1}{4}G_{i\mu\nu}(x)G_i^{\mu\nu}(x). \tag{1.50}$$

The full Lagrangian density for the strong interaction is obtained by combining Equations (1.42) and (1.50),

$$\mathcal{L} = \bar{\Psi}_q(x)[i\gamma_\mu D^\mu - m_q]\Psi_q(x) - \frac{1}{4}G_{i,\mu\nu}(x)G_i^{\mu\nu}(x). \tag{1.51}$$

Rewriting $\mathcal{L}_G$ in Equation (1.50) using Equation (1.49) we obtain

$$\begin{aligned}\mathcal{L}_G = &-\frac{1}{4}F_{i,\mu\nu}(x)F_i^{\mu\nu}(x) + g_s f_{ijk} A_{i,\mu}(x) A_{j,\nu}(x) \partial^\mu A_k^\nu(x) \\ &-\frac{1}{4}g_s^2 f_{ijk} f_{ilm} A_j^\mu(x) A_k^\nu(x) A_{l,\mu}(x) A_{m,\nu}(x).\end{aligned} \tag{1.52}$$

The first term represents eight non-interacting massless gluon fields. The second and third terms represent self-interactions of the gluon fields, as illustrated in Figure 1.7(b).

1.2.4 The Brout-Englert-Higgs mechanism

In the previous sections all lepton and boson masses were set to zero, while in Nature the weak gauge bosons $W^\pm$ and Z^0 and all the fermions have a non-zero mass. Simply adding a mass term (e.g. $-m_l\bar{\psi}_l(x)\psi_l(x)$ for leptons) spoils the gauge invariance of the theory. The solution is spontaneous symmetry breaking (SSB) of the $\mathrm{SU}(2)_\mathrm{L} \times \mathrm{U}(1)_\mathrm{Y}$ invariance while preserving the $\mathrm{U}(1)$ invariance of QED and keeping the photon massless.

In the following we focus on symmetry breaking in the lepton sector of the electroweak theory. Similar arguments could be made also for quarks.

The Lagrangian density of the electroweak theory is

$$\mathcal{L} = \mathcal{L}_\mathrm{L} + \mathcal{L}_\mathrm{B}$$

where $\mathcal{L}_\mathrm{L}$ is the leptonic Lagrangian density in Equation (1.33) and $\mathcal{L}_\mathrm{B}$ is the gauge boson Lagrangian density in Equation (1.41). We know that the Lagrangian density $\mathcal{L}$ is exactly invariant under $\mathrm{SU}(2)_\mathrm{L} \times \mathrm{U}(1)_\mathrm{Y}$ gauge transformations. In the following we introduce the Brout-Englert-Higgs (BEH) field, that is a scalar field with a non-vanishing vacuum expectation value (VEV) which is not invariant under the gauge transformations. This will result in a spontaneous symmetry breaking.

We want to break the $\mathrm{SU}(2)_\mathrm{L}\times\mathrm{U}(1)_\mathrm{Y}$ symmetry, and therefore we introduce a new weak isospin doublet

$$\Phi(x) = \begin{pmatrix}\phi_a(x)\\ \phi_b(x)\end{pmatrix}$$

where $\phi_a(x)$ and $\phi_b(x)$ are scalar fields under Lorentz transformations. This new doublet transforms the same way as the isospin doublet $\Psi_l^\mathrm{L}(x)$ in Equations (1.26) and (1.30) under $SU(2)_\mathrm{L}\times\mathrm{U}(1)_\mathrm{Y}$ gauge transformations, i.e. under $SU(2)_\mathrm{L}$ transformations according to

$$\begin{aligned}\Phi(x) &\to \Phi'(x) = e^{\frac{1}{2}ig\tau_j\omega_j(x)}\Phi(x)\\ \Phi^\dagger(x) &\to \Phi^{\dagger\prime}(x) = \Phi^\dagger(x)e^{-\frac{1}{2}ig\tau_j\omega_j(x)}\end{aligned} \tag{1.53}$$

and under $U(1)_\mathrm{Y}$ according to

$$\begin{aligned}\Phi(x) &\to \Phi'(x) = e^{ig'Yf(x)}\Phi(x)\\ \Phi^\dagger(x) &\to \Phi^{\dagger\prime}(x) = \Phi^\dagger(x)e^{-ig'Yf(x)}\end{aligned} \tag{1.54}$$

We now add a new term $\mathcal{L}_\mathrm{H}$ to the Lagrangian density to include the BEH field $\Phi(x)$ and its interactions with the gauge boson fields, while retaining the $\mathrm{SU}(2)_\mathrm{L}\times\mathrm{U}(1)_\mathrm{Y}$ gauge-invariance,

$$\mathcal{L}_\mathrm{H} = [D^\mu\Phi(x)]^\dagger[D_\mu\Phi(x)] - \mu^2\Phi^\dagger(x)\Phi(x) - \lambda[\Phi^\dagger(x)\Phi(x)]^2. \tag{1.55}$$

The covariant derivatives are

$$D^\mu\Phi(x) = \left[\partial^\mu + \frac{1}{2}ig\tau_jW_j^\mu(x) + ig'YB^\mu(x)\right]\Phi(x).$$

in analogy with Equation (1.28).

The two last terms of Equation (1.55) define the potential energy density of the field. For it to be bounded from below, we require $\lambda > 0$. For μ^2 we choose $\mu^2 < 0$, which gives the potential its characteristic shape, namely that of a Mexican hat, or the bottom of a bottle, as illustrated in Figure 1.8. This shape enables a spontaneous symmetry breaking. The energy density is at a minimum for a constant BEH field

$$\Phi(x) = \Phi_0 = \begin{pmatrix}\phi_a^0\\ \phi_b^0\end{pmatrix}, \quad \Phi_0^\dagger\Phi_0 = |\phi_a^0|^2 + |\phi_b^0|^2 = \frac{v^2}{2}, \quad v = \sqrt{-\frac{\mu^2}{\lambda}}.$$

Choosing any one point induces a spontaneous symmetry breaking. We choose

$$\Phi_0 = \begin{pmatrix}\phi_a^0\\ \phi_b^0\end{pmatrix} = \frac{1}{\sqrt{2}}\begin{pmatrix}0\\ v\end{pmatrix}.$$

Any other choice of Φ_0 is related to this value by a global phase transformation.

In general, the BEH field of the vacuum ground state Φ_0 is *not* $SU(2)_\mathrm{L}\times\mathrm{U}(1)_\mathrm{Y}$ gauge-invariant. It must however be invariant under electromagnetic $\mathrm{U}(1)$ gauge transformations

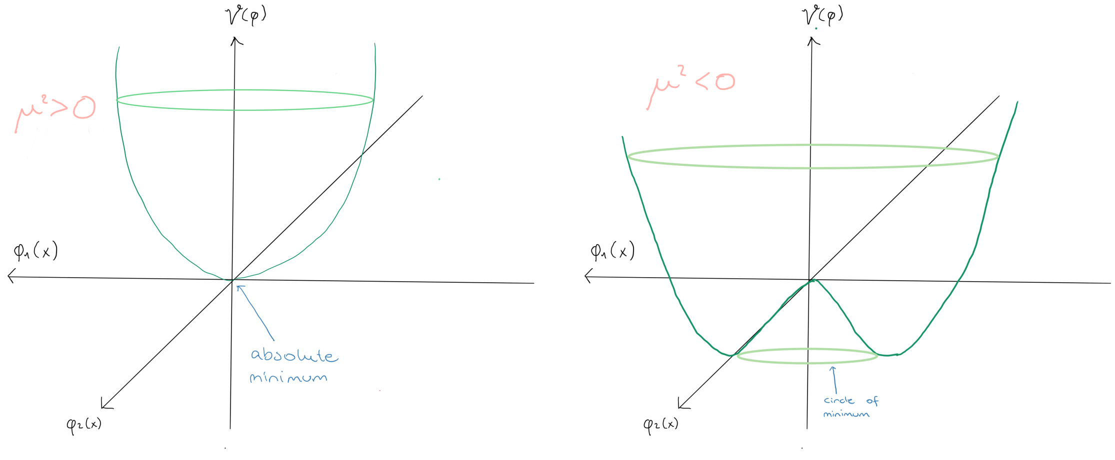

(a) $\mu^2 > 0$ (b) $\mu^2 < 0$

Figure 1.8: The potential energy density $\mathcal{V}(\Phi)$ for $\lambda > 0$. Choosing a value $\mu^2 > 0$ generates a function with one absolute minimum, while $\mu^2 < 0$ generates a local maximum and a whole circle of absolute degenerate minima.

due to the zero photon mass that is indicative of an unbroken symmetry. We assign the weak hypercharge $Y = \frac{1}{2}$ to the Higgs field. With this choice we see that the lower component, with $I_3 = -\frac{1}{2}$, has electric charge 0 according to Equation (1.23). Looking at the electromagnetic $\mathrm{U}(1)$ transformation of the BEH field,

$$\Phi(x) \to \Phi'(x) = e^{-i(Y+I_3^W)ef(x)}\Phi(x),$$

we see that this ensures that the lower component of the BEH field is invariant.

The upper component, with $I_3 = \frac{1}{2}$, is not invariant under this transformation.

To account for the lepton masses we need another term in the Lagrangian density, $\mathcal{L}^{\mathrm{LH}}$, a Yukawa interaction of the following form:

$$\begin{aligned} \mathcal{L}_{\mathrm{LH}} = &- g_l\left[\bar{\Psi}_l^{\mathrm{L}}(x)\psi_l^{\mathrm{R}}(x)\Phi(x) + \Phi^\dagger(x)\bar{\psi}_l^{\mathrm{R}}(x)\Psi_l^{\mathrm{L}}(x)\right] \\ &- g_{\nu_l}\left[\bar{\Psi}_l^{\mathrm{L}}(x)\psi_{\nu_l}^{\mathrm{R}}(x)\tilde{\Phi}(x) + \tilde{\Phi}^\dagger\bar{\psi}_{\nu_l}^{\mathrm{R}}(x)\Psi_l^{\mathrm{L}}(x)\right], \end{aligned} \tag{1.56}$$

where g_l and g_{ν_l} are dimensionless coupling constants and $\tilde{\Phi}(x)$ is given by

$$\tilde{\Phi}(x) = -i[\Phi^\dagger(x)\tau_2]^\top = \begin{pmatrix} \phi_b^\star(x) \\ -\phi_a^\star(x) \end{pmatrix}.$$

The Lagrangian density $\mathcal{L}_{\mathrm{LH}}$ can be shown to be invariant under $\mathrm{SU}(2)_{\mathrm{L}} \times \mathrm{U}(1)_{\mathrm{Y}}$ gauge transformations.

The total Lagrangian density of the standard electroweak theory for leptonic processes is summarized as

$$\mathcal{L} = \mathcal{L}_{\mathrm{L}} + \mathcal{L}_{\mathrm{B}} + \mathcal{L}_{\mathrm{H}} + \mathcal{L}_{\mathrm{LH}}$$

with $\mathcal{L}_\text{L}$ from (1.33), $\mathcal{L}_\text{B}$ from (1.41), $\mathcal{L}_\text{H}$ from (1.55) and $\mathcal{L}_\text{LH}$ from (1.56):

$$\begin{aligned}\mathcal{L} = {} & i\left[\bar{\Psi}_l^\text{L}(x)\gamma^\mu D_\mu \Psi_l^\text{L}(x) + \bar{\psi}_l^\text{R}(x)\gamma^\mu D_\mu \psi_l^\text{R}(x) + \bar{\psi}_{\nu_l}^\text{R}(x)\gamma^\mu D_\mu \psi_{\nu_l}^\text{R}(x)\right] \\ & - \frac{1}{4}B_{\mu\nu}(x)B^{\mu\nu}(x) - \frac{1}{4}G_{i,\mu\nu}(x)G_i^{\mu\nu}(x) \\ & + [D^\mu\Phi(x)]^\dagger[D_\mu\Phi(x)] - \mu^2\Phi^\dagger(x)\Phi(x) - \lambda[\Phi^\dagger(x)\Phi(x)]^2 \\ & - g_l\left[\bar{\Psi}_l^\text{L}(x)\psi_l^\text{R}(x)\Phi(x) + \Phi^\dagger(x)\bar{\psi}_l^\text{R}(x)\Psi_l^\text{L}(x)\right] \\ & - g_{\nu_l}\left[\bar{\Psi}_l^\text{L}(x)\psi_{\nu_l}^\text{R}(x)\tilde{\Phi}(x) + \tilde{\Phi}^\dagger\bar{\psi}_{\nu_l}^\text{R}(x)\Psi_l^\text{L}(x)\right],\end{aligned} \tag{1.57}$$

In order to facilitate a more practical interpretation of the Lagrangian density, we change now to the unitary gauge. Any BEH field can be reparametrized in terms of its deviation from the vacuum field Φ_0 in the form

$$\Phi(x) = \frac{1}{\sqrt{2}}\begin{pmatrix}\eta_1(x) + i\eta_2(x) \\ v + \sigma(x) + i\eta_3(x)\end{pmatrix} \tag{1.58}$$

with $\sigma(x)$ and $\eta_i(x)$, $i = 1, 2, 3$ as real fields. Written from now on in the unitary gauge, the BEH field $\Phi(x)$ can be written as

$$\Phi(x) = \frac{1}{\sqrt{2}}\begin{pmatrix}0 \\ v + \sigma(x)\end{pmatrix}. \tag{1.59}$$

The three $\eta(x)$ fields are now gone.[6] The gauge transformation used to transform Equation (1.58) to (1.59) is a $SU(2)_\text{L}\times\text{U}(1)_\text{Y}$ transformation, see equations (1.54) and (1.53). All other fields also transform according to equations (1.26), (1.29) and (1.30), (1.32). In the following we assume all fields are expressed in the unitary gauge.

We now transform the Lagrangian density in Equation (1.57) into the unitary gauge. This is done by writing $\Phi(x)$ in the unitary gauge and using Equations (1.36) and (1.38) to replace the fields $W_j^\mu(x)$ and $B^\mu(x)$ by $W^\mu(x)$, $W^{\dagger\mu}(x)$, $Z^\mu(x)$ and $A^\mu(x)$. The actual calculations are omitted here, only the result is quoted.

Transforming the terms $\mathcal{L}_\text{B} + \mathcal{L}_\text{H}$ from Equations (1.33) and (1.41) we get

$$\begin{aligned}\mathcal{L}_\text{B} + \mathcal{L}_\text{H} = & -\frac{1}{4}F_{\mu\nu}(x)F^{\mu\nu}(x) \\ & - \frac{1}{4}F^\dagger_{W\mu\nu}(x)F_W^{\mu\nu}(x) + m_W^2 W_\mu^\dagger(x)W^\mu(x) \\ & - \frac{1}{4}Z_{\mu\nu}(x)Z^{\mu\nu}(x) + \frac{1}{2}m_Z^2 Z_\mu(x)Z^\mu(x) \\ & + \frac{1}{2}(\partial^\mu\sigma(x))\partial_\mu\sigma(x)) - \frac{1}{2}m_H^2\sigma(x)^2 \\ & + \mathcal{L}_\text{BB,I} + \mathcal{L}_\text{HH,I} + \mathcal{L}_\text{HB,I} + \text{constant term},\end{aligned} \tag{1.60}$$

---

[6] The unitary gauge is designed for exactly this purpose, to transform away the so-called Golds tone fields, $\eta_i(x)$, associated with massless Goldstone bosons. No such Goldstone bosons have ever been observed in Nature. The three fields $\eta_i(x)$ are unphysical (if they had not been, they could not have been simply transformed away), and the associated Goldstone bosons are often said to be "eaten" by $W^\pm$ and Z^0 so that they acquire their mass.

with

$$F^{W\mu\nu}(x) \equiv \partial^\nu W^\mu(x) - \partial^\mu W^\nu(x), \text{ and } Z^{\mu\nu}(x) \equiv \partial^\nu Z^\mu(x) - \partial^\mu Z^\nu(x),$$

and

$$\begin{aligned} m_W &= \frac{1}{2} v g, \quad m_Z = \frac{m_W}{\cos\theta_W}, \quad m_h = \sqrt{-2\mu^2} \\ v &= \sqrt{-\frac{\mu^2}{\lambda}} > 0, \quad g\sin\theta_W = g'\cos\theta_W = e. \end{aligned} \tag{1.61}$$

The exact expression for $\mathcal{L}_{\text{BB,I}} + \mathcal{L}_{\text{HH,I}} + \mathcal{L}_{\text{HB,I}}$ and $\mathcal{L}_{\text{LB,I}}$ in Equation (1.62) will not be discussed further, the interested reader is referred to reference [17].

We now perform the same transformations for the two last terms, $\mathcal{L}_{\text{L}} + \mathcal{L}_{\text{LH}}$ from Equations (1.33) and (1.56), also replacing the left- and right-handed lepton fields ψ_{L} and ψ_{R} by the complete field ψ using Equation (1.12),

$$\begin{aligned} \mathcal{L}_{\text{L}} + \mathcal{L}_{\text{LH}} =& \bar{\psi}_l(x)(i\gamma^\mu\partial_\mu - m_l)\psi_l(x) + \bar{\psi}_{\nu_l}(x)(i\gamma^\mu\partial_\mu - m_{\nu_l})\psi_{\nu_l}(x) \\ &+ \mathcal{L}_{\text{HL,I}} + \mathcal{L}_{\text{LB,I}}, \end{aligned} \tag{1.62}$$

with

$$\mathcal{L}_{\text{HL,I}} = -\frac{1}{v} m_l \bar{\psi}_l(x)\psi_l(x)\sigma(x) - \frac{1}{v} m_{\nu_l}\bar{\psi}_{\nu_l}(x)\psi_{\nu_l}(x)\sigma(x)$$

and

$$m_l = \frac{v g_l}{\sqrt{2}}, \quad m_{\nu_l} = \frac{v g_{\nu_l}}{\sqrt{2}}. \tag{1.63}$$

Combining Equations (1.60) and (1.62) we get the complete Lagrangian density of the (leptonic) electroweak theory in the unitary gauge,

$$\mathcal{L} = \mathcal{L}_0 + \mathcal{L}_{\text{I}} \tag{1.64}$$

where

$$\begin{aligned} \mathcal{L}_0 =& \bar{\psi}_l(x)(i\gamma^\mu\partial_\mu - m_l)\psi_l(x) + \bar{\psi}_{\nu_l}(x)(i\gamma^\mu\partial_\mu - m_{\nu_l})\psi_{\nu_l} \\ &- \frac{1}{4} F_{\mu\nu}(x)F^{\mu\nu}(x) \\ &- \frac{1}{2} F^\dagger_{W\mu\nu}(x)F^{\mu\nu}_W(x) + m_W^2 W^\dagger_\mu(x)W^\mu(x) \\ &- \frac{1}{4} Z_{\mu\nu}(x)Z^{\mu\nu}(x) + \frac{1}{2} m_Z^2 Z_\mu(x)Z^\mu(x) \\ &+ \frac{1}{2}(\partial^\mu\sigma(x))(\partial_\mu\sigma(x)) - \frac{1}{2} m_H^2\sigma(x)^2 \end{aligned} \tag{1.65}$$

and

$$\mathcal{L}_{\text{I}} = \mathcal{L}_{\text{LB,I}} + \mathcal{L}_{\text{BB,I}} + \mathcal{L}_{\text{HH,I}} + \mathcal{L}_{\text{HB,I}} + \mathcal{L}_{\text{HL,I}}. \tag{1.66}$$

The second, third and fourth lines of Equation (1.65) respectively represent massless photons, $W^{\pm}$ bosons of mass m_W and Z^0 bosons of mass m_Z. The last line describes the neutral spin 0 boson of mass m_H. The interaction Lagrangian density in Equation (1.66) represent the interaction between particles.

As the observant reader might have noticed, the boson and lepton masses are related to some of the free parameters of the Standard Model. In fact, the W and Z boson masses can actually be calculated in terms of three experimentally well known quantities: the fine structure constant $\alpha = \frac{e^2}{4\pi} = \frac{1}{137.04}$ [16], the Fermi coupling constant $G = 1.166{\cdot}10^{-5}\,\mathrm{GeV}^{-2}$ [16] and the weak mixing angle $\sin^2\theta_W = 0.23129$. Combining Equation (1.61) and the fact that the parameter v can be expressed in terms of the Fermi coupling constant, $v = \frac{1}{\sqrt{G\sqrt{2}}}$ gives

$$m_W = \sqrt{\frac{\alpha\pi}{G\sqrt{2}}}\frac{1}{\sin\theta_W}, \quad m_Z = \sqrt{\frac{\alpha\pi}{G\sqrt{2}}}\frac{2}{\sin 2\theta_W}. \tag{1.67}$$

Inserting numbers we get

$$m_W = 76.9 \pm 0.8\,\mathrm{GeV}, \quad m_Z = 87.9 \pm 0.6\,\mathrm{GeV}.$$

These numbers are based on a tree-level calculation, neglecting higher-order corrections. The current measured values of the masses of the W and Z bosons are, as listed in Figure 1.1, 80.379 ± 0.012 GeV and 91.1876 ± 0.0021 GeV respectively, making the first-order calculations exact to within 5%.

1.3 Higher order corrections

In the previous chapters, we reviewed briefly the mathematics behind the Standard Model, taking into account only the lowest order of perturbation theory. When taking higher orders into account, we expect corrections of the order of the coupling constant of the theory in question to the tree-level results. This is known as radiative corrections. However, often the integrals involved in calculations are divergent. To deal with this, we need to go through three steps.

The first step is to regularize the theory, i.e. to introduce a parameter called a *regulator* or *cutoff* defining a point in some space which defines the boundary of validity of the theory, so that it is finite and well-defined.

In the second step, known as renormalization, the properties of the *physical* particles are related to those of the *bare* particles. The bare particles are the non-interacting particles, different from the actual physical particles that interact.

The third step is to hide the original infinities in the relations between the bare and physical particles. Both the bare particles themselves and these relations are unobservable.

After performing these three steps, the observable predictions of the theory are now finite again. This procedure can be carried through to all orders of perturbation theory, which enables the calculation of extremely precise predictions. The interested reader is encouraged to read more about this subject in reference [17].

1.4 Summary

In this chapter, we first saw how the Standard Model was developed through history and then quickly reviewed the particle content. The majority of the chapter was devoted to a simplified mathematical description, covering the QED, electroweak interactions, QCD and the Brout-Englert-Higgs mechanism. In the last section we briefly mentioned the technical difficulties encountered when taking higher order effects into account, and how to solve this. In the next chapter, we will discover why the Standard Model is not the Final Theory of Nature.

Chapter 2

Beyond the Standard Model – new, neutral gauge bosons

We have now reached the point where our adventure starts - the continued search for the Final Theory of Nature. During the last two millennia, brilliant minds have gradually figured out how reality as we observe it can be described in terms of mathematical models. Technological advances allow us to make predictions and perform measurements, ultimately leading to the exclusion of most theories. Still no measurement that contradict the Standard Model's predictions has been made[1], but there are many examples of phenomena that the SM cannot explain or describe. Because of this, we know that we need to search for an explanation beyond the SM. The amount of models that have the possibility of describing Nature is vast, and the search for the best one is a huge undertaking. Most probably, we have not even yet thought of the theory that might describe everything, as illustrated in Figure 2.1.

Figure 2.1: The vast theoretical space.

---

[1] There are examples of measurements that *might* not fit the SM predictions, but the statistical significance is not large enough to conclude. More data or better experiments are needed to conclude.

2.1 Going beyond the Standard Model

We now take a look at a few of the unresolved mysteries that the Standard Model cannot encompass.

2.1.1 Dark Matter and Dark Energy

Looking out at the universe we see twinkling stars, mighty galaxies and glowing gas, and it might come as a surprise[2] to hear that all of this in fact makes up about 15% of the total amount of matter in the universe, and only about 5% of the total energy content. This is nothing new. Already in 1884 Sir William Thomson, more fameously known as Lord Kelvin, said "many of our stars, perhaps a great majority of them, may be dark bodies" [18]. He based this surprising statement on the fact that he observed a velocity dispersion of stars orbiting the center of our galaxy. From this he estimated the mass of the galaxy, which he compared to the mass of visible stars in our galaxy, and concluded that the two were different. The name "dark matter" came from Henri Poincaré discussing Lord Kelvin's work and named it "matière obscure" in French.

Not much is known about dark matter, but as we have not yet observed it directly we concluded it does not interact electromagnetically (thus it is dark, no light is emitted). It does however interact gravitationally. The presence of dark matter in the universe is implied in several astrophysical observations, including observations in gravitational lensing and galaxy rotation curves.

In 1998 the Hubble Space Telescope observed very distant supernovae and it was calculated that at the time when these supernovae exploded, the universe was expanding more slowly than it is today. This came as a surprise to the scientific community, as it was thought that the universe would either stop expanding and collapse again or never stop expanding, only slowing the expansion rate down with time. The solution to this problem is known as dark energy, although one might argue that it is no solution at all since almost nothing is known about this dark form of energy. From the dark energy's effect on the expansion rate of the Universe, we can calculate that about 68% of the Universe's energy content is dark. One intriguing theory is that dark energy in fact is a feature of empty space. If this empty space possesses its own energy, then it is not diluted as space expands. In fact the total energy content grows with the universe. Another possible explanation is that it is some kind of fluid or field (named "quintessence") filling all of space, that affects the expansion of the universe in another way than that of matter and normal energy. Still no observations have been made to verify or falsify either explanation.

2.1.2 Matter-antimatter asymmetry

According to theory, equal amounts of matter and antimatter should have been created in the Big Bang. Matter and antimatter particles are produced in pairs, and when a particle comes in contact with its antiparticle, they annihilate and create photons. However, from today's universe it is obvious that everything we see is made almost entirely of matter. The origin of

---

[2] This will probably *not* come as a surprise to most readers of this thesis.

this asymmetry is unknown. Calculations indicate that about one matter particle per billion survived [19]. Physics experiments have shown that the laws of physics seem to treat matter particles different than antimatter particles, but as of now the violation observed is too small to account for the observed matter-antimatter asymmetry.

2.1.3 Gravity

The Standard Model of particle physics includes three of the four forces of Nature, skipping the force of gravity completely. This leaves scientists feeling uneasy, why should the fourth force be left out? Could gravity in fact be mediated by a particle (the *graviton*)? Several searches are performed and nothing has been discovered, but the future might bring news. As for now, gravity is well described by the theory of general relativity, developed by Albert Einstein and published in 1915. One of the most prominent problems within theoretical physics today is how to combine QFT at the microscopic scale with GR at the macroscopic scale to create a more complete theory.

2.2 Theories beyond the Standard Model

We now take a very brief look at a few of the theories beyond the SM.[3]

2.2.1 Grand Unified Theory (GUT)

Just like magnetic and electric forces are unified in the electromagnetic force, and just as the electromagnetic and weak forces are unified in the electroweak force, it is thought that all the three forces of the Standard Model might be unified at some higher energy [20]. If this is indeed the case, then at some point in the past, all three forces acted as one force, with a single coupling constant. When the universe cooled and passed a critical point, the symmetry was broken. This symmetry breaking resulted in new heavy gauge bosons.

$\mathrm{SU}(5)$ is the simplest GUT, proposed by Howard Georgi and Sheldon Glashow in 1974 [21], containing the SM group as a subgroup. The breaking of $\mathrm{SU}(5)$ occurs (as in the SM) when a scalar field (such as the BEH field) acquires a vacuum expectation value, creating 24 gauge bosons, doubling the 12 gauge bosons in the SM. The 12 extra gauge bosons violate baryon and lepton number and carry flavor and color. This enables proton decay with a lifetime lower than observed lower limits, thus excluding the theory. Many other, more complex GUTs also exist and are possible candidates for SM extensions.

2.2.2 Supersymmetry

Supersymmetry, or SUSY, introduces a symmetry between fermions and bosons. None of the SM particles can be superpartners of the others, so this would mean a doubling of the particle content. An unbroken symmetry would mean that the superpartners had the same mass and quantum numbers (except for spin) as their partners, but as no superpartners are observed, the symmetry must be broken at some higher energy.

---

[3] This section is based mostly upon reference [20].

A prospective benefit of this theory is a naturally occurring cancellation of large higher-order corrections at high energies, reducing the need for fine-tuning and partially removing some infinities without the need to define an energy cut-off scale where the model is no longer valid. Another enticing consequence, is the fact that the running couplings of the electromagnetic, weak and strong forces seem to meet at a very high energy - without SUSY they do not.[4] SUSY also offers a potential candidate for dark matter - if imposing an additional discrete symmetry called R-parity,[5] the lightest superparticle is stable.

Even the smallest SUSY extension of the SM - the minimal supersymmetric Standard Model, or MSSM - has around 120 free parameters,[6] which makes some physicists uncomfortable - the theory solves some problems, but adds a lot of complexity. The parameter space is highly constrained by searches at the LHC, but SUSY as a concept is not excluded.

2.2.3 Theory of Everything

A Theory of Everything (ToE) is nothing less than the Final Theory of Nature. One candidate is string theory, where the point particles of the SM are replaced by one-dimensional objects known as *strings* that exist in ten spatial dimensions. This theoretical framework reproduces QFT at low energies. The strings can form closed loops, or they can exist as open strings with free ends. In the SM, the particles trace out a *worldline* in space-time, as illustrated in Feynman diagrams. In string theory, the strings trace out a surface, or *worldsheet*, in space-time, as illustrated in Figure 2.2. At low energies, or at distance scales much larger than the size of a string, the strings look like point particles and the worldsheet diagrams look like Feynman diagrams. Several Feynman diagrams are incorporated in a worldsheet. The strings can vibrate, and they have infinitely many vibrational modes, and it is these vibrations that we observe as the different fundamental particles. In fact, string theory can generate all the particles in the SM.

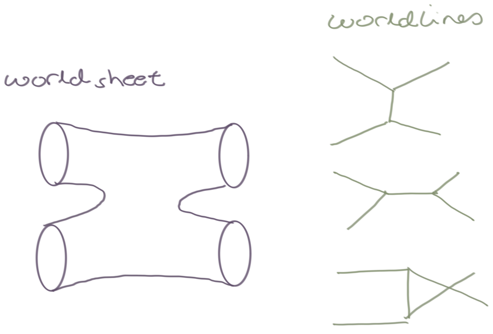

Figure 2.2: The worldsheets in string theory incorporates several Feymman diagrams, or worldlines, in QFT.

Since string theory sprang to life in 1968, it has evolved immensely. By the 1990s, several string theories were found. An unexpected realization was made when it was discovered that the massive and static *membranes* (or *branes*) that acted as places where the open string could end, actually became dynamic when the string coupling increased. This was followed by the even more unexpected realization that all the discovered string theories were in fact

---

[4] This might also happen in other BSM theories, but the running couplings do not meet at high energy when extrapolating using only the information contained within the SM.

[5] Each SM particle has R-parity equal to 1 and each superparticle has R-parity equal to -1.

[6] There are less than 30 free parameters in the SM.

related to one another via several so-called *dualities*. This pointed to a more fundamental theory, in eleven dimensions, which was named *M-theory*. The theory still evolves today. A major drawback of the theory is that it offers no testable predictions at an energy we can access today.

2.3 New neutral gauge bosons

Many theories beyond the Standard Model predict the existence of a new neutral gauge boson Z'. In this section we explore a selected few of these theories, most of which we will follow up later.

2.3.0.1 The sequential Standard Model Z'_{SSM}

The sequential SM is a non-renormalizable toy model in which the new Z' boson, Z'_{SSM}, has the same couplings to fermions as the SM Z^0 boson, but a higher mass [22]. It is often used as a benchmark model, although not representing any physically possible theory.

2.3.0.2 E_6-motivated Z' models

In E_6-motivated Grand Unified models, the E_6 group can break to the SM in a number of different ways, predicting two new neutral gauge bosons that can mix in general [1][23]. In many of them, E_6 first breaks to $\mathrm{SO}(10) \times U(1)_\psi$ (see Figure 2.3 for a schematic view), followed by $\mathrm{SO}(10)$ breaking to either $\mathrm{SU}(4) \times \mathrm{SU}(2)_{\mathrm{L}} \times \mathrm{SU}(2)_{\mathrm{R}}$ or $\mathrm{SU}(5) \times U(1)_\chi$.

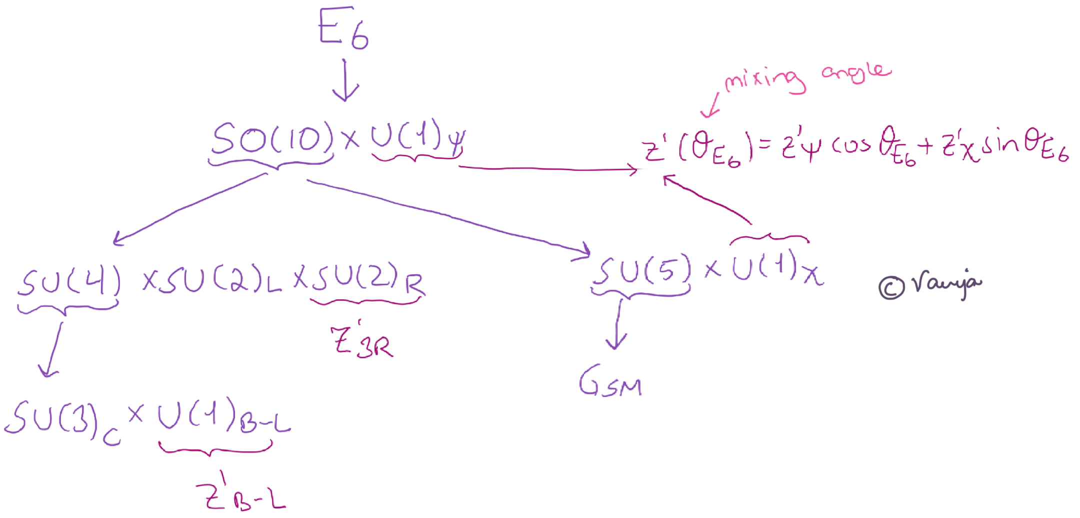

Figure 2.3: A schematic view of two possible scenarios in E_6-motivated Z' models.

In the former case we can get the $Z'_{3\mathrm{R}}$ coming from $\mathrm{SU}(2)_{\mathrm{R}}$ or the $Z'_{\mathrm{B-L}}$ coming from the breaking of $\mathrm{SU}(4)$ into $\mathrm{SU}(3)_{\mathrm{C}} \times U(1)_{\mathrm{B-L}}$, both of which could exist at the TeV scale. The $Z'_{3\mathrm{R}}$ is one example of a left-right symmetric model, restoring the parity symmetry broken by the weak interactions. These two models also appear in the framework of minimal Z' models, described in Section 2.3.0.3.

In the $\mathrm{SU}(5)$ case the gauge bosons associated with the $U(1)_\psi$ and $U(1)_\chi$ groups can mix to create a potentially observable Z' boson defined by

$$Z'(\theta_{E_6}) = Z'_\psi \cos\theta_{E_6} + Z'_\chi \sin\theta_{E_6},$$

with θ_{E_6} as the mixing angle that also specifies the Z' boson's coupling strength to the fermions in the SM and also its intrinsic width. While the Z'_{SSM} has a width of approximately 3% of its mass, the Z'_ψ has a width of 0.5% of its mass while the Z'_χ has a width of 1.2% of its mass. The other Z' bosons within this framework, defined by specific values of the mixing angle $\theta_{E_6} \in [-\pi, \pi]$, have widths between the two extremes defined by the Z'_χ ($\theta_{E_6} = \frac{\pi}{2}$) and the Z'_ψ ($\theta_{E_6} = 0$) models. Some often-used models are the Z'_S (width 1.2% of its mass), Z'_I (width 1.1%), Z'_η (width 0.6%) and Z'_N (width 0.6%) [23].

2.3.0.3 Minimal Z' models

In *minimal* Z' models, the phenomenology is controlled by three new parameters only – the Z' mass and two effective coupling constants [24] [1]. The width of the the Z' depends on the two effective couplings, enabling width effects to be taken into account.

Minimal models extend the Standard Model with an extra $U(1)$ expansion with the smallest possible number of additional free parameters that still ensure that the theory remains renormalizable. In general, there are no exotic vectors apart from the Z' associated with the additional $U(1)$ group, which commutes with the SM group $\mathrm{SU(3)_C} \times \mathrm{SU(2)_L} \times \mathrm{U(1)_Y}$, no exotic fermions, apart from the right-handed neutrinos, one for each SM generation, and lastly, there are no exotic scalars.

The two effective coupling constants are g_{BL} (the Z' coupling to the $(B - L)$ current) and g_Y (the Z' coupling to the weak hypercharge Y) [1].[7] We often define the ratios

$$\tilde{g}_{BL} \equiv \frac{g_{BL}}{g_Z}, \quad \tilde{g}_Y \equiv \frac{g_Y}{g_Z}, \tag{2.1}$$

where g_Z is the coupling of the Standard Model Z^0 boson defined by $g_Z = \frac{2M_Z}{v}$, with v as the Higgs boson vacuum expectation value of 246 GeV. It is customary to reparametrize, using γ' and θ_{Min} as the independent parameters,

$$\tilde{g}_{BL} = \gamma' \cos\theta_{\mathrm{Min}}, \quad \tilde{g}_Y = \gamma' \sin\theta_{\mathrm{Min}}, \tag{2.2}$$

where γ' measures the strength of the Z' boson coupling relative to the SM Z^0 boson coupling, and θ_{Min} is the mixing angle between the generators of the $B - L$ and the weak hypercharge Y gauge groups. For specific values of the two coupling constants we find several known models, including the Z'_χ from the E_6-motivated models and the Z'_{3R} in left-right symmetric models, as illustrated in Table 2.1. For the minimal Z' models, the width of the Z' depends on γ' and θ_{Min}, and the interference with the SM Z^0/γ processes are included.

---

[7] This is highly technical, and goes beyond the scope of this thesis. However, we decided to add it for completeness, and for the small additional clarity it provides. Interested readers are referred to references [24] [1].

	γ'	$\cos\theta_{\text{Min}}$	$\sin\theta_{\text{Min}}$
Z'_{B-L}	$\sqrt{\frac{5}{8}}\sin\theta_W$	1	0
Z'_{χ}	$\sqrt{\frac{41}{24}}\sin\theta_W$	$\sqrt{\frac{25}{41}}$	$-\sqrt{\frac{16}{41}}$
Z'_{3R}	$\frac{5}{\sqrt{12}}\sin\theta_W$	$\frac{1}{\sqrt{5}}$	$-\frac{2}{\sqrt{5}}$

Table 2.1: Values for γ' and θ_{Min} corresponding to the three specific Z' bosons: $Z'_{\text{B}-\text{L}}$, Z'_{χ} and Z'_{3R}. The Standard Model weak mixing angle is denoted by θ_W.

2.4 Summary

In this chapter we have explored some of the many unexplained mysteries in the Universe, and we also looked at a handful of theories that could add a few more pieces to the puzzle. In the next chapter, we will see one of the available tools in the hunt for the Final Theory, namely the Large Hadron Collider at CERN, and more specifically the ATLAS detector, which is one of the four main particle detectors there.

Chapter 3

The Large Hadron Collider and the ATLAS detector

In this chapter we describe the Large Hadron Collider (LHC), with a brief history and a look at the large LHC complex with its many accelerators. We focus on one of the four largest experiments, the ATLAS experiment, as it is data from the ATLAS detector that is used in the dimuon analysis described in Chapters 4 to 7. The last sections in this chapter consider several important physics-related subjects important at proton-proton collider experiments.

3.1 The LHC

The Large Hadron Collider is a very large complex located mostly underground on the border between France and Switzerland, near Geneva. In a ring with circumference 27 kilometers, located up to 175 meters under ground, protons or heavy ions (e.g. lead ions) are accelerated up to speeds that are very close to the speed of light. This is the world's largest particle accelerator, planned and built by the European Organization for Nuclear Research (CERN, from the French name Conseil Européen pour la Recherche Nucléaire).

3.2 CERN

The CERN convention was signed in 1954 by the 12 founding states,[1] including Norway. Currently it has 23 member states, as illustrated in Figure 3.1, and each member state has duties and privileges and is represented in the council. They all make great contributions to the operation of CERN's programs. Some states and organizations that are not members have an observer status, which means they receive information from the CERN council, but they are not allowed to take part in the decision-making.

There are over 600 universities and institutes all over the world that use CERN's facilities. About 2600 people are employed directly by CERN, and about 12500 scientists of 110 nationalities, from institutes in over 70 countries [26] are registered users within the CERN community.

---

[1] Belgium, Denmark, France, the Federal Republic of Germany, Greece, Italy, the Netherlands, Norway, Sweden, Switzerland, the United Kingdom and Yugoslavia.

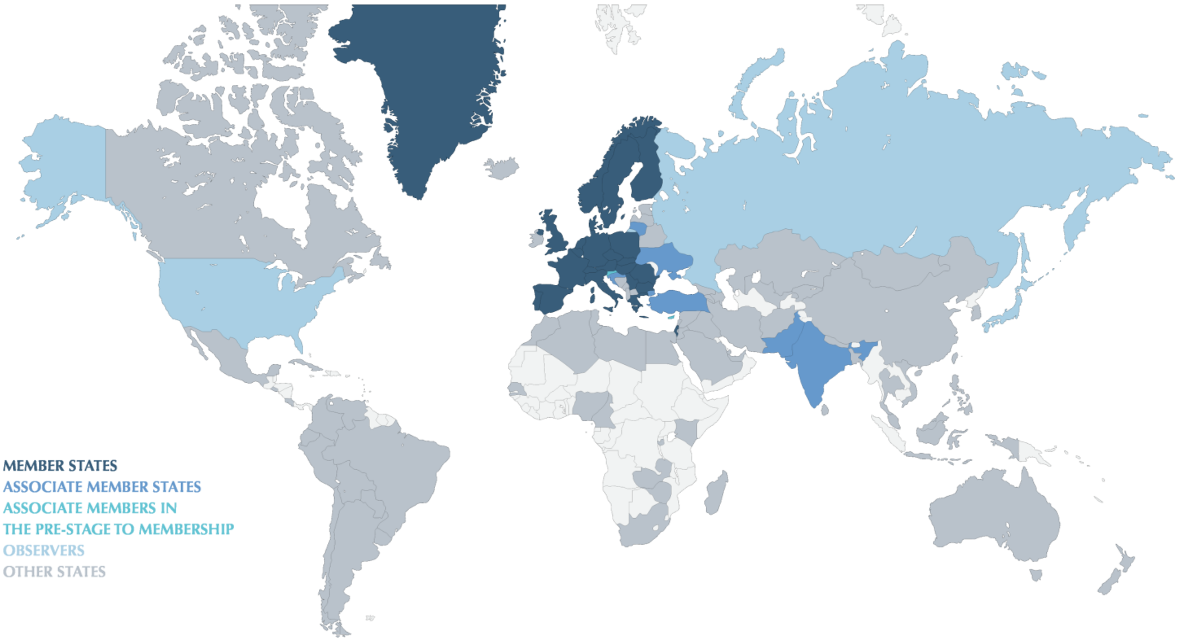

Figure 3.1: This map of the world shows the status of the countries in different shades of blue [25]. The darkest blue represents the member states.

3.3 Building the LHC

The planning stage started already back in the early 1980's, when the LHC's predecessor, the Large Electron Positron Collider (LEP), was under construction. In 1994, CERN's governing body, the CERN Council, approved the construction of the LHC. The four main experiments – ATLAS, CMS, ALICE and LHCb – received official approval in the years between 1996 and 1998. Today there are three smaller experiments attached to the larger ones – TOTEM (installed next to CMS), LHCf (installed next to ATLAS), and MoEDAL (installed next to LHCb).

3.4 Main goals

With this gigantic machine we are searching for a more complete understanding of our Universe. The last undiscovered particle in the Standard Model, the Higgs boson, was discovered at the LHC in July 2012, thus fulfilling one of the main goals of the LHC. Other main goals include unravelling the mystery of the nature of dark matter, searching for supersymmetric particles which may (or may not) help in unifying the four fundamental forces at some high energy level, finding an explanation for why our Universe is dominated by matter when matter and antimatter were created in equal amounts during the Big Bang, and examining the quark-gluon plasma (free quarks and gluons) that filled our Universe at a very early age [27].

3.5 The LHC complex

The LHC is not perfectly circular – it has eight straight sections and eight arcs as illustrated in Figure 3.2. ATLAS and CMS, the two high luminosity experiments, are placed opposite to each other, in the straight sections of octant 1 and 5 respectively. The remaining two of the four main experiments, ALICE and LHCb, are placed on either side of ATLAS, in octants 2 and 8 respectively. The remaining straight sections have no beam crossings.

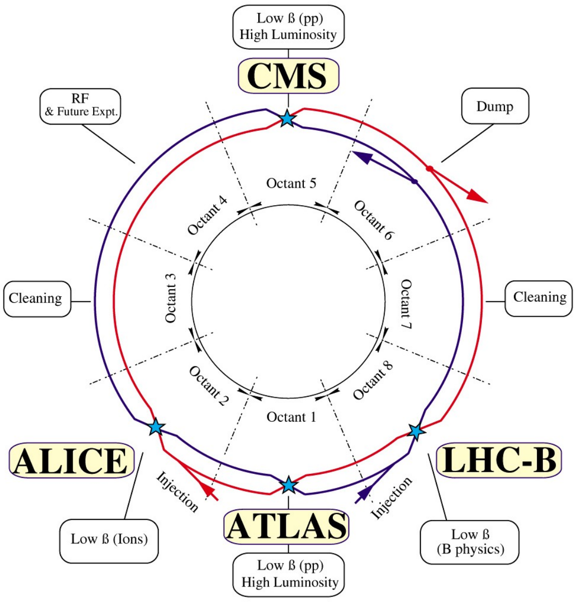

Figure 3.2: Schematic layout of the LHC [28] showing the eight straight sections (named Octant 1 to 8), the four interaction points where the four main experiments are placed and the injection sites.

The LHC complex is a series of connected particle accelerators, as shown in Figure 3.3. One after the other they accelerate the beam to the maximum energy before they inject it into the next one where it is accelerated to even higher energies (or delivered to an experiment), until finally the beams enter the LHC ring.

3.5.1 Accelerating protons to 6.5 TeV

The source of the protons is a bottle of hydrogen gas. Using an electric field, the hydrogen atoms are stripped of their electrons, leaving only the protons. The Linac 2 linear accelerator accelerates the protons to an energy of 50 MeV, and sends them to the Proton Synchrotron Booster (PSB). There they gain energy until they reach 1.4 GeV and are sent to the Proton Synchrotron (PS) where they gain a total energy of 25 GeV. The last part of the chain before entering the LHC ring is the Super Proton Synchrotron (SPS), where the protons are accelerated to 450 GeV. The beams are then transferred to the LHC, where one beam is sent in the clockwise direction and another beam in the anti-clockwise direction. The total fill time is 4 minutes 20 seconds for each ring. It takes another 20 minutes to reach the maximum energy of 6.5 TeV for each beam. Under normal conditions the beams can circulate in the LHC ring up to 10 hours before needing a refill.

The beams are brought together in four collision points in the ring, with a total collision energy of maximum 13 TeV. Each of these collision points has a surrounding detector – ATLAS, CMS, ALICE and LHCb.

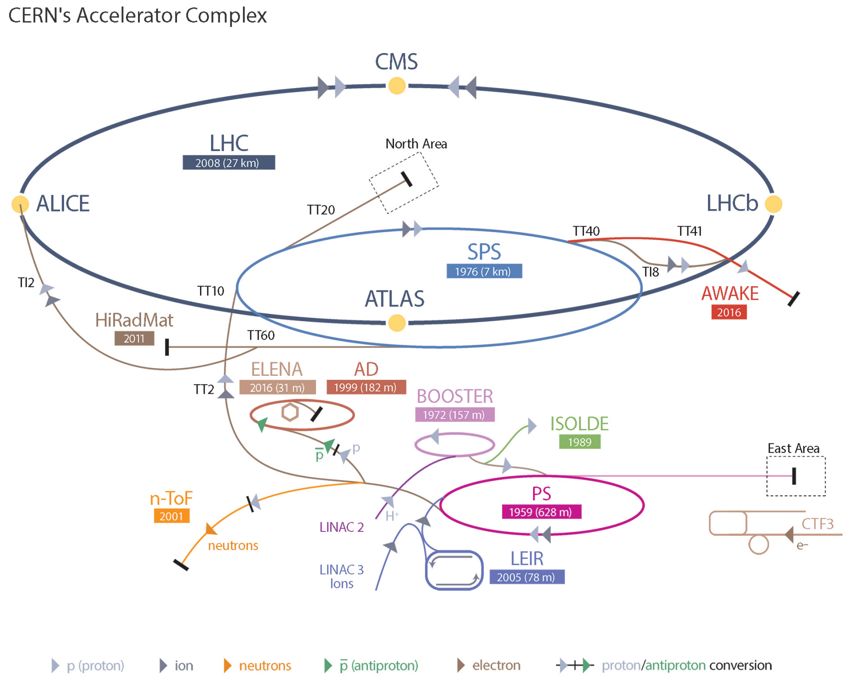

Figure 3.3: A schematic of the large LHC complex showing the many detectors and accelerators, including the LHC ring and the ATLAS detector [29].

3.5.2 LHC magnets

To send the protons on the complicated path as laid out in the previous subsection, keeping them bunched up and travelling without losing speed, more than 50 types of magnets are needed. All of these types of magnets are electromagnets.[2]

The main dipole magnets in the LHC tunnel are superconducting electromagnets, kept at a temperature of 1.9 K, and generate a 8.3 T magnetic flux density field by sending a 12 kA current through the superconducting niobium-titanium cables. There are 1232 of these dipole magnets, each is 15 m long and weighs 35 metric tons. The dipole magnets keep the protons on their almost-circular path in the LHC tunnel, and because of their construction have opposite magnetic fields in the two beam pipes sending the proton bunches in the opposite direction around the ring. To correct for small imperfections in the magnetic field at the extremities of the dipole magnets, sextupole, octupole and decapole magnets are used. To keep the protons bunched together, quadropole magnets with four magnetic poles arranged symmetrically around the beam pipe squeeze the beam vertically and horizontally.

---

[2] This section is based on [30] and [31] unless stated otherwise.

3.5.3 RF cavities

The protons are accelerated from 450 GeV to 6.5 TeV in the LHC ring.[3] This work is done by the radiofrequency (RF) cavities. All accelerated charged particles radiate energy, known as synchrotron radiation, and the RF cavities also need to supply the beams with the energy they lose to keep the energy at its maximum value for long periods of time.

The RF cavities, 16 in total, are hollow copper structures, with a 1.5 μm thick niobium layer coating on the inside. The coppers structures are cooled to a temperature of 4.5 K using liquid helium, causing the niobium to be superconducting. The RF cavities contain an electromagnetic field, supplied by high-power RF generators known as *klystrons*. The electromagnetic field oscillates inside the RF cavity, resulting in standing waves, creating an electric field along the beams' direction. The arrival of each proton bunch is timed in such a way that each bunch sees an accelerating field when passing through a cavity. For each lap around the LHC ring, every proton gains 485 keV of energy on average.

3.6 A Toroidal LHC ApparatuS

The ATLAS (short for "A Toroidal LHC ApparatuS") detector is the largest (in volume) detector ever constructed for particle collisions.[4] It is 46 meters long and 25 meters high, and weighs about 7000 metric tons. Figure 3.4 shows a mural of the ATLAS detector, about one third of its actual size.

Figure 3.4: A huge mural of the ATLAS detector by the American artist Josef Kristofoletti, about one third [35] of the actual size of ATLAS.

3.6.1 ATLAS coordinate system

Figure 3.5 illustrates the ATLAS coordinate system. The nominal interaction point (IP) is

---

[3] This section is based on [30] and [32] unless stated otherwise.

[4] Unless specifically stated otherwise, all details are from [33] and [34].

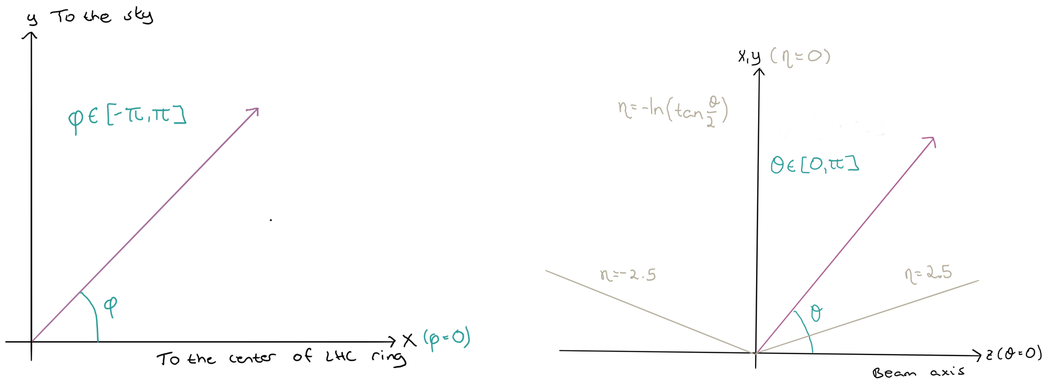

(a) The transverse plane

(b) The longitudinal plane

Figure 3.5: Two projections of the ATLAS coordinate system. One in the transverse plane (a) and one in the longitudinal plane (b).

in the middle of the detector and defines the origin of the coordinate system, the beam pipe defines the z-axis and the x-y plane is perpendicular to the beam axis. The positive x-axis points toward the center of the LHC ring, and the positive y-axis points upwards to the sky.

The azimuthal angle $\phi \in [-\pi, +\pi]$ is the angle between the positive x-axis and the position vector projected onto the transverse (x -y) plane. It increases clockwise when looking in the positive z-direction. The polar angle $\theta \in [0, \pi]$ is the angle between the positive z-axis and the position vector projected onto the longitudinal plane.

The pseudorapidity η is defined as

$$\eta = -\ln\left(\tan\frac{\theta}{2}\right),$$

and is therefore zero in the transverse plane (x-y) and increases towards positive (negative) infinity as it approaches the positive (negative) z-axis.

A distance ΔR e.g. between two particle tracks in the $\eta - \phi$ plane is defined as

$$\Delta R = \sqrt{(\Delta\eta)^2 + (\Delta\phi)^2}.$$

The transverse momentum p_{T}, the transverse energy E_T and missing transverse energy $\not{E}_T$ are defined in the x-y plane (more on these physical concepts in Sections 3.7.2 and 3.7.3).

3.6.2 The detector – a quick overview

The ATLAS detector is constructed like an onion, with layer upon layer of detector parts, electronics and read-out systems, in an attempt to detect everything that passes through it. The interaction point, where the proton beams collide, is in the center.

ATLAS has four main parts – the Inner (tracking) Detector (Section 3.6.4), the calorimeters (Section 3.6.5), the Muon Spectrometer (Section 3.6.6) and the magnet system (Section 3.6.7). Figure 3.6 shows the location of the main parts - the SCT tracker, the pixel detector and the TRT tracker are the three main parts of the inner detector. In Figure 3.7 we see how

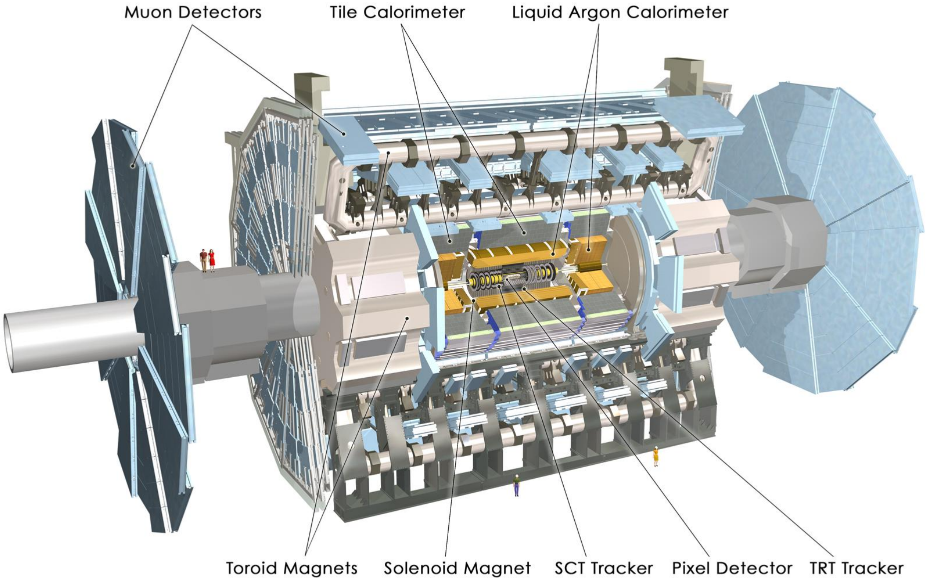

,

Figure 3.6: A cut-away view of the ATLAS detector showing all the main components.

the ATLAS detector detects all stable[5] particles, except for the neutrino (and possibly particles from Beyond the Standard Model theories). The inner detector, closest to the interaction point, detects the momentum, charge and position of all particles with electric charge. The solenoid magnet is on the outside of the inner detector, ensuring a near-uniform magnetic field in whole volume of the ID. Following this are the calorimeters. The electromagnetic calorimeter (drawn in brown) detects and measures the energy of electrons, positrons and photons by the creation of electromagnetic showers that are fully contained in the calorimeter. The hadronic calorimeter (drawn in blue) works much the same way as the electromagnetic calorimeter, only with the strong interaction, creating hadronic showers. It detects and measures the energy of hadrons, like the proton and neutron. The outermost part of ATLAS is the Muon Spectrometer, that detects and measures the positions and momenta of passing muons. The muon system is immersed in a magnetic field from the toroidal magnet system. The neutrino is not detected at all, but its existence can be inferred from the missing energy (Section 3.7.3 provides a definition).

The main performance goals of the ATLAS detector are listed in Table 3.1. Note that while the relative energy resolution for the calorimeters improve with increasing particle energy, the relative transverse momentum resolution worsen with increasing particle transverse momentum for the ID. This is also true for the MS, as they use conceptually the same idea for measuring the transverse momentum. The relative muon momentum resolution is described in more detail in Section 3.6.3.2.

---

[5] A stable particle is in this context defined as a particle that does not decay before leaving the detector.

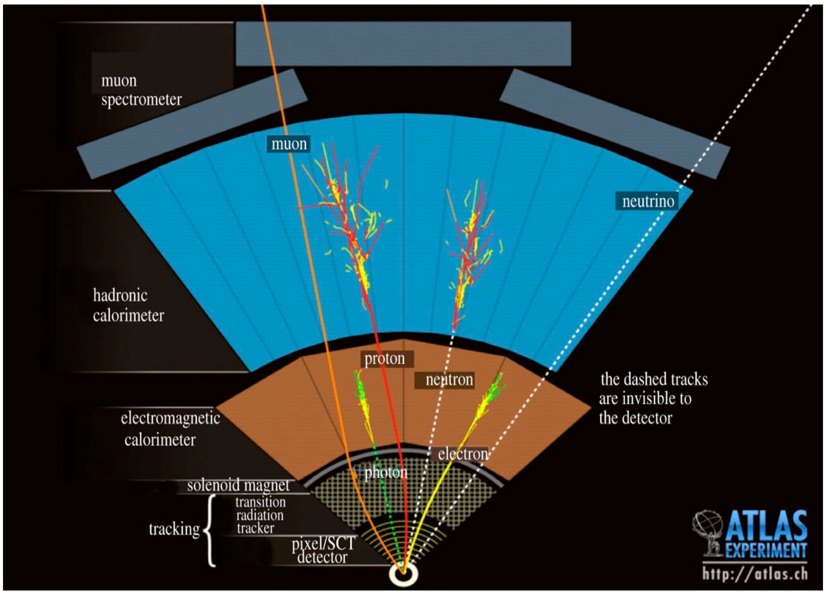

Figure 3.7: The various layers of the ATLAS detector and an overview of the detectable stable particles.

Sub-detector	**Relative resolution**	**Acceptance**	
		Measurement	Trigger
Inner detector	$\sigma_{p_\mathrm{T}}/p_\mathrm{T} = 0.05\% \cdot p_\mathrm{T} \oplus 1\%$	$\lvert\eta\rvert < 2.5$	
EM calorimeter	$\sigma_E/E = 10\%/\sqrt{E} \oplus 0.7\%$	$\lvert\eta\rvert < 3.2$	$\lvert\eta\rvert < 2.5$
Hadronic calorimeter			
barrel and end-cap	$\sigma_E/E = 50\%/\sqrt{E} \oplus 3\%$	$\lvert\eta\rvert < 3.2$	$\lvert\eta\rvert < 3.2$
forward	$\sigma_E/E = 100\%/\sqrt{E} \oplus 10\%$	$3.1 < \lvert\eta\rvert < 4.9$	$3.1 < \lvert\eta\rvert < 4.9$
Muon spectrometer	$\sigma_{p_\mathrm{T}}/p_\mathrm{T} = 10\%$ at $p_\mathrm{T} = 1$ TeV	$\lvert\eta\rvert < 2.7$	$\lvert\eta\rvert < 2.4$

Table 3.1: General performance goals of the ATLAS detector. The units for energy E and transverse momentum p_T are in GeV. The $\oplus$ symbol denotes addition in quadrature.

3.6.3 Measuring muon properties

3.6.3.1 Electrically charged particles

The direction, momentum and charge of electrically charged particles are measured in the tracking detectors, the ID and the MS. As mentioned in the previous section, muons are the only charged SM particles that pass through to the MS in the outermost layer of the ATLAS detector. To enable the measurement of the electric charge and momentum, the tracking detector must be immersed in a magnetic field so that the amount of bending of the particle trajectory can be measured.

In general, a tracking detector consists of many modules which each give a signal (a *hit*) when an electrically charged particle passes through it. This allows us to know the position of the charged particle at a given time. Combining information from the hits in all the modules traversed by the charged particle, the trajectory of the particle can be reconstructed. This is called a *track*. A set of five parameters is used to define the track — the transverse and longitudinal impact parameters d_0 and z_0 (the transverse and longitudinal distances from the nominal interaction point where the beams collide), the polar θ and the azimuthal ϕ angles (as defined in Section 3.6.1) and the electric charge divided by the particle momentum q/p [36].

The trajectory of a charged particle in a magnetic field is bent. The motion is governed by the relativistic equation of motion

$$\frac{d\mathbf{p}}{dt} = \mathbf{F} = q\mathbf{v} \times \mathbf{B}, \tag{3.1}$$

where $\mathbf{F}$ is the force on the charged particle with charge q going with velocity $\mathbf{v}$ in a plane perpendicular to the homogeneous magnetic field of magnetic flux density $\mathbf{B}$, and the relativistic momentum is $\mathbf{p} = \gamma m\mathbf{v} = \frac{1}{\sqrt{1-\left(\frac{v}{c}\right)^2}} m\mathbf{v}$. Because the force $\mathbf{F}$ is perpendicular to the velocity $\mathbf{v}$, no work is done, and the particle's energy $E = \gamma mc^2$ remains unchanged, which means that γ is constant. Thus we see that

$$\frac{d\mathbf{p}}{dt} = \gamma m\mathbf{a}. \tag{3.2}$$

Combining Equations (3.1) and (3.2) and taking the magnitude, we get

$$\gamma ma = |q|vB. \tag{3.3}$$

As the motion is circular, we can insert the centripetal acceleration $a = \frac{v^2}{r}$, with r as the radius of the circle,

$$\gamma m\frac{v}{r} = \frac{p}{r} = |q|B, \quad \rightarrow r = \frac{p}{|q|B}. \tag{3.4}$$

From this expression we see that the track of a slower particle is bent more than that of a faster particle. Because of this, the momentum resolution of the ID gets worse with increasing particle velocities. We revisit the topic of momentum resolution in Section 3.6.3.2.

In the case when the charged particle has a component of its velocity parallel to the magnetic field,[6] the particle trajectory will trace out a helix, and the magnitude of the total momentum in Equation 3.4 should be exchanged by the magnitude of the transverse momentum, $p_\perp$,

$$p_\perp = |q|rB. \tag{3.5}$$

This expression explains how the transverse momentum of a charged particle can be measured – knowing the value of B and $|q|$ (it is safe to assume that the charge of the final state particles in a collider experiment is the elementary charge) and measuring the curvature of the track r, we get the value of $p_\perp$. The full momentum vector p of the charged particle can be reconstructed by looking at the full three-dimensional track.

The bending radius r depends on the momentum of the particle, and high-momenta charged particles in magnetic fields follow an almost straight trajectory. This makes it difficult to measure the radius directly. Consider a charged particle passing through a homogeneous magnetic field [37][38]. The particle follows a trajectory which is a segment of a circle as illustrated in Figure 3.8. Using the Pythagorean theorem we get

---

[6] We here remind the reader that the magnetic field lines are parallel to the beam axis in the ID and tangential to a circle in the transverse plane around the beam axis in the MS

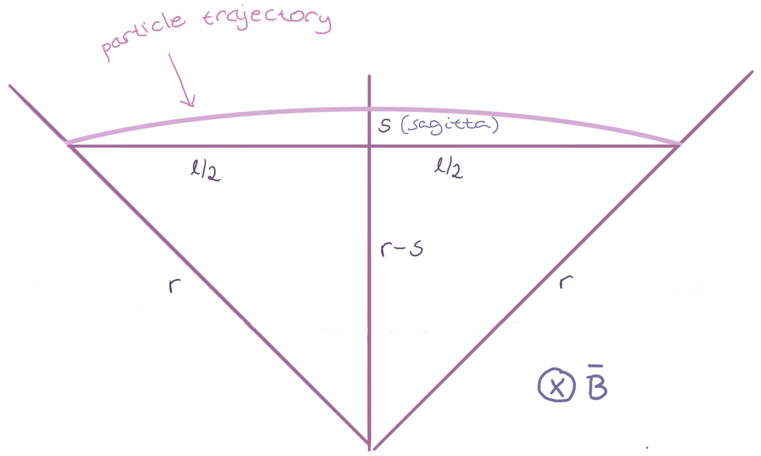

Figure 3.8: The trajectory of a charged particle in a homogeneous magnetic field. The higher the momentum of the particle, the smaller the sagitta s becomes.

$$(r-s)^2+\left(\frac{l}{2}\right)^2=r^2, \tag{3.6}$$

which leads to the following expression for the radius r,

$$r=\frac{\frac{l^2}{4}+s^2}{2s}. \tag{3.7}$$

When only a small segment of the circle is measured ($l \gg s$) then the radius r is given by

$$r=\frac{l^2}{8s}, \quad l \gg s, \tag{3.8}$$

thus by measuring the sagitta s we get a measurement of the $p_\perp$ by using Equation (3.5).

$$p_\mathrm{T}=|q|Br=\frac{|q|Bl^2}{8s}. \tag{3.9}$$

3.6.3.2 Muon momentum resolution

Ideally we would measure the charged particle properties exactly, but in reality we are limited by the resolution of the detector. As noted in Table 3.1, the MS aims at measuring the transverse momentum of a 1 TeV track with a resolution of approximately 10%. This translates into a sagitta along the beam axis of about $500\ \mu$m that needs to be measured with a resolution of approximately $50\ \mu$m.

The relative transverse momentum resolution $\frac{\sigma_{p_\mathrm{T}}}{p_\mathrm{T}}$ can be parameterized in the MS as follows [39][40] for a given value of η:

$$\frac{\sigma(p_\mathrm{T})}{p_\mathrm{T}}=\frac{p_0^\mathrm{MS}}{p_\mathrm{T}}\oplus p_1^\mathrm{MS}\oplus p_2^\mathrm{MS}\cdot p_\mathrm{T}, \tag{3.10}$$

with $\oplus$ denoting the quadratic sum. The first term accounts mainly for fluctuations of the energy loss in the traversed material (mainly the dense calorimeters, so this is mostly relevant when the MS measurement is extrapolated in to the ID), the second term mainly for multiple scattering and local magnetic field inhomogeneities, and the third term mainly for the limited position resolution of hit measurements and the misalignment of the MS.

For the ID, the relative resolution parameterization is divided into two $|\eta|$ ranges, $|\eta| < 1.9$ (well within the TRT fiducial volume) and $|\eta| > 1.9$,

$$\frac{\sigma(p_\mathrm{T})}{p_\mathrm{T}} = p_1^\mathrm{ID} \oplus p_2^\mathrm{ID} \cdot p_\mathrm{T}, \quad |\eta| < 1.9, \tag{3.11}$$

$$\frac{\sigma(p_\mathrm{T})}{p_\mathrm{T}} = p_1^\mathrm{ID} \oplus p_2^\mathrm{ID} \cdot p_\mathrm{T} \frac{1}{\tan^2\theta}, \quad |\eta| > 1.9, \tag{3.12}$$

$$\tag{3.13}$$

where p_1^ID and p_2^ID are the multiple scattering and intrinsic resolution terms, respectively.

The term p_2^MS is determined from alignment studies using runs with the toroidal magnetic field off. The remaining terms are determined using events from Z^0 and J/Ψ decays. The results are listed in Table 3.2. We see that for muons with low momenta, the p_1 term dominates the resolution, and the relative momentum resolution is better in the ID than in the MS for all regions $|\eta| < 2.0$. For muons with higher momenta (tens of GeV to hundreds of GeV) the p_2 term, which is linear in p_T, starts to dominate the resolution. We see that the MS has a much better momentum resolution compared to the ID for these high-$p_\mathrm{T}$muons.

Region	p_0^ID [TeV]	p_1^ID [%]	p_2^ID [TeV^{-1}]
$\lvert\eta\rvert < 1.05$	-	1.55 ± 0.01	0.417 ± 0.011
$1.05 < \lvert\eta\rvert < 1.7$	-	2.55 ± 0.01	0.801 ± 0.567
$1.7 < \lvert\eta\rvert < 2.0$	-	3.32 ± 0.02	0.985 ± 0.019
$2.0 < \lvert\eta\rvert < 2.5$	-	4.86 ± 0.22	0.069 ± 0.003
Region	p_0^MS [TeV]	p_1^MS [%]	p_2^MS [TeV^{-1}]
$\lvert\eta\rvert < 1.05$	0.25 ± 0.01	3.27 ± 0.05	0.168 ± 0.016
$1.05 < \lvert\eta\rvert < 1.7$	0	6.49 ± 0.26	0.336 ± 0.072
$1.7 < \lvert\eta\rvert < 2.0$	0	3.79 ± 0.11	0.196 ± 0.069
$2.0 < \lvert\eta\rvert < 2.5$	0.15 ± 0.01	2.82 ± 0.58	0.469 ± 0.028

Table 3.2: Extracted values of the Inner Detector and Muon Spectrometer muon momentum resolution terms from Equations (3.11) and (3.10) [39]. The uncertainties represent the quadratic sum of the statistical and systematic uncertainties. A dash means the corresponding parameter is not applicable to the current case.

Whenever two muons from the same decay have similar momentum resolution and angular effects are neglected, the relative mass resolution $\frac{\sigma_{\mu\mu}}{M_{\mu\mu}}$ is proportional to the relative momentum resolution [40],

$$\frac{\sigma_{\mu\mu}}{M_{\mu\mu}} = \frac{1}{\sqrt{2}} \frac{\sigma_{p_\mathrm{T}}}{p_\mathrm{T}}, \tag{3.14}$$

a factor $\frac{1}{\sqrt{2}}$ better than for a single muon.

3.6.4 The inner detector

The inner detector (ID) is a close-to-hermetic detector that measures the momentum of charged particles. It is shaped like a cylinder, 6.2 meters long and with a radius of 1.08 meters. Figure 3.9 shows the location of the sub-detectors in the barrel and end-caps. It

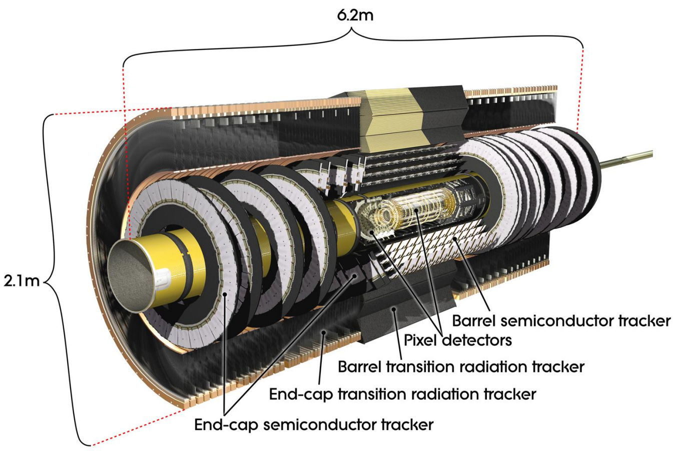

Figure 3.9: A cut-away view of the ATLAS inner detector.

consists of three independent sub-detectors — the pixel detector, the semiconductor tracker (SCT) and the transition radiation tracker (TRT) — constructed as concentric cylinders in the barrel region and disks perpendicular to the beam axis in the end-cap region. Figure 3.10 shows tracks going through the ID at four different pseudorapidities η. The charged track momentum must be above a certain threshold, nominally 0.5 GeV, and within the pseudorapidity range $|\eta| < 2.5$. In addition the ID can identify electrons over a large range of energies, from 0.5 GeV to 150 GeV, with pseudorapidity within the range $|\eta| < 2.0$ (the TRT) , and reconstruct the primary vertex from the interaction point of the proton-proton collision and secondary vertices from decayed particles (the Pixel detector).

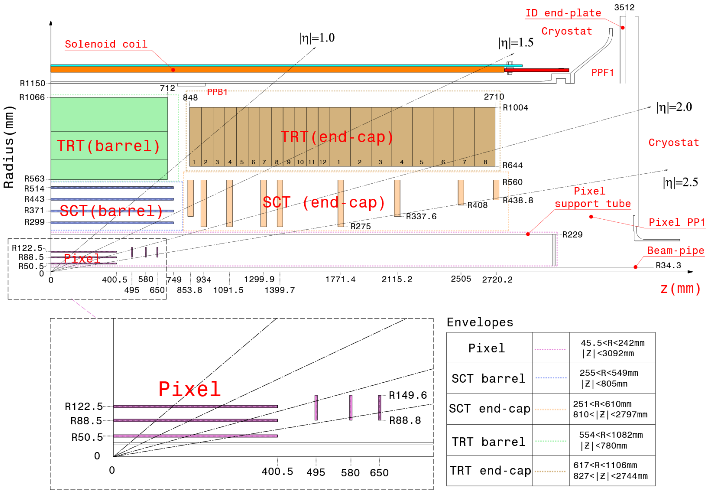

Envelopes

Pixel	┈	45.5<R<242mm |Z|<3092mm
SCT barrel	┈	255<R<549mm |Z|<805mm
SCT end-cap	┈	251<R<610mm 810<|Z|<2797mm
TRT barrel	┈	554<R<1082mm |Z|<780mm
TRT end-cap	┈	617<R<1106mm 827<|Z|<2744mm

Figure 3.10: A schematic cross-section of the ATLAS inner detector, displaying the main parts together with tracks at different pseudorapidities η. Insertable B-layer not included.

The whole ID is immersed in an axial, uniform 2T magnetic field, provided by the solenoid magnet located between the inner detector and the electromagnetic calorimeter (more details regarding the magnet system is found in Section 3.6.7). The field is homogeneous inside the solenoid, and the field is parallel to the beam line. Charged particles will bend in the transverse plane (ϕ is the bending plane).

3.6.4.1 Pixel detector

Originally there were three cylindrical layers in the barrel region of the pixel detector, at approximately 5, 9 and 12 cm distance, and six disk layers perpendicular to the beam axis, three disks in each of the forward and backward directions, as illustrated in Figure 3.11. A pixel module is about 6 cm long and 2 cm wide with 46080 pixels. In total, the pixel detector has 1744 pixels detector modules, and thus approximately 80 million pixels (i.e. readout channels) — 67 million in the barrel and 13 million in the end-cap. The intrinsic measurement accuracies per module are 10 μm in R-ϕ and 115 μm in z in the barrel region, and 110 μm in R-ϕ and 115 μm in R in the end-cap region. The pixel detector covers the region $|\eta| < 2.5$.

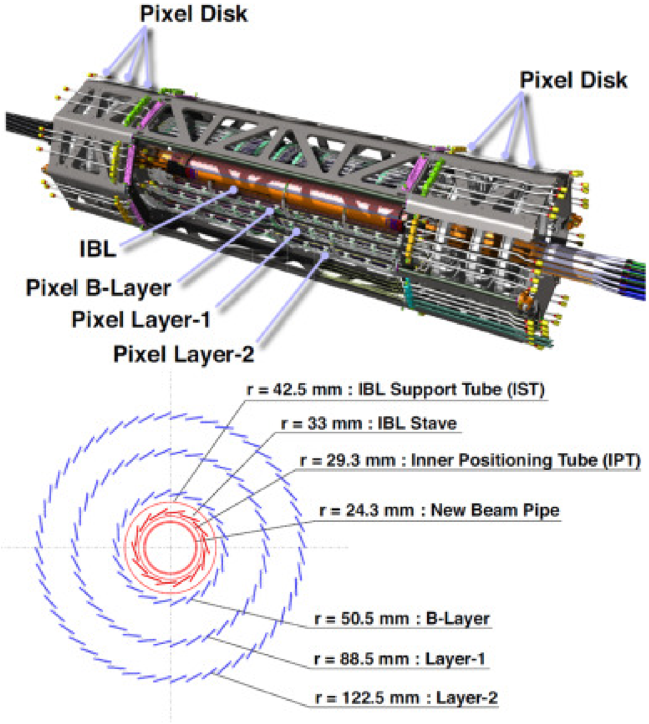

Figure 3.11: Schematic overview of the pixel detector, showing the four different layers and the pixel disks [41].

The insertable B-layer (IBL) is a more recent addition, installed in May 2014, and is now the innermost layer of the pixel detector. It was inserted in the gap between the existing pixel detector and the new, smaller beam pipe. It has 244 modules, with 12 million readout channels. The intrinsic measurement accuracies are 8 μm in R-ϕ and 40 μm in z [42].

Both the pixel detector and the SCT (Section 3.6.4.2) are silicon semiconductor detectors. Semiconductors are materials whose outer shell atomic levels have a distinct energy band structure and with a large forbidden energy gap (a region without any allowed energy levels), much greater than for conductors (which have small or no gap), but smaller than for insulators [43]. On opposite sides of this forbidden gap is the conduction (highest energy level) band and the valence band. When a charged particle traverses the semiconductor, valence electrons are kicked into the conduction band, leaving positively charged holes behind. Both the electrons in the conduction band and the holes in the valence band can be the charge carriers of an electric current.[7] When a charged particle, e.g. a muon, passes through the material, it can ionize the semiconductor, creating electron-hole pairs. When an electric field is applied to the semiconductor, the holes and electrons create a current that can be measured. The average energy required to create electron-hole pairs is about 10 times smaller than for gas ionization (which is what is used e.g. in the MS, more details about this is located in Section 3.6.6).

Because of the excellent spatial resolution and 3-dimensional position measurement, the pixel detector plays a key role in the reconstruction of charged particles and primary and secondary vertices.

3.6.4.2 SemiConductor Tracker

The SemiConductor Tracker (SCT) is the middle part of the inner detector, located between the pixel detector and the Transition Radiation Tracker (Section 3.6.4.3). As for the pixel detector, the modules are placed in concentric cylinders around the beam axis in the barrel and on disks perpendicular to the beam axis in the end-caps. Particles from a collision typically traverse the eight strip layers of the SCT (four points in space), which enables the SCT to measure momentum, impact parameter and vertices.

There are four layers in the barrel region, at radii of 299 mm, 371 mm, 443 mm, and 514 mm from the z-axis, with a total of 2112 silicon modules [44]. The two end-caps are made up of 9 disks each with a total of 1976 modules located between 835 and 2788 mm from the interaction point. Figure 3.12 offers a schematic view of the layout of the SCT, showing the location of the layers.

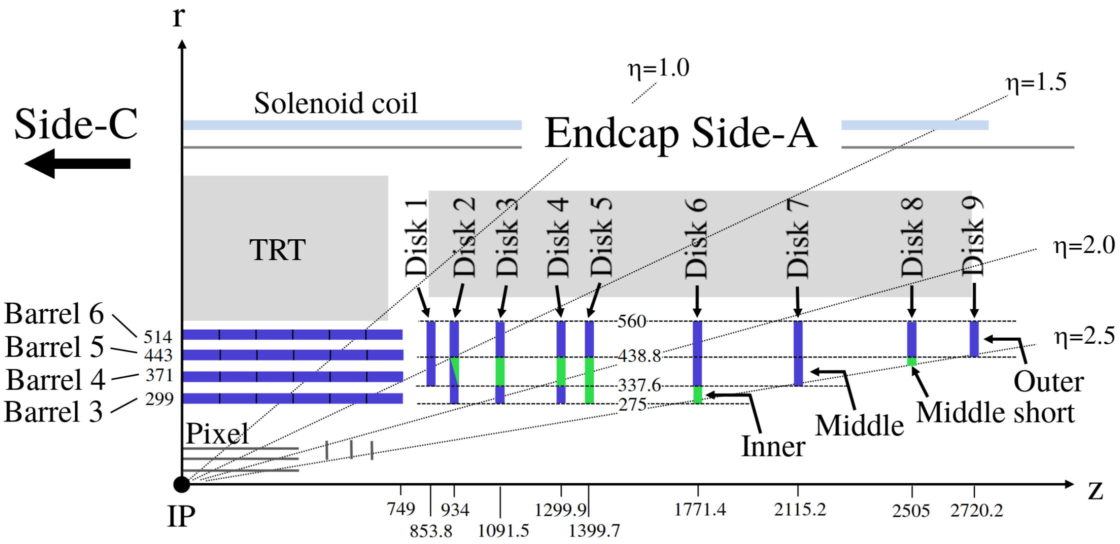

Figure 3.12: A schematic view of the layout of the SCT [44]. The radial and longitudinal coordinates are given in millimeters. The green and blue colors on the modules denotes sensors from different suppliers.

---

[7] The holes are not actually moving. When a hole is present, a neighbouring valence electron might jump into it, leaving a new hole behind. A series of these events can be seen as an apparent movement of a positive hole.

The barrel modules are all equal, with strips that are approximately parallel to the magnetic field. Each module consists of two silicon-strip sensors, and two identical silicon-strip sensors glued back-to-back with the first pair at a small angle (40 mrad). The modules are mounted in such a way that the plane of the modules are approximately tangential to a circle around the beam-axis, overlapping by a few millimeters to provide hermetic tiling in the transverse plane ϕ. The endcap disks consist of up to three rings of modules containing trapezoidal sensors, with the strip direction being radial. The intrinsic accuracies are 16 μm in R-ϕ and 580 μm in z (barrel) and R (end-caps) per module [34]. In total the SCT has about 6.3 million readout channels

3.6.4.3 Transition Radiation Tracker

The outermost part of the inner detector is called the Transition Radiation Tracker (TRT). The barrel section is built of individual modules with between 329 and 793 straws each, all parallel to the beam axis, located at between 56 and 107 cm from the z-axis. Each end-cap consists of 18 wheels. The 14 nearest to the interaction point are located between 64 and 103 cm from the center, in the z-direction, while the last four wheels extend out from 848 to 2710 cm, with radii between 617 and 1106 mm. In total there are about 50000 straws in the barrel section and 320000 in the end-caps.

A wire with a diameter of 4 mm is strung in the middle of each straw. When a charged particle passes through the straws, the Coulomb interaction between the particle and electrons in the gas can free some of the electrons. Holding the outer wall at high negative voltage, the wire in the middle will act as the anode and the outer wall as the cathode, separating the now freed electrons from the ionized gas. If electrons are freed close to the wire, they will be seen almost immediately. If not, they will have a drift time of at most 40 ns [45]. The drift time is used to infer the distance from the wire. Typically a track will leave 36 hits in the TRT.

Due to the construction, the TRT only provides R-ϕ information. Each straw has an measurement accuracy of 130 μm. The TRT covers the pseudorapidity range $|\eta| < 2.0$.

The TRT also has the ability to distinguish between electrons and hadrons. The straws are filled with a xenon-gas[8] (70% Xe, 20% CO_2, 10% CF_4), and when a relativistic particle crosses an inhomogeneity e.g. the boundary between the gas filled wire and the area outside, it has a probability of radiating energy in the form of a photon. The TRT can separate electrons from charged pions by using the fraction of high threshold (HT) hits[9] on the track. The probability of generating a HT hit depends on the Lorentz γ-factor ($\gamma = \frac{1}{\sqrt{1-\frac{v}{c}^2}}$) of the particle. Figure 3.13 shows the HT probability as a function of the γ-factor for the barrel section of the TRT for electrons and muons from J/Ψ and Z^0 decays. The probability is small for γ-factors under 10^3 and rapidly increasing between 10^3 and 10^4. Note that the heavier muons reach the turn-on curve at much higher momentum than the lighter electrons. When the muon momentum reaches several GeV, the HT probability increases. At particle

---

[8] Originally at least. Due to gas leaks, parts of the TRT are now flushed with a gas composed mainly of the much cheaper argon [46].

[9] Hits generating a pulse in the electronics above a defined threshold value

momenta above approximately 100 GeV, the pions emit transition radiation at a comparable rate to electrons, making them indistinguishable to the TRT [46][33].

Figure 3.13: The probability for electrons and muons from J/Ψ and Z^0 decays to emit transition radiation that triggers the high threshold limit as a function of the γ-factor for tracks within the TRT barrel region [46]. Data points are presented as solid symbols and simulation as open symbols.

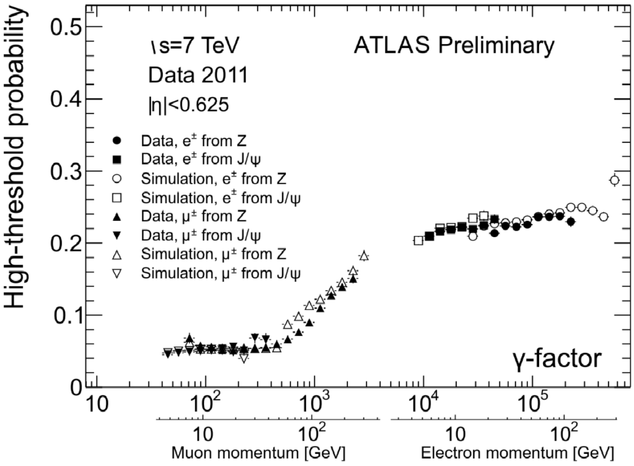

Figure 3.14 shows the charged pion misidentification probability for the HT fraction criteria that ensures a 90% electron identification efficiency as a function of $|\eta|$. The performance of the detector is better than expected, especially for higher values of $|\eta|$, as is easily seen when comparing simulation to data. Overall the misidentification probability is well below 10%, going as far down as 1% and lower for certain parts of the pseudorapidity interval. The observed shape is correlated to the number of TRT straws crossed by the track, which is low in the transition region between the barrel and end-cap at $0.8 < |\eta| < 1.1$ and at the highest values above $|\eta| < 1.8$.

Figure 3.14: Charged pion misidentification probability for the HT fraction criteria that ensures a 90% electron identification efficiency as a function of $|\eta|$ [46].

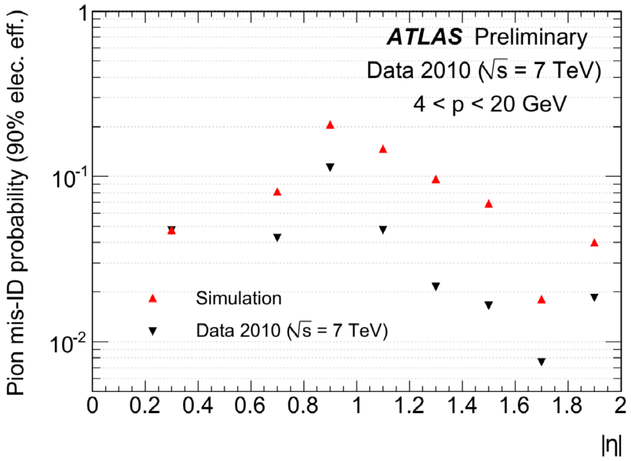

3.6.5 The calorimeters

There are two main parts of the ATLAS calorimeter system – the electromagnetic calorimeter (ECAL) and the hadronic calorimeter (HCAL), as illustrated in Figure 3.15. The purpose of these systems is to measure the energy and direction of photons and electrons (ECAL), and hadrons (HCAL). They cover the range $|\eta| < 4.9$.

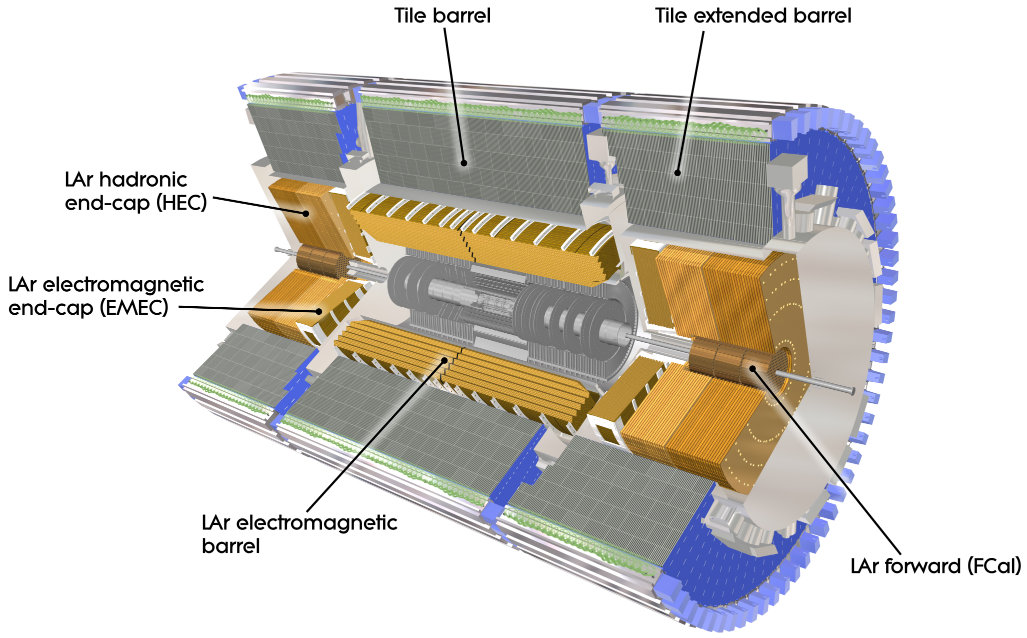

Figure 3.15: A cut-away view of the ATLAS calorimeters system, showing both the ECAL (LAr) barrel and end-caps and the HCAL (Tile) barrel and end-caps.

3.6.5.1 LAr electromagnetic calorimeter

When a photon, electron or positron enters the electromagnetic calorimeter, it interacts electromagnetically with the material in the calorimeter and initiates an electromagnetic shower. The electron/positron emits bremsstrahlung and the photon pair-produces an electron-positron pair. Depending on the energy of the incoming particle this happens time and time again, producing a shower that points in the direction of the original particle. The showering continues until the electrons/positrons/photons have so little energy left that collision effects dominate over pair-production. The larger the energy of the incoming particle, the deeper the shower is.

The electromagnetic calorimeter is a lead-liquid Argon (LAr) calorimeter. The barrel part of the ECAL extends out to $|\eta| < 1.475$, and the two end-caps cover the range $1.375 < |\eta| < 3.2$. The barrel itself is divided into two identical half-barrels that are separated by 4 mm at $z = 0$. The length of a half-barrel is 3.2 m, and their inner and outer diameters are 2.8 m and 4.0 m respectively. The end-caps are divided into two coaxial wheels, the inner wheel covering $2.5 < |\eta| < 3.2$ and the outer wheel covering $1.375 < |\eta| < 2.5$. The region $|\eta| < 1.8$ also has a presampler detector that is used to correct for energy loss by electrons and photons before reaching the calorimeter (e.g. inner detector, cryostats).

The section $|\eta| < 2.5$ is devoted to precision physics. In this region, the calorimeter has three different segments in depth, as illustrated in Figure 3.16. For the region $1.5 < |\eta| < 3.2$ and in the overlap between the barrel and end-caps, there are two layers. Most of the energy is deposited in the middle layer, while the back layer catches the tail of the shower, enabling the reconstruction of the incident particle energy. The first, highly segmented layer in direction of η, ensures a precise reconstruction of the particle direction.

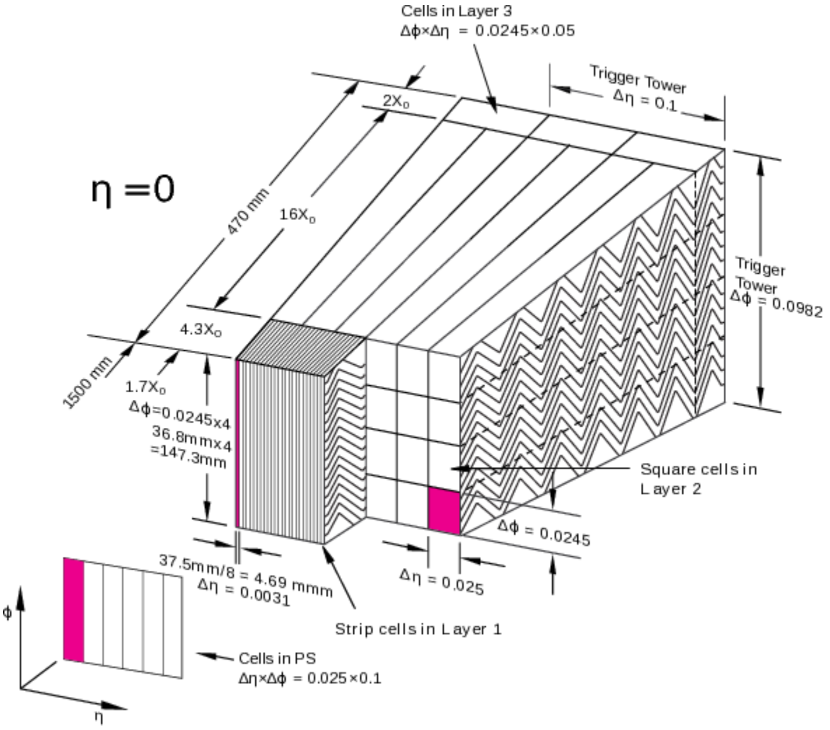

Figure 3.16: Sketch of the ECAL modules, showing the three layers [47]. The parameter X_0 is the *radiation length*, a characteristic of a material, the mean distance an electron or positron travels before loosing all but $\frac{1}{e}$ of its energy by bremsstrahlung [48].

3.6.5.2 Hadronic calorimeter

The hadronic calorimeter works in much the same way as the electromagnetic calorimeter, only there are hadrons initiating the hadronic showers through the strong interaction. The HCAL is quite dense to ensure that the entering hadrons come close enough to the nucleons to interact strongly and initiate a hadronic shower. New hadrons, mostly pions, are created in these collisions and can interact further with the material. However, hadronic showers are much more complicated than their electromagnetic siblings, as they also have an electromagnetic component, e.g. electrically neutral pions π^0 decay almost exclusively to diphotons. Also leptons and neutrinos from hadronic decays makes it hard to get a precise measurement of the energy of the incoming particle.

There are three subdetectors in the hadronic calorimeter: the tile calorimeter, the LAr hadronic end-cap calorimeter (HEC) and the LAr forward calorimeter (FCal).

The tile calorimeter is situated just outside the ECAL and covers the region up to $|\eta| < 1.7$. It is a sampling calorimeter[10] that uses steel as the absorber and plastic scintillating tiles as the active material. It is divided into a 5.8 m long central barrel and two extended barrels 2.6 m long with an inner radius of 2.28 m and an outer radius of 4.25 m.

The HEC is a copper-liquid argon sampling calorimeter. It covers the range $1.5 < |\eta| < 3.2$ and consists of two wheels in each end-cap. The wheels have a radius of 2.03 m.

---

[10] A sampling calorimeter has layers of passive absorber alternating with active detector layers, in constrast to homogeneous calorimeters that have a single medium throughout the volume of the detector.

Lastly, the FCal covers the range $3.1 < |\eta| < 4.9$, located about 4.7 m from the interaction point.

3.6.6 Muon Spectrometer

The only SM particles that are not stopped in the ATLAS detector, are muons and neutrinos. Of these, only muons can be detected directly. This is done in the Muon Spectrometer (MS). Figure 3.17 illustrates the various subdetectors of the MS. This is the outermost part of the ATLAS detector, and its purpose is to measure the momentum of all electrically charged particles that exit the calorimeters in the pseudorapidity range $|\eta| < 2.7$. In the range $|\eta| < 2.4$ it also acts as a hardware-based trigger. The MS can singlehandedly and quite accurately measure the momentum of particles down to a few GeV and up to several TeV, or it can combine forces with the ID for an even more accurate measurement of the muon properties. The relative muon momentum resolution was discussed in Section 3.6.3.2).

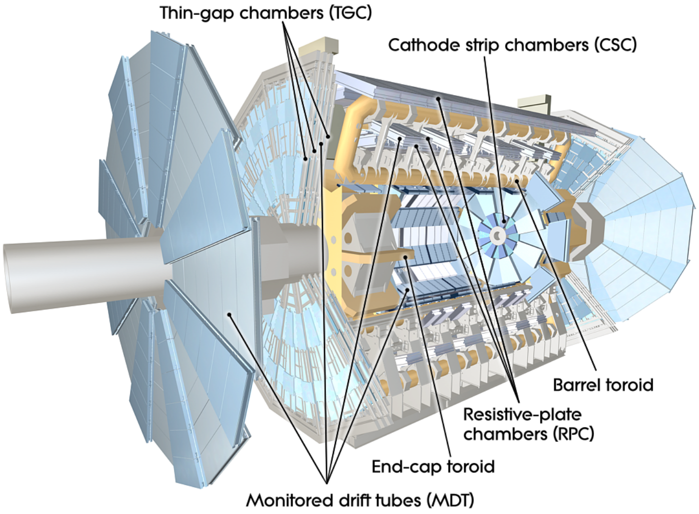

Figure 3.17: A cut-away view of the ATLAS Muon Spectrometer [49].

For $|\eta| < 1.4$, magnetic bending is provided by the large toroid magnets in the barrel. The magnetic flux density is about 1 T. Between $1.6 < |\eta| < 2.7$, magnetic bending is provided by two smaller end-cap magnets. The magnetic flux density in the end-caps are about 0.5 T. In the transition region $1.4 < |\eta| < 1.6$ the magnetic field is a combination of the two. The magnetic field is tangential to a circle in the transverse plane around the beam axis, thus bending the charged particles (muons) in the longitudinal plane (η defines the bending plane).

The muon chambers in the barrel are composed of three concentric cylindrical shells, with the beam axis on the axis of the cylinder. The radii of these shells are approximately 5 m, 7.5 m and 10 m. In the end-cap regions the muon chambers form large wheels, with the center of the wheel located on the z-axis about 7.4 m, 10.8 m, 14 m and 21.5 m from the interaction point. Figure 3.18 shows two different cross-sections of the Muon Spectrometer.

The muon system is composed of four sub-detectors: the Monitored Drift Tube chambers and the Cathode-Strip Chambers are the precision trackers while the Resistive Plate Chambers and the Thin Gap Chambers are supporting trackers and triggers.

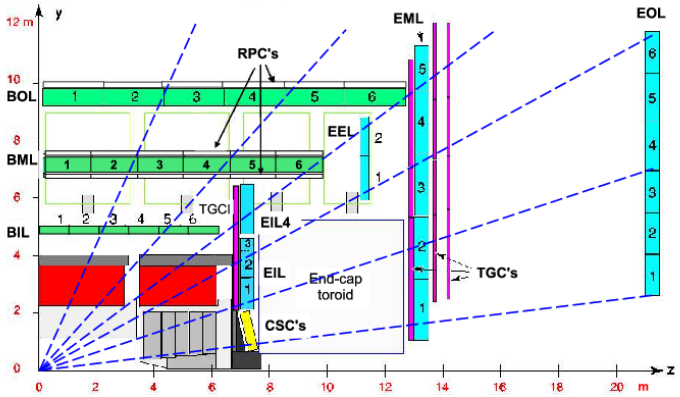

(a) Cross-section of the muon system in the longitudinal plane, the plane containing the beam axis. The dashed lines are the trajectories of muons with infinitely large momenta.

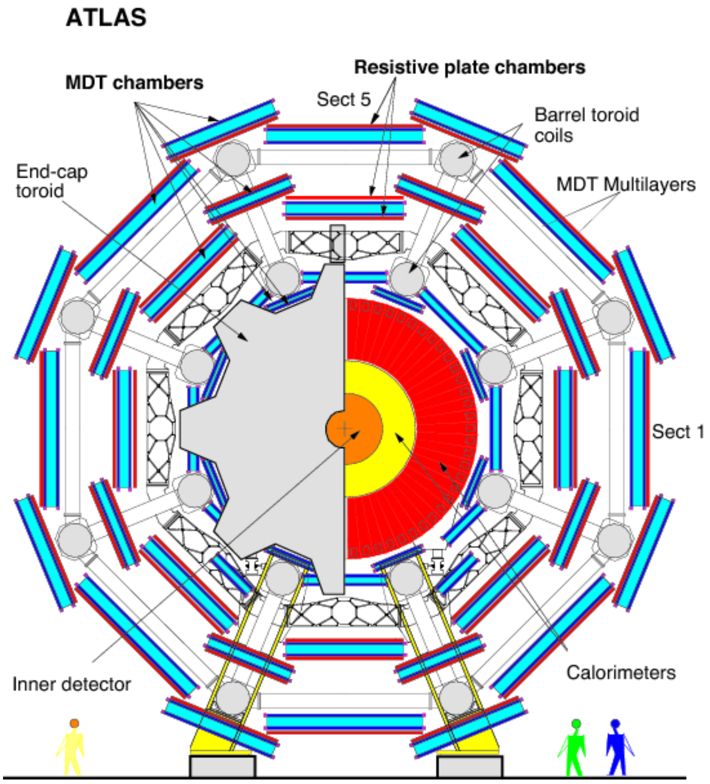

(b) Cross-section of the muon system in the transverse plane, the plane perpendicular to the beam axis, showing the three concentric cylindrical layers with eight small and eight large chambers. [50]

Figure 3.18: Cross-sections of the muon system in the longitudinal (a) and transverse (b) planes.

3.6.6.1 The Monitored Drift Tube chambers

The Monitored Drift Tube chambers (MDT) are the main tool for precision momentum measurement. They cover the range $|\eta| < 2.7$, except in the innermost end-cap layer where they cover up to $|\eta| < 2.0$. They consist of three to eight layers of drift tubes. The resolution is 80 μm per tube, or approximately 35 μm per chamber.

The MDT chambers are rectangular in the barrel and trapezoidal in the end-caps. The direction of the tubes in the chambers in the barrel and end-caps are along ϕ, i.e. the center of each tube is tangential to circles around the beam axis. All MDT chambers consist of two groups of tube layers, so-called multi-layers. In the inner layer of the MDT, each multi-layer consists of four tube layers, while in the middle and outer layer each multi-layer consists of three tube layers. Figure 3.19 shows the structure of a MDT chamber in the barrel.

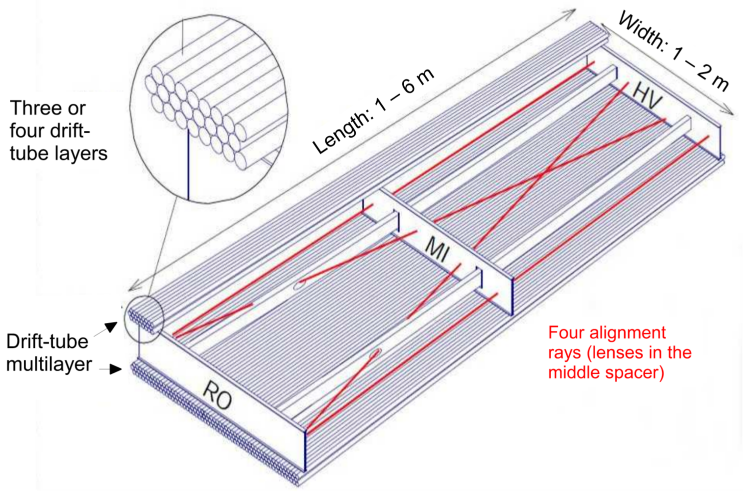

Figure 3.19: The mechanical structure of a barrel MDT chamber [33].

The tubes are drift tubes, each with a diameter of 29.970 mm, filled with Ar/$\mathrm{CO_2}$ gas at a pressure of 3 bar. When a muon passes through a straw, the gas inside is ionized, as illustrated in Figure 3.20. The freed electrons drift toward the wire (a tungsten-rhenium wire with diameter 50 μm, held at a potential of 3080 V) in the center of the drift tube and are registered there.

At high momentum, the relative muon p_T resolution $\frac{\sigma(p_\mathrm{T})}{p_\mathrm{T}}$ is dominated by the term $p_2^\mathrm{MS} \cdot p_\mathrm{T}$, as discussed in Section 3.6.3.2, where the term p_2^MS mainly accounts for the limited position resolution of the detector parts and the misalignment of the MS. For the MDT, the design resolution is 80 μm for the single-hit spatial resolution, and according to recent measurements [51] the current resolution approaches the design value for all MDT chambers in the MS.

3.6.6.2 The Cathode-Strip Chambers

The region $|\eta| > 2.0$ is subject to high doses of radiation, and here the first layer of the MDTs is replaced by the much more radiation hard Cathode-Strip Chambers (CSCs). They cover the region up to $|\eta| < 2.7$. In addition to being more radiation hard, the CSCs also have better time resolution than the MDTs.

Figure 3.20: Cross-section of a MDT tube, showing the ionization of the gas in the tube when a muon traverses the medium [33].

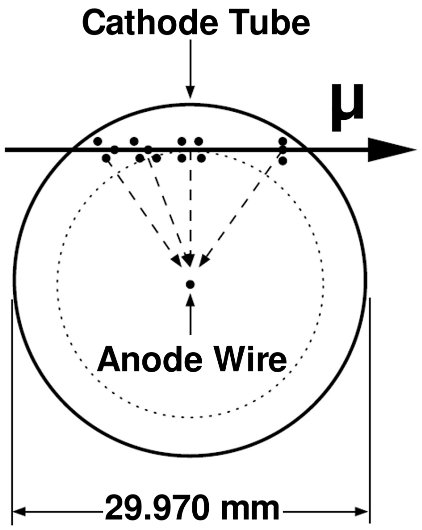

As can be seen from Figure 3.21, the CSCs have eight small and eight large chambers, segmented in ϕ, in each end-cap. Each chamber has four CSC planes, which allows for four independent measurements of η and ϕ along the particle trajectory. They are located at a distance of about 7 m from the interaction point, measured along the beam line. Together with the MDTs and the TGCs (Section 3.6.6.3) they form the "small wheel", with inner radius 881 mm and outer radius 2081 mm, corresponding to the range $2.0 < |\eta| < 2.7$.

Figure 3.21: Layout of a CSC end-cap showing clearly the eight small and eight large chambers.

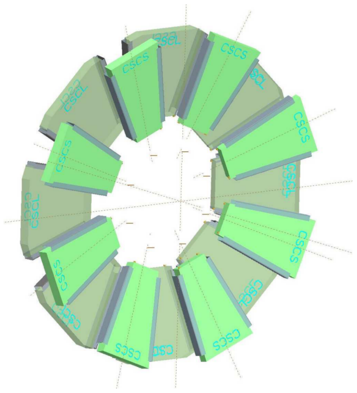

The CSCs are multiwire proportional chambers with wires going outward in the radial direction from the beam line. As illustrated in Figure 3.22, they have plates segmented into strips as cathodes and wires going orthogonal to the strips as anodes (measuring the precision coordinate η in the bending plane), but also strips going parallel to the wires, measuring the position in the non-bending (ϕ) plane [33]. The cathode strips are held at a high negative voltage compared to the anode wires. When a muon traverses the chamber, it ionizes the gas mixture (80% Argon, 20% CO_2) in the chamber. The liberated electrons and ions drift toward the nearest anode wire and opposing cathode strip respectively. When the electrons are close enough to the wire, the electrical field increases rapidly and accelerates the electrons. The electrons collide with the material in the detector, creating an avalanche of freed electrons and positive ions. The electrons are collected very quickly ($\sim$ 1 ns) while the positive ions drift towards the cathode [43]. This process induces a signal that can be read out of from the cathode strips. The η and ϕ coordinates are inferred from the induced-charge distribution.

The resolution is 60 μm per CSC plane in the bending direction (η), and 5 mm in the non-bending direction (ϕ).

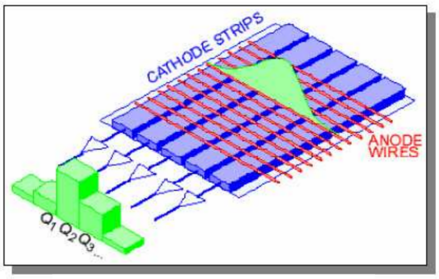

Figure 3.22: Segmentation of a CSC cathode, showing the cathode strips that are held at a high negative voltage, and the anode wires held at a high positive voltage.

3.6.6.3 The Resistive Plate Chambers and the Thin Gap Champers

A trigger system is needed to make a quick decision on whether the data from a certain event should be stored or not. This is done by Resistive Plate Chambers (RPCs) in the barrel region and Thin Gap Chambers (TGCs) in the end-cap region. The trigger detectors (the L1 muon trigger, described in Section 3.6.8) provide acceptance in the range $|\eta| < 2.4$ and over the full ϕ-range.

The RPCs are in the barrel section of the ATLAS detector and consist of three concentric cylindrical layers around the beam axis (the three trigger stations) at radii of approximately 5 m, 7.5 m and 10 m [52]. Each station consists of two independent layers, each of which measures both η and ϕ, giving a total of six measurements for a track going through all three layers. The chambers in the barrel region are located in between and on the eight coils of the superconducting toroid magnet (more details can be found in Section 3.6.7). The RPC is a gaseous parallel electrode-plate detector. Each RPC unit consists of two resistive plates parallel to each other at a distance of 2 mm, one held at a high voltage and the other at ground. The passage of a charged particle (i.e. a muon) causes ionization, and an avalanche of electrons is created in the field between the plates, and the signal is read out.

The TGCs are a type of multiwire proportional chambers that form large wheels in the end-caps. The middle layer of the MDTs in the end-cap are accompanied by seven layers of TGCs while the inner layer is accompanied by two layers of TGCs. The inner layer is further divided radially into two non-overlapping regions: the end-cap and forward. The TGCs also measure the azimuthal coordinate ϕ in the non-bending plane.

3.6.7 Magnet system

The ATLAS superconducting magnet system consists of one solenoid and three toroids (one barrel and two end-caps), as shown in Figure 3.23, all held at a temperature of about 4.6 K.

The inner and outer diameters of the solenoid are 2.46 m and 2.56 m, and the length is 5.8 m. It is aligned on the beam axis and provides a 2 T magnetic flux density in the volume of the whole inner detector directed along the beam axis.

The overall size of the barrel toroid magnets is 25.3 m in length, and with inner and outer diameters of 9.4 m and 20.1 m. The toroid magnet produces a toroidal magnetic flux density of approximately 0.5 T and 1 T in the central and end-cap regions respectively. The field is tangential to a circle parallel to the transverse (ϕ) plane. The eight barrel toroid coils are interleaved with the end-cap coils.

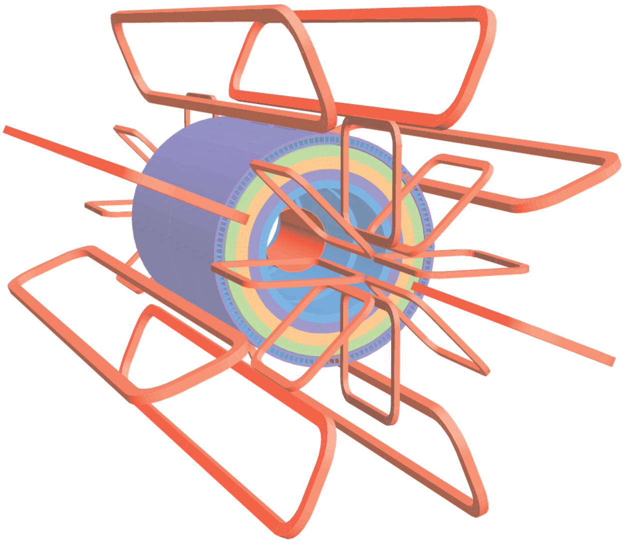

Figure 3.23: The ATLAS magnet system, showing the central cylinder containing the solenoid windings and the toroid magnet system coils.

3.6.8 Trigger system

The ATLAS trigger system decides which events to keep for further analysis and which events to discard. This is a crucial part of the operation, as events containing New Physics, should it manifest at this energy, could be thrown away.[11]

The Run 2 trigger system consists of the hardware-based Level-1 (L1) trigger and the software-based high level trigger (HLT). The L1-trigger determines Regions-of-Interests (RoIs) in the detector by taking coarse granularity input from the calorimeters and the muon detector, reducing the event rate from approximately 30 MHz to 100 kHz, leaving the L1 trigger with 2.5 μs to decide to keep or discard each event. Possible signatures of events to keep are high-p_T muons, electrons, photons and jets, or large missing transverse energy (MET) and large total transverse p_T.

Each RoI is sent to the HLT where sophisticated algorithms using the full granularity detector information reduces the rate from 100 kHz to approximately 1 kHz. The processing time is about 200 ms per event.

---

[11] This section is mainly based on [53].

3.7 Relevant physics concepts at the LHC

3.7.1 Luminosity

The instantaneous luminosity is an important parameter for a particle collider, measuring how many particle collisions there are per square centimeter per second ($\mathrm{cm}^{-2}\mathrm{s}^{-1}$),

$$\mathcal{L} = f_{\mathrm{B}} \frac{n_1 n_2}{4\pi\sigma_x\sigma_y}$$

where n_1 and n_2 are the number of particles in bunches 1 and 2 that go in opposite directions and collide head-on with frequency f_{B}, and σ_x and σ_y denote the transverse size of the beam [48]. Nominal values for these parameters are listed in Table 3.3. The LHC was designed to collide 2808 bunches consisting of 10^{11} protons each up to 40 million times per second at a center of mass energy of 14 TeV, with an instantaneous luminosity of $10^{34}\,\mathrm{cm}^{-2}\mathrm{s}^{-1}$.

Parameter	Value	Comments
N	2808	Number of bunches
σ	$16.7\ \mu\mathrm{m}$	Transverse beam size ($\sigma_x = \sigma_y$)
f_B	$40\ \mathrm{MHz}$	Bunch crossing frequency
n	1.15×10^{11}	Protons per bunch

Table 3.3: Nominal beam parameters [54].

The time integral of the instantaneous luminosity $\mathcal{L}$, the *integrated luminosity* $\int \mathcal{L}dt$, is a quantity used as a measure of the amount of data collected, in units of inverse barns, a unit that is reversely proportional to length squared. One barn ($1\,\mathrm{b}$) is equal to $10^{-28}\,\mathrm{m}^2$.

The event rate R, the number of events per second, $d\mathrm{N}/dt$, for any given process is proportional to the instantaneous luminosity,

$$\mathrm{R} = \frac{d\mathrm{N}}{dt} = \sigma\mathcal{L},$$

where σ is the theoretical process cross-section, given by the Standard Model for ordinary SM processes, or a BSM theory for BSM interactions. The cross-section is measured in barns.

The expected number of events N for any given process, e.g.

$$p\bar{p} \to Z' + X \to \mu^+\mu^- + X,$$

is given by

$$\mathrm{N} = \sigma \int \mathcal{L}dt,$$

with σ as the cross-section of the particular process in question.

3.7.2 Transverse momentum

In the ATLAS coordinate system, as described in Section 3.6.1 and drawn schematically in Figure 3.5, the beam pipe is parallel to the z-axis. The plane perpendicular to the beam axis, the x -y-plane, or ϕ-plane, is referred to as the transverse plane. The transverse momentum, p_{T}, is the component of the momentum in the transverse plane. This is a very important variable in proton-proton collisions. High p_{T} final state particles also are hints of a hard scattering process.

Looking at a hard scattering process, where two partons collide, the total momentum of the final state particles along the beam axis is equal to the vector sum of the momenta of the colliding particles. Any given parton carry a momentum $p_{\mathrm{proton}} \cdot x$, where p_{proton} is the momentum of the proton, and x is the fraction of the proton momentum carried by the parton. As this size in general is different for any parton, there is a non-zero total momentum along the beam axis.

The situation in the transverse plane is dramatically different. The transverse momentum of any parton is in general negligible compared to that of the total momentum. We can see this by performing a back-of-the-envelope calculation, using the Heisenberg uncertainty principle, and the fact that the partons are confined within the proton which has a size of about 1 fm. This gives the order of magnitude of the intrinsic momentum of a parton

$$\Delta x \Delta p_x \sim \hbar \rightarrow \Delta p_x \approx \frac{\hbar}{\Delta x} \approx \frac{0.2\,\mathrm{GeV\,fm}}{1\,\mathrm{fm}} = 0.2\,\mathrm{GeV},$$

which is negligible compared to the TeV scale of the proton-proton collisions at the LHC. Because of this we assume that the total transverse momentum of the final state particles in such collisions is zero. This naturally leads to another important quantity, namely the missing energy.

3.7.3 Missing energy

Knowing that the sum of the transverse momenta in a hard scattering process should be zero, it is possible to detect particles that leave no trace in the detector. Within the SM this is the neutrino, but if we go beyond the SM there are many candidates, for example dark matter particles. Dividing particles into “visible” and “invisible”, we can write in general

$$\sum_{\text{visible}} \mathbf{p}_{\mathrm{T}} + \sum_{\text{invisible}} \mathbf{p}_{\mathrm{T}} = 0,$$

which leads us directly to an expression for the total transverse momenta of the invisible particles,

$$\sum_{\text{invisible}} \mathbf{p}_{\mathrm{T}} = - \sum_{\text{visible}} \mathbf{p}_{\mathrm{T}}.$$

For highly relativistic particles, the transverse momentum equals the transverse energy (in natural units), and the missing transverse momentum is often referred to as missing transverse energy, $\not{E}_{\mathrm{T}}$.

Note that there is no information on individual invisible particles, only the vector sum is known.

3.7.4 Cross-sections at the LHC

Events can be categorized as stemming from either soft or hard processes. The Z', if it exists, is produced in a hard scattering process. Soft scattering processes are very important for e.g. the total cross-section and the underlying event. At hadron colliders, like the LHC, QCD is the underlying theory for either process, but whereas for hard processes perturbation theory can be used with a high level of certainty, the soft processes must be described by non-perturbative QCD, which is more complicated.

The total cross-section at LHC is decomposed into several main components – elastic ($pp \to pp$) collisions, single diffractive dissociations (SD, $pp \to Xp$), double diffractive dissociation (DD, $pp \to XY$), central diffractive dissociation, non-diffractive (ND) events and hard collisions [55][56]. In elastic scattering, the two initial state protons change direction, and nothing else happens – the absolute values of their momenta remain the same. The interaction is often described as an exchange of a *pomeron*. For all diffractive processes and elastic scattering, the pomeron is a colorless object, e.g. a gluon pair. All other scattering processes are inelastic scatterings, where one or both of the protons dissociate and additional particles appear in the final state. In single-diffractive dissociations (leftmost illustration of Figure 3.24), one of the incoming protons remains intact, while the other proton dissociates and hadronizes. In double diffractive dissociations (middle illustration of Figure 3.24), both incoming protons dissociate and hadronize. In central diffractive processes (rightmost illustration of Figure 3.24), both incoming protons remain intact, but the double pomeron exchange create a system of particles. Non-diffractive inelastic scatterings (not illustrated) can exchange colored pomerons.

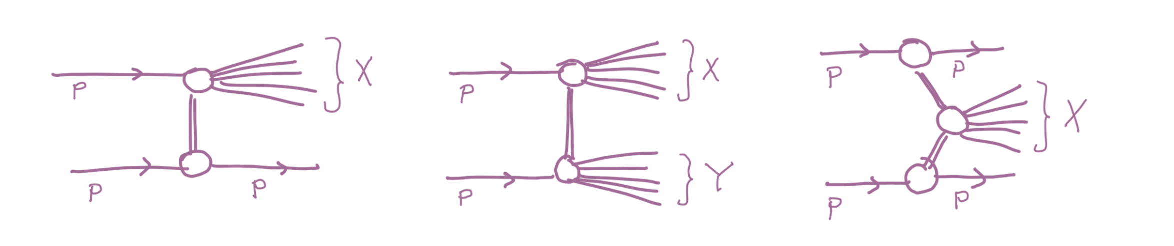

Figure 3.24: Illustrations of single diffractive, double diffractive and central diffractive processes.

By far, the hard collisions are the smallest part of the total production cross-section at LHC. Figure 3.25 illustrates this fact. The total cross-section is many orders of magnitude above the hard scattering cross-sections in which for example the gauge bosons of the Standard Model are created.

3.7.5 Parton Distribution Functions

The Parton Distribution Function (PDF) of a hadron, like the proton which is of interest at the LHC, is a function $f_i(x, Q^2)$ which tells us the probability of finding a parton (i.e. quark, antiquark or gluon) with flavor i carrying the fraction x of the proton's momentum, where Q is the energy scale of the hard interaction. Obviously this is an important piece of

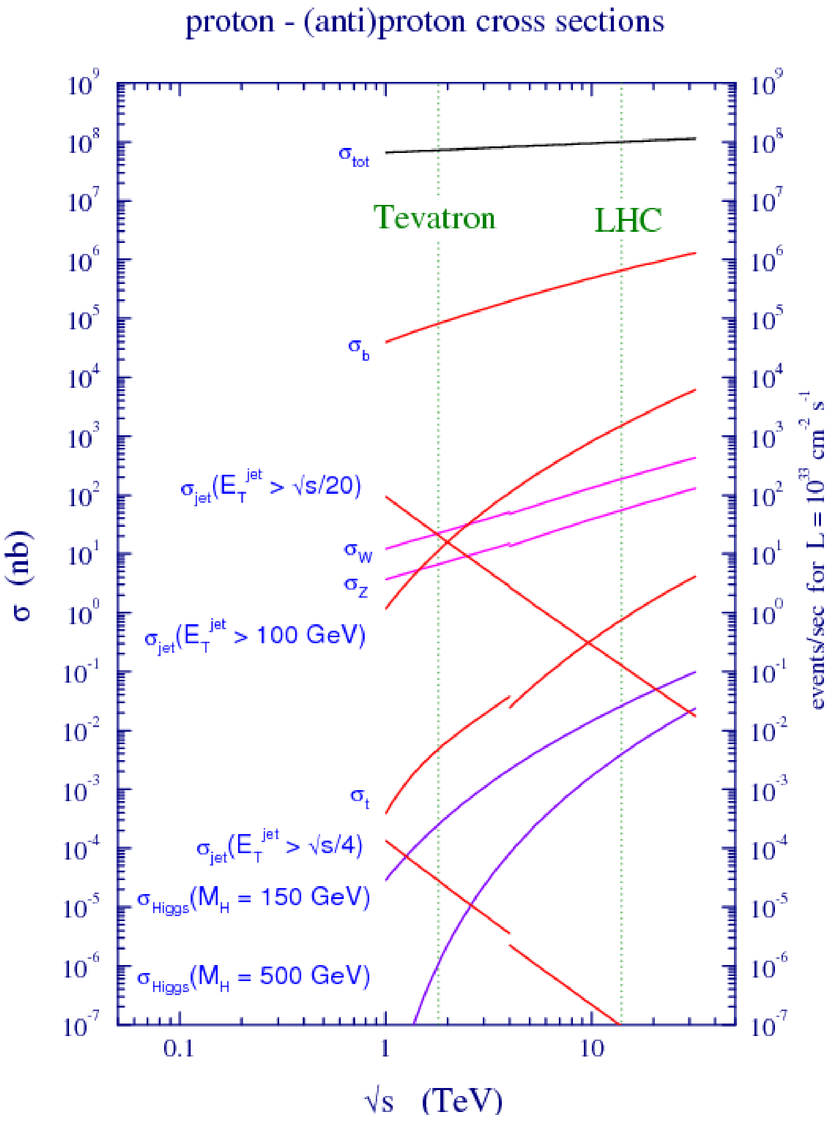

Figure 3.25: Standard Model cross-sections as functions of center-of-mass energy [57]. The total cross-section is many orders of magnitude above the hard scattering cross-sections in which for example the gauge bosons of the Standard Model are created.

information as it is the partons that participate in the hard collisions, and every cross-section prediction includes the PDFs in the calculations.

There are several different PDF sets available, accurate to next-to-leading order (NLO) or next-to-next-to-leading order (NNLO) in QCD. At the heart of these different PDF fits lies, among others, deep-inelastic scattering (DIS) data obtained at the HERA electron-proton collider and in fixed-target experiments. In addition high precision Drell-Yan data obtained at the LHC or the Tevatron experiments are used in the fits. Differences in what data is used, in object definitions and in cuts lead to differences in the resulting PDF fits. This can be taken into account in a specific analysis as a systematic uncertainty. An example of a PDF set is shown in Figure 3.26.

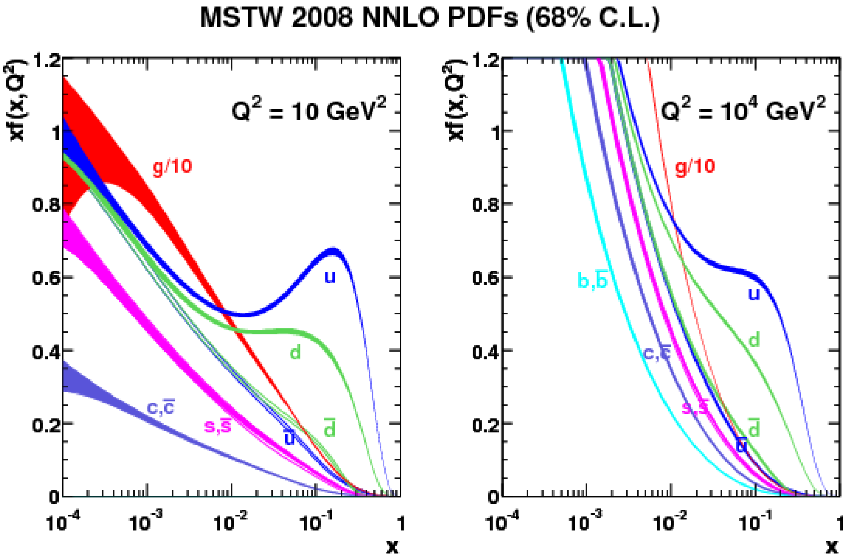

Figure 3.26: The MSTW 2008 NNLO PDF set for (left) $Q^2 = 10\,\mathrm{GeV}^2$ and (right) $Q^2 = 10^4\,\mathrm{GeV}^2$ [58]. The width of the bands reflect the uncertainties of the estimates at the 68% confidence level.

3.8 Summary

In this chapter, we took a close look at CERN, the LHC and in particular the ATLAS detector which was described in detail, including information on how muon properties are measured in the ATLAS detector. We also looked at important physics concepts at the LHC, some of which we will encounter often in the following.

In the next chapter, we will learn what we need to analyze the data collected with the ATLAS detector.

Chapter 4

Searching for the Z' – basic concepts and tools

In Chapter 1 we looked into what we know about our world in terms of particles and forces, and the mathematical framework used in experimental particle physics, the Standard Model. In Chapter 2 we saw a few examples of Nature's unsolved mysteries and a handful of carefully selected beyond the Standard Model theories that might offer potential solutions to some open questions. Finally in Chapter 3 we looked at how to experimentally detect particles produced in proton-proton collisions at the LHC using the ATLAS detector.

In this chapter we explore the last ingredient needed, namely the methodology used to analyze the vast amount of data collected at the ATLAS detector in the search for a new, neutral gauge boson, the Z'.

4.1 The importance of invariant mass

The beams that circulate in the LHC collide at four different points in the ring, one of which is in the center of the ATLAS detector. In most cases the protons in the beam collide elastically, exchanging some fraction of their energy, but continuing on their merry way (see Section 3.7.4 for more details about this). But sometimes the quarks or gluons inside the protons crash violently into each other in a hard collision, and are transformed into other particles. Usually well-known particles are created in the collisions, like quarks or gluons that are seeds for jets, or the gauge bosons of the SM – $W^{\pm}$ or Z^0. But every once in a while, if it exists at all, a Z' may be produced.

The *invariant mass method* uses the concept of invariant mass. When colliding beam particles of energies E_1 and E_2 and momenta $\mathbf{p}_1$ and $\mathbf{p}_2$ collide, the heaviest on-shell[1] particle that can be created in this collision has the mass m equal to the invariant mass of the collision,

$$\sqrt{s} = m = \sqrt{(E_1 + E_2)^2 - (\mathbf{p}_1 + \mathbf{p_2})^2}. \tag{4.1}$$

This is the center-of-mass energy, the total energy in the frame where the sum of momenta is zero. We see from the expression above that $\mathbf{p}_1 = -\mathbf{p}_2$ yields the largest mass. In practice

---

[1] On-shell particles satisfy the energy-momentum relation in Equation (4.1). Off-shell particles are virtual particles that do not obey this relation.

this is achieved in the experiment by circulating beams of particles in opposite directions and colliding them head on. The situation is complicated by the fact that it is the partons inside the protons that actually collide. The momentum carried by a parton is described statistically by PDFs, as described in Section 3.7.5, and we cannot expect that the vector sum of the longitudinal momenta of two colliding partons is zero. In addition there is an effect from the partons' momenta not in the direction of motion, but this is negligible as the momentum transverse to the direction of motion is tiny compared to the momenta of the partons.

The mass of a decayed particle can be reconstructed by calculating the invariant mass of the N lighter particles it decayed to,

$$m = \sqrt{\left(\sum_{i=1}^{N} E_i\right)^2 - \left(\sum_{i=1}^{N} \mathbf{p}_i\right)^2}. \tag{4.2}$$

In this thesis, we focus on the process

$$pp \rightarrow Z' + X \rightarrow \mu^+\mu^- + X,$$

i.e. the production of a new neutral gauge boson that decays to two muons.[2] Therefore it is the reconstructed invariant mass of the muon pair that is of interest,

$$m = \sqrt{(E_{\mu^+} + E_{\mu^-})^2 - (\mathbf{p}_{\mu^+} + \mathbf{p}_{\mu^-})^2}.$$

A decay of the Z' to two muons (i.e. the signal) is actually swamped by so-called background processes. In Figure 4.1 we see a histogram with the invariant mass of two muons of opposite electric charge on the x-axis and the number of events on the y-axis. The muons in question are carefully selected with the method that is discussed in Section 5.1. The Standard Model processes are drawn in black and the new physics, the Z', is drawn in purple. We see that the large majority of events are to the left in the histogram, at low invariant masses (where the SM Z^0 boson is very prominent) and a peak marked "New physics" is at high invariant mass. The invariant mass is a discriminating variable, separating the signal from the background (the SM processes).

To illustrate the technique with a real-life example, we see in Figure 4.2 the dimuon invariant mass distribution for oppositely charged, combined[3] muon pairs with transverse momentum above 4 GeV and pseudorapidity $|\eta| < 2.5$, using $6.6\ \mathrm{pb}^{-1}$ of ATLAS data [59]. We see the following resonances clearly, J/Ψ (~3.1 GeV), Ψ' (~3.7 GeV), Υ (1S) (~9.5 GeV)[4] and Z^0 (~ 91 GeV).

Before looking at data, we need to model the background as accurately as possible to be able to distinguish a possible signal from background in real data. It is especially important to be able to estimate the background under a peak. We thus need to know what processes make up the background for our search. This is covered in Section 4.4. Then we need to make simulated events for all of the background processes. In addition we need to make

---

[2] Technically a muon and an antimuon, but we often refer to this as two muon.

[3] This will be explained in Section 4.3.1, but for now we can think of combined muons as particles that are reconstructed as muons based on information from both the ID and the MS.

[4] Possibly with another Υ resonance just above, but less pronounced.

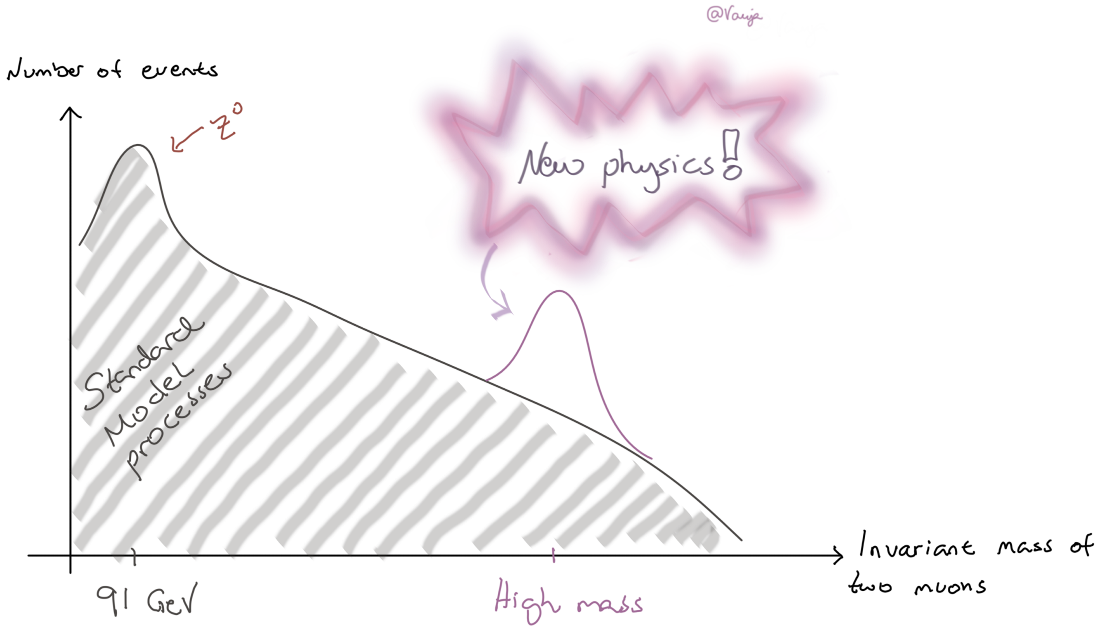

Figure 4.1: A drawing illustrating the invariant mass search technique. The well-known SM processes are drawn in black while the hypothetical new physics is drawn in purple as a very visible peak over the black background. The figure has the dimuon invariant mass on the x-axis, and the number of events on the y-axis.

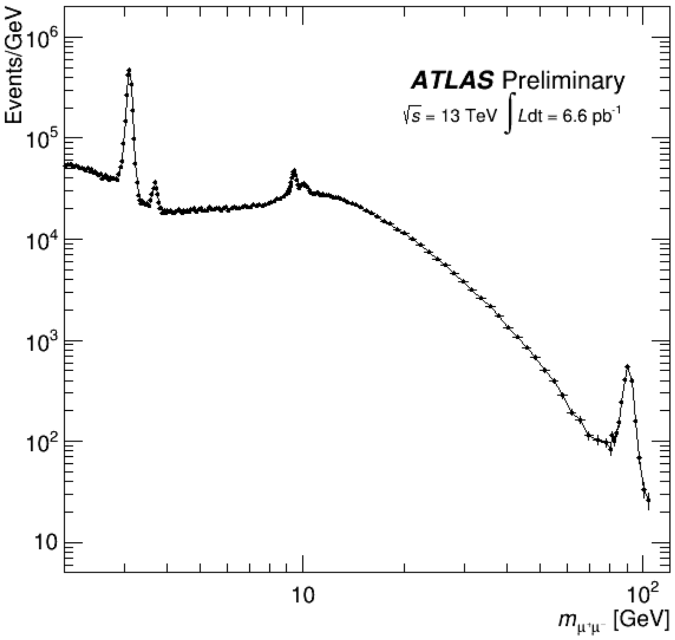

Figure 4.2: The dimuon invariant mass distribution for oppositely charged, combined muon pairs with transverse momentum above 4 GeV and pseudorapidity $|\eta| < 2.5$ using early 2015 data [59].

simulated data for some representative signal models. The process of simulating events is covered briefly in Section 4.2.

4.2 Simulated events

Simulated data are an integral part of any ATLAS analysis. They are needed to describe what we expect to see, such that it is possible to detect the unexpected. At the heart of simulated data we find the Standard Model of particle physics or a Beyond the Standard Model theory, and the Monte Carlo event generators (to be described in Section 4.2.1). After generation, the events are sent through a simulated version of the ATLAS detector (more on this in Section 4.2.4). The output from the simulation stage are MC events that ideally should accurately model data in all aspects. However, as an absolutely perfect description of both the ATLAS detector and Nature is an unrealistic goal, simulated data are compared to real data in several aspects and are then modified to fit the data. As an example, consider events from the process $Z^0 \to \mu^+\mu^-$. Events from data believed to originate from this process are carefully picked out and compared to simulated data. Deviations from data are transformed into so-called *scale factors* (SFs) based on e.g. η and ϕ coordinates of the particles, and applied as event weights[5] on an event-by-event basis to simulated data. More specifics on the applied SFs will be discussed in Section 4.3.4.

Two examples that shows how we compare data from MC generators to collision data are discussed in more detail in Appendix A. This work was a part of my qualification work to be an official ATLAS author.

4.2.1 A short introduction to MC generation

In order to generate events, we start with the physical theory, the SM or a BSM theory, and information about the colliding particles. At the LHC the particles circulating in the ring are protons or heavy ions, but as this thesis concerns protons we focus on this.[6]

4.2.1.1 Sampling the phase space

We then need to know the process to simulate, e.g. $u\bar{u} \to Z^0/\gamma \to \mu^+\mu^-$, and what the expression for the differential cross-section $\mathrm{d}\sigma$ for this process is. The differential cross-section is usually referred to as the *event weight* when dealing with event generators.[7] It involves the decay angles, the center-of-mass energy of the collision and the relevant matrix elements of the process (as described in Section 1.2.1.2). The event weight is directly related to the probability of this process happening.

Now we sample the phase space, i.e. the multi-dimensional hyper cube spanning all the degrees of freedom. In the limit of infinite number of candidate events the integral $\int \mathrm{d}\sigma$ converges to the measured cross-section. There is no physical information in the distributions at this stage, as the candidate events are distributed flat in phase space. The events will now be *unweighted* such that they are distributed according to theory, and such that each of the simulated events can be seen as a simulation of a real event.

---

[5] Event weights are factors that are multiplied into the event count.

[6] This section is based mainly on references [60] and [61].

[7] Not to be confused with the event weights applied in the event selection in Section 5.1.

4.2.1.2 Unweighting events

A much-used technique to unweight events is the hit-and-miss technique (also known as the Von Neumann method or the acceptance-rejection method). For each candidate event, the ratio of the event weight divided by the maximum event weight,[8] $\frac{\mathrm{d}\sigma}{\mathrm{d}\sigma_{\max}}$, is compared to a random number g generated uniformly between 0 and 1, and events that fulfill the requirement $g < \frac{\mathrm{d}\sigma}{\mathrm{d}\sigma_{\max}}$ are accepted. The rest are discarded. The accepted events have the frequency and the distribution predicted by theory.

4.2.1.3 Higher order corrections

There are several elements left out in this simple description. The incoming initial state partons can radiate particles, so-called initial state radiation (ISR), via the weak, the electromagnetic or the strong force. Also particles in the final state can radiate particles, so-called final state radiation (FSR) via the same mechanisms as ISR. Also several different Feynman diagrams can represent the same process, both at tree level and at higher order perturbations in the weak and/or electromagnetic and/or strong force. In addition we know that quarks and gluons are not directly observable, they appear in the detector as jets, and this process of hadronization needs to be modelled.

The modelling of the higher order perturbations can either be done by theory calculations, using the Standard Model to compute exactly the result of a given, small number of emissions, or via estimating the dominant effects due to emissions at all orders in perturbation theory. Tree Level Matrix Element generators consider only the diagrams corresponding to the emission of real particles. These generators can then be coupled to other generators that handle the hadronization, but care has to be taken when combining the two to avoid double counting of partons/jets. Another strategy is to decide on an order in perturbation theory and then compute all diagrams, real and virtual, that contribute to this. Yet another strategy is to use the fact that the dominant effects in certain regions of phase space have close to trivial dynamics, enabling the possibility of recursively describing extra emissions. It is within this strategy that one of the methods is called the Parton Shower technique.

4.2.2 Parton shower generators

The event generators that employ the Parton Shower technique, referred to as showering and hadronization generators (SHG), are general purpose event generators (GPEG) that enjoy widespread use in the field of experimental particle physics, for example PYTHIA [62] [63] or Herwig [64], which is in heavy use in the analysis described in Chapters 5 to 7. The following description is based on QCD showers only, but the same prescription is applied to electromagnetic showers to incorporate higher order QED corrections.

The SHGs start with a leading order hard subprocess, and the higher orders are added by evolving the event using parton showers, allowing the partons to split (or branch) into new pairs of partons, as illustrated in Figure 4.3. The shower continues until the energy is low enough to allow for hadronization (the hadronization scale). The partons are grouped

---

[8] This maximum event weight $\mathrm{d}\sigma_{\max}$ might be calculable from theory, or it can be approximated by scanning the parameter space.

together (hadronized) into colorless combinations and these resonances are decayed. Only FSR is shown in the figure, but the same prescription applies to ISR.

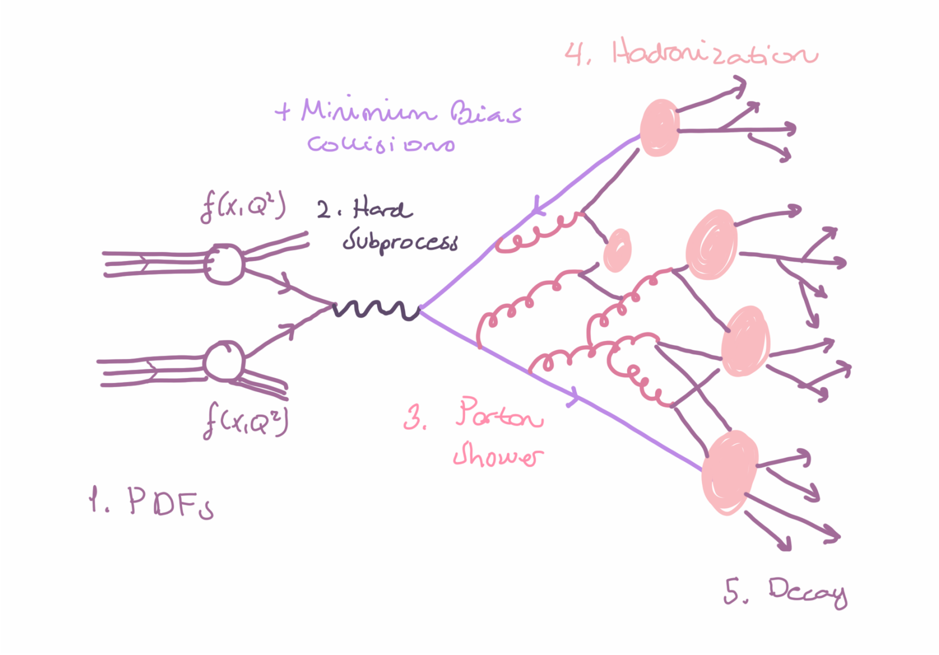

Figure 4.3: Schematic figure of the inner machinery in a showering and hadronization generator.

After hadronization, the remaining event is generated – beam remnants, interactions from other partons in the hadrons, and collisions between other hadrons in the colliding beams (known as *in-time pile-up*, see Section 4.6.3 for more information on pile-up). The beam remnants are what was left of the proton after the hard subprocess. The partons inside protons have a small (around $1\,\mathrm{GeV}$) primordial transverse momentum. The beam remnants recoil against this. Being colored, the beam remnants are a part of the same hadronization system as the hard subprocess, ensuring overall color neutrality.

4.2.3 Relevant event generators

In the dimuon analysis covered in this thesis we encounter several event generators. The different event generators have different specialties – some have the best description of diboson events, others might be best suited for generating events at the matrix element level for processes with varying number of partons in the final state, while others again are best at hadronization. Thus in any given sample a number of different event generators might be involved. The simulated data used in this thesis are produced using PYTHIA, Sherpa, Powheg BOX, Photos and MadSpin (Section 4.4 offers an overview of the simulated data).

PYTHIA [62] [63] is a general-purpose event generator that contains a large library of over 200 available hard processes. It can add initial and final state radiation, and hadronization is based on the Lund string fragmentation framework [65].

Sherpa [66] is also a general-purpose event generator, containing a flexible tree-level matrix-element generator for calculation of hard processes within both the Standard Model and selected BSM theories. ISR and FSR is described using the parton shower technique, based on the Catani-Seymour dipole factorization formalism [67].

Photos [68] is a generalized tool used for generation of bremsstrahlung corrections, and MadSpin [69] is a tool used to decay heavy resonances at NLO.

PYTHIA is used to generate the dedicated $Z' \to \mu^+\mu^-$ samples at invariant masses 2, 3, 4 and 5 TeV. Also PYTHIA is used in combination with Powheg in several samples, i.e. DY ($Z^0 \to \mu^+\mu^-$), single top and $t\bar{t}$ samples, where it generates the parton showering. For the the DY samples, Photos is also used to handle the electromagnetic showers. For the single top samples, MadSpin handles the decay of the top quark and W bosons. Sherpa is used to generate the mass-binned diboson samples used in the dimuon analysis in Chapter 5, and also the W+jets samples used in the QCD background study in Chapter 7.

4.2.4 Detector simulation

The MC generators are responsible for prompt decays, e.g. Z or W bosons, but all stable particles are handled by the detector simulation.[9] Stable particles are in this context defined as particles with proper lifetime $c\tau > 10\,\mathrm{mm}$. The particles with proper lifetimes less than 10 mm, which is well inside the beam pipe, are decayed by the event generator and their interactions with detector material or the magnetic field are ignored.

In both event generation and detector simulation so-called *truth* information is recorded for each particle and each event, from the collision of the partons to all information available on all tracks and particles generated in the event.

Events can be filtered at generation time such that only events with certain required properties (e.g. a minimum of transverse momentum, or only leptonic decays) are kept. Then all remaining events are read into the simulation. Each particle is propagated through the simulation, which can either be full simulation using GEANT4 [72], which is the standard strategy of ATLAS, or a less computationally expensive fast simulation [71].

GEANT4 contains a simulation of the ATLAS detector, including misalignments and dead material (e.g. cables and supporting pillars). The description is kept up-to-date by adding information on e.g. dead modules. It also contains detailed physics models for particle interaction with matter and the propagation of the particles through the detector. The complexity of the simulation requires a lot of computing resources and time, and several faster simulation strategies have been developed.

About 80% of the simulation time is spent on the simulation of particle showers in the calorimeters, and mostly in the electromagnetic calorimeter. The aim of the Fast GEANT4 Simulation is to speed up this process by replacing the low energy electromagnetic particles in the calorimeter with pre-simulated *frozen showers* that are stored in libraries. This cuts the CPU time by a factor of three in hard scattering events, still with most of the physics in the event complete.

Atlfast-II uses a similar approach, but cuts the simulation time by more than 90% by parameterizing calorimeter response, based on GEANT4 simulation of single particle showers in a fine grid of particle energies and directions. The accuracy is less than for full simulation,

---

[9] This section is based mainly on references [70] and [71].

but it can be tuned to the data. This algorithm is known as the FastCaloSim [73], and it is in widespread use.

Another order of magnitude in simulation time is gained by using Atlfast-IIF, using the Fast ATLAS Tracking Simulation (Fatras) [74] for the inner detector and muon system. Fatras uses simplified parameterizations of physics processes and simplified geometry for the ATLAS detector.

4.2.5 Digitization and reconstruction

After simulation, the ATLAS digitization software converts the simulation into detector responses, called *digits*, to mimic what happens in the detector for collision data. Depending on the exact subdetector, a digit is typically produced when the voltage or current on a readout channel rises above a threshold within a given time window. For some detector parts also the signal shape is included in the digits. Each subdetector is modelled in a specific digitization software, also including electronic noise and cross-talk.

Pile-up, to be further defined and described in Section 4.6.3, is simulated by reading in various types of events and overlaying hits from each of these on the simulated event.

The Level-1 triggers (see Section 3.7 for more information) are simulated at the digitizations stage, not discarding events, only marking them as passed or not.

The digits are converted to something similar to the data output from the detector, called Raw Data Object (RDO) files. The ATLAS high level trigger and full ATLAS reconstruction are run on the RDO files. With the exception of simulated data that contain truth information, simulated and real data are treated equally in the reconstruction stage. Reconstruction in general and reconstruction of muons in particular are covered in the next section.

4.3 Reconstructed muons in the ATLAS detector

Whenever a collision occurs in the heart of ATLAS, the task pf identifying the type of collision and the particles involved is a complicated one.[10] When particles traverse the detector, most leave many traces of their existence, raising the voltage or current in some specific modules within the detector that happen to lie on their path. All the little clues they leave behind must be interpreted and connected to the particle that left them. Advanced software was developed to perform this task with a high level of accuracy. In the following we focus on the prompt muon[11] reconstruction, identification and isolation, but more or less similar ideas are behind the algorithms for reconstructing other particles.

4.3.1 Muon reconstruction

Muon reconstruction is first performed independently in the inner detector (ID) and the muon spectrometer (MS). Secondly the two are combined to form the muon tracks that are used in physics analyses.

---

[10] This section is based mainly on references [40], [75] and [76].

[11] Muons from the decay of heavy particles, like the Z^0 or the Z', but also other particles, like τ and J/Ψ.

4.3.1.1 Muon reconstruction in the ID

In the ID, muons are reconstructed like any other charged particle. The main track reconstruction algorithm is performed in a series of steps [76][77]. First a set of *clusters* (several hits in adjacent silicon cells) are created in the Pixel and SCT detectors, and correspondingly *drift circles* in the TRT detector. These clusters and drift circles are transformed into 3D space-points.

Sets of three space-points are formed to a seed, either Pixel-only, SCT-only or Mixed seed. These seeds are checked against some initial requirements on the transverse momentum and impact parameter resolution, and if they pass they are required to match a fourth space-point compatible with the particle's trajectory as estimated from the seed. Track candidates are formed on the basis of this.

Track candidates are further processed based on a series of quality criteria, including fit quality, holes and hits shared between several track candidates, the goal being to eliminate track candidates from random hit combinations or track duplicates. The remaining track candidates are finally extended to the TRT (if they are within the acceptance of the TRT detector) if a valid set of matching drift circles is found. A track fit is performed to estimate the final track parameters. This increases the momentum resolution significantly.

4.3.1.2 Muon reconstruction in the MS

In the MS, segments of the track are formed by searching for hit patterns inside each muon chamber of the subdetectors (MDT, RPC, TGC and CSC). Track candidates are built from these by performing a general fit of all the segments in the different layers.

The algorithm for this task runs in several steps, using as seeds the segments generated in the different layers of the detector and performing a combinatorial search, selecting segments based on hit-multiplicity and fit quality. At least two matching segments are required to build a track, except in the barrel-endcap transition region where a single high-quality segment can build a track. The same segments can initially be included in more than one track candidate. An overlap removal algorithm later resolves the issue, either by selecting one best fit to a single track or by allowing the segment to be shared between two tracks.[12]

The hits associated with each track candidate are then fitted using a global χ^2 fit. If any hits have large contributions to the χ^2, they are removed and the track fitting procedure is repeated. The track candidate is accepted if the χ^2 is below a certain threshold, indicating a well behaved and defined track candidate.

4.3.1.3 Muon types – combined, extrapolated, segment-tagged and calorimeter-tagged

Four different muon *types* are defined, depending on which subdetectors are used in the reconstruction of the track. Reconstructed muons belong to exactly one of the four types. If the muon fits more than one category, the type is selected according to a prioritized list.

---

[12] This is to ensure high efficiency for muons close to each other – all track candidates with segments in three different layers of the MS are kept when they are identical in two out of three layers and share no hits in the outermost layer.

Combined (CB) muons are tracks reconstructed using a global refit that uses hits from both the ID and MS. During the global fit procedure, MS hits can be added to or removed from the track to improve the overall fit quality. This is the type used in the dimuon analysis in Section 5.

Extrapolated (ME) muons, also known as standalone muons, are mainly used to extend the acceptance for muon reconstruction beyond the scope of the ID into the region $2.5 < |\eta| < 2.7$. The muon track is reconstructed based mainly on the MS track, but with a loose requirement on compatibility with originating from the interaction point. In addition, the muon is required to traverse at least two layers of MS chambers (three in the forward region).

A track in the ID is classified as a *segment-tagged (ST)* muon if it, once extrapolated to the MS, it is associated with at least one track segment in the MDT or CSC chambers. A track in the ID is classified as a *calorimeter-tagged (CT)* muon if it can be matched to an energy deposit in the calorimeter compatible with a minimum-ionizing particle.[13]

4.3.2 Muon identification

By applying several quality requirements on tracks, the background from mainly pions and kaons can be suppressed, while selecting prompt muons with a high efficiency and guaranteeing a good momentum measurement. There are five different selections defined. They are called *Loose, Medium, Tight*, *Low-p_T* and *High-p_T*.

4.3.2.1 Medium muons

The Medium identification criteria are the default selection. It is designed to minimize the systematic uncertainties associated with muon reconstruction and calibration. Medium muons can be either combined muons or standalone muons.

For combined muons the following requirements apply: at least 3 hits in at least two MDT layers, except for tracks in the region $|\eta| < 0.1$, where tracks with at least one MDT layer but at most one MDT hole layer are used. Tracks with q/p significance higher than 7σ are vetoed to remove tracks where the ID and MS momentum measurements are very different. The q/p significance is defined as the absolute value of the difference between the ratio of the charge and momentum of the muon in the ID and MS extrapolated to the ID divided by the quadratic sum of the corresponding uncertainties.

Standalone muons are only used in the region $2.5 < |\eta| < 2.7$, and hits in at least 3 MDT and/or CSC layers are required.

4.3.2.2 Loose and Tight muons

Two other sets of identification criteria, *Loose* and *Tight*, are designed to provide the highest selection efficiency and the best fake-rate rejection, respectively. The selection efficiency is highest for Loose and lowest for Tight.

---

[13] This is a particle whose mean energy loss rate through matter is close to the minimum. Muons are in general minimum-ionizing particles.

4.3.2.3 Low-p_{T} muons

The Low-p_{T} identification criteria are designed for low mass resonance searches and B-physics studies, where there are large backgrounds from sources such as hadron decays in-flight. This set of criteria are optimized to allow muon identification down to 3 GeV in transverse momentum.

4.3.2.4 High-p_{T} muons

The High-p_{T} selection maximizes momentum resolution for muons with p_{T} above 100 GeV. This working point was optimized for searches for high-mass Z' and W' resonances. A muon passing the High-p_{T} working point is required to pass the medium selection criteria and to be a combined muon with at least 3 hits in at least three precision layers of the MS.[14] Specific chambers with suboptimal alignment are vetoed based on their η-ϕ coordinates and the barrel-endcap overlap region ($1.01 < |\eta| < 1.1$) is excluded.

4.3.2.5 Selection and misidentification efficiency

The reconstruction efficiencies for both prompt muons and non-prompt muons from hadrons decaying in-flight are shown in Table 4.1 [40]. The four identification selection criteria are shown separated into low ($4 < p_{\mathrm{T}} < 20$ GeV) and high ($20 < p_{\mathrm{T}} < 100$ GeV) transverse momentum muon candidates. No isolation requirement has been applied in the selection. Applying isolation requirements greatly reduces the misidentification rates, by more than an order of magnitude. The misidentification rates have been validated in data.

Selection	$4 < p_{\mathrm{T}} < 20$ GeV		$20 < p_{\mathrm{T}} < 100$ GeV	
	$\epsilon_{\mu}^{\mathrm{MC}}$ [%]	$\epsilon_{\mathrm{Hadrons}}^{\mathrm{MC}}$ [%]	$\epsilon_{\mu}^{\mathrm{MC}}$ [%]	$\epsilon_{\mathrm{Hadrons}}^{\mathrm{MC}}$ [%]
Loose	96.7	0.53	98.1	0.76
Medium	95.5	0.38	96.1	0.17
Tight	89.9	0.19	91.8	0.11
High-p_{T}	78.1	0.26	80.4	0.13

Table 4.1: Muon identification selection and misidentification efficiency using a $t\bar{t}$ MC sample [40]. The identification efficiency is based on prompt muons from W decays, and the misidentification efficiency on hadrons decaying in-flight. The four different identification selection criteria are shown, separated into low and high p_{T} momentum muon candidates, all for $|\eta| < 2.5$. The statistical uncertainties are negligible.

4.3.3 Muon isolation

Muons coming from the decay of heavy particles, like a Z', are produced isolated from other particles, thus we do not expect detector activity around these muons. In other words we expect the muons to be *isolated*. Requiring isolated muons removes a major fraction of muons from semileptonic decays, which are often embedded in jets.

---

[14] That means 3 layers of MDTs for $|\eta| < 2.0$, and 2 layers of MDTs and 1 layer of CSCs for $2.0 < |\eta| < 2.7$.

Two types of variables exist to define muon isolation, a track-based isolation variable and a calorimeter-based isolation variable. In the dimuon analysis in Chapters 5 and 6, the track-based version is used, and we focus on this in the following.

The track-based isolation variable $p_{\mathrm{T}}^{\mathrm{varcone30}}$ is defined as the scalar sum of the transverse momenta of the good-quality tracks originating from the primary vertex, with transverse momentum p_{T} above $1\,\mathrm{GeV}$ in a cone of size $\Delta R = \min(\frac{10\,\mathrm{GeV}}{p_{\mathrm{T}}^{\mu}}, 0.3)$ (where "min" picks out the smallest of the two values) around the muon with transverse momentum p_{T}^{μ}, not counting the muon track itself in the isolation variable.

The isolation selection criteria are determined on the basis of the relative isolation variables, defined as the ratios of the isolation variables to the transverse momentum of the muon. Seven different isolation selection criteria (*isolation working points*) are defined. For the dimuon event selection in the dimuon search as described in this thesis, the "FixedCut-TightTrackOnly" requiring $\frac{p_{\mathrm{T}}^{\mathrm{varcone30}}}{p_{\mathrm{T}}^{\mu}} < 0.06$ was chosen. Figure 4.4 shows the distribution of the relative isolation variable for muons from $Z \to \mu\mu$ events. The selected muons are required to satisfy the Medium identification criteria, and are separated from the other muon coming from the Z^0 boson.

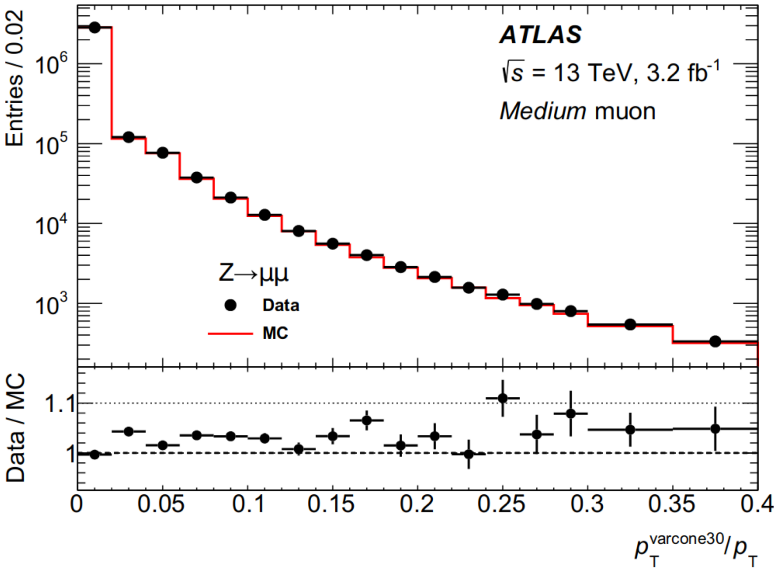

Figure 4.4: Distribution of the track-based relative isolation variables measured in $Z \to \mu\mu$ events [40]. Muons are required to pass the Medium identification algorithm and to be well separated from the other muon coming from the Z^0 boson. The bottom panel shows the ratio of data to simulation.

4.3.4 Corrections to simulated data

In an ideal particle physics world, simulated data would describe data very precisely in all imaginable ways. Our world, however, is not this idealized world, and the agreement between MC and data muons is evaluated and corrected by the Muon Combined Performance working group.

4.3.4.1 Muon momentum scale and resolution

The muon momentum scale and the muon momentum resolution are corrected on a muon-by-muon basis to agree to the per mille and the percent level respectively [78][40], using $J/\Psi \rightarrow \mu^+\mu^-$ and $Z^0 \rightarrow \mu^+\mu^-$ decays to extract corrections to the muon momentum as functions of p_{T} in various detector regions. Figure 4.5 displays the Z^0 candidate events before and after the muon momentum corrections.

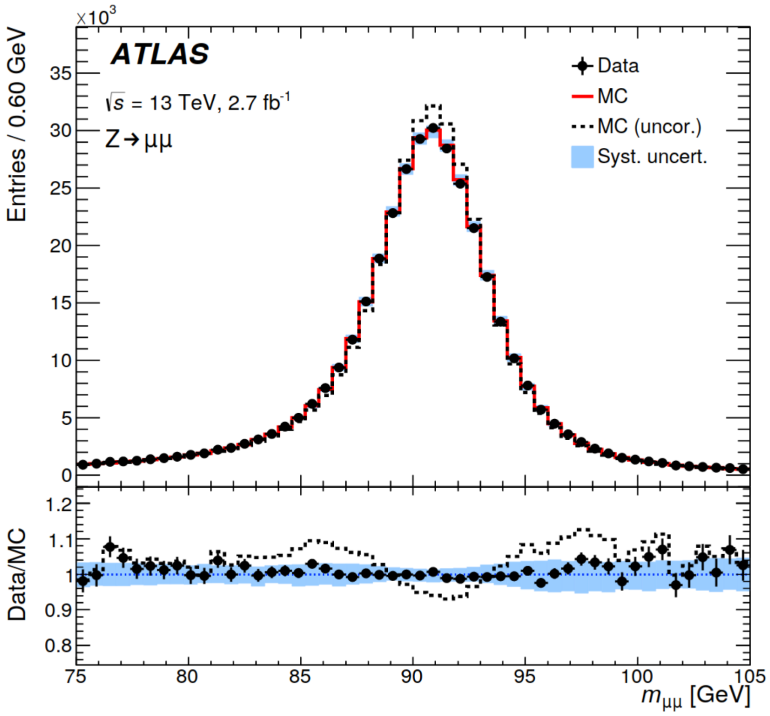

Figure 4.5: Dimuon invariant mass distribution of $Z^0 \rightarrow \mu^+\mu^-$ candidate events reconstructed using Combined muons [78]. The top panel shows the invariant mass distribution for data and for corrected (solid line) and uncorrected MC (dashed line). The blue band represents the effects of the systematic uncertainties on the momentum corrections. The bottom panel shows the data to MC ratio, for the corrected MC in black dots and for the uncorrected MC in the dashed line. MC is normalized to data.

4.3.4.2 Efficiency scale factors

The ratio between the efficiencies for certain selection criteria obtained in data and MC are referred to as *efficiency scale factors*. An example of a measurement is shown in Figure 4.6, where the muon reconstruction efficiencies for the Medium identification algorithm is measured in Z^0 and J/Ψ events as a function of the muon momentum, shown together with the expectations from simulated data. These ratios are used to correct the simulated data. Scale factors for the muon trigger, isolation, reconstruction and identification and track-to-vertex-association (TTVA) efficiencies are applied. The scale factors are applied to MC on an event-level basis for the trigger and on a muon-level basis for the other efficiencies.

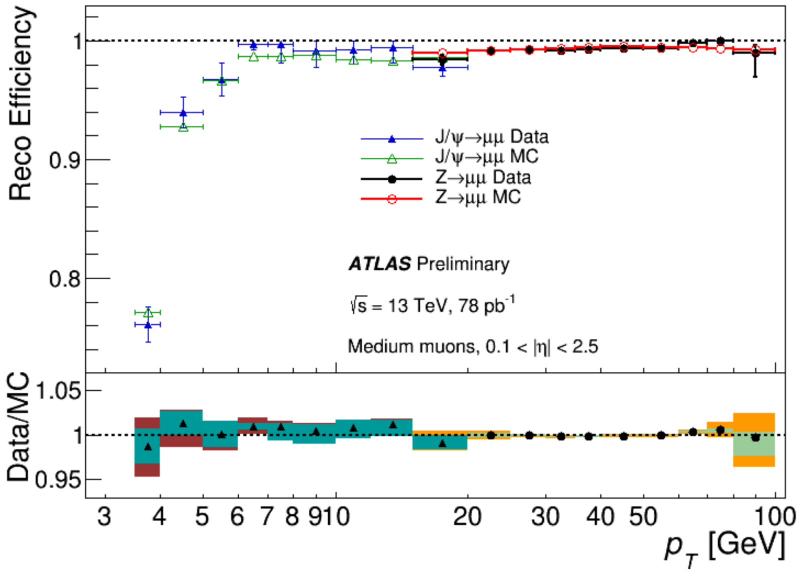

Figure 4.6: Muon reconstruction efficiencies for the Medium muon identification algorithm measured in Z^0 and J/Ψ events as a function of the muon momentum [78]. The MC prediction is shown as open red circles and open green triangles, while black dots and blue triangles are data points. The bottom panel shows the data to MC ratio, these are the efficiency scale factors. The green and cyan shaded areas indicate the statistical uncertainty while the orange and red shaded areas show the total statistical and systematic uncertainty for the Z^0 and J/Ψ events.

4.4 Background processes

Background processes are Standard Model processes that have the same experimental signature as signal processes. In our case, this is every process that leaves us with two muons that passes the signal selection criteria. A large part of the experimental search consists of trying to reduce the number of events from the background processes while leaving the signal events untouched (see Section 5.1 for the dimuon selection used in this thesis). The following is a description of the relevant backgrounds for this search, as well as relevant information about the MC samples used.

4.4.1 Drell-Yan

The largest background for the production and decay of a Z' in the dimuon channel is the Drell-Yan (DY) process:

$$q\bar{q} \to \gamma/Z^0 + X \to \mu^+\mu^- + X.$$

Figure 4.7 illustrates the process using a Feynman diagram. This background, where the Z^0 decays to two muons, is one of the two so-called irreducible backgrounds, where two real muons are created promptly (i.e. not via other particles). Even though this is considered as a separate background, in reality this is also the process in which a Z' is created,

$$q\bar{q} \to \gamma/Z^0/Z' + X \to \mu^+\mu^- + X,$$

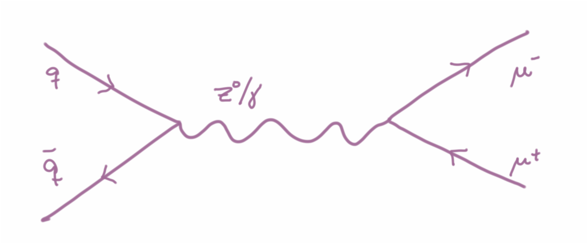

Figure 4.7: Feynman diagram for the Drell-Yan process, $q\bar{q} \rightarrow \gamma/Z^0 + X \rightarrow \mu^+\mu^- + X$.

which means that the production and decay of the Z' actually interferes with the DY "background".

Table B.1 lists the relevant information about the MC samples that represent this background. The samples are produced binned in dimuon invariant mass to ensure a high number of events over a large mass range, with all massbins populated adequately. All samples are generated with POWHEG BOX [79] matrix-element calculations at next-to-leading order (NLO) in perturbative QCD (pQCD) using the CT10 [80] NLO PDFs, with PYTHIA 8 [63] handling the parton showers, hadronization and underlying event, using the CTEQ6L1 [81] PDF set.

The cross-sections for the binned DY processes are corrected to NNLO in QCD by applying mass-dependent *k-factors* to the generator cross-sections (more details on this can be found in Section 4.4.6). The higher order EW contributions due to final state radiation are already simulated at the generator level, using PHOTOS [68]. Some remaining higher order electroweak (EW) corrections are applied as mass-dependent k-factors.

The DY process also produces pairs of taus. When the two taus both decay to muons, as shown in Figure 4.8, this is a reducible background in the dimuon channel. A tau will decay to a muon in 17 out of 100 events, and the probability for a di-tau event to be a background in the dimuon channel is therefore about 3%. As in the dimuon case, all samples are generated

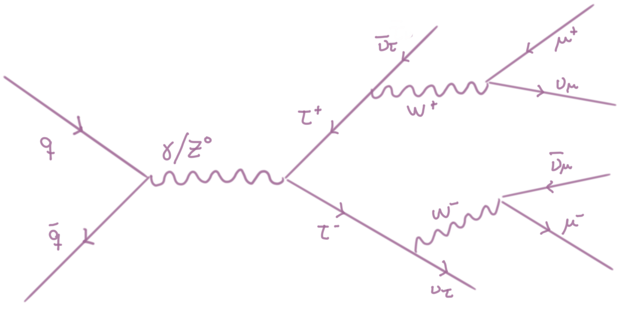

Figure 4.8: Feynman diagram showing the production of two taus of opposite charge, both decaying leptonically to muons.

with POWHEG BOX at NLO using the CTEQ6L1 PDF set, with PYTHIA 8 handling the parton showering. Table B.1 lists the samples used. The cross-sections are corrected to NNLO in QCD and EW, as in the dimuon case.

4.4.2 Photon-induced events

Two photons that collide and produce two opposite-sign muons are a background to the search, and contributes to the irreducible background. The process in which two muons are created proceeds through t- and u-channel processes, as illustrated in Figure 4.9. There are no simulated data for this process, it is taken into account through k-factors, as described in Section 4.4.6.

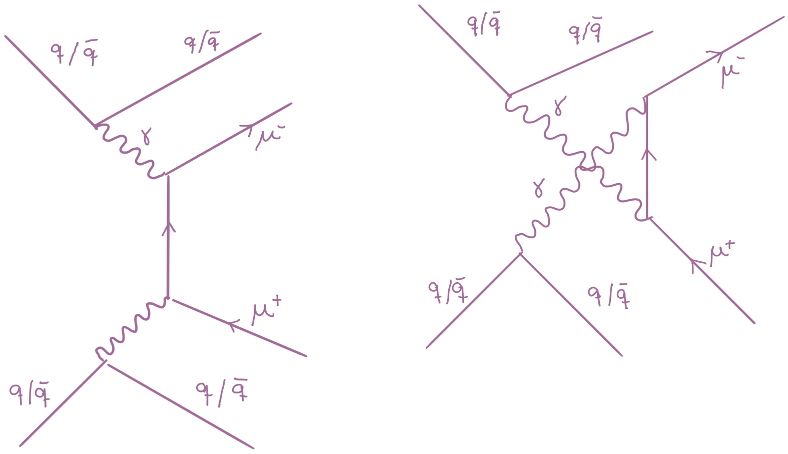

Figure 4.9: Feynman diagrams showing photon-induced dimuon events. Note that the right hand diagram does not contain a four-photon vertex, the photon lines are simply crossing to create a u-channel process.

4.4.3 Dibosons

Events with two SM bosons are a large part of the reducible background. These events are referred to as *diboson events*. For this analysis, there are three categories of diboson events that contribute to the background – WW, WZ, and ZZ events. Feynman diagrams for the most important diboson processes are shown in Figure 4.10.

The diboson samples are generated with the Sherpa 2.1.1 [66] [82] generator, with Sherpa also handling the parton showers, using the CT10 [80] NLO PDF.

Table B.2 displays information about the relevant MC samples used. Note that in the analysis, the cross-section is scaled by 0.91, due to the fact that the inclusive diboson cross-section is affected by some known discrepancies [83]. In this category of events, we find only the leptonic decays. The events containing hadronic decays are described in Section 4.4.5.

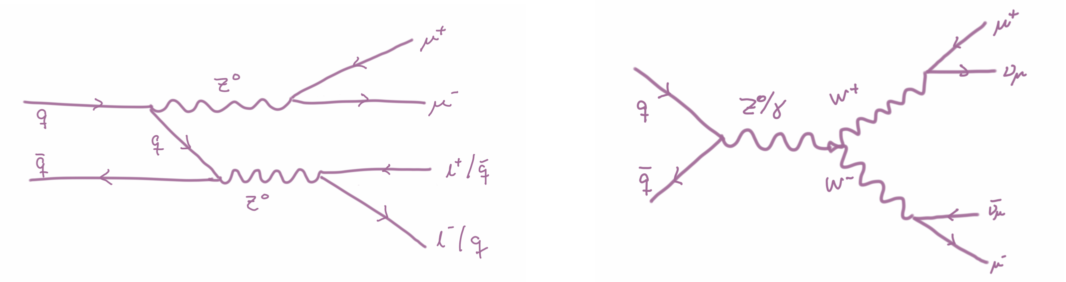

(a) Production of two Z bosons, where at least one of them decays to muons.

(b) Production of two W bosons decaying to muons.

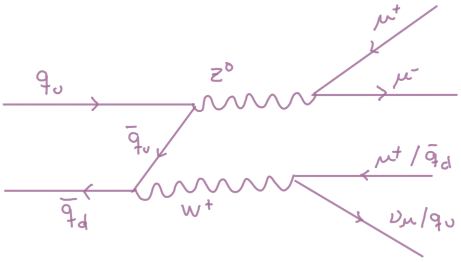

(c) Production of a Z and a W boson, where the Z decays to muons. The W can decay hadronically or leptonically.

Figure 4.10: Feynman diagrams of the three leading contributions to the diboson background.

4.4.4 Top

The production of a top and an antitop (referred to as “ttbar” or $t\bar{t}$) creates a background to the Z' search in the dimuon channel. The top (antitop) will almost exclusively decay to a bottom (antibottom) quark and a W boson. The bottom quarks appear in the detector as jets, but the two W bosons will occasionally both decay to muons, as illustrated in Figure 4.11). Note that only the fully leptonic decays are considered as part of this background. Muon candidates can also be found in the jets when the top decays hadronically – this is a part of the fake background, discussed in Chapter 7).

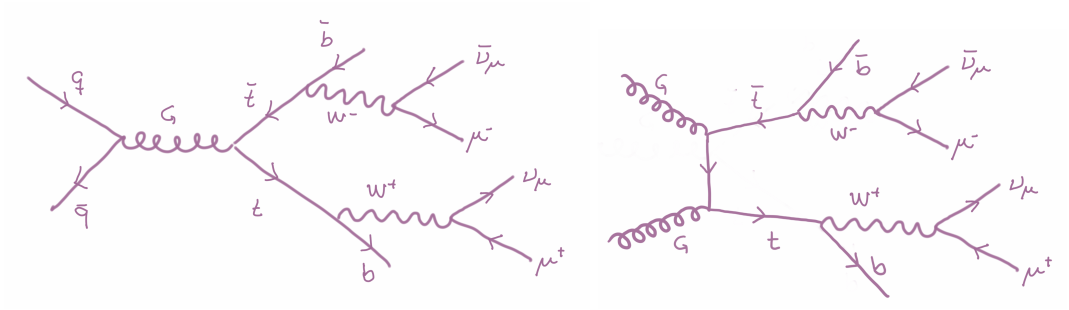

Figure 4.11: Feynman diagrams of the main contributions to the ttbar background in the dimuon channel (Feynman diagram with gluons in place of the incoming quark in the left diagram is not drawn). Both W bosons decay leptonically to muons.

In addition to the top-pair produced via strong interactions, there are several ways to produce single top quarks via weak interactions. The single top in $W + t$ associated production mode is illustrated in Figure 4.12, and the s-channel and t-channel single top production are illustrated in Figure 4.13

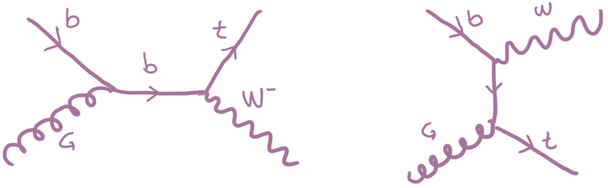

Figure 4.12: Feynman diagrams showing two of the main contributions to the single top background, the $W + t$ associated production modes, in the dimuon channel. The charge conjugated processes with the production of the antitop and the W^+ are also important.

All samples were made with POWHEG BOX using the NNPDF3.0 NLO [84] PDF set, with PYTHIA 8 handling the parton showering, using the NNPDF2.3 LO [85] PDF set and the ATLAS A14 [86] set of tuned parameters for parton showering and hadronization. For the $W + t$ samples, the event generation used the so-called DR scheme [87] to subtract $t\bar{t}$ terms from the $W + t$ production. Table B.3 lists the samples used for the top background.

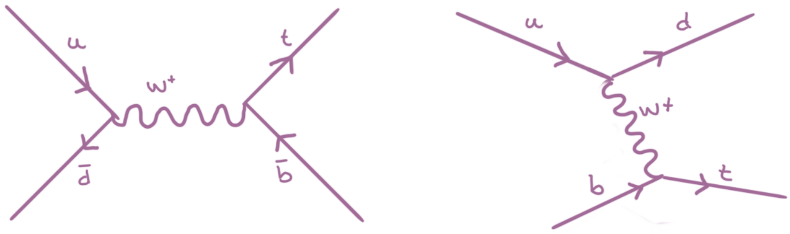

Figure 4.13: Feynman diagrams showing two of the main contributions to the single top background in the dimuon channel, the s-channel to the left and the t-channel to the right. The charge conjugated processes with the production of the $\bar{t}$ are also important.

4.4.5 Events with jets - fake background

Occasionally jets are reconstructed as muons, either because there is a real muon inside a jet or because an energetic jet puched through to the MS. These are referred to as “fake” and a part of the fake background. Thus in rare cases events with e.g. a W boson decaying to a muon and a neutrino and jets or multijets are a background to the Z' search in the dimuon channel.

Because the cross-sections for events that contain jets are so high, the number of MC events required to get a reasonably low statistical uncertainty is too high to be feasible. For this reason, a data-driven method, which is described in Chapter 7, is used to conclude about the relative size of the W+jets and dijets background, and it is found to be negligible.

4.4.6 Higher order corrections

It is desirable to estimate the backgrounds as precisely as possible, and because of this we apply higher order corrections to the simulated samples where possible. While mass-independent corrections exist, higher order QCD and EW corrections in general modify the shape of the differential cross-section as a function of the invariant mass. This motivates the use of *mass-dependent k-factors*, which are derived by taking the ratio of the higher-order differential cross-section calculation – e.g. next-to-next-to-leading order (NNLO) in the case of DY – over the differential cross-section of the sample in question, generated to a lower order, i.e. LO or NLO. The derived mass-dependent k-factor for each process is then applied on an event-by-event basis to the truth dimuon invariant mass distribution.

The DY cross-section is corrected from CT10 NLO (Section 4.4.1) to next-to-next-to-leading-order (NNLO) using the CT14NNLO PDF set [88] by calculating a mass-dependent k-factor using VRAP0.9 [89] for QCD corrections, and `mcsanc`-v1.01 [90] for EW corrections. The contribution to the cross-section from photon-induced events is described with a k-factor using MRST2004QED [91].

For the $t\bar{t}$ sample, a flat k-factor of 1.14 is applied, calculated with the Top++2.0 [92] program at NNLO in pQCD, including soft-gluon resummation to next-to-next-to-leading logarithmic accuracy [93].

4.5 Signal processes

4.5.1 Dedicated Z'_χ samples

A few dedicated samples are produced for the reference model, the Z'_χ from the E_6-motivated Z' models at four polemasses – 2, 3, 4 and 5 TeV. Chapter 2.3 contains more information on the different theoretical Z' models. Relevant information on these samples are found in Table B.4. They are generated with PYTHIA 8 at leading order using the NNPDF2.3 PDF set and the ATLAS A14 set of tuned parameters for parton showering and hadronization.

4.5.2 Z' signal reweighting from SM Drell-Yan MC samples

The dilepton search group has developed a methodology to reweight leading order (LO) Drell-Yan Monte Carlo samples to a variety of LO Z' samples [94]. A class of Z' models is often defined by one or more continuously adjustable parameters (like the mass or the coupling to SM particles), which makes generating MC samples for all of these too computationally expensive to be practical or even feasible (depending on how small the spacing between model parameters is). The reweighting procedure makes it possible to produce the needed high number of Z' samples for a variety of theoretical models, at any given value of the parameter of interest (usually the mass of the Z' in question).

To perform this reweighting procedure, a SM Drell-Yan ($q\bar{q} \to \gamma/Z^0 \to \mu^+\mu^-$) MC sample is needed. The reweighting is done on an event-by-event basis, weighting each event by a scale factor defined by the ratio of the differential cross-section of the process $q\bar{q} \to Z' \to \mu^+\mu^-$ divided by the differential cross-section of the process $q\bar{q} \to \gamma/Z^0 \to \mu^+\mu^-$,

$$\frac{\mathrm{d}\sigma(q\bar{q} \to Z' \to \mu^+\mu^-)}{\mathrm{d}\sigma(q\bar{q} \to \gamma/Z^0 \to \mu^+\mu^-)}$$

or the ratio of $q\bar{q} \to \gamma/Z^0/Z' \to \mu^+\mu^-$ to $q\bar{q} \to \gamma/Z^0 \to \mu^+\mu^-$ if including interference effects. The differential cross-sections are functions of the event kinematics, making it possible to reweight any SM kinematic variable into the corresponding BSM one.

Table B.5 lists the relevant information about the MC samples used for the signal reweighting procedure. The samples are produced binned in dimuon invariant mass to ensure a high number of events over the relevant mass range, from 70 GeV to over 5 TeV. All samples are generated with PYTHIA 8 at leading order using the NNPDF2.3 PDF set and the ATLAS A14 set of tuned parameters for parton showering and hadronization.

In Figure 4.14 the signal reweighting to a Z'_χ at a pole mass of 2, 3, 4 and 5 TeV are plotted with the corresponding dedicated Z'_χ samples. The reweighting is for the full Z' process only, without interference with SM processes. Both the dedicated samples and the reweighted samples are normalized to integrated luminosity. We see that the agreement is good and we consider the reweighting procedure as validated. The low-mass tail that emerges as the Z' pole mass increases is known as the *parton luminosity tail*, and it grows as the kinematic limit of the Z' production is approached.

Figure 4.15 displays distributions of the dimuon invariant masses at truth-level (top) and reconstructed-level (bottom) of three different Z' models – Z'_χ, Z'_ψ and Z'_{SSM} – with signal

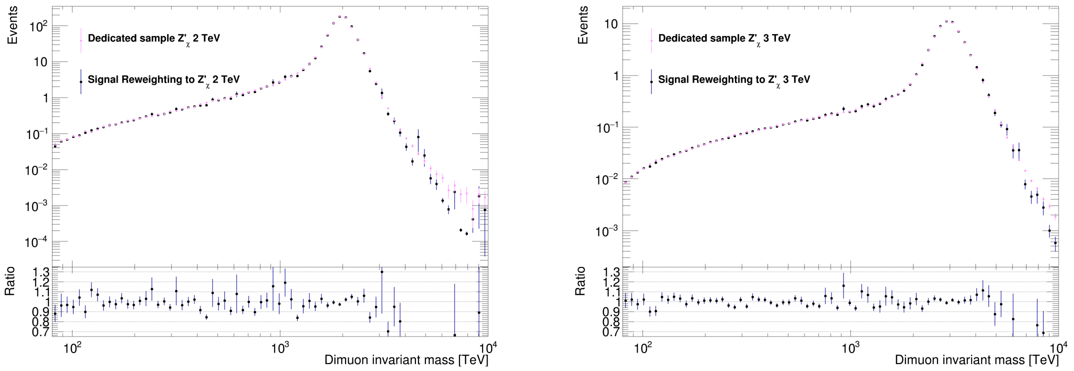

(a) Z'_χ 2 TeV (b) Z'_χ 3 TeV

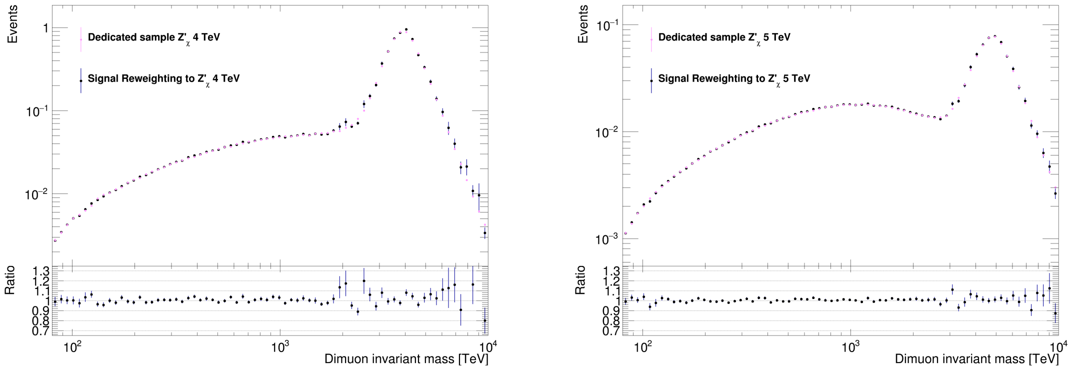

(c) Z'_χ 4 TeV (d) Z'_χ 5 TeV

Figure 4.14: Comparisons of the dedicated MC signal samples and the LO DY MC samples reweighted to Z'_χ (without interference) for pole masses 2, 3, 4 and 5 TeV. The samples are scaled to integrated luminosity of the full Run 2 dataset, 139 fb^{-1}.

pole masses of 2 TeV (a) and 5 TeV (b). We observe that the cross-section of the SSM models is highest, followed by the Z'_χ, while the Z'_ψ is lowest. We also note that the parton luminosity tail is relatively more important for the models with larger Z' widths.

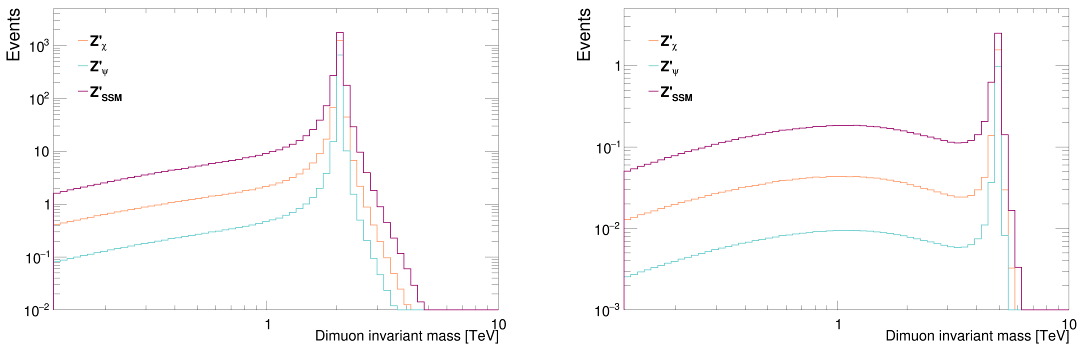

(a) Z' 2 TeV - truth-level (b) Z' 5 TeV - truth-level

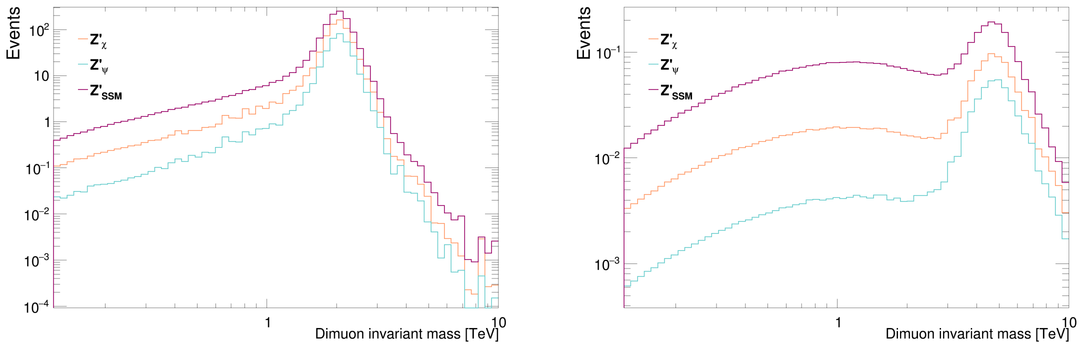

(c) Z' 2 TeV - reconstructed-level (d) Z' 5 TeV - reconstructed-level

Figure 4.15: Distributions of the truth (top) and reconstructed (bottom) invariant masses of three different Z' models – Z'_χ, Z'_ψ and $Z'_{\rm SSM}$ – with pole masses of 2 TeV (left) and 5 TeV (right). The samples are scaled to integrated luminosity of the full Run 2 dataset, 139 fb^{-1}.

4.5.3 Higher order corrections

The signal samples – both the dedicated samples and the reweighted samples – are corrected from LO to NNLO in QCD using VRAP0.9 (same as for the DY background samples) to calculate mass-dependent k-factors. There is no EW k-factor applied as it is not straightforward to generalize from the DY background to the Z' signal processes [95].[15]

4.6 13 TeV proton-proton collision data

The data used in this thesis are from four years of data taking with the ATLAS detector, between 2015 and 2018, often referred to as the “Full Run 2 dataset”. The amount of data in the

---

[15] The EW k-factor is model dependent. One can image, for example, vertices including both the Z' and SM bosons, that do not correspond to anything similar within the SM.

recommended physics GRLs are $3.2\,\text{fb}^{-1}$, $33.0\,\text{fb}^{-1}$, $44.3\,\text{fb}^{-1}$ and $58.5\,\text{fb}^{-1}$ for 2015, 2016, 2017 and 2018 respectively. The integrated luminosity of the full Run 2 dataset is determined to be $139.0 \pm 2.4\,\text{fb}^{-1}$, using methods similar to the ones used in the reference [96].

4.6.1 Instantaneous luminosity

Figure 4.16 shows the peak instantaneous luminosity delivered to ATLAS during stable beams for proton-proton collisions at 13 TeV for each LHC fill as a function of time in the years 2015 (Figure 4.16(a)), 2016 (Figure 4.16(b)), 2017 (Figure 4.16(c)) and 2018 (Figure 4.16(d)). We see that the instantaneous luminosity increased from 2015 to 2018.

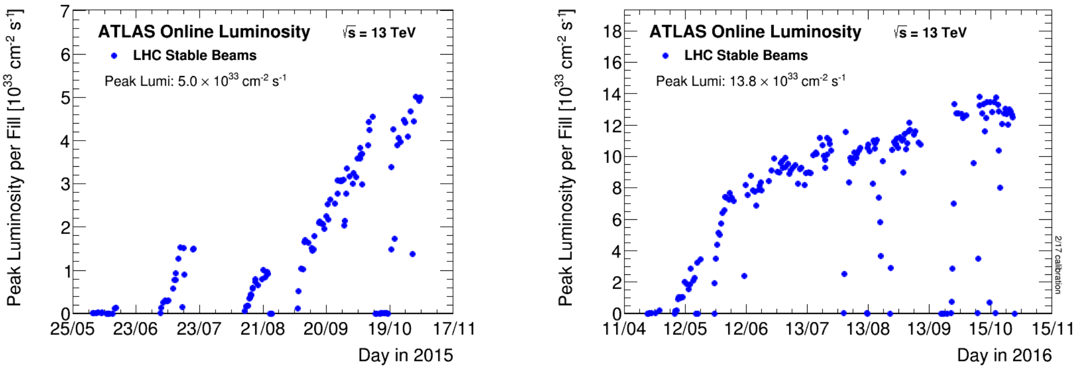

(a) 2015

(b) 2016

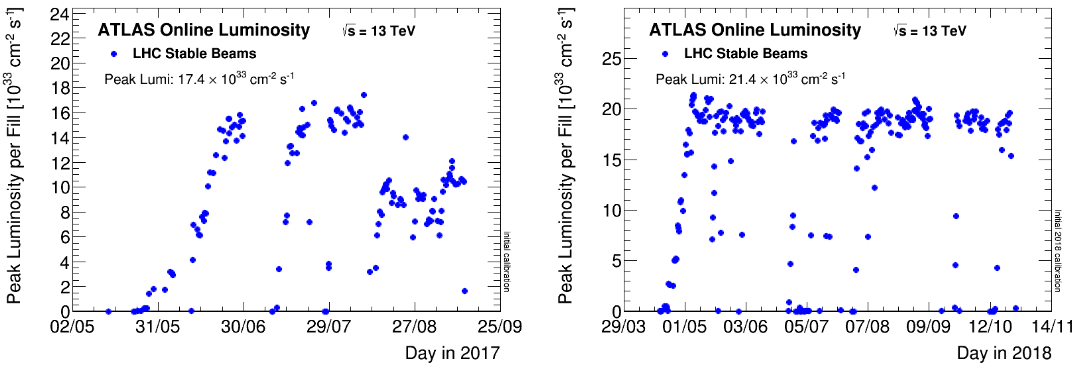

(c) 2017

(d) 2018

Figure 4.16: The peak instantaneous luminosity for each LHC fill as a function of time delivered to ATLAS during stable beams in 2015, 2016, 2017 and 2018 for proton-proton collisions at 13 TeV center-of-mass energy [97].

4.6.2 Integrated luminosity

Figure 4.17 shows a cumulative plot of the delivered integrated luminosity for the years 2011 to 2018. The amount of data gathered during a single year has been increasing, as can be seen from the figure.

Figure 4.18 shows the cumulative luminosity versus time. The delivered luminosity includes all data delivered from the start of stable beams until the ATLAS detector goes in a

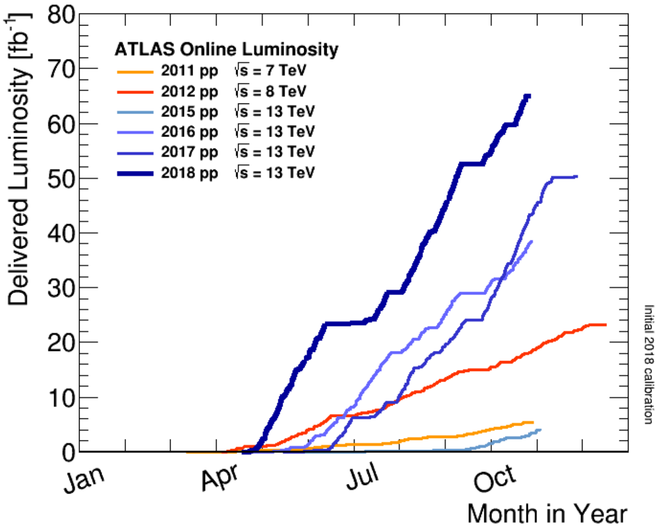

Figure 4.17: Cumulative luminosity versus time delivered to the ATLAS detector during stable beams and for proton-proton collisions at 7, 8 and 13 TeV center-of-mass energy [97].

safe standy mode to allow for beam dump. The recorded luminosity reflects the fact that some small fraction of data is not recorded in e.g. a “warm start”, when the stable beam flag is raised and the tracking detectors ramp up the high-voltage. The good quality data reflects the amount of data that can be used for physics analysis.

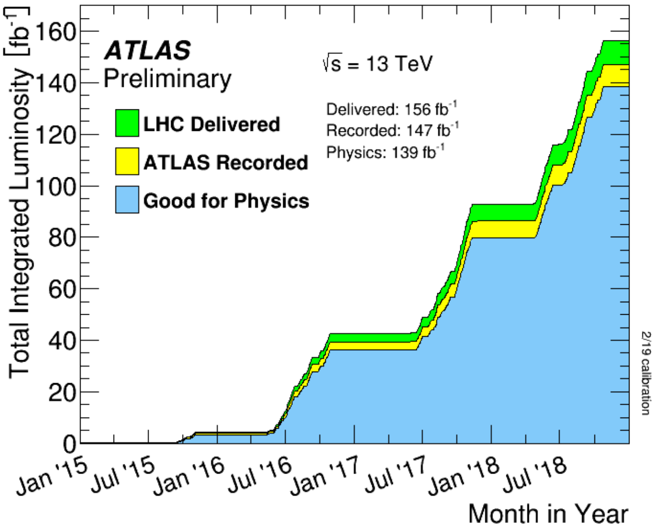

Figure 4.18: Cumulative luminosity versus time delivered to the ATLAS detector (green), recorded by the ATLAS detector (yellow) and good quality data (blue, corresponding roughly to the data in the Good Runs Lists (GRLs) used for data analysis) during stable beams for proton-proton collision at 13 TeV centre-of-mass-energy in the whole LHC Run 2 (from 2015 up to and including 2018) [97].

4.6.3 Pile-up

Figure 4.19 shows the observed maximum number of inelastic collisions per beam crossing during stable beams for proton-proton collisions at 13 TeV center-of-mass energy for each fill in 2015 (Figure 4.19(a)), 2016 (Figure 4.19(b)), 2017 (Figure 4.19(c)) and 2018 (Figure 4.19(d)). This is known as *pile-up*.

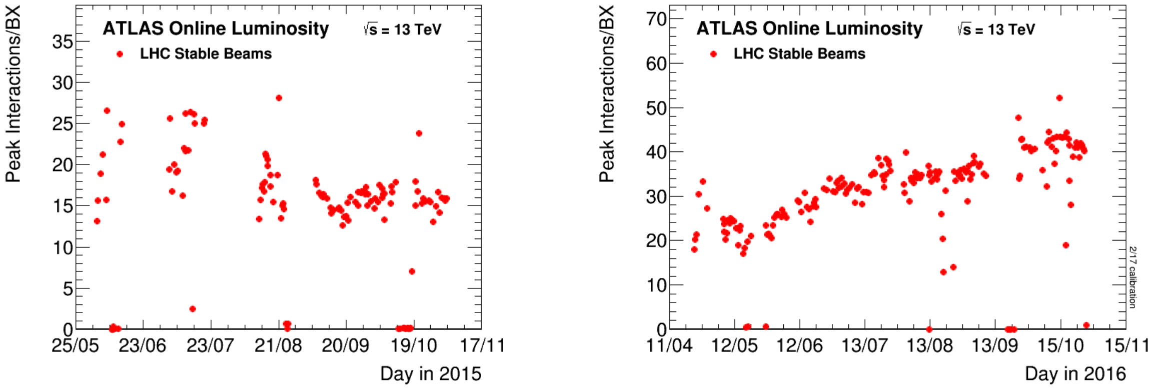

(a) 2015

(b) 2016

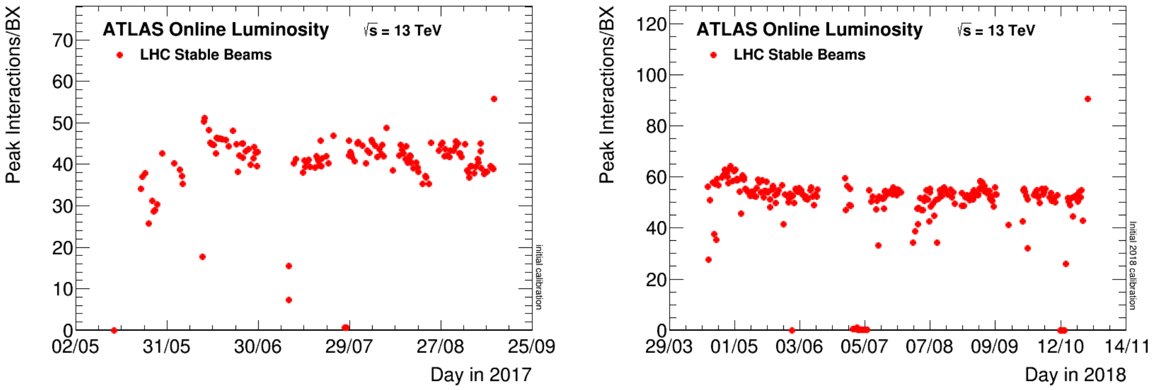

(c) 2017

(d) 2018

Figure 4.19: The maximum number of inelastic collisions per beam crossing during stable beams for proton-proton collisions at 13 TeV center-of-mass energy for each fill in 2015 (a), 2016 (b), 2017 (c) and 2018 (d) [97].

We see that the number of proton-proton collisions per bunch crossing reaches as high as 65. This influences the measurements of observables; for example the measurement of missing E_{T} is very sensitive to pile-up. In addition to this in-time pile-up, coming from extra collisons in the same bunch crossing, we have out-of-time pile-up, where neighbouring bunch-crossings interfere with measurements in the bunch-crossing of interest. This happens when the response time of the read-out system, or some part of it, is larger than the time between two neighbouring bunch-crossings. In addition to in-time and out-of-time pile-up, there are four additional sources of backgrounds in the ATLAS detector. These are

- Cavern background: random hits in the muon system (mostly) from neutrons and photons flying around in the cavern.
- Beam gas events: when the proton beam hits residual gas in the beam pipe.
- Beam halo events: typically a spray of muons going parallel to the beam line, from the scraping of the proton beam against the collimators.

- Cosmic muons: Muons from the cosmic rays from our Sun and the Universe that collide with particles in the Earth's atmosphere. Cascades of particles, including muons, are created in the process. As the ATLAS detector is located far below the ground, only the muons are registered in the detector.

4.7 Summary

In this chapter we have gathered all the tools we need in the search for a new hypothetical gauge boson Z' decaying to two muons. The invariant mass technique was introduced in the beginning of the chapter, followed by general information on simulated data, including specific information about the relevant MC generators used in the analysis performed in this thesis work. We looked at how muons are reconstructed in the ATLAS detector, different definitions of reconstructed muons and how isolated the different muons are expected to be. Further we looked at the different backgrounds to the high-mass dimuon search, and listed the MC samples, with the higher order corrections, both for signal and background samples. Finally, we reviewed some important information, e.g. on the luminosity and pile-up, for the ATLAS data collected between 2015 and 2018. All this knowledge will then be used in the next chapter, where the dimuon search is described in detail.

Chapter 5

Searching for the Z' – a dimuon analysis

During the preceding chapters, all the tools needed to perform a dimuon search have been gathered. In this chapter we finally fulfill the goal of this thesis and perform the high-mass dimuon resonance search, using the whole Run 2 dataset from 13 TeV proton-proton collisions at the LHC, as gathered by the ATLAS detector.

We start with the dimuon event selection performed on data and MC, and continue with a thorough look at data/MC agreement. We further discuss the various systematic uncertainties considered in the analysis, both from experimental and theoretical sources. The statistical framework is discussed in detail, including discovery statistic and exclusion limits, and compared to the published results from both the ATLAS Collaboration and the CMS Collaboration.

5.1 Dimuon event selection

The dimuon event selection is discussed in detail in this section. Table 5.1 offers a quick overview. The event level cuts are described in Section 5.1.1, the muon level cuts are described in Section 5.1.2, and the dimuon pair cuts are described in Section 5.1.3. The selection follows closely the selection described in reference [23].

	Cut	**Notes**
Event level	Good Runs List	Applied only to data
	Trigger	`(HLT_mu26_ivarmedium or HLT_mu26_imedium) or HLT_mu50`
	Event Cleaning	Applied only to data
Muon level, $n > 1$	Combined muon	
	Transverse momentum	$p_{\mathrm{T}} > 30\,\mathrm{GeV}$
	ID+MS	$\lvert\eta\rvert < 2.5$ and the high-p_{T} working point
	Bad muon veto	
	d_0^{BL} significance	$\lvert d_0^{\mathrm{BL}}(\sigma)\rvert < 3$
	$\Delta z_0^{\mathrm{BL}} \cdot \sin\theta$	$\lvert\Delta z_0^{\mathrm{BL}} \sin\theta\rvert < 0.5\,\mathrm{mm}$
	Isolation	"FixedCutTightTrackOnly" isolation criteria
Leading dimuon pair	Opposite charge	
	Invariant mass	$M_{\mu\mu} > 80\,\mathrm{GeV}$

Table 5.1: An overview of the cuts and selections used in the dimuon analysis.

5.1.1 Event level selection

Events from data and MC are subjected to the same basic analysis requirements, with the exception that all data events are required to pass a set of specific data quality requirements ensuring that all parts of the detector system were operational and performing optimally at the time of data-taking. The high-quality data are listed in a so-called *Good Runs List* (GRL). A procedure known as *event cleaning* removes single events – if the detector is working as a whole but some events in any given lumiblock are affected by one or more of a set of known issues, only these events are marked as "unclean" so as to keep the bulk of the data in this lumiblock. Known sources of problems include noise bursts in the electromagnetic calorimeter and data corruption in the hadronic calorimeter.

For both data and MC we require that each event sets off one or both of the two separate single-muon triggers [98].[1] The triggers are chosen to ensure a high efficiency both around the Z peak, at low transverse momentum p_{T}, and at high p_{T}, in the signal region. The low-p_{T} trigger selects events with at least one muon with p_{T} larger than 26 GeV, where the triggering muon is also isolated and passes the Medium muon identification criteria [40] (more on these criteria can be found in Section 4.3.2). This trigger is one of the lowest p_{T} threshold unprescaled[2] triggers. The high-p_{T} trigger selects events with at least one muon with p_{T} above 50 GeV. The low-p_{T} trigger efficiency begins to drop at high values of transverse momentum because of the isolation requirement, but at this point the high-p_{T} trigger has reached a high efficiency plateau and maintains this high efficiency out to the largest muon p_{T} range of interest in this search.

5.1.2 Muon level selection

In the following, we require at each step in the muon level signal selection that all events contain at least two muons that each pass the specific cuts in the order listed in Table 5.1 (marked as $n > 1$ in the table).[3] If the event contains muons that do not pass the separate cuts, they are simply not counted and the next muon, if any, is checked against the requirements.

In this analysis we need muons that are well reconstructed at high values of transverse momentum and high dimuon invariant mass. A separate working point for muon identification, the *high-p_{T} working point* was developed by the Muon Combined Performance group within the ATLAS Collaboration to cover these needs. Further details can be found in Section 4.3.2.

Some muons have problems with the combined track fit, and the *bad muon veto* is designed to reject these muons based on a p_{T}-dependent cut on the relative q/p error on the combined track fit [99]. The majority of muons flagged as "bad" traverse the MS barrel-endcap "transition region" at $1.0 < |\eta| < 1.3$ or the CSC region at $2.0 < |\eta| < 2.7$.

---

[1] The exact names of the required triggers are `HLT_mu26_ivarmedium for 2016, 2017 and 2018 data, HLT_mu26_imedium for 2015 data and HLT_mu50 for 2015, 2016, 2017 and 2018 data.`

[2] Prescaling means that some known fraction of data is thrown away to reduce the trigger rate.

[3] To make it absolutely clear, first we require events to contain at least two combined muons. All events selected are then required to contain at least two muons each with a transverse momentum above 30 GeV. And so it continues for all the muon level cuts. If an event at any point fail to contain two muons, the event is thrown away.

The Inner Tracking Combined Performance group recommends that analyses ensure that their leptons are associated with the primary vertex (marking the point of the hard collision) using so-called *Track-to-vertex association*, or *TTVA*, by applying cuts on two variables – the transverse impact parameter with respect to the beam line, $d_0^{\mathrm{BL}}(\sigma)$, and the longitudinal impact parameter with respect to the reconstructed primary vertex, $\Delta z_0^{\mathrm{BL}} \cdot \sin\theta$. Figure 5.1 illustrates schematically how these two parameters are defined.

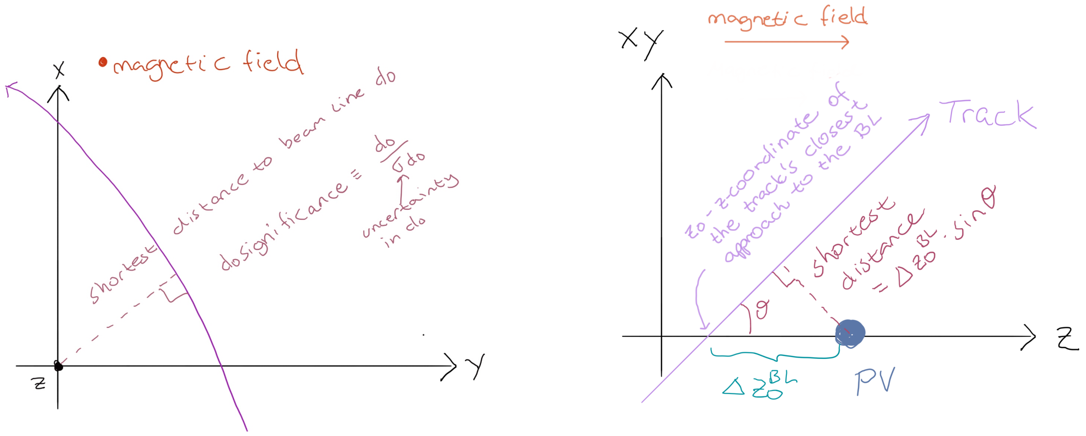

(a) Transverse impact parameter with respect to the beam line, d_0^{BL}, with d_0^{BL} significance also defined.

(b) Longitudinal impact parameter with respect to the reconstructed primary vertex, $\Delta z_0^{\mathrm{BL}} \cdot \sin\theta$.

Figure 5.1: Lepton track impact parameters definitions.

The exact cuts are on the d_0^{BL} significance, $d_0^{\mathrm{BL}}(\sigma)$ (d_0^{BL} divided by its uncertainty), and on $|\Delta z_0^{\mathrm{BL}} \cdot \sin\theta|$:

$$d_0^{\mathrm{BL}}(\sigma) = \frac{d_0^{\mathrm{BL}}}{\sigma_{d_0^{\mathrm{BL}}}} < 3.0, \quad |\Delta z_0^{\mathrm{BL}} \cdot \sin\theta| < 0.5\,\mathrm{mm}.$$

To further discriminate between signal and background from non-prompt and fake muons, a track-based isolation requirement is used. For the dimuon event selection, the "FixedCutTightTrackOnly" working point, with the requirement $\frac{p_{\mathrm{T}}^{\mathrm{varcone30}}}{p_{\mathrm{T}}^{\mu}} < 0.06$, was chosen to harmonize with the $W' \rightarrow l\nu$ search [100] [101]. This working point was discussed in Section 4.3.3.

5.1.3 Dimuon pair selection

We now select only events that contain at least two muons that have passed all the requirements up to this point. The two muons with the highest transverse momenta, the two leading muons, are selected and required to have opposite electric charge. Requiring opposite sign muons will help reduce the background from dibosons, and also from the fake background. The charge misidentification probability for high-p_{T} muons is very low, $< 0.1\%$ throughout the p_{T} spectrum [95], thus only a very few signal events are removed with this cut. The last cut is on the invariant mass of the dimuon, requiring $M_{\mu\mu}$ to be above 80 GeV.

5.1.4 Corrections to simulated data

Corrections to the simulated muons are applied as described in Section 4.3.4. The corrections used in this analysis are for the muon trigger, isolation, reconstruction and identification and track-to-vertex-association (TTVA) efficiencies.

5.1.4.1 Pile-up reweighting

In addition, an event-level reweighting for multiple proton-proton collisions (pile-up) is applied. As described in Section 4.2.2, there are many proton-proton collisions in one bunch-crossing. The simulated data are generated with a specific pile-up profile, i.e. a histogram of the number of inelastic collisions per beam crossing (often referred to as μ, or "mu"), that most probably does not match perfectly the one in collision data. The MC events are therefore scaled on an event-by-event basis to match the distribution of mu in data. Because of observed differences between data and MC in pile-up-dependent physical observables, a scale factor was introduced to deliberately mismatch the pile-up distributions [101]. The pile-up reweighting is illustrated schematically in Figure 5.2.

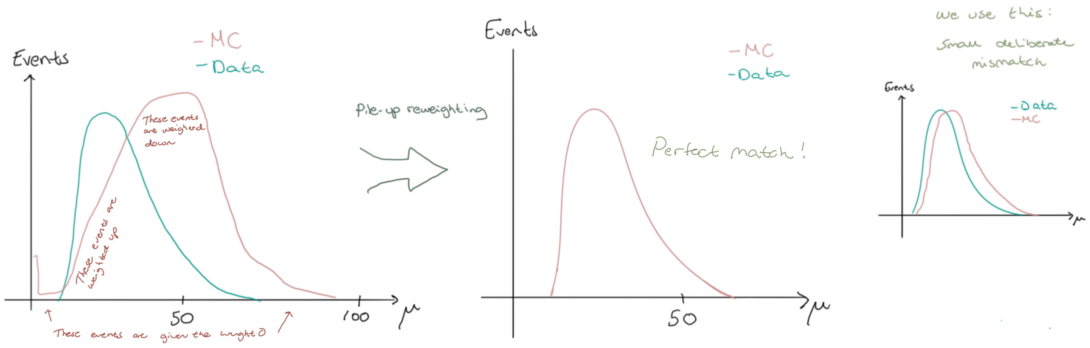

Figure 5.2: Schematic illustration of pile-up reweighting of simulated data.

5.1.5 Cutflows and efficiency of cuts for data and MC

Figure 5.3 displays the cutflow for the whole event selection described in this section in absolute number of events ((a) and (c)), and with the number of events normalized to the original number of events to easily compare the relative effect of the different cuts ((b) and (d)), for data (top) and MC (bottom). We see that the diboson and top backgrounds are more reduced by the cuts than the non-reducible background and the signal. We also note that the High-p_{T}working point removes a large portion of the signal. This is expected, as we can see from Table 4.1 - the identification efficiency for single muons is approximately 80%, which makes the identification efficiency for two muon approximately 65%.

5.1.6 Signal acceptance times efficiency

Figure 5.4 shows the product of the acceptance and efficiency (acceptance×efficiency), i.e. the probability of signal events to pass the full event selection chain, for three hypothetical Z' models. This is an input to the statistical analysis to be described in Section 5.5.3.

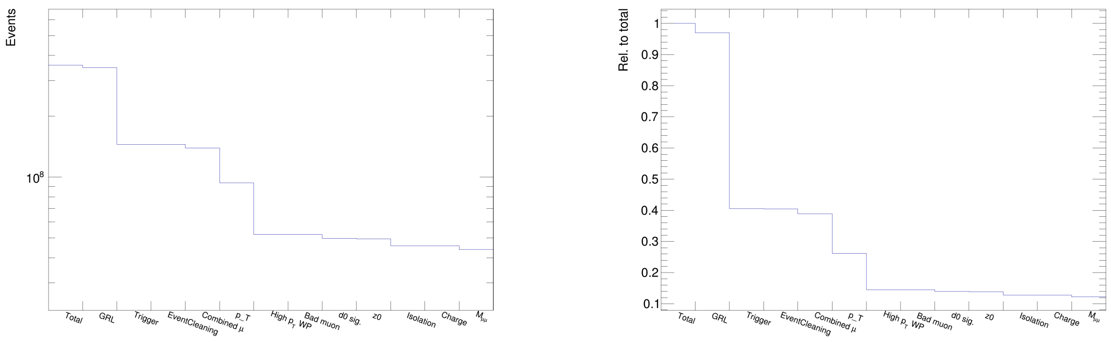

(a) Data Run 2 (139 fb^{-1}), absolute number of events (b) Data Run 2 (139 fb^{-1}), relative number of events

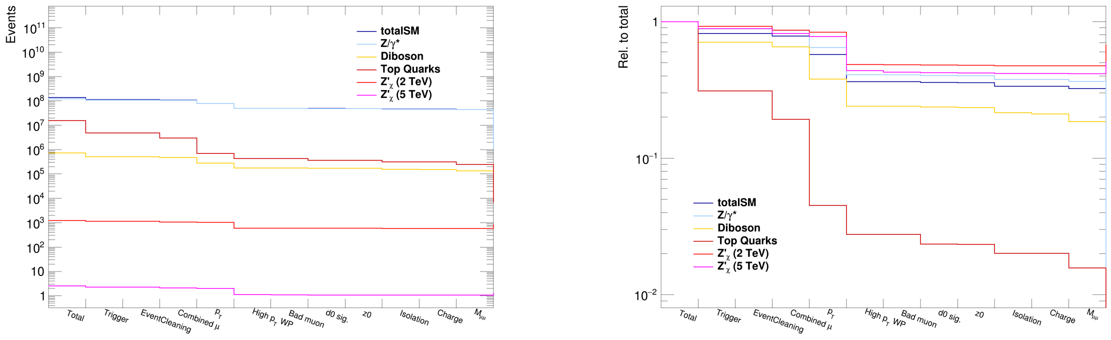

(c) MC, absolute number of events (d) MC, relative number of events

Figure 5.3: Cutflows for the whole event selection described in this section in absolute number of events ((a) and (c)), and with the number of events normalized to the original number of events to easily compare the relative effect of the different cuts ((b) and (d)), for data (top) and MC (bottom).

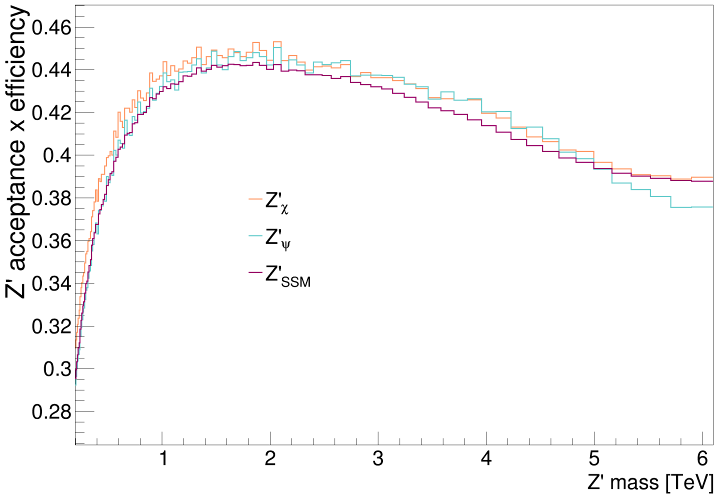

Figure 5.4: Signal acceptance×efficiency for the dimuon event selection for three hypothetical Z' bosons as a function of the Z' mass.

5.2 Data/MC comparisons

Applying the dimuon event selection with the cuts as described in Section 5.1 to the simulated data described in Section 4.4 and data described in Section 4.6 we arrive at the data, signal and total background estimate for the Z', dimuon search at center-of-mass energy 13 TeV. Table 5.2 lists the expected and observed number of events.

$M_{\mu\mu}$ [GeV]	80-120	120-250	250-400	400-500
Drell-Yan	$4.09 \cdot 10^7 \pm 2.21 \cdot 10^6$	$7.29 \cdot 10^5 \pm 3.37 \cdot 10^4$	$6.67 \cdot 10^4 \pm 3.09 \cdot 10^3$	$1.18 \cdot 10^4 \pm 589$
$t\bar{t}$	$1.04 \cdot 10^5 \pm 4.35 \cdot 10^4$	$1.41 \cdot 10^5 \pm 6.21 \cdot 10^4$	$3.27 \cdot 10^4 \pm 1.53 \cdot 10^4$	$5.64 \cdot 10^3 \pm 2.82 \cdot 10^3$
Dibosons	$1.03 \cdot 10^5 \pm 2.9 \cdot 10^3$	$2.19 \cdot 10^4 \pm 564$	$4.75 \cdot 10^3 \pm 131$	$1.01 \cdot 10^3 \pm 32.2$
Total SM	$4.11 \cdot 10^7 \pm 2.22 \cdot 10^6$	$8.92 \cdot 10^5 \pm 3.68 \cdot 10^4$	$1.04 \cdot 10^5 \pm 4.06 \cdot 10^3$	$1.84 \cdot 10^4 \pm 762$
Data	$4.31 \cdot 10^7$	$9.05 \cdot 10^5$	$1.02 \cdot 10^5$	$1.80 \cdot 10^4$
Z'_χ (4 TeV)	$3.45 \cdot 10^{-2} \pm 1.74 \cdot 10^{-3}$	$0.139 \pm 6.50 \cdot 10^{-3}$	$0.185 \pm 8.70 \cdot 10^{-3}$	$0.156 \pm 7.69 \cdot 10^{-3}$
Z'_χ (5 TeV)	$0.0143 \pm 7.02 \cdot 10^{-4}$	0.0564 ± 0.0026	$7.54 \cdot 10^{-2} \pm 3.45 \cdot 10^{-3}$	$6.35 \cdot 10^{-2} \pm 3.14 \cdot 10^{-3}$
$M_{\mu\mu}$ [GeV]	500-700	700-900	900-1200	1200-1800
Drell-Yan	$5.21 \cdot 10^3 \pm 286$	$1.42 \cdot 10^3 \pm 90.9$	500 ± 37.8	181 ± 17.8
$t\bar{t}$	$1.99 \cdot 10^3 \pm 1.02 \cdot 10^3$	349 ± 191	79.6 ± 46.1	18.7 ± 8.04
Dibosons	503 ± 16.4	145 ± 5.3	54.1 ± 2.54	19.9 ± 1.34
Total SM	$7.7 \cdot 10^3 \pm 349$	$1.91 \cdot 10^3 \pm 105$	634 ± 41.8	219 ± 19.9
Data	$7.41 \cdot 10^3$	$1.78 \cdot 10^3$	595	198
Z'_χ (4 TeV)	$0.23 \pm 1.28 \cdot 10^{-2}$	0.222 ± 0.0145	0.242 ± 0.0195	0.367 ± 0.0415
Z'_χ (5 TeV)	$9.03 \cdot 10^{-2} \pm 4.87 \cdot 10^{-3}$	0.0854 ± 0.00531	0.089 ± 0.00658	0.118 ± 0.0119
$M_{\mu\mu}$ [GeV]	1800-3000	3000-10000		
Drell-Yan	26.9 ± 4.49	1.22 ± 0.546		
$t\bar{t}$	0.402 ± 0.323	0 ± 0		
Dibosons	2.64 ± 0.376	0.09 ± 0.0381		
Total SM	30 ± 4.73	1.31 ± 0.579		
Data	24	0		
Z'_χ (4 TeV)	1.12 ± 0.287	5.44 ± 2.81		
Z'_χ (5 TeV)	0.13 ± 0.0276	0.611 ± 0.444		

Table 5.2: Expected and observed event yields divided into mass bins in the dimuon channel for $139.0 \pm 2.4\text{fb}^{-1}$ of collision data. The errors quoted correspond to the combined statistical, theoretical and experimental systematic uncertainties.

5.2.1 Main distributions

The distribution of the dimuon invariant mass is shown in Figure 5.5. The MC expectations are displayed as stacked histograms in solid colors: dibosons in yellow, combined $t\bar{t}$ and single top in red and DY in blue. We remind the reader that the fake background is negligible, as mention in Section 4.4.5 and discussed at length in Chapter 7, and therefore not included in the following data/MC comparisons or in the statistical analysis. Hypothetical Z'_χ bosons with masses of 2, 3, 4 and 5 TeV are shown as red, green, blue and magenta unfilled histograms. The total SM expectation is normalized to the integrated luminosity. Data are displayed as black points with an error bar. The error bar on the data is the standard deviation $\sqrt{N}$ on the Poisson distribution (more on this in Section 5.4.1) with an expectation value N. The bottom panel shows the data to MC ratio. The error bars represent the statistical error on the ratio, calculated using a standard error propagation, taking into account the uncertainty on the data and the weighted number of MC events. The shaded band represents one standard deviation up and down of the combined systematic uncertainties. The individual systematic uncertainties are discussed in Section 5.3.

We see that there is a trend in the invariant mass distribution in Figure 5.5 - in the data to MC ratio panel we see that the data points lie on the upper boundary of the uncertainty band around the Z boson peak, and then move steadily towards the lower boundary of the uncertainty band. The ratio of data to MC stays within the boundaries as described by the systematic uncertainty. even if single points fall outside. We interpret this as a slight hint of mismodelling in the MC. This trend is also seen in the dilepton publication from 2017 [102].

In Section 5.2.4 the distributions for dimuon invariant mass and muon p_{T}, ϕ and η are shown for each data-taking period.

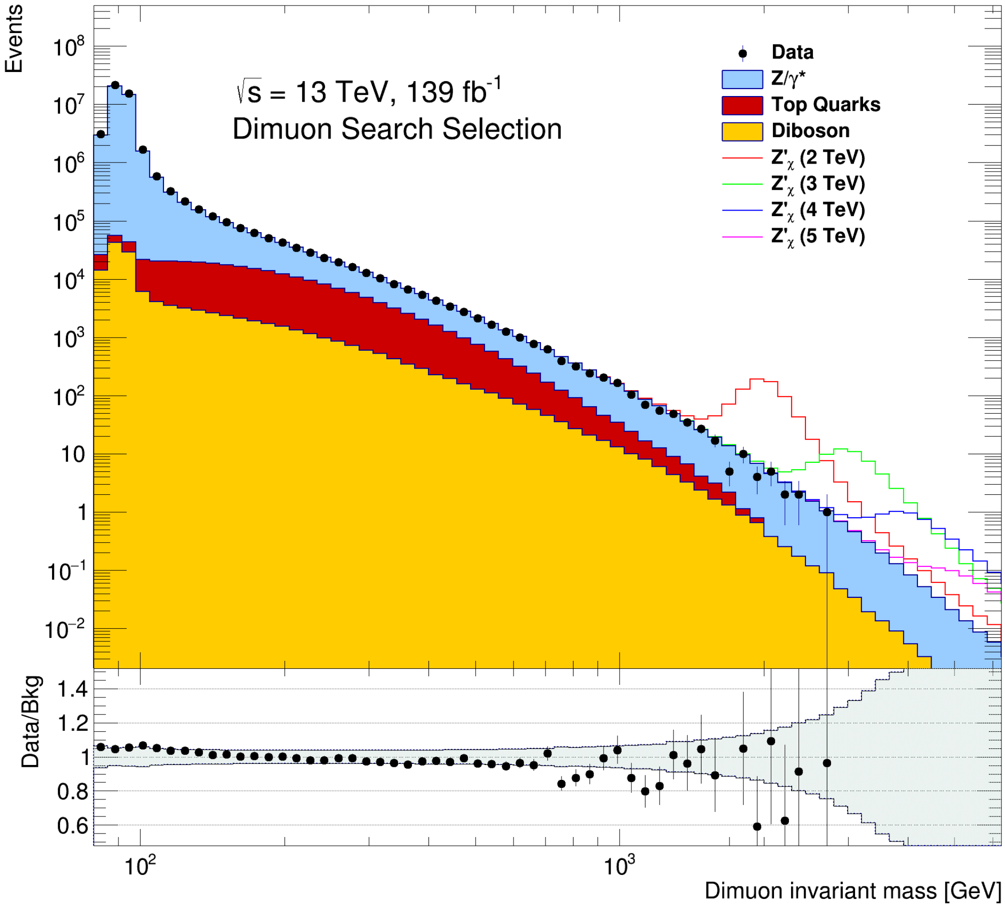

Figure 5.5: Distribution of the dimuon invariant mass ($M_{\mu\mu}$), showing the stacked sum of all expected backgrounds and four resonant Z'_{χ} signals. The bin width is constant in $\log M_{\mu\mu}$. The total MC expectation is normalized to the integrated luminosity. The bottom panel shows the ratio of data to MC (black points), with the shaded band representing the combined systematic uncertainties.

Distributions for p_{T}, η, ϕ and dimuon p_{T} for the two leading muons are presented in Figure 5.6 for the signal region $M_{\mu\mu} > 120$ GeV, avoiding the Z boson peak. Distributions for p_{T}, η and ϕ separated into leading and subleading muon are shown in Figure 5.7. There is a clearly visible trend in the muon p_{T} distributions in the data to MC ratio, with the ratio going to lower values at higher values of the muon p_{T}. This trend also falls below the shaded region that describes the systematic uncertainties, leading us to think there might be some uncertainty, affecting the p_{T} of the muon more than the dimuon mass, that is not taken into account. The muon η and ϕ distributions are well described by MC, and the data to MC ratio is flat in general, keeping within the band of the systematic uncertainties. The two largest dips in the η distribution at approximately $|\eta| = 1$, are in the barrel end-cap transition region, where some chambers are vetoed because of misalignment issues. At the very center of the pseudorapidity distribution, at $\eta = 0$, there is a large dip caused by a gap intentionally left in the chamber coverage to allow for services to the solenoid magnet, the calorimeters and the inner detector. The dips in the ϕ distribution is caused by a non-uniform distribution of material and various detector parts in the transverse plane around the beam-axis. The two largest dips are caused by the feet of the detector.

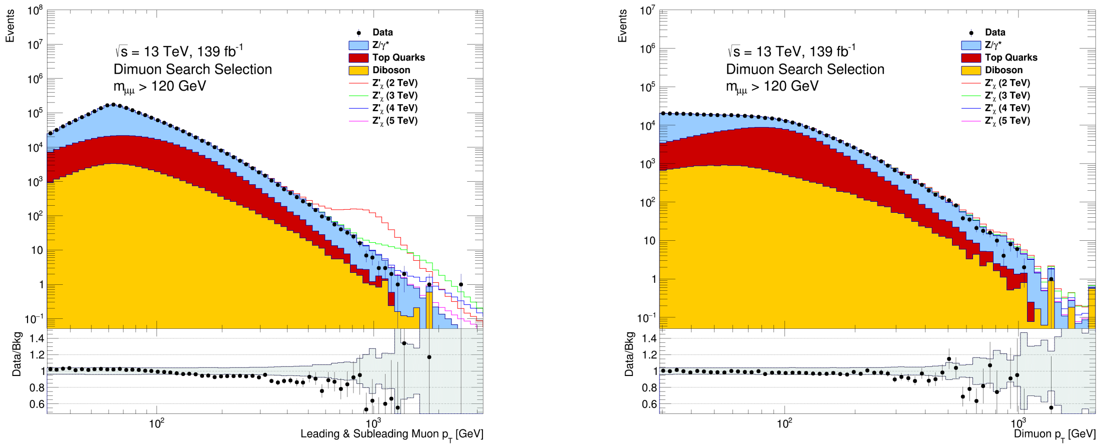

(a) Muon transverse momentum distribution.

(b) Dimuon transverse momentum distribution.

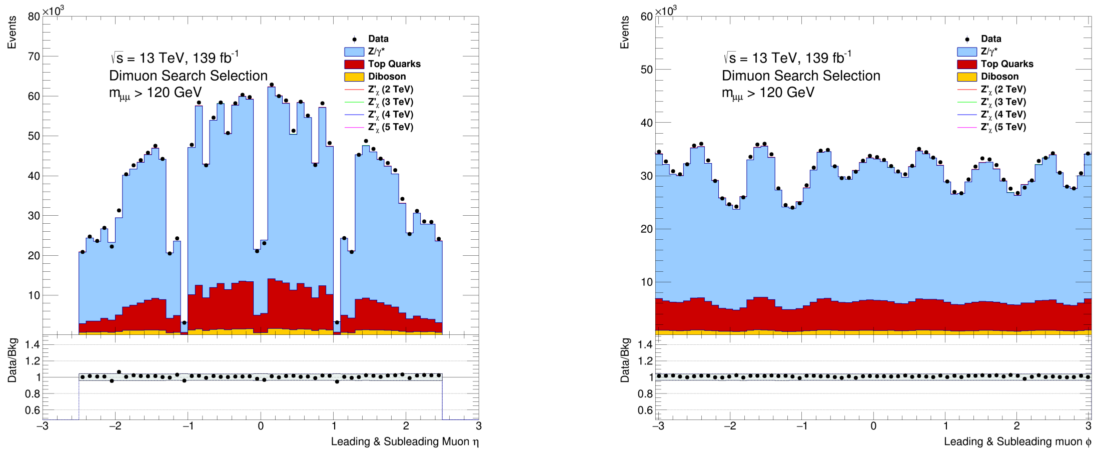

(c) Muon η distribution.

(d) Muon ϕ distribution.

Figure 5.6: Transverse momentum p_{T} distributions for the two leading muons in the signal region (a), dimuon p_{T} (b), η (c) and ϕ (d) distributions of the two leading muons with invariant mass above 120 GeV after the dimuon search event selection. The plots show the stacked sum of all expected backgrounds, normalized to the integrated luminosity. The bottom panel shows the ratio of data to MC (black points), with the shaded band representing the combined systematic uncertainties.

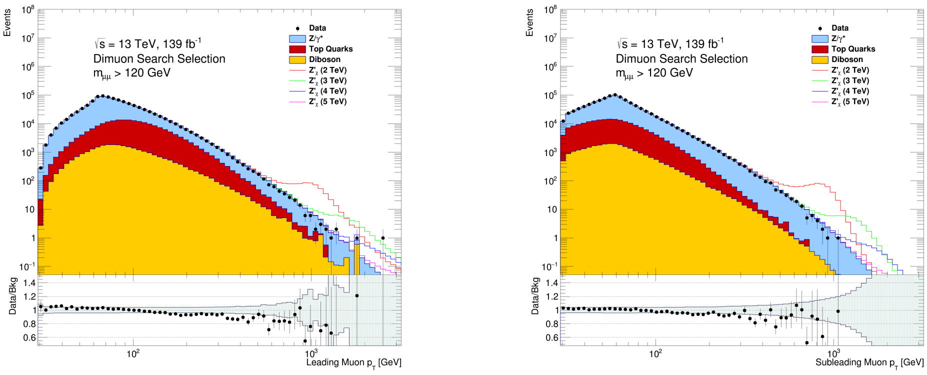

(a) Leading muon transverse momentum distribution.

(b) Subleading muon transverse momentum distribution.

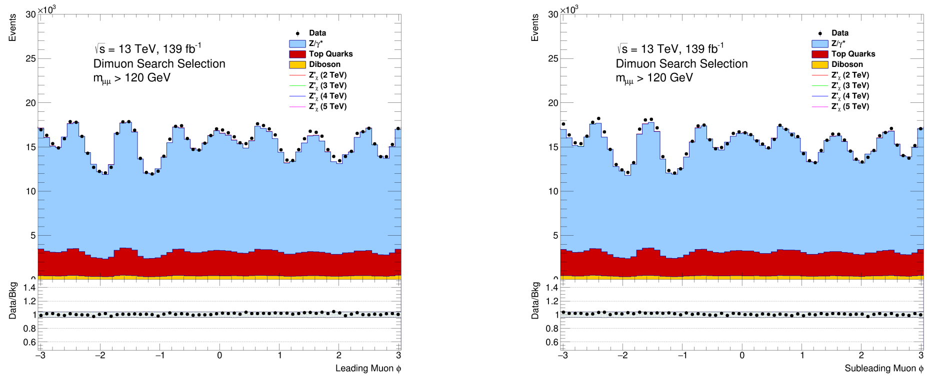

(c) Leading muon ϕ distribution.

(d) Leading muon ϕ distribution.

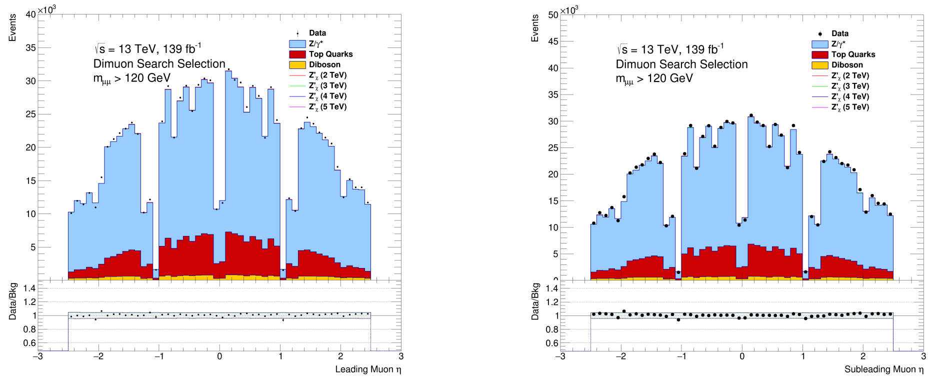

(e) Leading muon η distribution.

(f) Subleading muon η distribution.

Figure 5.7: Transverse momentum p_{T}, η and ϕ distributions for the leading (left) and subleading (right) muons in the signal region above an invariant mass of 120 GeV. The plots show the stacked sum of all expected backgrounds, normalized to the integrated luminosity. The bottom panel shows the ratio of data to MC (black points), with the shaded band representing the combined systematic uncertainties.

5.2.1.1 MC mismodelling

There is a known poor modelling of the lepton and dilepton p_{T} from higher-order jet effects in the Z^0 peak region [95], and the result of this is clearly visible in the distribution for the p_{T} and the dimuon p_{T} of the two leading muons when including the dimuon invariant mass down to 80 GeV, as seen in Figure 5.8(a) and (b). This issue is avoided by not including the Z boson peak in the signal region. The distributions of η and ϕ in (c) and (d) respectively display no structures caused by the mismodelling in the data to MC ratio plots in the bottom panels.

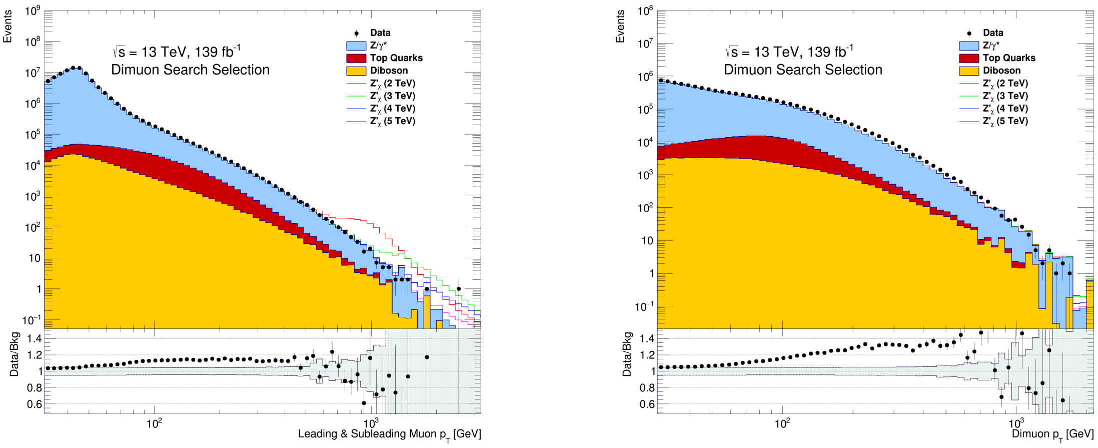

(a) Muon transverse momentum distribution.

(b) Dimuon transverse momentum distribution.

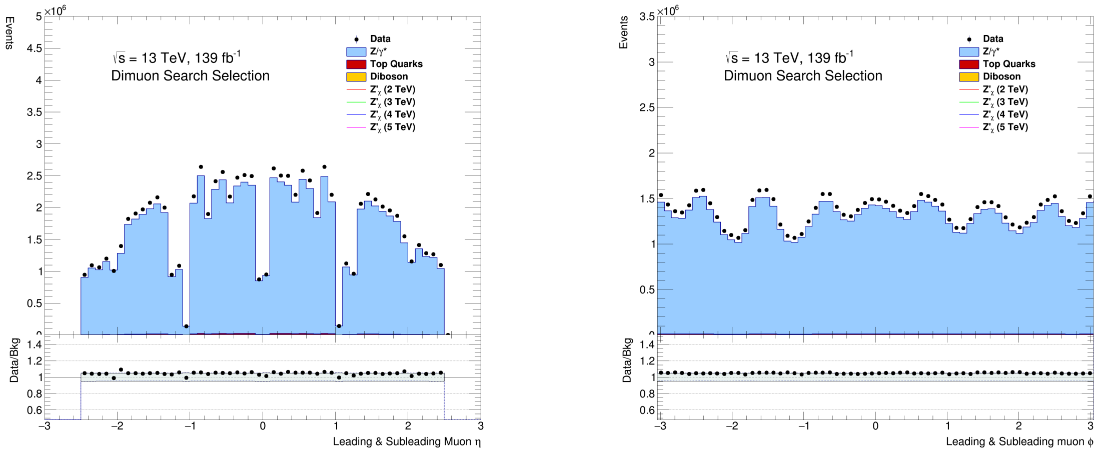

(c) Muon η distribution.

(d) Muon ϕ distribution.

Figure 5.8: Transverse momentum p_{T} distributions for the two leading muons over the full dimuon invariant mass range above 80 GeV (a), dimuon p_{T} (b), η (c) and ϕ (d) distributions of the two leading muons the dimuon search event selection. The plots show the stacked sum of all expected backgrounds, normalized to the integrated luminosity. The bottom panel shows the ratio of data to MC (black points), with the shaded band representing the combined systematic uncertainties.

5.2.2 Isolation and impact parameter distributions

The distributions of the isolation, $|\Delta z_0^{\mathrm{BL}} \cdot \sin\theta|$ and $|d_0^{\mathrm{BL}}(\sigma)|$ distributions for the invariant mass region $M_{\mu\mu} > 80\,\mathrm{GeV}$ are shown in Figure 5.9. Figure 5.10 shows the same distributions only divided into separate plots for the leading and subleading muons. The disagreement between data and MC seems striking and might leave the reader feeling uneasy, but rest assured that this difference is covered by the TTVA and isolation efficiency scale factors.[4]

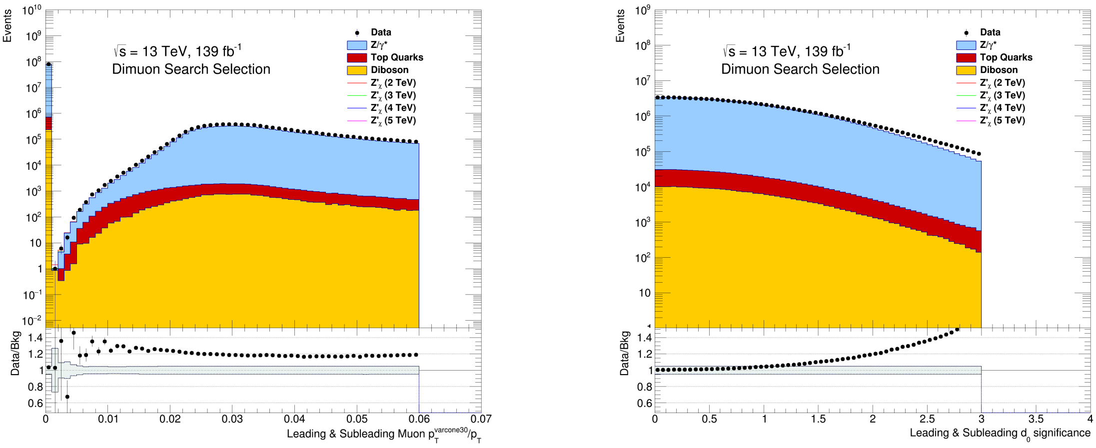

(a) Isolation variable used in the “FixedCutTight-TrackOnly” definition, for leading and subleading muons.

(b) $|d_0^{\mathrm{BL}}(\sigma)|$ for leading and subleading muons.

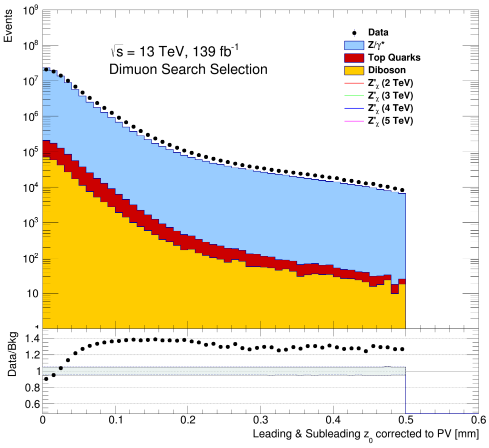

(c) $|\Delta z_0^{\mathrm{BL}} \cdot \sin\theta|$ for leading and subleading muons.

Figure 5.9: Distributions of the isolation variable and the impact parameters for the leading and subleading muons.

5.2.3 Event displays for the highest dimuon invariant mass events

Figures 5.11 and 5.12 show the event displays made with the Atlantis tool [103] with the two highest dimuon invariant mass events (2.75 TeV and 2.42 TeV) in the Run 2 dataset [100].

---

[4] Note that efficiency scale factors do not correct the distributions of e.g. isolation or impact parameters directly, but ensure that the cut efficiencies are equal for data and MC.

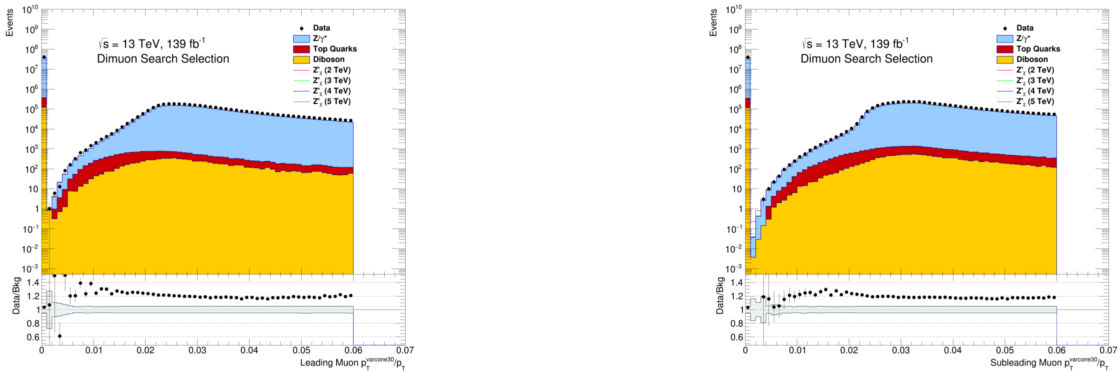

(a) Isolation variable used in the "FixedCutTightTrackOnly" definition, for leading muon.

(b) Isolation variable used in the "FixedCutTightTrackOnly" definition, for subleading muon.

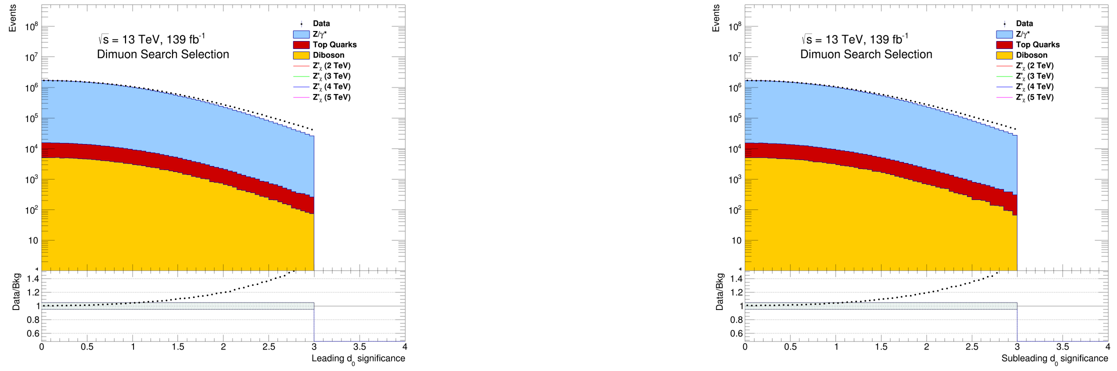

(c) $|d_0^{\mathrm{BL}}(\sigma)|$ for leading muon.

(d) $|d_0^{\mathrm{BL}}(\sigma)|$ for subleading muon.

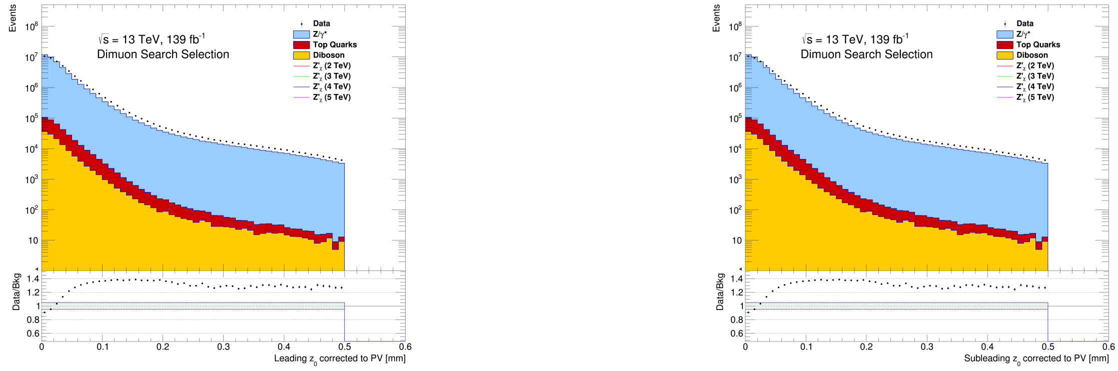

(e) $|\Delta z_0^{\mathrm{BL}} \cdot \sin\theta|$ for leading muon.

(f) $|\Delta z_0^{\mathrm{BL}} \cdot \sin\theta|$ for subleading muon.

Figure 5.10: Distributions of the isolation variable and the impact parameters for the leading (left) and subleading (right) muons separately.

Both events show signs of two well reconstructed muons with high values of transverse momentum (from 0.62 TeV to 1.82 TeV) going completely or almost back-to-back in the transverse plane. For the highest invariant mass event, however, the missing transverse energy is 800 GeV in the direction of the subleading muon, which probably means that either the leading muon's p_{T} is overestimated or that the subleading muon's p_{T} is underestimated, or both.[5]

5.2.4 Data/MC comparisons for each data-taking period

The four years of data-taking (Run 2), are divided into three sub-campaigns, each with their own set of simulated data – mc16a corresponds to the 2015 and 2016 run, mc16d corresponds to the 2017 run and mc16e corresponds to the 2018 run [104]. The mc16a and mc16d sub-campaigns were launched *after* the data taking was complete, thus making it possible to match the corresponding data conditions, trigger menu and the pile-up distribution. The mc16e samples are designed to match the 2018 data conditions, the trigger menu and the pile-up profile, but as the production was launched after finalizing the trigger-menu but *before* the data run finished, the pile-up profile is based on an educated guess. Figure 5.13 shows the luminosity-weighted distribution of the mean number of interactions per beam crossing separately for all the five years of data-taking in Run 2.

The basic event selection is the same for all sub-campaigns. Differences in the corrections to the simulated data as described in Section 4.3.4 occur. In addition there are certain period-dependent differences in the systematic uncertainties.

In Figure 5.14 the dimuon invariant mass distribution is shown divided into the three sub-campaigns. Comparing the three, we see that the 2015/2016 and mc16a campaign are different from the two other distributions, most noticeably the Z' peak is narrower. This is caused by an observed deterioration in the alignment quality between 2016 and 2017.

Figures 5.15, 5.16 and 5.17 show the distributions for p_{T}, η and ϕ respectively for the leading and subleading muons separately.

---

[5] The two leading muons are back-to-back in the transverse plane and they are completely dominating the event, their transverse momenta should balance each other.

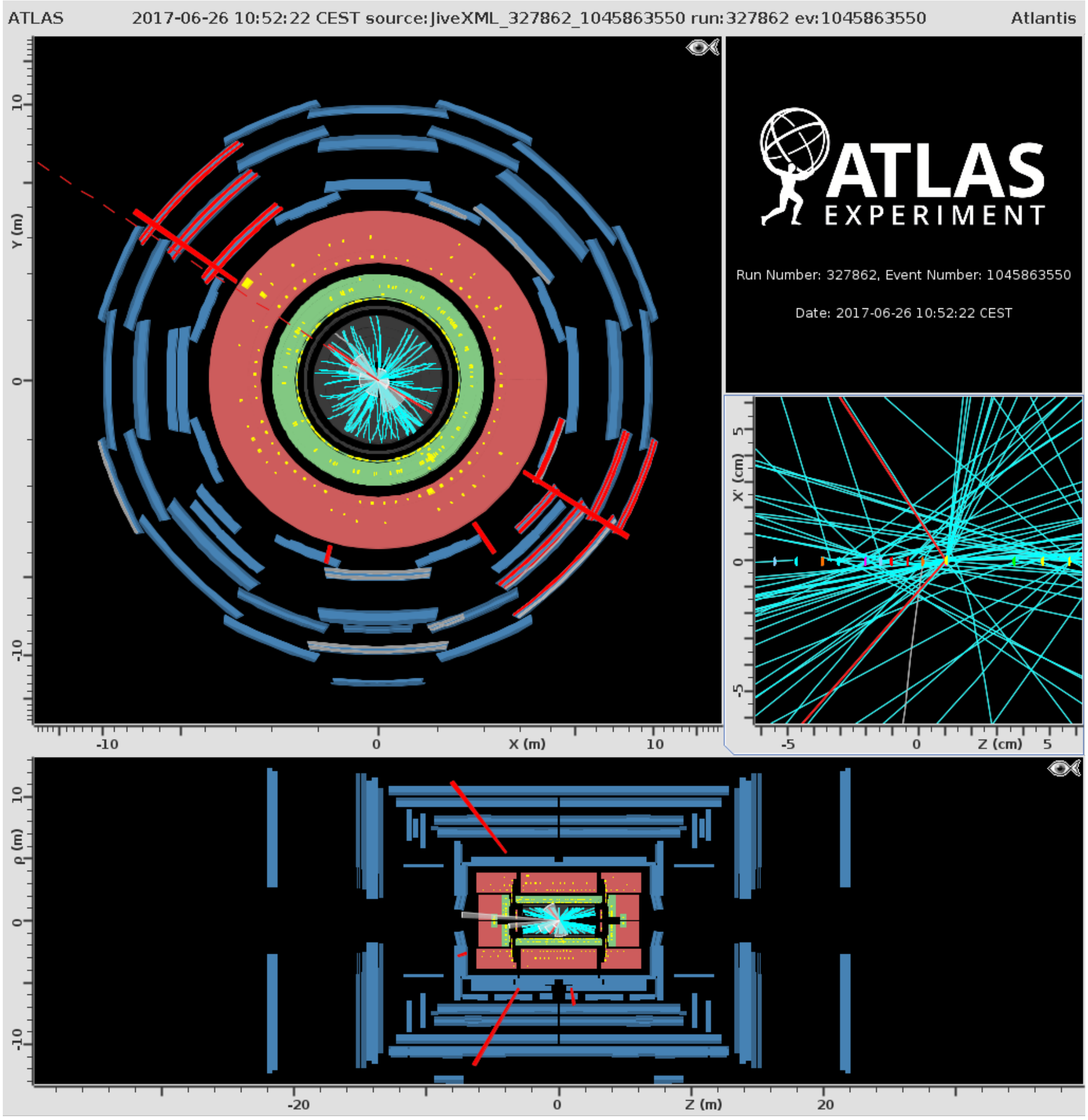

Figure 5.11: Atlantis event display of the highest invariant mass event candidate passing the whole event selection in the Run 2 data taking period. The invariant mass of the two leading muons is 2.75 TeV. The properties of the leading muon are $p_{\mathrm{T}} = 1.82\,\mathrm{TeV}$, $\eta = -0.52$, $\phi = -0.56$. The properties of the subleading muon are $p_{\mathrm{T}} = 1.04\,\mathrm{TeV}$, $\eta = -0.67$, $\phi = 2.53$. The E_T^{miss} of the event is approximately 800 GeV and is pointing in the direction of the subleading muon. The reconstructed jets that are overlapping with the two leading muons have $p_{\mathrm{T}} < 50\,\mathrm{GeV}$ and are therefore thought to be induced by the calorimeter deposits of the muons.

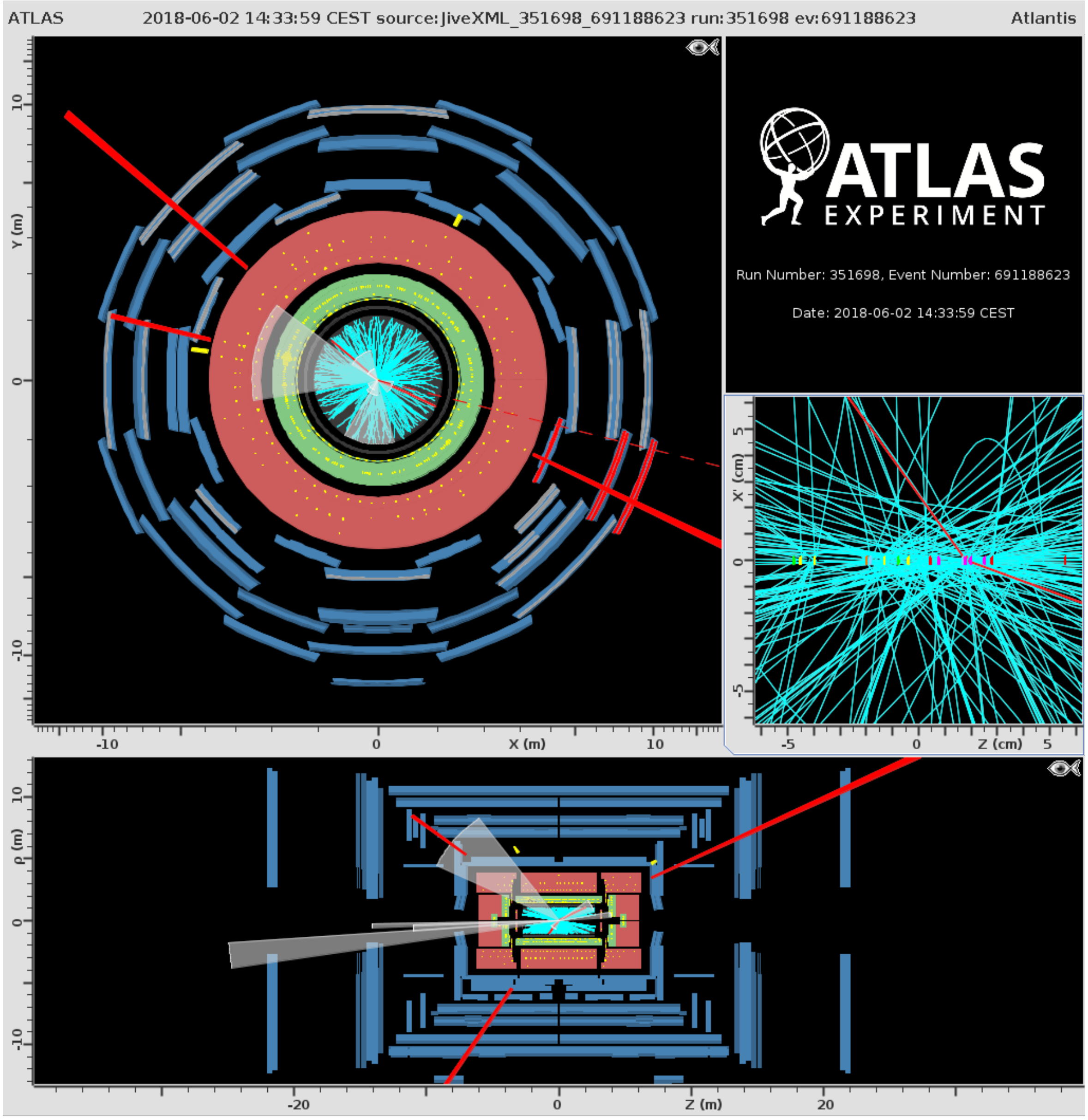

Figure 5.12: Atlantis event display of the second highest invariant mass event candidate passing the whole event selection in the Run 2 data taking period. The invariant mass of the two leading muons is 2.42 TeV. The properties of the leading muon are $p_{\mathrm{T}} = 0.94\,\mathrm{TeV}$, $\eta = -0.61$, $\phi = -0.45$. The properties of the subleading muon are $p_{\mathrm{T}} = 0.62\,\mathrm{TeV}$, $\eta = 1.46$, $\phi = 2.42$. The E_T^{miss} of the event is approximately 40 GeV. The reconstructed jets that are overlapping with the two leading muons have $p_{\mathrm{T}} < 50\,\mathrm{GeV}$ and are therefore thought to be induced by the calorimeter deposits of the muons.

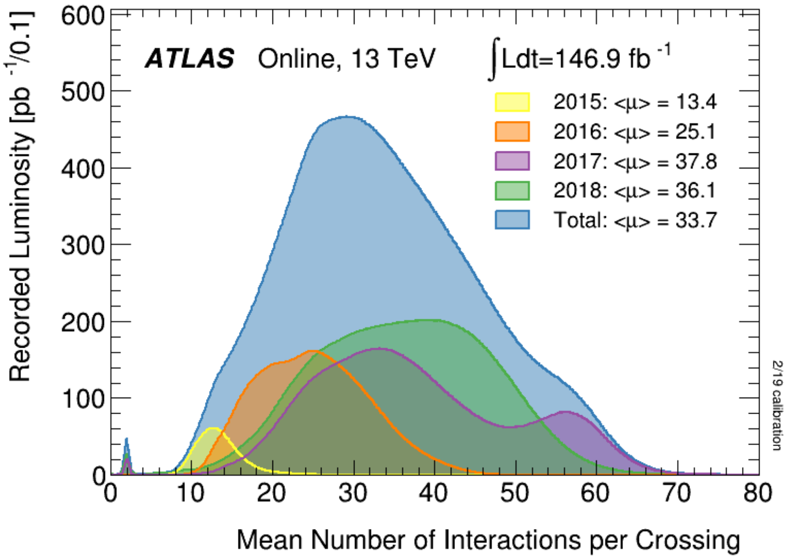

Figure 5.13: The luminosity-weighted distribution of the mean number of interactions per bunch crossing for the five years of data-taking in Run 2 [97]. All data recorded by ATLAS during stable beams is used, 146.9 fb^{-1} in total for Run 2. Note that the amount of data differs from the data in the GRLs, which is 139 fb^{-1}.

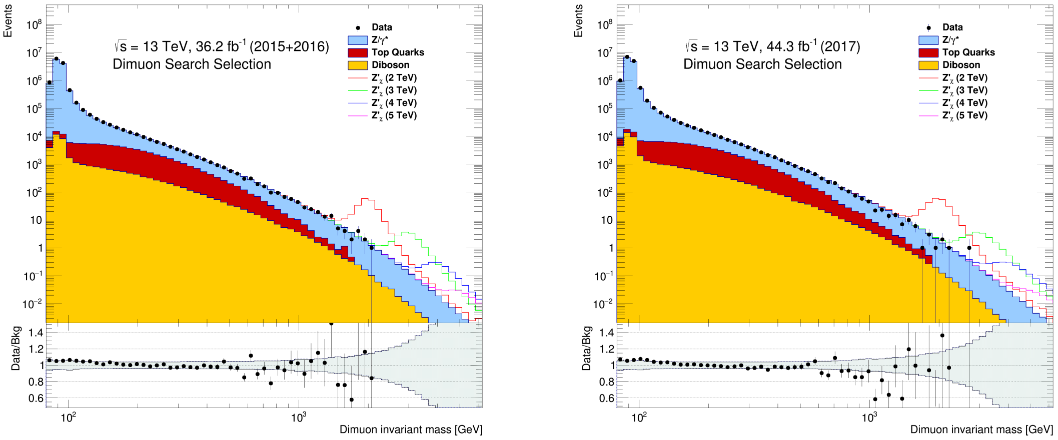

(a) Data from 2015+2016 and mc16a

(b) Data from 2017 and mc16d

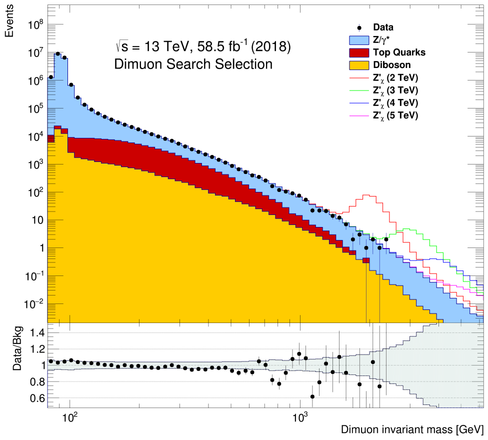

(c) Data from 2018 and mc16e

Figure 5.14: Distribution of the dimuon invariant mass ($M_{\mu\mu}$), showing the stacked sum of all expected backgrounds and four resonant Z'_χ signals, divided into the three sub-campaigns representing data-taking during 2015/2016, 2017 and 2018. The bin width is constant in $\log M_{\mu\mu}$. The total MC expectation is normalized to the integrated luminosity. The bottom panel shows the ratio of data to MC (black points), with the shaded band representing the combined systematic uncertainties.

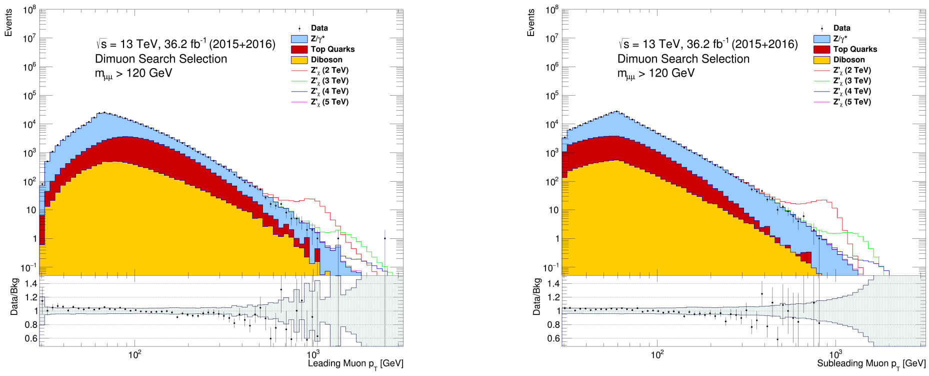

(a) Data from 2015+2016 and mc16a

(b) Data from 2015+2016 and mc16a

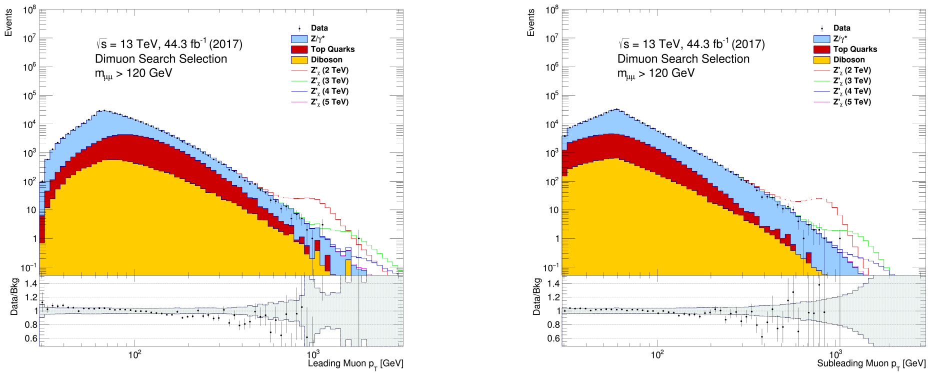

(c) Data from 2017 and mc16d

(d) Data from 2017 and mc16d

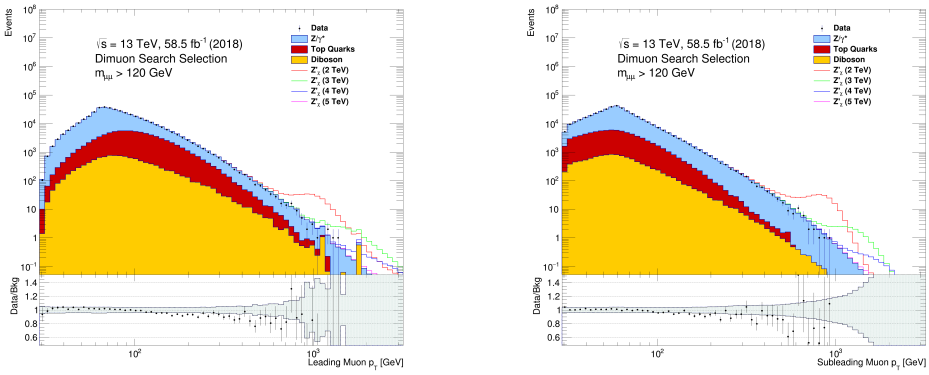

(e) Data from 2018 and mc16e

(f) Data from 2018 and mc16e

Figure 5.15: Transverse momentum p_{T} distributions for the two leading muons in the signal region (a), dimuon p_{T} (b), η (c) and ϕ (d) distributions of the two leading muons with invariant mass above 120 GeV after the dimuon search event selection. The plots show the stacked sum of all expected backgrounds, normalized to the integrated luminosity. The bottom panel shows the ratio of data to MC (black points), with the shaded band representing the combined systematic uncertainties.

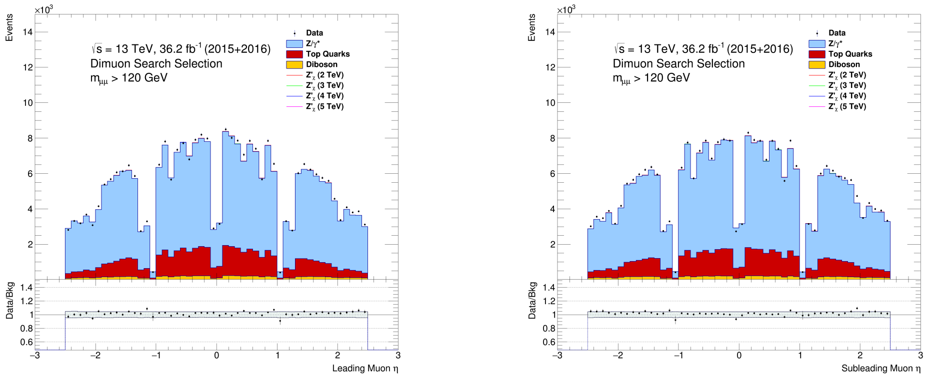

(a) Data from 2015+2016 and mc16a

(b) Data from 2015+2016 and mc16a

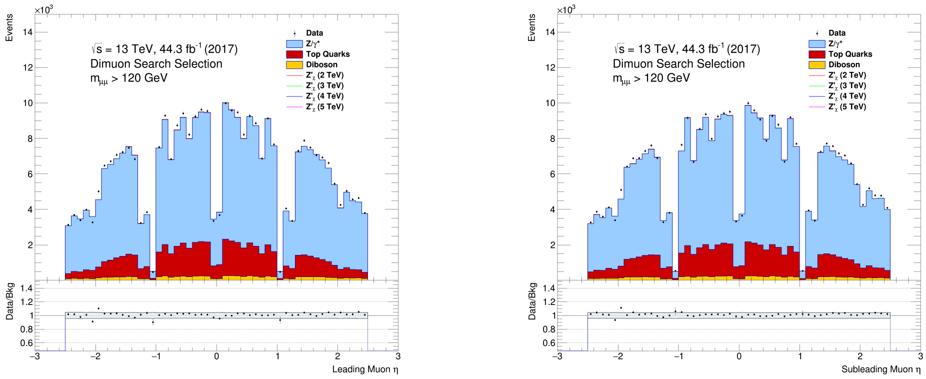

(c) Data from 2017 and mc16d

(d) Data from 2017 and mc16d

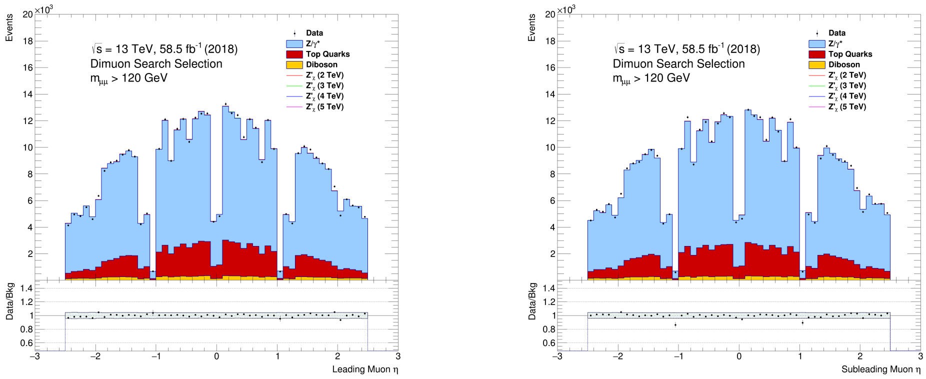

(e) Data from 2018 and mc16e

(f) Data from 2018 and mc16e

Figure 5.16: Pseudorapidity η distributions for the two leading muons showed separately. All events are selected with the dimuon search event selection, as described in Section 5.1, and have an invariant mass above 120 GeV. Data are divided into the three sub-campaigns representing data-taking during 2015/2016, 2017 and 2018. The plots show the stacked sum of all expected backgrounds, normalized to the integrated luminosity. The bottom panel shows the ratio of data to MC (black points), with the shaded band representing the combined systematic uncertainties.

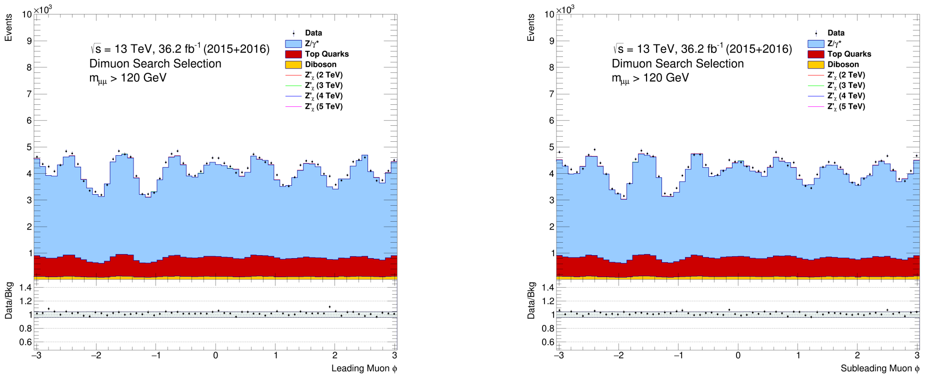

(a) Data from 2015+2016 and mc16a (b) Data from 2015+2016 and mc16a

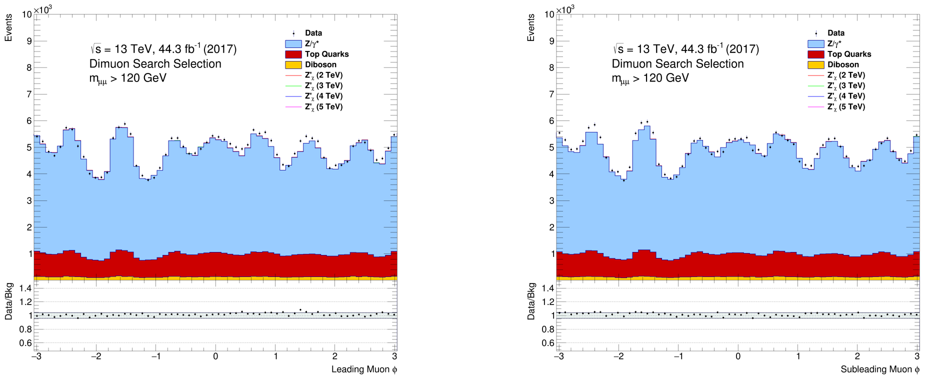

(c) Data from 2017 and mc16d (d) Data from 2017 and mc16d

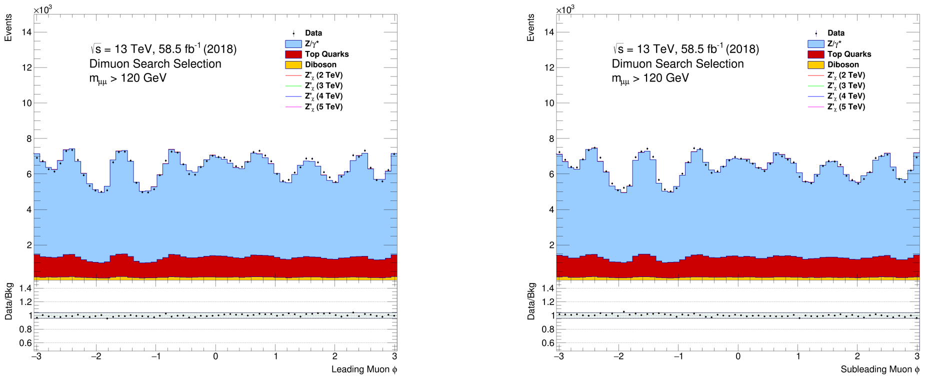

(e) Data from 2018 and mc16e (f) Data from 2018 and mc16e

Figure 5.17: ϕ distributions for the two leading muons showed separately. All events are selected with the dimuon search event selection (see Section 5.1) and have an invariant mass above 120 GeV. Data are divided into the three sub-campaigns representing data-taking during 2015/2016, 2017 and 2018. The plots show the stacked sum of all expected backgrounds, normalized to the integrated luminosity. The bottom panel shows the ratio of data to MC (black points), with the shaded band representing the combined systematic uncertainties.

5.3 Systematic uncertainties

Systematic uncertainties above a certain size will have a non-negligible impact on the cross-section limit. These are added to the statistical framework in the form of nuisance parameters, as will be covered in Section 5.4. The systematic uncertainties include both experimental and theoretical effects on the total background expectation and the experimental effects on the total signal expectation. Table 5.3 provides a summary, and displays the absolute value of the relative deviation from the nominal.

Source	Background [%]		Signal [%]	
	2 TeV	4 TeV	2 TeV	4 TeV
Luminosity	1.7	1.7	1.7	1.7
Beam energy	1.8	3.2	2.2	4.2
Pile-up	<0.1	<0.1	<0.1	<0.1
DY PDF choice	<0.1	1.8	N/A	N/A
DY PDF variation	7.2	13	N/A	N/A
DY PDF scale	0.84	1.5	N/A	N/A
DY α_s	1.2	2.3	N/A	N/A
DY EW corrections	1.9	4.0	N/A	N/A
DY γ-induced corrections	2.8	5.5	N/A	N/A
Top quarks theoretical	0.1	<0.1	N/A	N/A
Dibosons theoretical	2.7	2.0	N/A	N/A
Muon reconstruction efficiency	5.5	10	5.2	8.9
Muon isolation efficiency	0.46	0.47	0.46	0.46
Muon trigger efficiency	0.21	0.21	0.21	0.21
Track-to-vertex association	<0.1	<0.1	<0.1	<0.1
Bad muon veto	9.0	51	8.0	45
Muon momentum resolution (ID)	0.21	1.8	0.3	0.7
Muon momentum resolution (MS)	1.1	8.9	4.0	5.4
Muon momentum resolution (RESBIAS)	2.6	12	2.8	0.5
Muon momentum scale	0.38	0.43	0.10	0.19
Total	14	56	11	46

Table 5.3: Summary of relative systematic uncertainties (the absolute value of the ratio of the deviation to the nominal) in the expected number of event at dilepton masses of 2 TeV and 4 TeV. “N/A” represents cases where the uncertainty is not applicable.

There are separate groups within the ATLAS collaboration that estimate the systematic uncertainties, and the results of these studies are used within groups performing dedicated searches, like the resonant dilepton search group. In Table 5.3 all the relevant systematic uncertainties and their influence on signal and total background are listed at dimuon invariant masses of 2 TeV and 4 TeV. Figure 5.18 shows all relevant systematic uncertainty distributions as a function of the dilepton invariant mass for the background, and Figure 5.19 all the relevant distributions for two hypothetical Z'_χ bosons with pole masses of 2 TeV and 4 TeV. The distributions of the systematic uncertainties show the effect of shifting the value of one nuisance parameter one standard deviation on the full background or signal yield. All the experimental systematic uncertainties are discussed in Section 5.3.1 and the theoretical systematic uncertainties in Section 5.3.2.

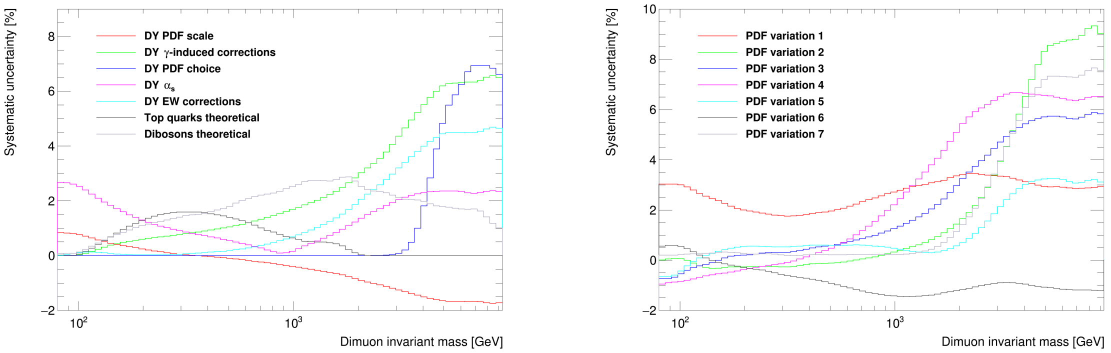

(a) Theoretical sources (b) Theoretical sources

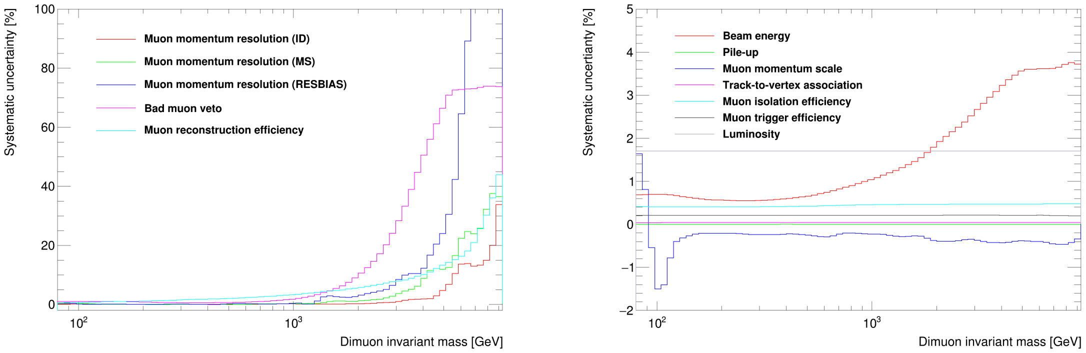

(c) Experimental sources (d) Experimental sources

Figure 5.18: The relative systematic uncertainties on the total background yield in the muon channel due to theoretical ((a) and (b)) and experimental sources ((c) and (d)).

5.3.1 Experimental systematic uncertainties

The muon efficiency corrections for reconstruction, isolation and trigger (marked as “Muon reconstruction efficiency”, “Muon isolation efficiency” and “Muon trigger efficiency” respectively in Figures 5.18 and 5.19 and Table 5.3 are obtained using the tag and probe method on $Z \to \mu\mu$ and $J/\Psi \to \mu\mu$ in data, and by comparing efficiencies in collision data and simulation one can extract corrections to simulated data. The uncertainties on these corrections are derived from variations in the method of extracting the efficiency correction, see [40] for more detailed information. The work is performed within the MCP group. An uncertainty is assigned to the “bad muon veto”, in association with the high-p_{T} working point due to an observed difference between data and MC. A small uncertainty is assigned to the efficiency of the track-to-vertex association. One additional uncertainty, the sagitta residual bias (marked as “Muon momentum resolution (RESBIAS)” in the table and figures), is added to account for an observed charge-dependent difference in the sagitta (defined in Figure 3.8) due to misalignments in the detector. This is not corrected for in data, after recommendations from the MCP group, applying to all searches in which individual candidates in the tail of the distribution can impact the results.

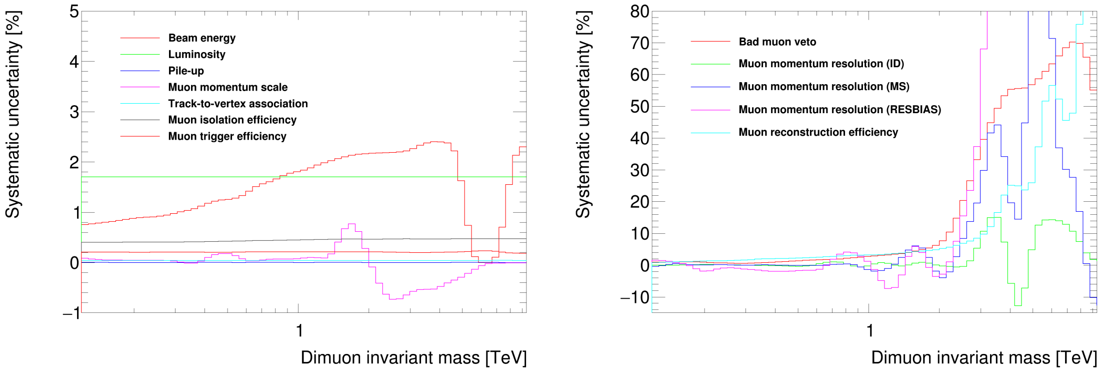

(a) Z'_χ 2 TeV

(b) Z'_χ 2 TeV

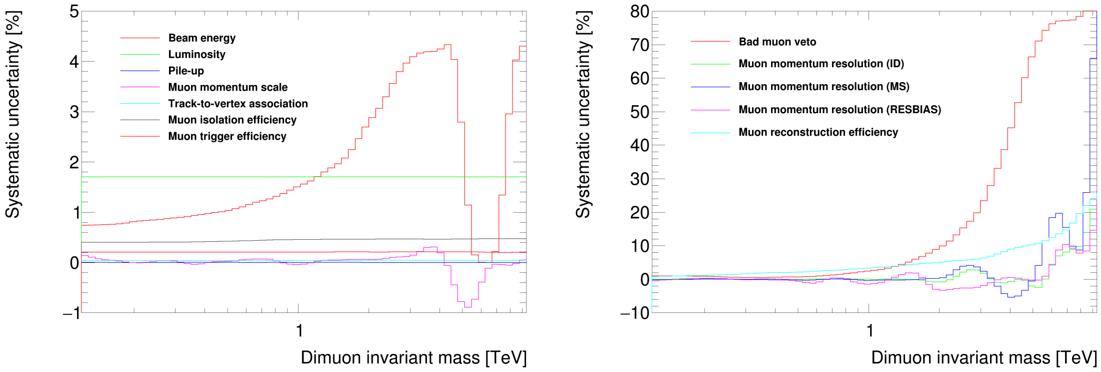

(c) Z'_χ 4 TeV

(d) Z'_χ 4 TeV

Figure 5.19: The relative systematic uncertainties due to experimental sources on the total signal yield for a Z'_χ with mass 2 TeV (top) and 4 TeV (bottom) in the muon channel.

The scale factor that was introduced to deliberately mismatch the pile-up distributions in data and MC, as described in Section 5.1.4.1, has an uncertainty attached to it. The estimation of this uncertainty is performed within the Physics Modelling Group (PMG) in ATLAS.

While the ATLAS detector geometry, magnetic field and material distribution are accurately modelled and included in the Monte Carlo simulations, the small effects missed in this modelling and changes to the geometry, magnetic field or material distribution result in the need for additional corrections to simulated data. Corrections to the simulated muon momentum scale and resolution (marked as “Muon momentum scale”, “Muon momentum resolution (MS)” and “Muon momentum resolution (ID)”) in the table and figures) are obtained by defining a series of correction constants thought to influence the data/MC agreement and fitting these to match the mass distributions in $Z^0 \rightarrow \mu\mu$ and $J/\Psi \rightarrow \mu\mu$ decays in MC to the observed ones in data. Systematic uncertainties are derived from e.g variations in the fitting procedures. More details can be found in [40] and [105]. This work is performed by the MCP group.

The ATLAS luminosity working group estimated the uncertainty on the integrated luminosity from the full Run 2 to be 1.7% [106], corresponding to $139.0 \pm 2.4\,\text{fb}^{-1}$.

5.3.2 Theoretical uncertainties

Theoretical uncertainties on the production cross-section estimates introduce a theoretical uncertainty on the total background estimate. This section is a short summary of the work performed by a small group of people working within the dilepton high mass search group [95] [23].

5.3.2.1 Drell-Yan background

By using the VRAP [107] program, the systematic uncertainties for PDF variation and scale and the strong coupling constant α_s at NNLO are assessed.

Due to the fact that perturbative calculations of QCD processes are limited to a finite number of included higher-order terms, the differential cross-section have uncertainties that are estimated by varying the nominal CT14 NNLO PDF renormalization and factorization scales by a factor of two (marked as “DY PDF scale” in Table 5.3 and Figure 5.18).

The influence of the variation of α_s (marked as “DY α_s” in the table and figure) on the differential cross-section is computed using the value 0.1183 with an associated uncertainty at ± 0.003 at the Z-mass, a conservative estimate of the uncertainty compared to the PDF4LHC [108] recommendation of ± 0.0015. A conservative estimate is chosen to ensure that the uncertainty at high mass is not underestimated.

The PDF variation on the CT14 NNLO PDF is one of the largest theoretical uncertainties. Originally a set of 28 eigenvector error-set variations[6] of the PDF was associated to one single nuisance parameter in the statistical framework, as a function of the invariant dimuon mass. As this could lead to an underestimation of the effect, the CT14 authors provided a re-diagonalized set of 7 eigenvectors, where eigenvectors with similar behaviours were bundled together. These are treated as 7 separate nuisance parameters. The quadratic sum of these 7

---

[6] Each PDF set has a set of independent parameters that are associated with that set, that can be varied in orthogonal direction to evaluate the systematic uncertainties that are associated with the PDF variations. These are known as the eigenvector of the PDF set in the function space.

uncertainties are marked as “DY PDF variation” in Table 5.3 (only the combination of all 7 are shown) and Figure 5.18.

The EW corrections systematic uncertainty (marked as “DY EW corrections’“ in Table 5.3 and Figure 5.18) was estimated by comparing two different methods of computing the EW k-factor in the combination of the higher-order EW and QCD effects, the so-called additive (using $1 + \delta_{\mathrm{EW}} + \delta_{\mathrm{QCD}}$) and the factored (using $(1 + \delta_{\mathrm{EW}})(1 + \delta_{\mathrm{QCD}})$) methods, where the additive method was selected as the nominal method.

The uncertainty in the photon-induced correction (marked as “DY γ-induced corrections in Table 5.3 and Figure 5.18) is calculated based on the uncertainties in quark masses and the photon PDF.

An uncertainty due to the choice of PDF is investigated by comparing central values of several modern PDFs: MMHT14 [109], NNPDF3.0 [84], ABM12 [110] and JR14 [111]. The uncertainty on the nominal CT14NNLO PDF is evaluated in VRAP by varying the eigenvectors of the PDF set within 90% C.L. and calculating the DY cross-section. Out of the various PDFs the NNPDF3.0 is the one that is most dissimilar to the nominal CT14NNLO PDF, and above invariant dilepton mass of approximately $3\,\mathrm{TeV}$ it obtains values beyond the 90% C.L. of the CT14NNLO PDF, as shown in Figure 5.20. The systematic uncertainty associated with the choice of PDF is computed by quadratically subtracting the total variation of the nominal PDF from the variation of the NNPDF3.0.

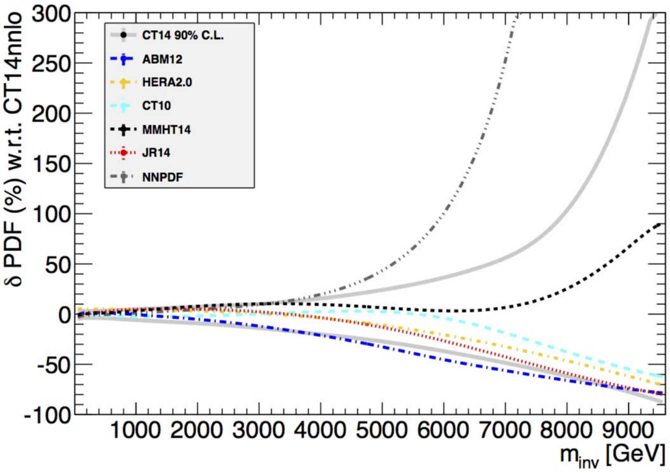

Figure 5.20: The uncertainty at 90% C.L. on the DY cross-section as function of the invariant mass $\mathrm{m_{inv}}$ due to the variations of the PDF eigenvectors, shown with the central values of several other possible PDF sets [112].

5.3.2.2 Top and diboson backgrounds

The theoretical uncertainties on the $t\bar{t}$ background is $^{+4.8\%}_{-5.5\%}$ [93]. We use a symmetric uncertainty of 5.5% in the statistical analysis. We use a symmetric 30% uncertainty on the dibosons background [101], which is considered a conservative estimate [83].

5.4 Statistical analysis – discovery and exclusion

Up until now, we have looked at data from Run 2, 139 fb^{-1}, comparing it to what we expect to find based on the assumption that the Standard Model is correct. We superimposed a few selected signal models, Z'_χ at masses of 2, 3, 4 and 5 TeV, but have made no comment regarding the existence of any new physics. This is about to change. We will focus on our main search variable, the dimuon invariant mass, and quantify the observed deviations from the SM (Section 5.4.2) and (in the absence of any observed signal) quantify what signal hypotheses are excluded after taking data into account (Section 5.4.3).[7]

5.4.1 The statistical framework

In any given bunch crossing in the ATLAS detector, there is a very small probability of producing an event that passes the event selection as described in Section 5.1 and has a dimuon invariant mass within a certain interval. This very small probability is constant in time, and each event is considered independent of all other events. The number of events in a given mass interval (mass bin) after any given number of bunch crossings can be considered a realization of a binomially distributed stochastic variable. As the number of bunch crossings grows to large values and since the probability of producing a signal event in a certain mass bin is so small, the number of events in any given mass bin can be approximated by a Poisson distribution. The probability of observing n events in a mass bin l of channel k, $P(n|\lambda_{kl})$, is given by the expression

$$P(n|\lambda_{kl}) = e^{-\lambda_{kl}}\frac{\lambda_{kl}^n}{n!},$$

where λ_{kl} is the expectation value in bin l of channel k. For this reason, the Poisson distribution plays an important role in the statistical framework. The expectation value λ_{kl} is taken from theory, i.e. the Standard Model or a Beyond the Standard Model theory. Note that in this analysis there is only one channel, the dimuon channel.

In this analysis, data is modelled using the multi-bin counting experiment approach. The expectation value λ_{kl} consists of contributions from signal s_{kl} (set to zero for the Standard Model) and the background b_{kl} in bin l of channel k, and is given by

$$\lambda_{kl}(\sigma,\boldsymbol{\theta}) = s_{kl}(\sigma,\boldsymbol{\theta}) + b_{kl}(\boldsymbol{\theta}), \tag{5.1}$$

where σ is the cross-section for Z' production and decay to two muons (the parameter of interest, PoI, in the statistical analysis) and $\boldsymbol{\theta}$ represents the nuisance parameters, describing the effects of systematic uncertainties (see Section 5.3 for a description of the relevant systematic uncertainties).

The observed event count in bin l of channel k is denoted n_{kl}, and the set of all individual-bin observations is denoted $\boldsymbol{n}$. The likelihood $\mathcal{L}$ is constructed with the observed data as

$$\mathcal{L}(\sigma,\boldsymbol{\theta}) = P(\boldsymbol{n}|\sigma,\boldsymbol{\theta}) = \prod_{k=1}^{N_\text{chan}}\prod_{l=1}^{N_\text{bin}} e^{-\lambda_{kl}(\sigma,\boldsymbol{\theta})}\frac{\lambda_{kl}(\sigma,\boldsymbol{\theta})^{n_{kl}}}{n_{kl}!}, \tag{5.2}$$

---

[7] This section is based largely on reference [113], also using a lot of notation from reference [114] in Section 5.4.2.

with N_{chan} as the number of channels in the statistical analysis (only the muon channel in this case) and N_{bin} as the number of bins included in the statistical analysis.

The number of expected signal events $s_{kl}(\sigma, \boldsymbol{\theta})$ in bin l of channel k can be written as

$$s_{kl}(\sigma, \boldsymbol{\theta}) = \overline{s_{kl}}(\sigma) \exp\left(\sum_{i=1}^{N_{\text{sys}}} \operatorname{sgn}\left[(\delta s_{kl})_i\right] \theta_i \sqrt{\ln\left[1 + \left(\frac{(\delta s_{kl})_i}{\overline{s_{kl}}}\right)^2\right]} \right), \tag{5.3}$$

with $\overline{s_{kl}}(\sigma)$ as the central value of $s_{kl}(\sigma, \boldsymbol{\theta})$,

$$\overline{s_{kl}}(\sigma) = L_{\text{int}} \sigma A_k \epsilon_{kl}. \tag{5.4}$$

L_{int} is the integrated luminosity of the collected data. The factor A_k is the total "acceptance×efficiency" for signal events in channel k that fire the trigger, pass the event selection and have a dimuon invariant mass within the range used in the statistical analysis. The acceptance×efficiency is shown in Figure 5.4. ϵ_{kl} is the fraction of events in the signal invariant mass histogram in channel k that goes into bin l, often denoted the signal shape. To retain (anti-)correlations, the sign of (δs_{kl}) is included. The fraction $\frac{(\delta s_{kl})_i}{\overline{s_{kl}}}$ describes the relative shift in the number of expected signal events s_{kl} induced by a variation of one standard deviation variation of the nuisance parameter θ_i. When the nuisance parameter θ_i that describes the systematic uncertainty number i in Equation (5.3) is modelled as a Gaussian distribution (i.e. chosen to have a Gaussian prior distribution, or constraint), then $s_{kl}(\sigma, \theta_i)$ is described by a log-normal distribution.[8]

Correspondingly, the number of expected background events is written out as

$$b_{kl}(\boldsymbol{\theta}) = \overline{b_{kl}} \exp\left(\sum_{i=1}^{N_{\text{sys}}} \operatorname{sgn}[(\delta b_{kl})_i] \theta_i \sqrt{\ln\left[1 + \frac{(\delta b_{kl})_i}{\overline{b_{kl}}}\right]^2} \right),$$

for channel k, bin l and nuisance parameter i, with $\overline{b_{kl}}$ as the central value of $b_{kl}(\boldsymbol{\theta})$ (taken from Monte Carlo simulations) and $\frac{(\delta b_{kl})_i}{\overline{b_{kl}}}$ are the relative shifts in the number of expected background events induced by a one standard deviation variation of the nuisance parameter θ_i, shown as a function of the dimuon invariant mass in Figure 5.18.

Note that the number of signal and background events both have the same set of nuisance parameters to properly account for correlations. All backgrounds in this analysis are taken from Monte Carlo simulations, and the uncertainties are calculated by various performance groups within the ATLAS Collaboration.

Also note that the integrated luminosity L_{int} in Equation 5.4 denotes the central value of the integrated luminosity measurement. The uncertainty in this measurement is accounted for in the statistical analysis by adding a nuisance parameter θ_i with the relative shifts $\frac{(\delta s_{kl})_i}{\overline{s_{kl}}} = \frac{\delta L_{\text{int}}}{L_{\text{int}}}$ for all channels k and mass bins l and $\frac{(\delta b_{kl})_i}{\overline{b_{kl}}}$ from scaling all the MC backgrounds by $\frac{1+(\delta L_{\text{int}})}{L_{\text{int}}}$. The fraction $\frac{(\delta L_{\text{int}})}{L_{\text{int}}}$ is the relative uncertainty on the integrated lumi-

---

[8] The log-normal description ensures that the signal contribution is constrained to a reasonable range $[0, \infty)$ without the need to truncate negative values. Most importantly it avoids the problems with improper posterior distributions that arise in the limit setting procedure when a Gaussian distribution is used to describe the signal contribution (see more on this in references [113] and [115]).

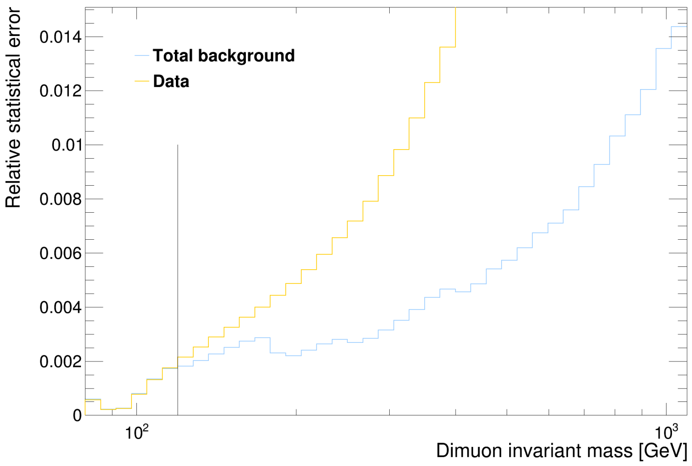

Figure 5.21: Relative statistical uncertainty on the total background estimate compared to that of the data in Run 2. The expected background is scaled to the integrated luminosity 139 fb^{-1}. The vertical line at 120 GeV indicates the lowest value of the dimuon invariant mass included in the statistical analysis.

nosity measurement.

Whenever the statistical uncertainty on the background estimate is larger than or similar in size to the "statistical uncertainty" of data, that is the square root of the number of events $\sqrt{N}$ in a given mass bin as explained in Section 5.2, it can have a non-negligible impact on the statistical analysis. As there is no correlation between the separate bins in invariant mass, one nuisance parameter θ_i must be added for each of these bins, with a corresponding relative uncertainty $\frac{(\delta b_{kl})_i}{b_{kl}} = \frac{(\delta b_{kl})_{\text{stat}}}{b_{kl}}$ for the bin while setting all other bins to $\frac{(\delta b_{kl})_i}{b_{kl}} = 0$. Figure 5.21 shows the relative statistical uncertainties on the total background estimate and on the data. The vertical line at approximately 120 GeV indicates the lowest value of the dimuon invariant mass included in the statistical analysis. We see that the two curves follow each other closely in the low-mass region, indicating that the main MC in this part of the invariant mass spectrum (Z^0 production) contains a number of events corresponding to the integrated luminosity of the whole Run 2 dataset. Above invariant mass of 120 GeV, the relative statistical uncertainty on the total MC background estimate is lower than than on the data, with the relative difference between these two increasing with dimuon invariant mass. Based on these two curves, we decided to include the statistical uncertainty of the first 20 bins (above the line at 120 GeV) as 20 separate nuisance parameters. For bin number 21, the ratio of the relative statistical uncertainty of the data to that of the total MC background estimate is approximately 0.3.

5.4.2 Discovery

We define the null hypothesis, H_0, as what is expected to be observed, i.e. the background as described by the Standard Model. This is to be tested against an alternative hypothesis, H_1, describing all the known background processes *and* a new process, the signal, within a specific model. Our chosen tool to describe an excess of events above the background expectation in data is a standard frequentist p-value calculation using the profile likelihood ratio test statistic. We define a “frequentist likelihood”, the likelihood augmented with Gaussian constraints for the nuisance parameters,

$$\mathcal{L}_{\text{freq}}(\sigma, \boldsymbol{\theta}) = \mathcal{L}(\sigma, \boldsymbol{\theta}) \prod_{i=1}^{N_{\text{sys}}} \phi(\theta_i), \tag{5.5}$$

where the likelihood $\mathcal{L}(\sigma, \boldsymbol{\theta})$ is defined in Equation (5.2), and ϕ is the standard normal PDF,

$$\phi(\theta_i | \mu_{\theta_i}, \sigma^2_{\theta_i}) = \frac{1}{\sqrt{2\pi\sigma^2_{\theta_i}}} e^{-\frac{(\theta_i - \mu_{\theta_i})^2}{2\sigma^2_{\theta_i}}}.$$

The p-value p_0 is the probability that background processes from the Standard Model fluctuate and create a signal-like excess that is equal to or greater than what is observed. The test statistic used is defined as follows:

$$q_0 = \begin{cases} 0 & \text{for } \hat{\sigma} < 0 \\ -2 \ln \left[\frac{\mathcal{L}_{\text{freq}}(0, \hat{\boldsymbol{\theta}}_0)}{\mathcal{L}_{\text{freq}}(\hat{\sigma}, \hat{\boldsymbol{\theta}})} \right] & \text{for } \hat{\sigma} \geq 0, \end{cases} \tag{5.6}$$

with $\hat{\sigma}$ and $\hat{\boldsymbol{\theta}}$ as the maximum likelihood estimates (MLEs) of $\mathcal{L}_{\text{freq}}(\sigma, \boldsymbol{\theta})$ and $\hat{\boldsymbol{\theta}}_0$ as the maximum likelihood estimates of the nuisance parameters of $\mathcal{L}_{\text{freq}}(0, \boldsymbol{\theta})$ (the best-fit values under the background-only hypothesis). Figure 5.22 illustrates the procedure for finding the MLE of the signal cross-section. Note that the nuisance parameters are simultaneously fitted to maximize the likelihood. For clarity, consider the following example: if the Z' hypothesis is *narrower* than the observed excess in data, then the nuisance parameter that represents the muon resolution can get a *smaller* value than the nominal value to gain a higher value of the likelihood. Correspondingly, if the Z' hypothesis is *wider* than the observed excess, then the nuisance parameter that represents the muon resolution can get a *higher* value than the nominal value to gain a higher value of the likelihood.

Figure 5.23 illustrates the main elements in the procedure explained in the following, ultimately leading to a plot showing local p-values against the Z' pole mass. For any dataset $\mathcal{L}_{\text{freq}}(\hat{\sigma}, \hat{\boldsymbol{\theta}})$ is greater than or equal to $\mathcal{L}_{\text{freq}}(0, \hat{\boldsymbol{\theta}}_0)$. Large excesses in data lead to a large difference between $\mathcal{L}_{\text{freq}}(0, \hat{\boldsymbol{\theta}}_0)$ and $\mathcal{L}_{\text{freq}}(\hat{\sigma}, \hat{\boldsymbol{\theta}})$, yielding a larger q_0 value.

The background-only pseudo-experiments with the “observed” count in bin l of channel k are generated according to a Poisson distribution with expectation value $b_{kl}(\hat{\boldsymbol{\theta}}_0^{\text{obs}})$. Using the definition of the test statistic (5.6) we can now build the probability distribution of the test statistic for the background-only hypothesis, $f(q_0 | 0, \hat{\boldsymbol{\theta}}_0^{\text{obs}})$.[9] Note that the recommendations of [116] are followed when evaluating the profile likelihood ratio in a pseudo-experiment, replacing $\phi(\theta_i)$ by $\phi(\theta_i - \bar{\theta}_i)$ in Equation (5.5) with $\bar{\theta}_i$ generated according to a standard normal distribution centered at $\hat{\theta}_{0,i}^{\text{obs}}$ (referenced as the “unconditional ensemble”).

---

[9] Note that the superscript “obs” means we are referring to the use of actual observed data when evaluating quantities.

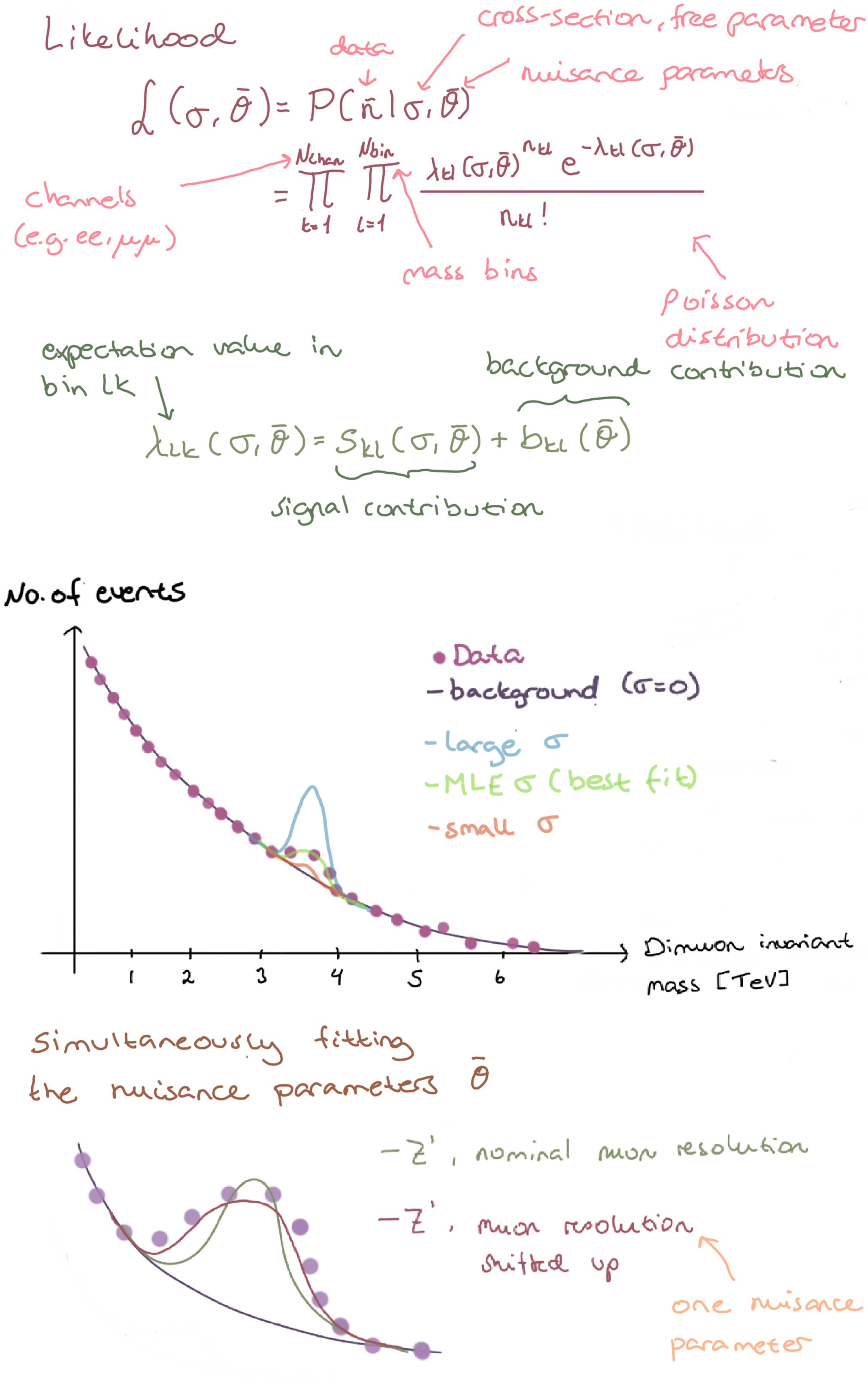

Figure 5.22: Illustration on the concept of finding the maximum likelihood estimate of the cross-section of a signal hypothesis. The nuisance parameters $\boldsymbol{\theta}$ are simultaneously fitted to maximize the likelihood $\mathcal{L}(\sigma, \boldsymbol{\theta})$.

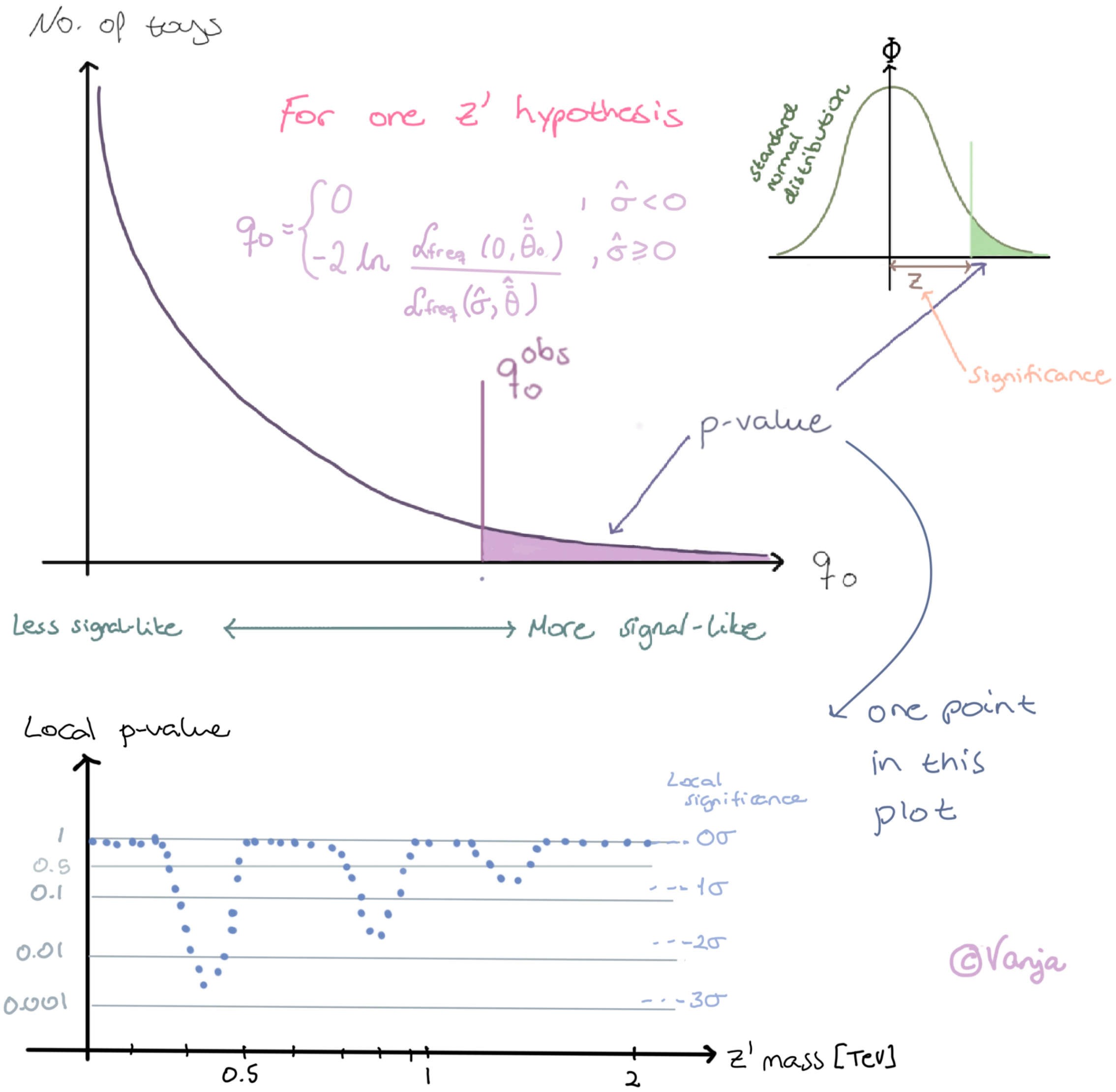

Figure 5.23: Illustration of the procedure of producing a p-value plot, from the definition of the test statistic (Equation (5.6)), via the definition of the significance, to the final plot showing the local p-values for each of the Z' pole masses in the defined signal grid.

Figure 5.24: Distribution of the test statistic q_0 (Equation (5.6)) for background-only pseudo-experiments for the most significant excess of events.

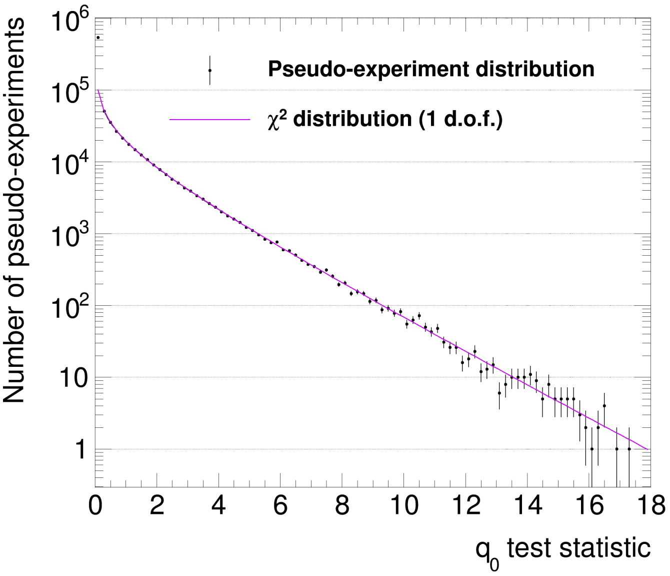

The p-value p_0 for a given observed value q_0^{obs} is calculated as

$$p_0 = P(q_0 \geq q_0^{\text{obs}} | \sigma = 0) = \int_{q_0^{\text{obs}}}^{\infty} f(q_0 | 0, \hat{\theta}_0^{\text{obs}}) dq_0. \tag{5.7}$$

The p-value can be translated into another equivalent value, the significance (Z), using the inverse of the cumulative distribution Φ of the standard normal distribution. If a Gaussian distributed variable is found Z standard deviations above its mean, then it has an upper-tail probability equal to p, thus

$$Z = \Phi^{-1}(1 - p).$$

It is a convention within the particle physics community to reject a background hypothesis – i.e. claim a "discovery" – with an observed significance of at least $Z = 5$ (often referred to as "5σ" or "5 sigma"). This corresponds to $p_0 = 2.87 \times 10^{-7}$. When excluding a signal hypothesis one usually uses a threshold p-value of 0.05, 95% confidence level, corresponding to $Z = 1.64$.

In the asymptotic limit, when the number of background events is large, the distribution of the test statistic q_0 for upwards fluctuations under the background-only hypothesis follows a χ^2 distribution with one degree of freedom (Wilk's theorem [117]). Figure 5.24 shows the distribution of the test statistic q_0 built using the pseudo-experiments and the χ^2 distribution with one degree of freedom. We see that the pseudo-experiments follow closely the χ^2 distribution, thus validating the use of the asymptotic limit in this analysis. Note that the requirement $\hat{\sigma} > 0$ in the definition of the test statistic in Equation 5.6 (i.e. not allowing the signal cross-section to be negative, which is a non-physical value) causes a peak in the distribution of the test statistic q_0 under the background-only hypothesis, at $q_0 = 0$. This peak represents the 50% of the background-only datasets that correspond to downward fluctuations. The probability p_0 is easily calculated directly from q_0 as

$$p_0 = 1 - \Phi(\sqrt{q_0}),$$

and the significance as

$$Z = \sqrt{q_0},$$

drastically reducing computing time and resources needed.

5.4.2.1 Look-elsewhere effect

When searching for a new particle, we scan a large range of masses, and the probability of an upward fluctuation located somewhere in this range increases with the number of points scanned. This increase in probability, known as the look-elsewhere effect (LEE), must be quantified. The description above regarding the p-value p_0 (Equation (5.7)) is the *local* p-value and corresponding significance. Taking the look-elsewhere effect into account, we get a new p-value, the *global* p-value and a global significance.

The global significance is evaluated by generating background-only pseudo-experiments using the best-fit values of the nuisance parameters. For each of the pseudo-experiments the whole Z' scan is performed and the highest local significance is noted, building up the probability density function $f(Z)$. By using the distribution of the highest local significances and the relation

$$p_{\text{global}} = \int_{Z}^{\infty} f(Z)dZ \tag{5.8}$$

between global p-value p_{global}, the highest local significance Z and the distribution $f(Z)$, we extract p_{global} for a given highest local significance Z. A local significance at the median of $f(Z)$ (i.e. $p_{\text{global}} = 0.5$) denotes the point where the global significance is zero. Lower values of the highest local significance yield negative global significances.

5.4.2.2 Results

Figure 5.25 displays the observed local p-values for the Z' search for three selected signal models – Z'_χ, Z'_ψ and Z'_{SSM}, starting at signal masses of 150 GeV. The most significant excess is at 271 GeV with a local significance of 1.7σ for all three signal models. Looking at the dimuon invariant mass distribution after the signal selection, in Figure 5.5, we see a slight excess above the trend in the data over MC ratio panel at the bottom. Using the information from Section 5.4.2.1 regarding the look-elsewhere effect, the distribution of the highest local significances for the background-only hypothesis is built, as shown in Figure 5.26. We see that the most probable value is around 2σ, which means that the observed significance of 1.7σ is actually a small downward fluctuation. Figure 5.27 shows the conversion curve between maximum local significance and global significance, calculated using the distribution of the highest local significances for the background-only hypothesis and Equation (5.8). This tells us that a local significance of 1.7σ corresponds to a global significance of -1.0σ.

5.4.3 Exclusion limits

The framework for exclusion limits is built upon Bayesian statistics. Figure 5.28 summarizes the method leading to the exclusion plots. According to Bayes' theorem the posterior

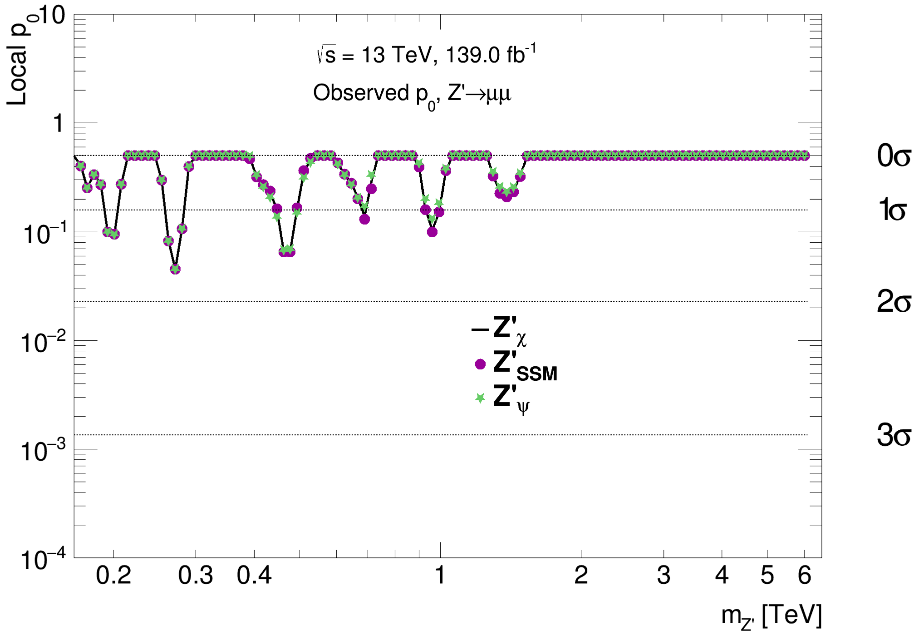

Figure 5.25: Local p-values for Z'_χ signals between 150 GeV and 2 TeV for the three models Z'_χ, Z'_{SSM} and Z'_ψ. The local p-value beyond 2 TeV is 0.5. The Z'_ψ is the model with the smallest width and Z'_{SSM} the one with the largest width. The corresponding significance levels are shown as horizontal dashed lines.

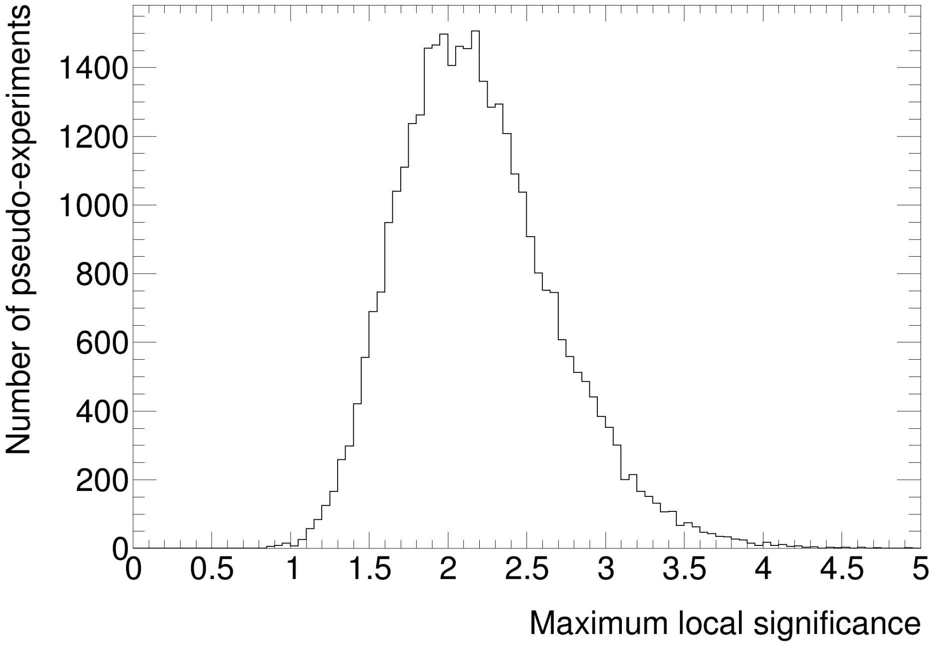

Figure 5.26: Distribution of the highest local significances for the background-only hypothesis, using the best-fit values of the nuisance parameters.

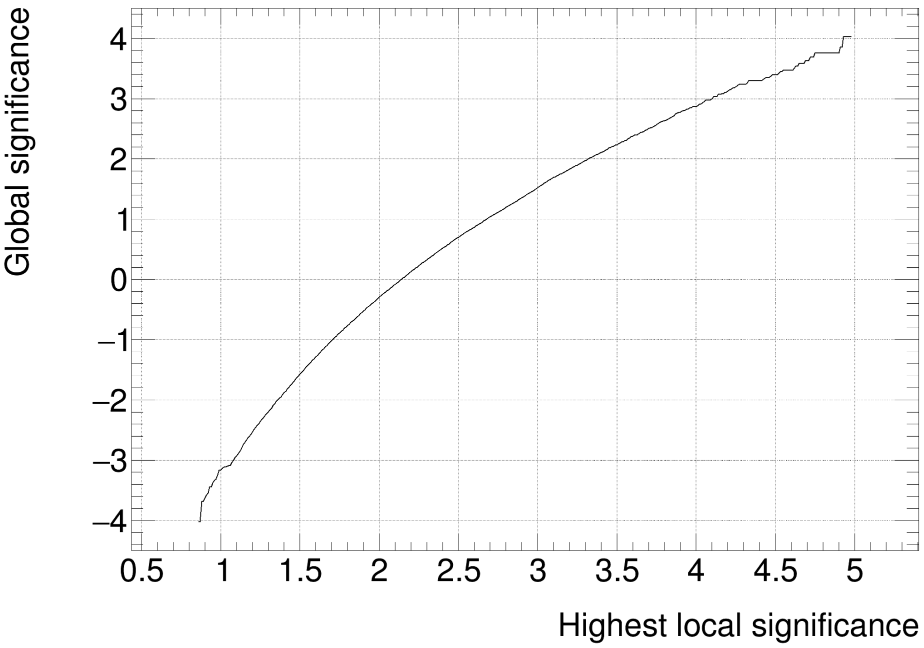

Figure 5.27: Conversion curve between maximum local significance and global significance, calculated using the distribution of the highest local significances for the background-only hypothesis and Equation (5.8).

probability $p(\sigma, \boldsymbol{\theta}|\boldsymbol{n})$ is proportional to the likelihood multiplied by a prior:

$$p(\sigma, \boldsymbol{\theta}|\boldsymbol{n}) = \frac{P(\boldsymbol{n}|\sigma, \boldsymbol{\theta})p(\sigma, \boldsymbol{\theta})}{P(\boldsymbol{n})}.$$

$p(\sigma, \boldsymbol{\theta})$ denotes the joint prior probability density for the signal cross-section σ and the nuisance parameters $\boldsymbol{\theta}$. The probability for the observed data $P(\boldsymbol{n})$ merely acts as a normalization constant. We assume a product form for the joint prior distribution $p(\sigma, \boldsymbol{\theta})$, with a Gaussian description of the prior probability distribution of the nuisance parameters,

$$p(\sigma, \boldsymbol{\theta}) = p(\sigma) \prod_{i=1}^{N_{\text{sys}}} \phi(\theta_i),$$

where ϕ denotes the standard normal probability distribution function and $p(\sigma)$ is the prior distribution of the cross-section. For $p(\sigma)$ we use a flat distribution, i.e. zero for $\sigma < 0$ and constant for $\sigma \geq 0$, thus also this distribution is absorbed into the normalization constant. Now we can marginalize $p(\sigma, \boldsymbol{\theta}|\boldsymbol{n})$ to get the posterior distribution for σ,

$$p(\sigma|n) = \int p(\sigma, \boldsymbol{\theta}|\boldsymbol{n}) d\boldsymbol{\theta} = N \int \prod_{k=1}^{N_{\text{chan}}} \prod_{l=1}^{N_{\text{bin}}} \frac{\lambda_{kl}(\sigma, \boldsymbol{\theta})^{n_{kl}} e^{-\lambda_{kl}(\sigma, \boldsymbol{\theta})}}{n_{kl}!} \prod_{i=1}^{N_{\text{sys}}} \phi(\theta_i) d\boldsymbol{\theta},$$

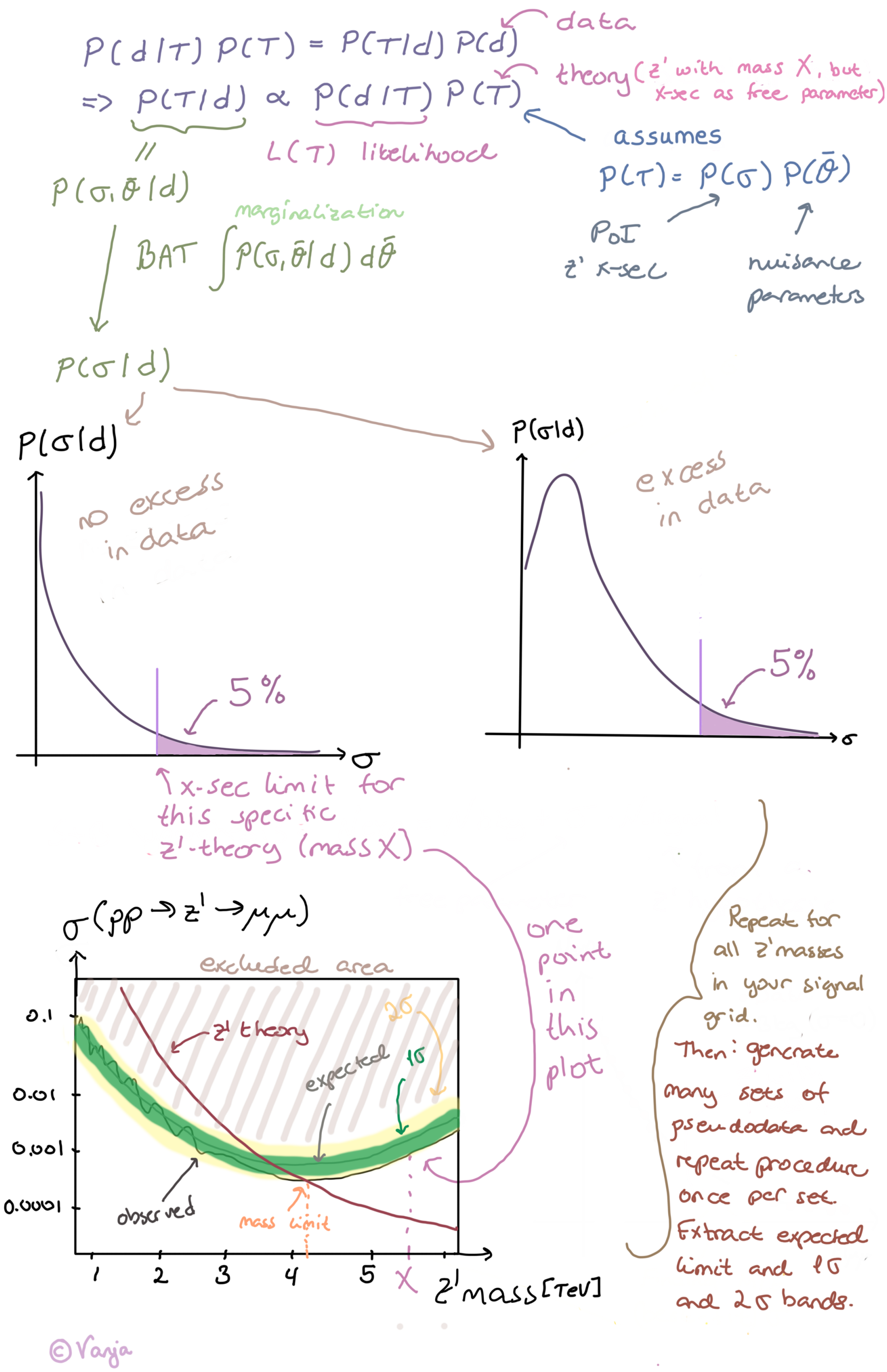

Figure 5.28: Illustration of the exclusion limit setting process, from Bayes' theorem, via BAT and marginalization to the posterior distribution and the cross-section limit plot.

where N is the normalization constant fulfilling the condition

$$\int_0^\infty p(\sigma|\boldsymbol{n})d\sigma = 1.$$

The marginalization is performed using Markov Chain Monte Carlo sampling in the Bayesian Analysis Toolkit (BAT)[118].[10]

The upper cross-section limit σ_{up} at credibility level (CL) $1-\delta$ is defined as the cross-section above which the posterior probability is δ, with

$$\int_{\sigma_{\mathrm{up}}}^\infty p(\sigma|\boldsymbol{n})d\sigma = \delta.$$

As mentioned before, in high-energy particle physics it is customary to exclude at 95% CL.

To obtain expected limits and the 68% and 95% quantiles (1σ and 2σ bands), the procedure described in this section is repeated for pseudodata. For one pseudo-experiment sample values for all the nuisance parameters are drawn according to their Gaussian prior distributions, and an "observed" event count in bin l of channel k is drawn according to the Poisson distribution with expectation value $b_{kl}(\boldsymbol{\theta})$. The pseudodata is treated as the real data, and the cross-section limits are calculated as above. After repeating this a large number of times (about 950 times to be more exact), the expected limit (the median of the cross-section limit distributions) is extracted, together with the 1σ and 2σ bands (green and yellow bands respectively).

5.4.3.1 Results - Z' cross-section and mass limits

In Figure 5.29 we see the result of the statistical procedure as described in this section. The cross-section limits for the $Z' \to \mu^+\mu^-$ are presented, and we can extract the mass limit by using the relationship between the Z' cross-section and pole mass. Table 5.4 summarizes the result.

Model	m'_Z lower limit [TeV]	
	Expected	Observed
Z'_ψ	3.7	3.8
Z'_χ	4.0	4.1
Z'_{SSM}	4.3	4.4

Table 5.4: Expected and observed lower mass limits on the Z'.

5.4.4 Post-fit background estimates

After running the statistical analysis, we can extract a "post-fit" estimate of the SM background, that is the expected background for the background-only hypothesis, after adjusting the nuisance parameters to their most likely values as calculated in the statistical analysis.

---

[10] BAT is a software package, implemented in C++ and interfaced with ROOT, that contains routines to aid in statistical analyses. In the heart of BAT lies Bayes' Theorem.

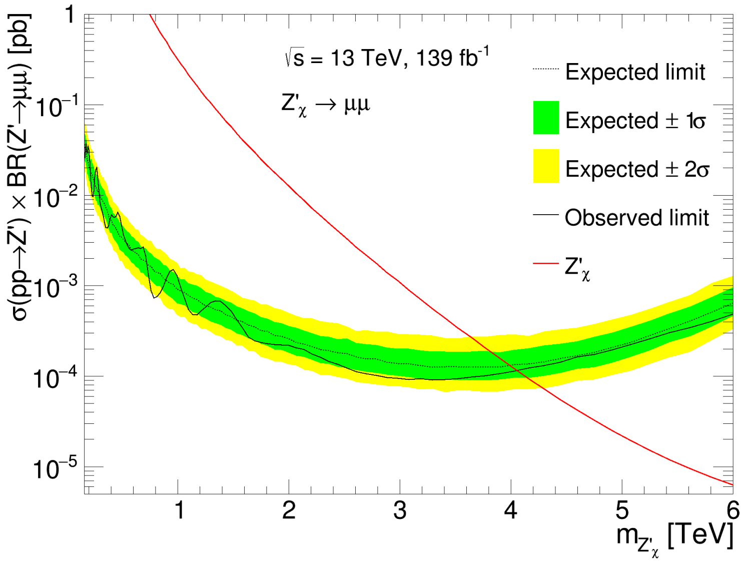

(a) Z'_χ

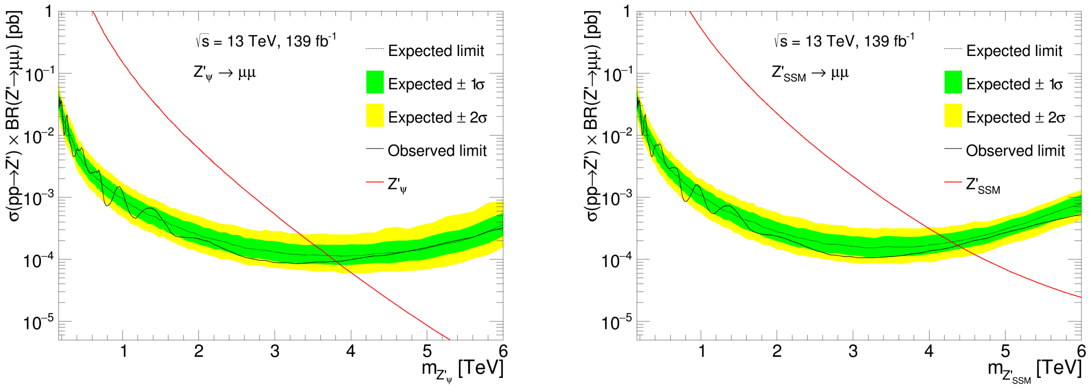

(b) Z'_ψ

(c) Z'_{SSM}

Figure 5.29: Expected and observed limits on the Z' production cross-section × branching ratio into $\mu^+\mu^-$ as a function of the Z' pole mass, m'_Z. The shaded bands correspond to the 68% (1 standard deviation) and 95% (2 standard deviations) quantiles for the expected limits.

Figure 5.30 shows the ratio of the raw (pre-fit) background to the data (black points) and the post-fit background to the data (red points). Figure 5.31 shows the dimuon invariant mass distribution above 120 GeV[11], with the ratio of data to the pre-fit background estimate in the middle panel, and the ratio of data to the post-fit background estimate in the lower panel. We see that the trend from the pre-fit background, showing lower values of the data over MC ratio for higher values of the dimuon invariant mass, is now gone. This is interpreted as a confirmation that we have included the necessary nuisance parameters to the statistical analysis.

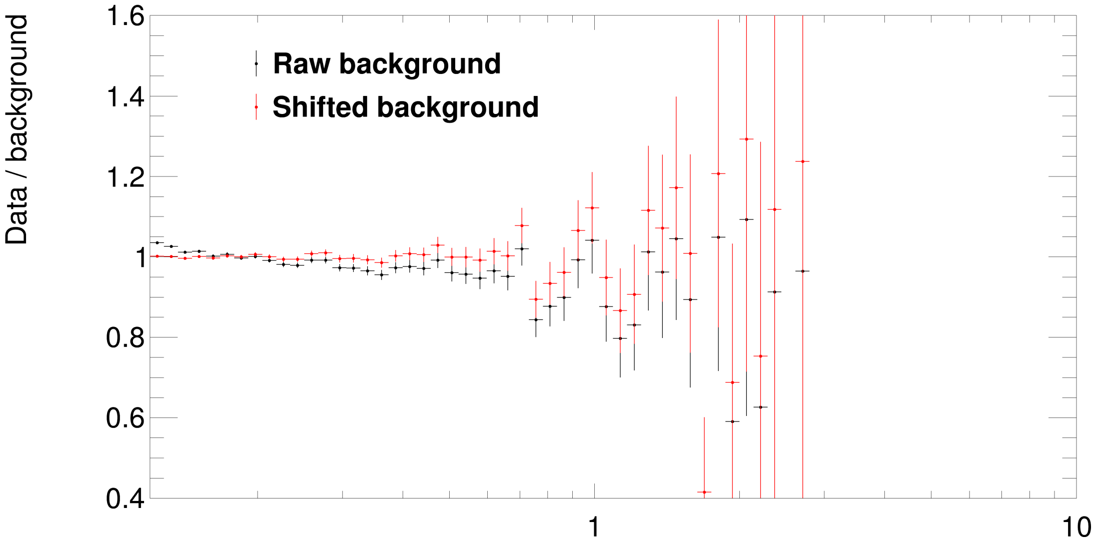

Figure 5.30: Data over MC ratio for the raw (pre-fit) and post-fit background estimates.

5.4.4.1 Nuisance parameter pulls

We now compute the nuisance parameter pulls introduced in producing the post-fit background estimate for the background-only hypothesis. Figure 5.32 shows the pulls with the corresponding uncertainties of all the systematic uncertainties considered in the analysis. Two different methods are used to extract the pulls and the uncertainties, both as the mean and standard deviation of the marginalized posterior distribution, and as the smallest 68% confidence interval and corresponding local mode. We see that the most influential nuisance parameters in this analysis are the “DY α_s” (variations in the strong coupling constant, explained in Section 5.3.2), “PDF Variation 6” (one of the 7 bundled variations on the CT14 NNLO PDF, also explained in Section 5.3.2), and “MC stat bin3” (one of the 20 nuisance parameters representing the statistical uncertainty on the background estimate in a single dimuon invariant mass bin, as described at the end of Section 5.4.1). None of them are pulled far from their a priori expectation, which serves as a sanity check for the statistical analysis.

---

[11] The two upper panels are identical to the panels in Figure 5.5, except that they do not include the masses between 80 GeV and 120 GeV and above 6 TeV. The lowest invariant mass included in the statistical analysis is 120 GeV.

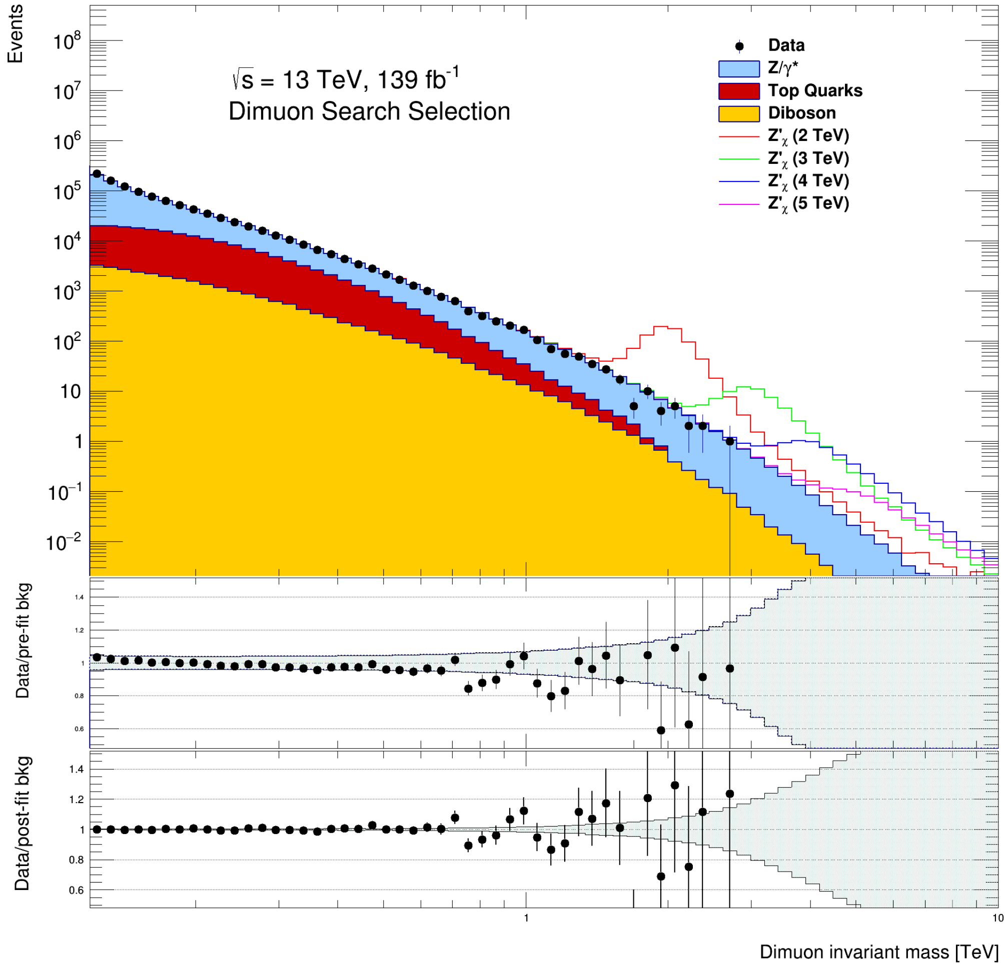

Figure 5.31: The upper panel shows the dimuon invariant mass distribution above 120 GeV, the middle panel shows the rato of data to the pre-fit background estimate, and the lower panel shows the rato of data to the post-fit background estimate.

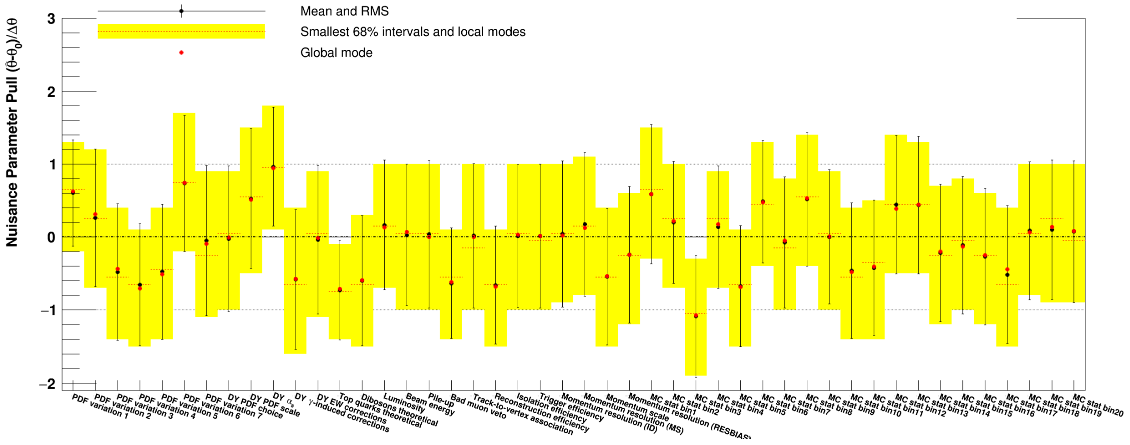

Figure 5.32: Nuisance parameter pulls introduced in the production of the post-fit background estimate for the background-only hypothesis as shown in Section 5.4.4.

5.4.4.2 Diagnostics plots

In Figure 5.33 we see the fits for the evaluation of the significance of the largest local excess, at dimuon invariant mass 271 GeV. The fits and the data points are shown relative to the background prediction evaluated with the nuisance parameter values of the signal-plus-background hypothesis (“best fit background (s+b)”).

The red curve is the ratio of the raw (pre-fit) background to the best fit background (s+b), and we see the same pattern as we saw in Figure 5.30, namely that the post-fit background pulls the data over MC ratio much closer to 1 than for the raw background[12], which is as expected.

The green line is the background prediction evaluated with the nuisance parameter values of the background-only hypothesis, and the magenta line is the best fit signal-plus-background prediction. We see that the magenta line reproduces the excess at 271 GeV. The green line is pulled somewhat upwards, but is unable to describe the excess adequately.

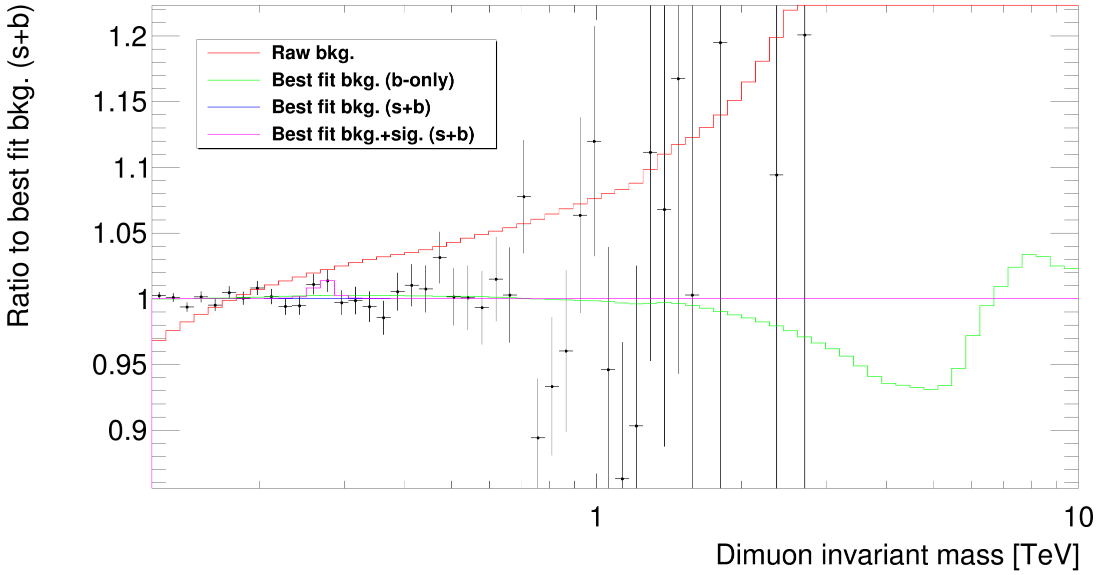

Figure 5.33: Fits for the evaluation of the significance of the largest local excess. Note that this plot displays the fits and the data points relative to the background prediction evaluated with the nuisance parameter values of the signal-plus-background hypothesis (“best fit background (s+b)”), which means the blue line is exactly equal to 1 over the whole mass range.

5.4.5 Effect of the bad muon veto systematic uncertainty

From Section 5.3 regarding the systematic uncertainties, and specifically Figure 5.19 showing how the experimental signal systematic uncertainties affect a 2 TeV and a 4 TeV Z', we suspect that the bad muon veto systematic uncertainty has a heavy impact on the exclusion

---

[12] Keep in mind that Figure 5.30 displays the ratio of data over MC and therefore the line representing the raw background has values above 1 for low masses, while Figure 5.33 displays the raw background divided by the post-fit background for the signal-plus-background hypothesis and therefore has a value below 1 at low dimuon invariant masses.

limits. Note that e.g. the systematic uncertainty on the muon momentum resolution does not have an equal impact, even if it is larger than the uncertainty on the bad muon veto, as the former will only affect the width of the resonance while the latter has the effect that it scales the resonance up or down. In this analysis, it scales the resonance down, as there is no excess in data.

In Figure 5.34 we see the asimov[13] (left) and observed exclusion (right) limits for the Z'_χ signal hypothesis with all the systematic uncertainties included (the nominal case, black line) compared to several cases: without any of the signal systematic uncertainties (green line), without the bad muon veto systematic uncertainty (blue line), with the bad muon veto systematic uncertainty decoupled for signal and background (orange line) and without the bad muon veto signal systematic uncertainty (magenta line). For the asimov limit, also the case where no systematics at all are taken into account (violet line). The bottom figures show the ratio of the various cases to the nominal line with all systematic uncertainties included, for the asimov dataset and the observed data. Looking at the asimov case, we conclude from these lines that the signal bad muon veto systematic uncertainty affects the cross-section limits considerably. If we now turn the attention to the observed limits, we see that in data the limit is stronger than expected in the case where the signal and background bad muon veto systematic uncertainties are decoupled, which means that when taking observed data into account, the correlation between the nuisance parameters that represents the bad muon veto systematic uncertainties for the signal and background has an impact on the cross-section limit.

The bad muon veto systematic uncertainty has been updated since this analysis was performed. As explained in Section 5.1.2, the bad muon veto relies on the relative q/p error on the combined track fit as a function of the muon transverse momentum. Figure 5.35 shows the systematic uncertainty on the bad muon veto criterion [119] as computed for an early Run 2 dataset (blue), corresponding to 36 fb^{-1}, and for the full Run 2 dataset (red), corresponding to $139\ \text{fb}^{-1}$. The dotted blue curve represents the extrapolation of the fitted curve at values of transverse momentum above 3 TeV. At the time when this analysis was performed, the blue curve was in use. The updated bad muon veto systematic uncertainty would presumably have a non-negligible impact on the cross-section limits obtained, in the direction of increasing mass limits.

5.5 Comparison to the published results from the dilepton group

The most recent publication from the dilepton group was published early in 2019 and was in fact the first publication from the ATLAS collaboration with the whole Run 2 dataset [120] [100]. Details of the analysis can be read in the publication, but a summary is provided below.

My contribution to this last round of published results was to run the traditional MC-based analysis in parallel to the new data-driven analysis. The dilepton group made data to MC comparison plots, without systematic uncertainties, to validate the use of MC in the

---

[13] I.e. calculating the "observed" limit using the background expectation as the asimov dataset. This procedure generates the expected limit.

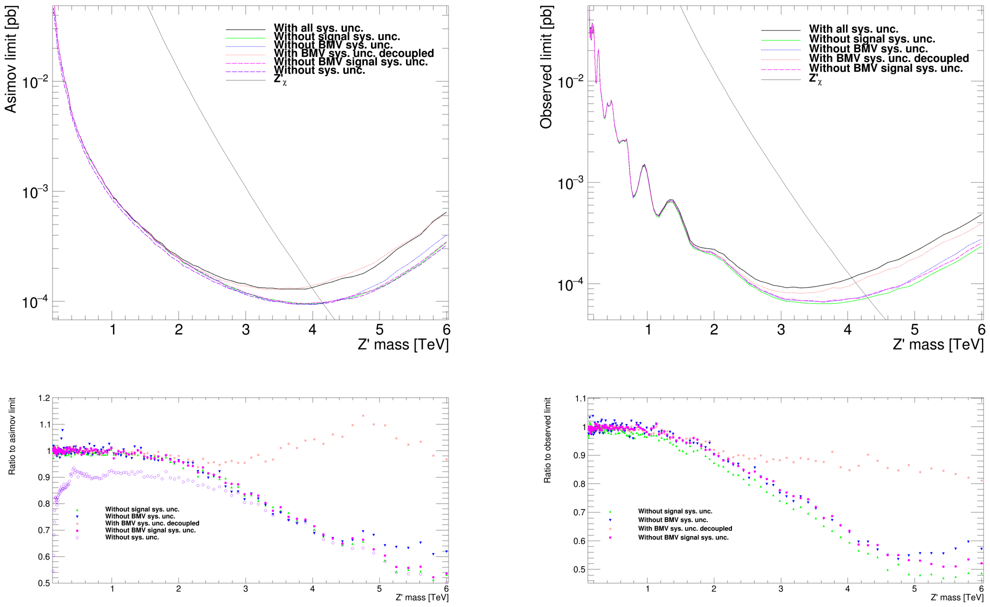

Figure 5.34: Top: The asimov (left) and observed (right) exclusion limit for the Z'_χ signal hypothesis with all the systematic uncertainties included (black line) compared to several cases: without any of the signal systematic uncertainties (green line), without the bad muon veto systematic uncertainty (blue line), with the bad muon veto systematic uncertainty decoupled for signal and background (orange line) and without the bad muon veto signal systematic uncertainty (magenta line). For the asimov limit, also the case where no systematics at all are taken into account (violet line). Bottom: the ratio of the various cases to the nominal line with all systematic uncertainties included, for the asimov dataset (left) and the observed data (right).

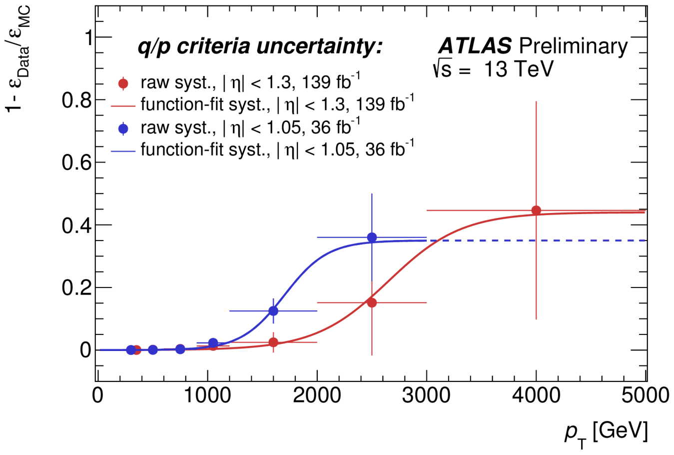

Figure 5.35: The systematic uncertainty on the bad muon veto criterion [119] as computed for an early Run 2 dataset (blue), corresponding to $36\ \mathrm{fb}^{-1}$, and for the full Run 2 dataset (red), corresponding to $139\ \mathrm{fb}^{-1}$.

analysis, e.g. the optimization of the data-driven fit strategies. This could be compared to my corresponding plots with full systematics, and produced on a completely independent framework. More about this is discussed in Section 5.5.2. I also ran the full statistical framwork enabling the comparison of two independent results for the discovery statistics, to be discussed in Section 5.5.3.1, and the exclusion limits, to be discussed in Section 5.5.3.2. The comparison of independently produced results are always important, and even more so when the whole anlaysis strategy is completely new.

5.5.1 Data-driven analysis strategy

Since the previous dilepton paper, published around fall 2017 with the 2015-2016 (~36 fb^{-1}) dataset [23], there has been a shift in analysis strategy, going from the traditional MC based analysis to a data-driven one. The reason for this change is primarily caused by the increasing amount of MC events needed to keep the statistical uncertainty on the background estimate low[14] compared to the statistical uncertainty on data. Figure 5.36 displays binned ratio of statistical errors between MC and data as a function of the dimuon mass for the 36 fb^{-1} publication. The situation is bound to get worse as the amount of data incrases, and the computational resources needed increases beyond what is feasible. The status for the full Run 2 dataset was shown earlier in Figure 5.21.

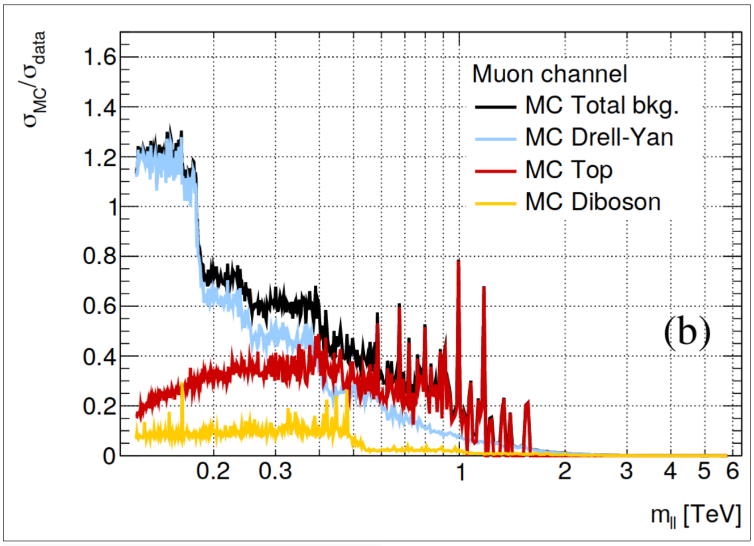

Figure 5.36: The binned ratio of statistical errors between MC and data as function of the dimuon mass for the 36 fb^{-1} publication [100].

5.5.2 Event selection and data distributions

The dimuon event selection follows closely the selection as described in reference [23] (which is also the case for the analysis described in Section 5.1). The search for a resonant signal is performed by fitting the dimuon invariant mass distribution, using a fit function that consists of a smooth functional form for the background and a generic signal shape. The smooth functional form for the background and the associated uncertainties are based on a MC background template. To minimize the statistical uncertainty on this procedure, the

---

[14] A rule of thumb is that the statistical uncertainty of the MC should be smaller than 20% of the statistical uncertainty on data [100].

background template for DY is produced from a sample with a very large number of events at generator level only. The sample is then smeared by the experimental dimuon mass resolution. The backgrounds from top quarks and diboson events are taken into account in a similar way. To select the background functional form, several fits to the dimuon mass background template are performed.

The distribution of the dimuon invariant mass for events passing the full event selection is shown in Figure 5.37.

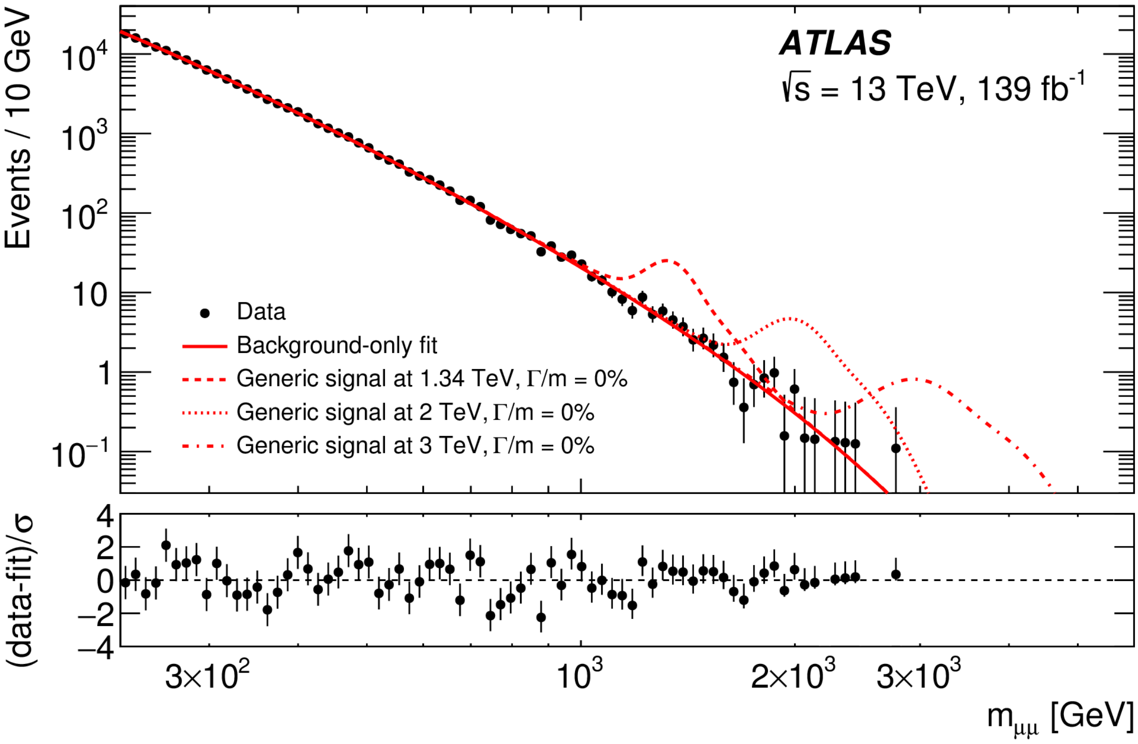

Figure 5.37: Published results using the full Run 2 dataset [120]. Distribution of the dimuon invariant mass for events passing the full event selection. Generic zero-width signal shapes ($\Gamma/m = 0\%$), scaled to 20 times the value of the corresponding expected upper limit at 95% CL on the fiducial cross-section times branching ratio, with pole masses of 1.34 TeV, 2 TeV and 3 TeV and a background-only fit are superimposed. The error bars indicate statistical uncertainties only. The bottom panel shows the differences between data and the fit results in units of standard deviations of the statistical uncertainty.

Figure 5.38(a) illustrates the level of data/MC agreement in the results from the dilepton group. The plot shows only statistical uncertainties. The diboson MC sample for the mc16e campaign were still under production at the time that the results were published, and the mc16d MC samples are overnormalized to account for the sum of the 2017 and 2018 integrated luminosity. Simulated data are not used to estimate the background processes, but it *is* used for optimization of the data-driven fit strategies, and also to determine the spurious signal[15] uncertainties. The corresponding results from the analysis performed in this thesis work is shown in Figure 5.38(b). Be aware that the first bin in invariant mass in (b) is the

---

[15] A spurious signal is the identification of a signal when none is present.

second bin in invariant mass in (a), and that the uncertainty on the data points are defined differently in the two cases. Comparing the two plots, we note a few differences. There is a small trend in the data over MC ratio visible in both plots, but the plot in (a) seems to be shifted upward by a few percent compared to the plot in (b). At high mass it becomes apparent that there are some differences in the top quark MC, probably caused by differences in the amount of events in the simulated top quark data. The data points in the high-mass tail seem to be identical, but there are differences in the data over MC ratio stemming from some small differences in the MC. Overall, the two results seem to be compatible.

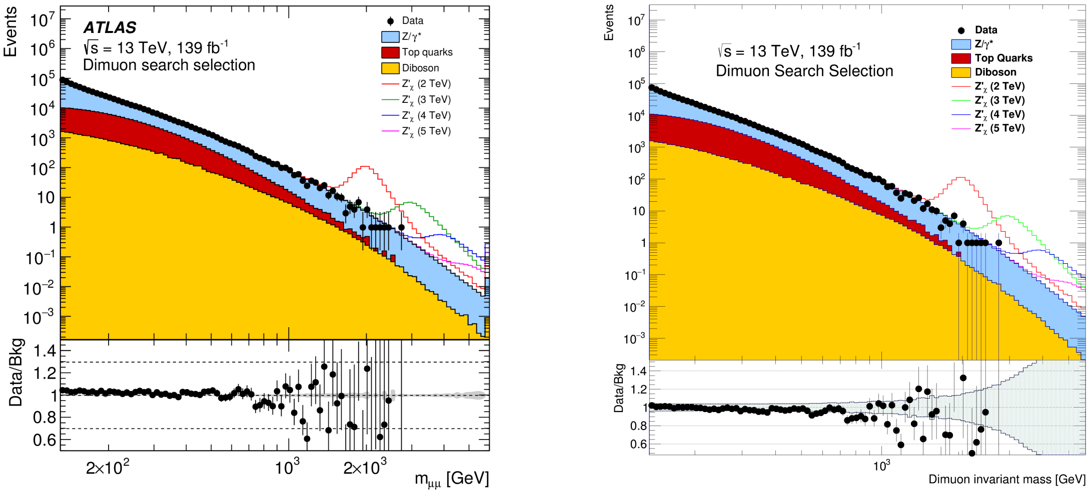

(a) Results from reference [100].

(b) Analysis performed in this thesis work.

Figure 5.38: Invariant mass distribution for the dimuon selection. Results from the dilepton group using the full Run 2 dataset is shown in (a), and the results from the analysis described in Sections 5.1 and 5.2 is shown in (b). The bottom panel shows the data/MC ratio. In (a) the plots show only uncertainties due to the limited amount of data and MC available, while in (b) the full set of systematic uncertainties are accounted for.

5.5.3 Statistical analysis

5.5.3.1 Discovery

The statistical analysis follows closely the procedure described in Section 5.4.2, with the exception that the test statistic q_0, previously defined in Equation (5.6), is modified.The new q_0 is defined as

$$q_0 = \begin{cases} +2\ln\left[\frac{\mathcal{L}_{\text{freq}}(0,\hat{\hat{\boldsymbol{\theta}}}_0)}{\mathcal{L}_{\text{freq}}(\hat{\sigma},\hat{\boldsymbol{\theta}})}\right] & \text{for } \hat{\sigma} < 0 \\ -2\ln\left[\frac{\mathcal{L}_{\text{freq}}(0,\hat{\hat{\boldsymbol{\theta}}}_0)}{\mathcal{L}_{\text{freq}}(\hat{\sigma},\hat{\boldsymbol{\theta}})}\right] & \text{for } \hat{\sigma} \geq 0. \end{cases} \tag{5.9}$$

This allows for quantification of negative fluctuations. Local p-values computed with this modified test statistic are called *un-capped p-values* and the ones calculated with the original definition of the test statistic are called *capped p-values* since they are always below 0.5. Figure 5.39 shows the observed local p-values for generic $\Gamma/M = 0\%$, $\Gamma/M = 1\%$ and $\Gamma/M = 3\%$ signals as a function of the signal pole mass (denoted m_X or $M_{Z'}$). Note that this plot includes also the dielectron and combined dilepton channels in addition to the dimuon channel (green dashed line). We can compare this to Figure 5.25. Looking past the large variations due to differences in signal mass spacing and the use of capped versus uncapped p-values, it seems both analyses display the same basic shapes with four small excesses below a signal mass of 1 TeV, and no large excesses above the expectation from the Standard Model. The largest fluctuation in the published analysis is at a signal mass of 267 GeV, with a local significance of 2.4 σ and a global significance of 0.3 σ for an intrinsic signal width assumption of $\Gamma/M = 0\%$, which is compatible with the background-only hypothesis. This is comparable to the result discussed in Section 5.4.2.2 regarding the results of the analysis performed in this thesis work, with the most significant excess at 271 GeV, with a local significance of 1.7σ.

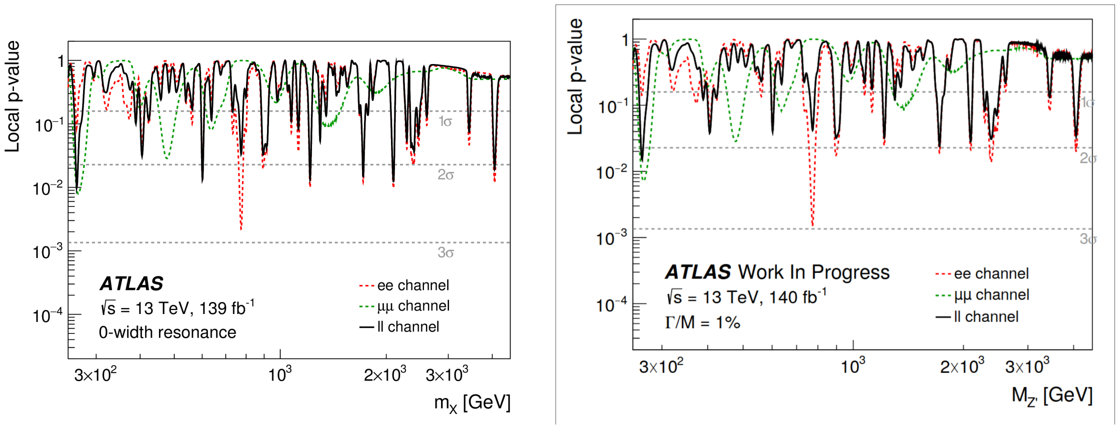

(a) Signal width assumption of $\Gamma/M = 0\%$ (b) Signal width assumption of $\Gamma/M = 1\%$l

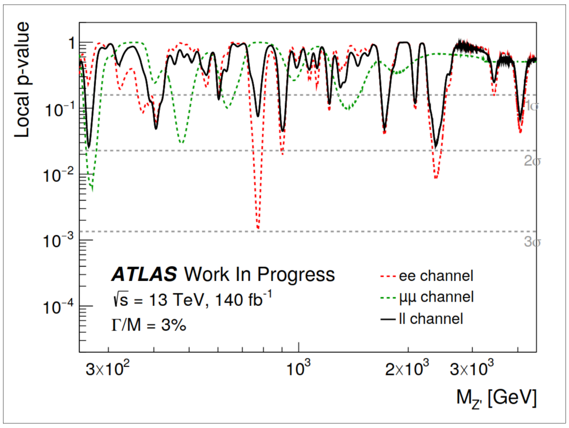

(c) Signal width assumption of $\Gamma/M = 3\%$

Figure 5.39: Results from the ATLAS Collaboration: Observed p-value scans of deviations from the background-only hypothesis as a function of the Z' signal pole mass m_X for a signal width assumption of $\Gamma/M = 0\%$ (a),$\Gamma/M = 1\%$ (b) and $\Gamma/M = 3\%$ (c) for the full Run 2 dataset [100]. All experimental uncertainties and the spurious signal uncertainty are taken into account. Note that both the dielectron (red dashed line) and dilepton (black solid line) channels are shown in addition to the dimuon channel (dashed green line).

5.5.3.2 Exclusion limits

The framework for exclusion was also changed as the analysis strategy went from MC-based analysis to data-driven analysis. The published analysis uses a framework based on RooFit [121] and RooStats [122]. RooStats is based on Frequentist statistics, but no significant differences between the Bayesian and Frequentist approaches are expected [123].

The generic cross-section limit in the dimuon channel is given in Figure 5.40 for various generic models with relative widths from 0% to 10%, with theoretical cross-sections for Z'_χ and Z'_ψ in (a), and for Z'_{SSM} in (b). The lower limits on the mass of the Z'_ψ, Z'_χ and Z'_{SSM} are listed in Table 5.5, together with the lower mass limits calculated in this thesis work. The lower mass limits on all three models are approximately equal in the thesis work compared to the published analysis, with the largest difference for the expected lower mass limit for the Z'_ψ, where the published limit is 0.3 TeV higher than what is found in this thesis work. We do however note that as found in Section 5.4.5, the bad muon veto systematic uncertainty has a larg impact on the cross-section limits. In the supporting information behind the dilepton search publication [100], the effect of the systematic uncertainties on the cross-section exclusion limits were studied, and were found to be of the order of maximum 25% at high signal masses, most prominently above 2-3 TeV, and less than 10% at lower masses. It was noted that this increase at high signal masses was due to the bad muon veto systematic uncertainty. This is a smaller effect than what is shown in Figure 5.34, where we see that the ratio of the asimov exclusion limits without any systematic uncertainties to the nominal exclusion limits (magenta open circles) also go above 10% beyond signal masses of 2-3 TeV, but then go as high as 45%-50% at the highest signal masses. We note that this explains the somewhat smaller lower signal mass limits found in this thesis work.

Model	Lower limits on $M_{Z'}$ [TeV]			
	Published results		Thesis work results	
	Expected	Observed	Expected	Observed
Z'_ψ	4.0	4.0	3.7	3.8
Z'_χ	4.2	4.2	4.0	4.1
Z'_{SSM}	4.5	4.5	4.3	4.5

Table 5.5: Lower limit on the mass of the Z'_ψ, Z'_χ and Z'_{SSM} in the dimuon channel as calculated in the published ATLAS results [120] and as calculated in this thesis work as reported in Table 5.4.

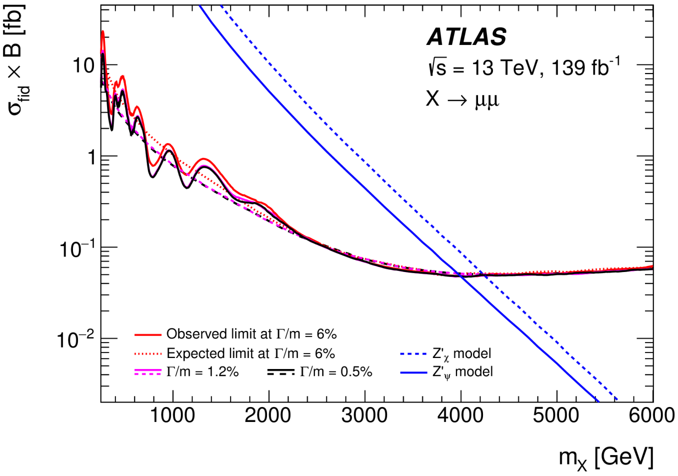

(a) Upper limits set at 95% C.L. on the fiducial cross-section times branching ratio as a function of the pole mass for signals with 0.5%, 1.2% and 6% relative width for the dimuon channel. The theoretical cross-sections for the Z'_χ and Z'_ψ in the fiducial region is also shown.

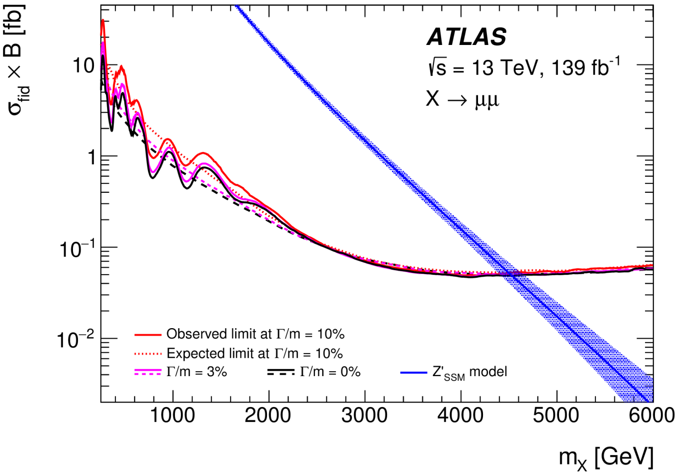

(b) Upper limits set at 95% C.L. on the fiducial cross-section times branching ratio as a function of the pole mass for signals with 0%, 3% and 10% relative width for the dimuon channel. The theoretical cross-section for the Z'_{SSM} in the fiducial region is also shown, with the signal theoretical uncertainties shown as a band (only shown for illustration purposes, the uncertainty on the signal is not included in the limit calculation).

Figure 5.40: Results from the ATLAS Collaboration: Expected and observed limits on the generic signal production cross-section times branching ratio into $\mu^+\mu^-$ [120]. All experimental uncertainties and the spurious signal uncertainty are taken into account. Observed limits are shown as a solid line and expected limits as dashed or dotted lines.

5.6 Results from the CMS Collaboration

Results from the CMS Collaboration were published in the fall of 2019 [124]. The interested reader is referred to the publication for a review of the analysis strategy. We will only briefly describe the results here, focusing on the dimuon channel only.

The publication uses the full dataset recorded at $\sqrt{s}$ =13 TeV during the years 2016 to 2018, corresponding to 140 fb^{-1} in the dimuon channel, searching for deviations from the SM expectation in the dimuon invariant mass spectrum. The SM expectations are taken from simulation, except for backgrounds that contain non-prompt leptons, which are estimated using data-driven methods. The background expectation is normalized to the observed data yields in a mass window around the Z boson peak, between 60 and 120 GeV. The dimuon invariant mass distribution is shown in Figure 5.41. There is good agreement between the data yields and the expected background.

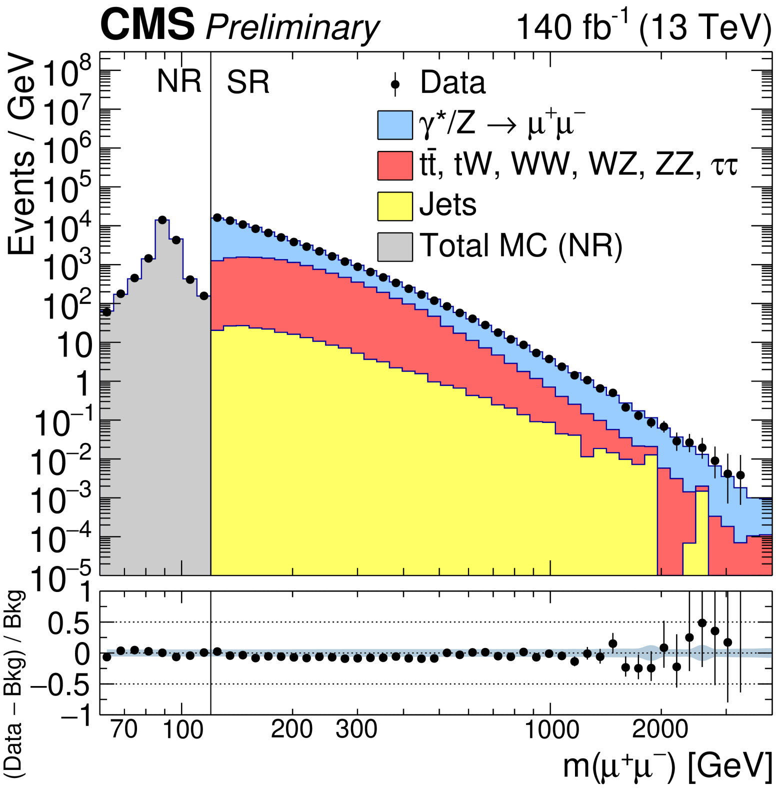

Figure 5.41: Results from the CMS Collaboration: The dimuon invariant mass distribution using the full dataset recorded between 2016 and 2018, showing data in black dots with statistical error bars and the expected SM background as stacked, filled histograms [124]. For the region below an invariant mass of 120 GeV (the normalization region (NR)), a prescaled trigger with a low p_T threshold (27 GeV) was used to collect events. For events in the signal region (SR), at masses above 120 GeV, an unprescaled muon trigger was used, triggering on single muon with p_T>50 GeV and $|\eta| < 2.4$. In the bottom panel, the ratio of the data yields after background subtraction to the background yields is shown, with the blue band representing the various statistical and systematic uncertainties on the background.

The exclusion limits are calculated at 95% C.L. using Bayesian techniques. Figure 5.42 shows the exclusion limits for a narrow resonance with an instrinsic width of 0.6% of the resonance mass, also displaying theoretical predictions for the Z'_{SSM} and Z'_{ψ} resonances. The expected and observed lower mass limits for the Z'_{χ} and Z'_{SSM} are shown in Table 5.6. Comparing to Table 5.5, we see that the exclusion limits from the CMS Collaboration are somewhat higher than the published limits from ATLAS, but still comparable in size.

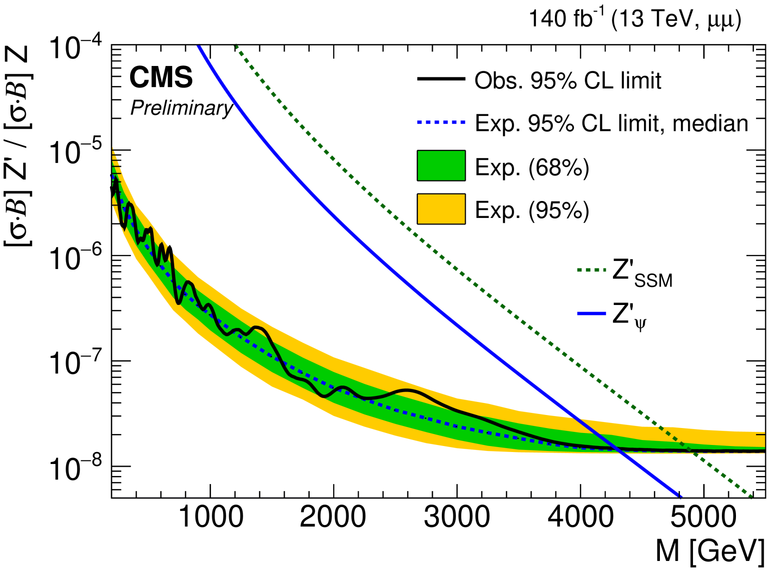

Figure 5.42: Results from the CMS Collaboration: Upper exclusion limits in the dimuon channel set at 95% C.L. on the product of the production cross-section and the branching fraction for a spin-1 resonance with at width equal to 0.6% of the resonance mass relative to the product of the production cross-section and branching fraction of the Z boson [124]. The shaded bands correspond to the 68% and 95% quantiles for the expected limits. Theoretical predictions for the Z'_{SSM} and Z'_{ψ} resonances are shown for comparison.

Channel	Z'_{SSM}		Z'_{ψ}	
	Obs. [TeV]	Exp. [TeV]	Obs. [TeV]	Exp. [TeV]
ee	4.72	4.72	4.11	4.13
$\mu^+\mu^-$	4.89	4.90	4.29	4.30
ee + $\mu^+\mu^-$	5.15	5.14	4.56	4.55

Table 5.6: Results from the CMS Collaboration: The observed and expected lower mass limits set at 95% C.L. for the Z'_{ψ} and Z'_{SSM}, assuming relative signal widths of 0.6% and 3.0% respectively.

5.7 Differences in analyses and comparison of results

The three Z' analyses presented here - from the ATLAS Collaboration [120], the CMS Collaboration [124] and this thesis work - offer slight differences in the results. Table 5.7 lists the lower mass exclusion limits as reported by these analyses, for two Z' theories, Z'_{ψ} and Z'_{SSM}. Only the dimuon channel is reported from the results of this thesis work.

As discussed in Section 5.5.3.2, the exclusion limits on the lower mass of the Z' differs slightly between the published ATLAS dilepton search results and the results of this thesis

		Lower mass limit [TeV]					
		CMS publication		ATLAS publication		Thesis work	
Channel	Theory	Expected	Observed	Expected	Observed	Expected	Observed
ee	Z'_ψ	4.13	4.11	4.3	4.1	-	-
$\mu\mu$	Z'_ψ	4.30	4.29	4.0	4.0	3.7	3.8
$ee + \mu\mu$	Z'_ψ	4.55	4.56	4.5	4.5	-	-
ee	Z'_{SSM}	4.72	4.72	4.9	4.9	-	-
$\mu\mu$	Z'_{SSM}	4.90	4.89	4.5	4.5	4.3	4.4
$ee + \mu\mu$	Z'_{SSM}	5.14	5.15	5.1	5.1	-	-

Table 5.7: The lower mass limits as observed by the ATLAS Collaboration [120], the CMS Collaboration [124] and in this thesis work.

work due to a difference in the affect the large bad muon veto uncertainty has on the statistical analysis.

We see some differences between the published results from the ATLAS Collaboration and the CMS Collaboration. The expected lower mass limits on both the relevant Z' models are lowest in the results from the ATLAS Collaboration in the dimuon channel, and highest in the dielectron channel. The expected combined limit is about the the same for both theories. The two analyses are quite different - the one from CMS Collaboration is very similar to the one used in this thesis work, while the one used in the ATLAS Collaboration is (as described in Section 5.5) data-driven and uses a frequentist limit setting framework. We interpret the similarity of the combined dilepton results as a sign that there are no obviuous advantages of one analysis over the other at this point in time. The higher values of the mass limits in the dimuon channel is suspected to be because of a higher reported muon acceptance - they report a 93% efficiency to trigger, reconstruct and identify muon pairs within the detector acceptance. As shown in Figure 5.4 the acceptance×efficiency for signal dimuons reaches a maximum of 44% around 2 TeV, which is less than half of what the CMS Collaboration reports.

5.8 Summary

In this chapter we performed the high-mass dimuon resonance search using the full Run 2 dataset containing $139.0 \pm 2.4\,\mathrm{fb}^{-1}$ of data. We saw in Section 5.2 that the data/MC agreement is good, but that there is a visible trend in the data over MC ratio, going to lower values at higher dimuon invariant masses. This trend disappeared in the post-fit estimate of background dimuon invariant mass distribution as shown in Section 5.4.4. The statistical analysis in Section 5.4 revealed no signs of new physics beyond the SM, and exclusion limits were set on three Z' models, Z'_ψ, Z'_ψ and Z'_{SSM} at 3.8 TeV. 4.1 TeV and 4.4 TeV respectively. These were compared to the limits as published by the ATLAS Collaboration in Section 5.5 and also as published by the CMS Collaboration 5.7, all found to be comparable in size.

Chapter 6

Dimuon analyses in 2015 to 2018

Chapter 5 included a detailed description of a dimuon resonance search, with full Run 2 results, using data collected by the ATLAS detector through four years at a center-of-mass energy of 13 TeV, finally concluding by setting exclusion limits that are comparable to public results from the ATLAS Collaboration and from the CMS Collaboration. In this chapter we review the published results in the years leading up to 2019, all of which I have also contributed to during my time as a Ph.D. candidate.

6.1 July 2015 - EPS-HEP conference

The European Physical Society Conference on High Energy Physics (EPS-HEP) 2015 was held in Vienna, Austria from 22 to 29 July. According to their information page [125] EPS-HEP "is one of the major international conferences that reviews the field every second year since 1971 organized by the High Energy and Particle Physics Division of the European Physical Society." The first physics analyses using 13 TeV proton-proton collisions were presented at this conference, including the most recent dilepton analysis, with 78 pb^{-1} of 13 TeV data. The dimuon analysis was essentially the same analysis as described in Section 5.1, with one exception: the sum of all expected backgrounds is normalized to data in the invariant mass region 80 to 120 GeV (i.e. to the Z^0 boson resonance). Only preliminary data plots were shown at the EPS-HEP 2015 conference, discovery statistics and exclusion limits were not explored until the next publication in December the same year.

The dimuon invariant mass distribution is shown in Figure 6.1. The highest dimuon invariant mass event of 881 GeV is shown in Figure 6.2 using the Atlantis [103] and VP1 [126] event displays.[1] We see a very well-balanced event, with the two muons exactly back-to-back in the transverse plane, and close to back-to-back in the longitudinal plane.

In this round of analysis I was one of a few main dimuon analyzers, working on the whole analysis chain implementing the recommended muon selection cuts and dimuon event selection cuts. Being more than one person running the whole analysis chain is important as the probability of doing something incorrectly without noticing it increases with the number

---

[1] Atlantis and VP1 are two of the most used visualization programs in ATLAS. Atlantis is a Java stand-alone application, while VP1 is integrated in Athena, the C++ framework in which data processing and analysis is performed [127].

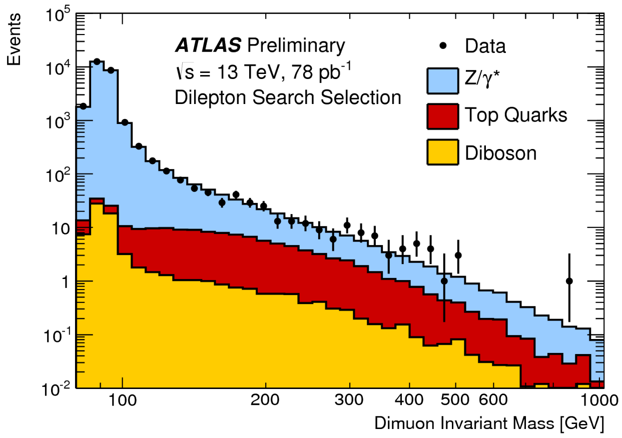

Figure 6.1: Results from July 2015 (EPS-HEP conference): Dimuon invariant mass distribution after the dimuon event selection, showing the stacked sum of all expected backgrounds [128].

of details, and the number of details in any given ATLAS analysis is very high. With several analyzers, these bugs are easy to find.

6.2 December 2015 - End Of Year Event

At the end of 2015, at the End Of Year Event (EOYE), new results from the dilepton group were shown [129][130] at CERN. The 13 TeV 2015 proton-proton collision dataset recorded by ATLAS, corresponding to 3.2 fb^{-1}, was used. The selection procedure was the same as for the EPS-HEP conference in July.

The reconstructed dimuon invariant mass distribution is shown in Figure 6.3. Two selected signals are overlaid, a resonant signal Z'_χ with a pole mass of 3 TeV, and a non-resonant contact interaction (CI) with LL constructive interference and CI scale at $\Lambda^-_{\mathrm{LL}} = 20$ TeV. Models with composite quarks and leptons predict new interactions involving the new constituents. These interactions are represented as contact interactions between initial-state quarks and final-state leptons. The notation “LL” (“Left-Left”) describes the chiral structure of the new interaction, and is one of four possible structures, the others being “RR” (“Right-Right”), “RL” and “LR”. The interested reader is referred to reference [129] where the compositeness model is described in more detail. We see that the data is well described by MC, as the data over MC ratio is centered on the value 1 over the majority of the invariant mass range, except for a possible deficit in data apparent around 300-500 GeV. This was to be investigated thoroughly before the next dilepton search publication in July 2016, more on this to come in Section 6.3.3.

The highest dimuon invariant mass event is shown in Figure 6.4 using the Atlantis and VP1 event displays. We see two well-defined muons back-to-back in the transverse plane, with both muons in the MS barrel.

The statistical analysis in this publication follows closely what is described in Chapter 5.4. The local p-values for the Z'_χ with pole masses between 0.15 TeV and 2.5 TeV in the

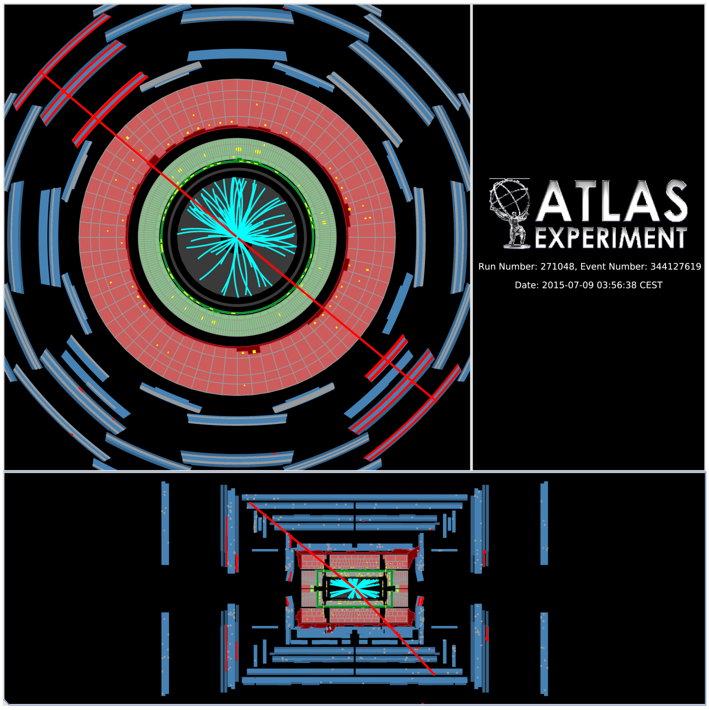

(a) Atlantis event display [103]

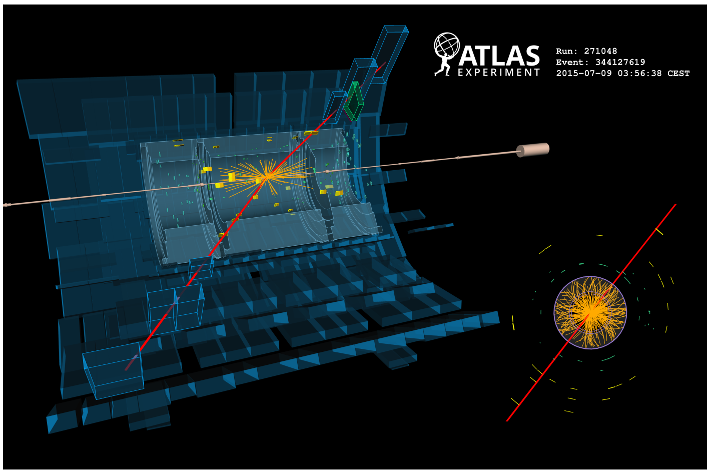

(b) VP1 event display [126]

Figure 6.2: Results from July 2015 (EPS-HEP conference): Highest dimuon invariant mass event in the first 78 fb^{-1} of 13 TeV data recorded in 2015, displayed in the Atlantis and VP1 event displays [128]. The leading muon has a p_T of 305 GeV and an η of -1.03. The subleading muon has a p_T of 300 GeV and an η of 0.82. The invariant mass of the dimuon pair is 881 GeV.

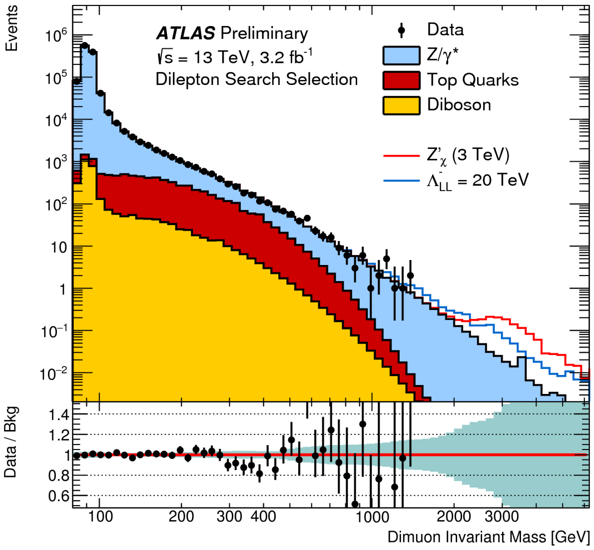

Figure 6.3: Results from December 2015 (EOYE): Dimuon invariant mass distribution after the dimuon event selection, showing the stacked sum of all expected backgrounds, for data and SM background estimates as well as their ratio. Two selected signals are overlaid, resonant Z'_χ with a pole mass of 3 TeV and non-resonant CI with LL constructive interference and $\Lambda^-_{\text{LL}} = 20$ TeV [129]. The bin width of the distribution is constant in $\log(M_{ll})$. The green band in the lower panel illustrates the total systematic uncertainty.

dimuon channel, with accompanying local and global significances shown as dashed lines, are shown in Figure 6.5. The largest deviation corresponds to a global p-value of 24%, thus no significant excesses are observed. Note that un-capped p-values are used for pole masses below 800 GeV, while capped p-values are used above. The difference between capped and un-capped p-values is described in Section 5.5.3.

Upper limits on Z' production cross-section times branching ratio to two muons σB are shown in Figure 6.6 for three Z' models - the SSM Z', the Z'_χ and the Z'_ψ, all of which are described in Section 2.3. Table 6.1 summarizes the observed and expected lower mass limits for various Z' scenarios. The additional Z' models (Z'_S, Z'_I, Z'_N and Z'_η) are described in Section 2.3.

Model	Width [%]	ee [TeV]		$\mu\mu$ [TeV]		$\ell\ell$ [TeV]	
		Exp	Obs	Exp	Obs	Exp	Obs
Z'_{SSM}	3.0	3.17	3.18	2.91	2.98	3.37	3.40
Z'_χ	1.2	2.87	2.88	2.64	2.71	3.05	3.08
Z'_{S}	1.2	2.83	2.84	2.59	2.67	3.00	3.03
Z'_I	1.1	2.78	2.78	2.53	2.62	2.95	2.98
Z'_{N}	0.6	2.64	2.64	2.38	2.48	2.81	2.85
Z'_η	0.6	2.64	2.65	2.38	2.48	2.81	2.85
Z'_ψ	0.5	2.58	2.58	2.32	2.42	2.74	2.79

Table 6.1: Results from December 2015 (EOYE): Observed and expected 95% C.L. lower mass limits in various Z' scenarios [129]. The widths are quoted as a percentage of the resonance mass.

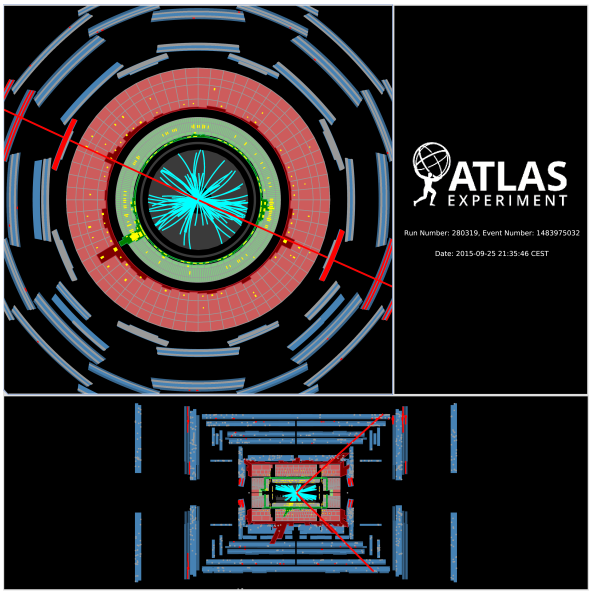

(a) Atlantis event display [103]

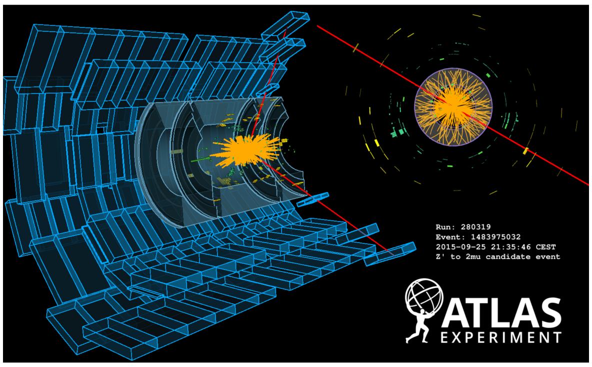

(b) VP1 event display [126]

Figure 6.4: Results from December 2015 (EOYE): Highest dimuon invariant mass event in the Atlantis and VP1 event displays [129]. The leading muon has a p_T of 712 GeV and an η of 0.87. The subleading muon has a p_T of 676 GeV and an η of 0.95. The invariant mass of the dimuon pair is 1390 GeV.

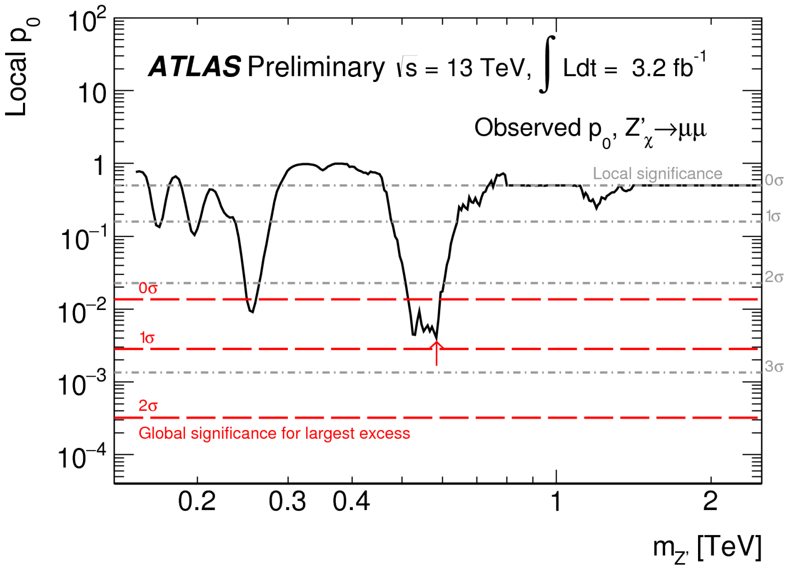

Figure 6.5: Results from December 2015 (EOYE): Local p-values in the dimuon channel derived for Z'_χ signals with pole mass between 0.15 and 2.5 TeV [129]. The accompanying local and global significance levels are shown as dashed lines. The most significant excess is marked with a red arrow.

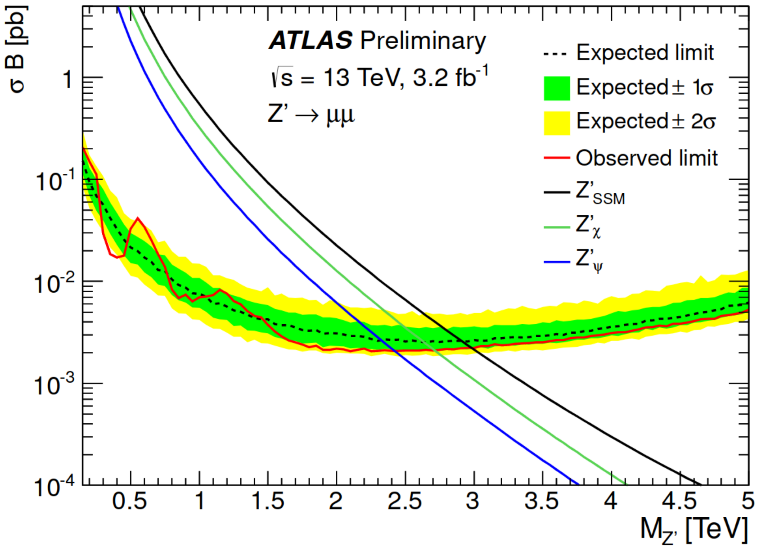

Figure 6.6: Results from December 2015 (EOYE): Upper 95% C.L. limits on the Z' production cross-section times branching ratio to two muons [129].

As in the previous round, my contribution was to run the event selection chain in the dimuon channel and also provide input for the SM background to the statistical analysis.

6.3 July 2016 - Physics Letters B Volume 761

Updated results were published in Physics Letters B Volume 761 in July 2016 [102]. I contributed again in general to the dimuon analysis, as detailed in the following subsections.

6.3.1 Updated results

There were several improvements compared to the results from half a year earlier. New MC samples were available, with a more appropriate average number of interactions per bunch-crossings (pile-up) profile, which in practice increased the number of MC events, thus decreasing the statistical uncertainty on the background expectation. The electron scale factors and the muon momentum smearing and scale factors had been updated. The high p_{T} muon working point was also updated, as it was discovered that the wrong region in η had been vetoed. This resulted in a 1$\%$ drop in overall efficiency of the events (removing 7$\%$ of the selected events and adding 6$\%$ of the originally removed events), and led to a new highest invariant mass dimuon event at 1587 GeV, about 200 GeV higher in mass than the previous highest. The analysis strategy and statistical analysis remained unchanged from the previous round. Figure 6.7 shows the dimuon invariant mass distribution after final selection. Comparing to Figure 6.3 it is easily seen that the shape of the background and the overlayed Z'_{χ} boson have changed a great amount, and especially that the Z' resonance appears much narrower in the newest results.

Figure 6.8 shows the new highest invariant mass dimuon event in the Atlantis and VP1 event displays. We see that this is an event with two muons and a jet, with both muons in the end-caps of the MS.

From the local p-value plot in Figure 6.9 we see no evidence of new physics - the largest excess in the dimuon channel is at 192 GeV with a local significance of 2.5σ, corresponding to a global p-value of 26$\%$, or 0.6σ.

Expected and observed upper limits on the Z' production cross-section times branching ratio (σB) to dimuons are shown in Figure 6.10, with lower pole mass limits for various Z' scenarios summarized in Table 6.2. Comparing to Table 6.1 we see that the limits are somewhat lower in the dimuon channel, for example we see that the observed lower mass limit in the $Z'_{\chi} \rightarrow \mu^{+}\mu^{-}$ scenario was 2.71 TeV in December 2015, and dropped to 2.57 TeV in July 2016.

6.3.2 Lepton track impact parameters study

To ensure that leptons are associated to the correct vertex, the ATLAS inner tracking working group made recommendations for requirements on lepton track impact parameters. The two relevant variables are the transverse impact parameter with respect to the beam line, d_0^{BL}, and the longitudinal impact parameter with respect to the vertex of the hard scattering (HS) interaction, $z_0 \cdot \sin\theta$ (previously schematically illustrated in Figure 5.1), and the recommended

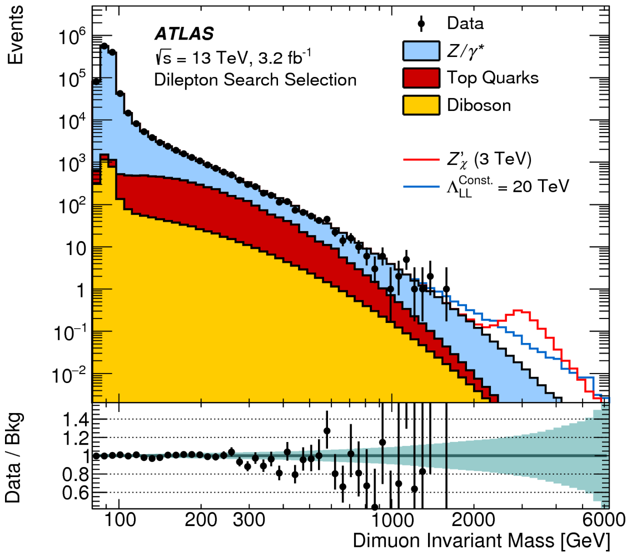

Figure 6.7: Results from July 2016 (Physics Letters B Volume 761): Dimuon invariant mass distribution after the dimuon event selection, showing the stacked sum of all expected backgrounds, for data and SM background estimates as well as their ratio [102]. Two selected signals are overlaid, resonant Z'_χ with a pole mass of 3 TeV and non-resonant CI with LL constructive interference and $\Lambda^-_{\rm LL} = 20$ TeV. The bin width of the distribution is constant in $\log(M_{ll})$. The green band in the lower panel illustrates the total systematic uncertainty.

Model	Width [%]	θ_{E_6} [rad]	Lower limits on $m_{Z'}$ [TeV]					
			ee		$\mu\mu$		$\ell\ell$	
			Obs	Exp	Obs	Exp	Obs	Exp
$Z'_{\rm SSM}$	3.0	-	3.17	3.16	2.83	2.89	3.36	3.36
Z'_χ	1.2	0.50 π	2.87	2.86	2.57	2.60	3.05	3.05
$Z'_{\rm S}$	1.2	0.63 π	2.83	2.81	2.54	2.57	3.00	3.00
Z'_I	1.1	0.71 π	2.77	2.76	2.49	2.51	2.94	2.94
Z'_η	0.6	0.21 π	2.63	2.62	2.35	2.36	2.81	2.80
$Z'_{\rm N}$	0.6	-0.08 π	2.63	2.62	2.35	2.36	2.80	2.80
Z'_ψ	0.5	0	2.57	2.55	2.29	2.29	2.74	2.74

Table 6.2: Results from July 2016 (Physics Letters B Volume 761): Observed and expected 95% C.L. lower mass limits in various Z' scenarios [102]. The widths are quoted as a percentage of the resonance mass. The variable θ_{E_6} is an angle related to the definition of the Z' in the various scenarios.

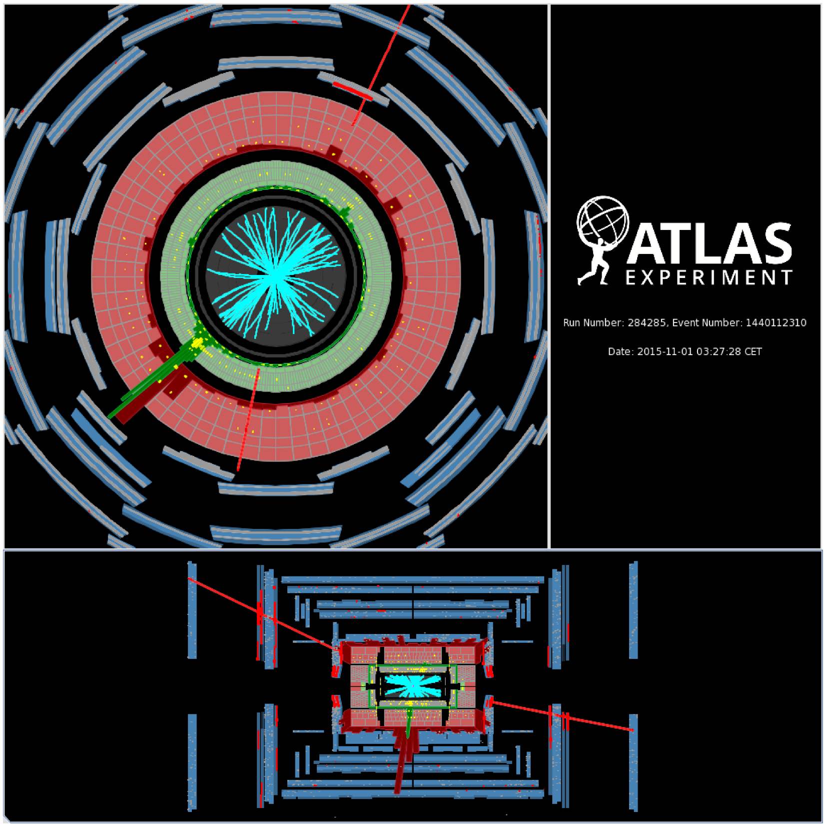

(a) Atlantis event display [103]

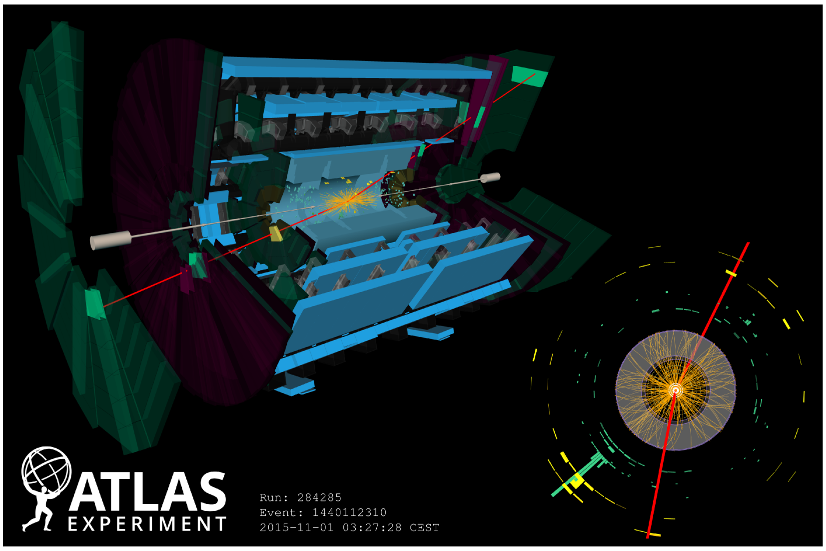

(b) VP1 event display [126]

Figure 6.8: Results from July 2016 (Physics Letters B Volume 761): Highest dimuon invariant mass event in the Atlantis and VP1 event displays [112]. The leading muon has a p_T of 279 GeV and an η of -1.47. The subleading muon has a p_T of 196 GeV and an η of 2.31. The invariant mass of the dimuon pair is 1587 GeV. The event also contains a jet with a p_{T} of 236 GeV, and has 90 GeV of missing transverse momentum.

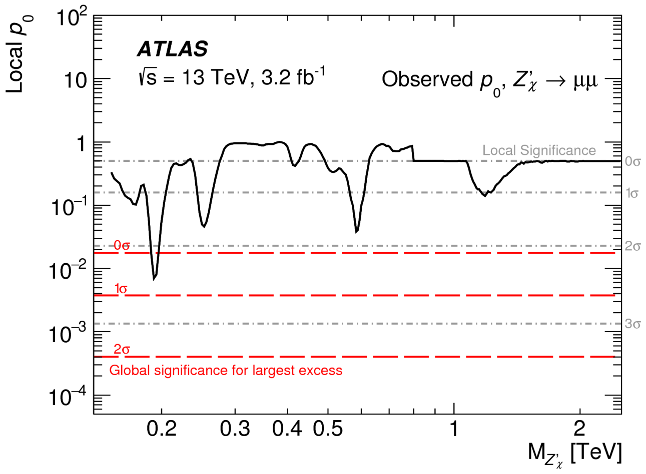

Figure 6.9: Results from July 2016 (Physics Letters B Volume 761): Local p-value as a function of the Z'_χ pole mass derived for signals with pole mass between 0.15 and 2.5 TeV for the dimuon channel [112]. The local and global significance levels are shown as dashed lines. Note that un-capped p-values are used for pole masses below 800 GeV, while capped p-values are used above. The difference between capped and un-capped p-values is described in Section 5.5.3.

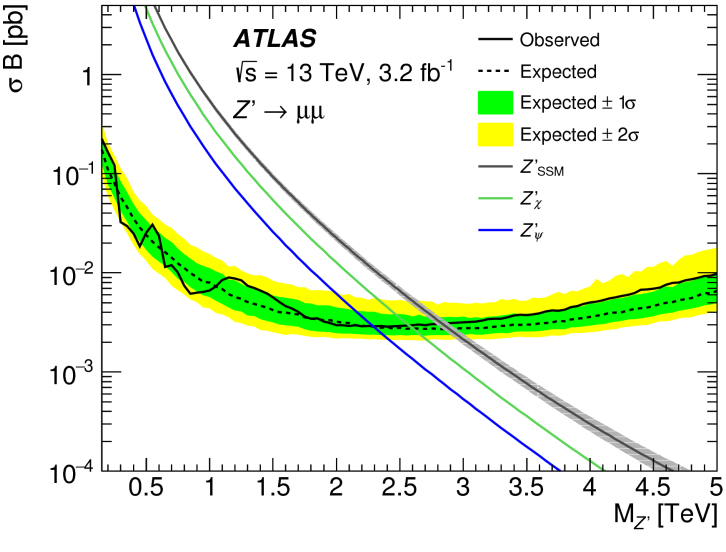

Figure 6.10: Results from July 2016 (Physics Letters B Volume 761): Upper 95% C.L. limits on the Z' production cross-section times branching ratio to two leptons [102].

cuts were

$$|d_0^{\mathrm{BL}}(\sigma_{d_0})| \equiv \frac{d_0}{\sigma_{d_0}} < 3, \quad |\Delta z_0^{\mathrm{BL}} \sin\theta| < 0.5\,\mathrm{mm}, \tag{6.1}$$

where σ_{d_0} represents the uncertainty in the measured transverse impact parameter d_0[2]. The combined tracks were used for the study (see Section 4.3.1 for further details regarding combined tracks).

When presented with new recommendations, it is important to check the impact they have on any given analysis. To do this for the dimuon search analysis we first required all events and muons to comply with the dimuon event selection up to, but not including, the impact parameter cuts, as listed in Table 5.1. Then we picked out all events with at least two muons, and plotted the values of the two impact parameters of the two leading muons. The distribution of the absolute value of $|\Delta z_0^{\mathrm{BL}} \cdot \sin\theta|$ is shown in Figure 6.11 for four different Z'_χ signal scenarios, for the leading (a) and the subleading (b) muon. We see that cutting this variable at the value 0.5 mm is unproblematic, removing a negligible amount of signal events.

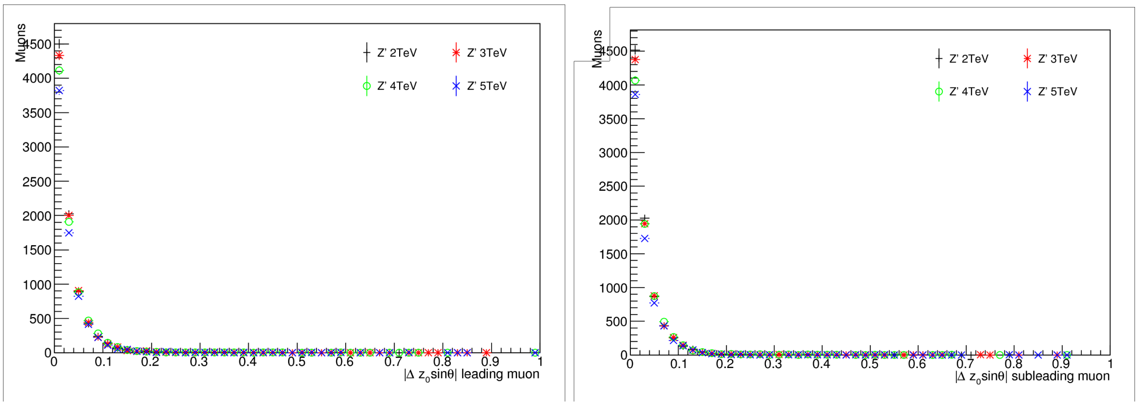

(a) Leading muon (b) Subleading muon

Figure 6.11: Results from July 2016: The distribution of the absolute value of the longitudinal impact parameter with respect to the reconstructed primary vertex for the leading (a) and the subleading (b) muon.

Figure 6.12 shows the distribution of the absolute value of $|d_0^{\mathrm{BL}}(\sigma)|$ for the leading (a) and the subleading (b) muon. It is obvious from the distributions that removing all events with values above 3 leads to a large loss (about 10%) of signal events. A solution to this problem emerged when adding the beam spot uncertainty to the definition of the transverse impact parameter,

$$d_0^{\mathrm{BL,BS}} \equiv \frac{d_0}{\sqrt{\sigma_{d_0}^2 + \sigma_{\mathrm{BS}}^2}},$$

with σ_{BS} as the beam spot uncertainty, see Figure 6.13. Now we see that cutting at the value 3 is unproblematic. This definition of the impact parameter became the default definition in the tracking group recommendations.

Figure 6.14 shows the distribution of the absolute value of the longitudinal impact parameter (with the definition as described in this section) after the dilepton event selection exclud-

---

[2] The parameter $d_0^{\mathrm{BL}}(\sigma_{d_0})$ is called the d_0 significance

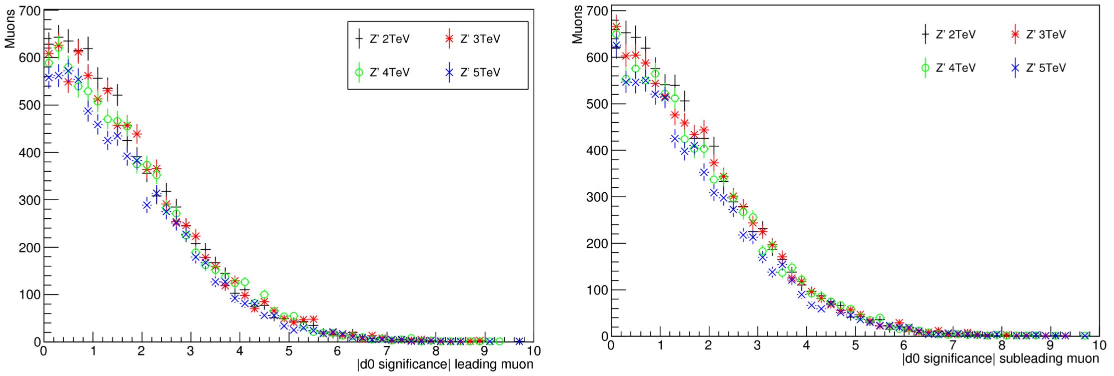

(a) Leading muon (b) Subleading muon

Figure 6.12: Results from July 2016: The distribution of the absolute value of the significance of the transverse impact parameter with respect to the beam line for the leading (a) and the subleading (b) muon.

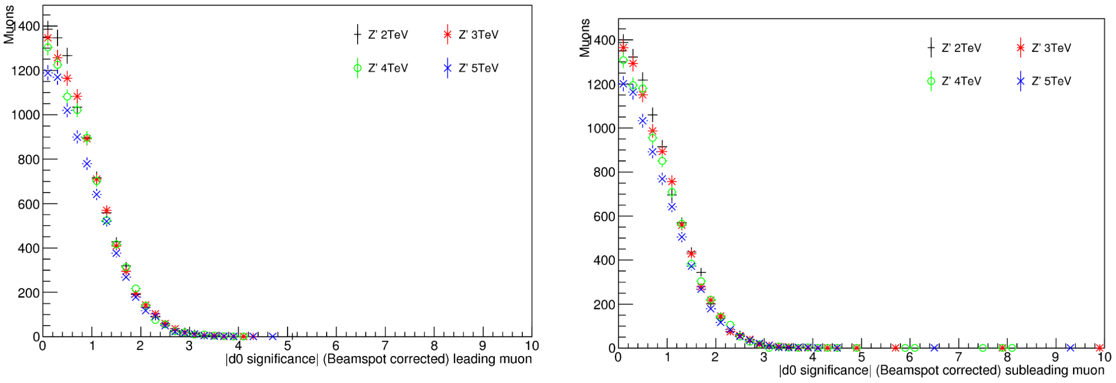

(a) Leading muon (b) Subleading muon

Figure 6.13: Results from July 2016: The distributions of the absolute value of the transverse impact parameter with respect to the beam line for the leading (a) and the subleading (b) muons.

ing the z_0^{BL} criterion, for the leading (a) and the subleading (b) muons, with the stacked sum of all the expected backgrounds and data overlaid [112]. Figure 6.15 shows corresponding distributions for the transverse impact parameter after the dilepton event selection excluding the d_0^{BL} criterion. The cut on the longitudinal impact parameter was changed to 10 mm, because of the obvious mismodelling issues in the z_0^{BL} distribution, and other studies had shown that a 10 mm cut guarded well against cosmic muons. Figure 6.16 presents the d_0^{BL}

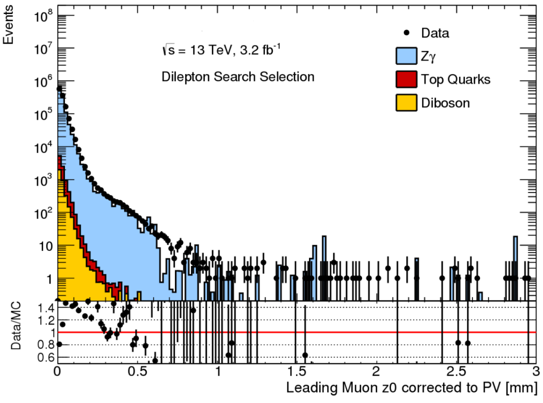

(a) Leading muon

(b) Subleading muon

Figure 6.14: Results from July 2016: The distributions of the absolute value of the longitudinal impact parameter with respect to the reconstructed PV for the leading (a) and the subleading (b) muon after the dilepton search event selection (except the z_0^{BL} criterion), showing the stacked sum om all expected backgrounds with data overlaid. The MC expectation is normalized to data in the invariant mass region 80-120 GeV [112].

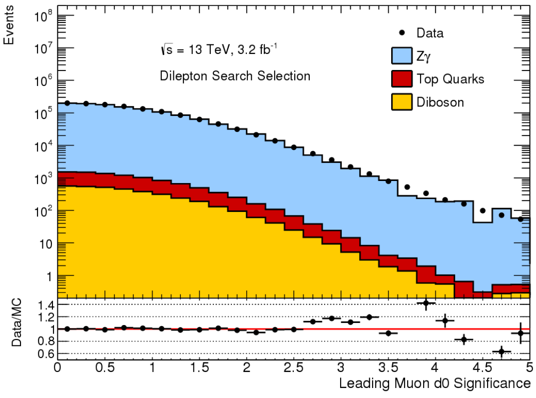

(a) Leading muon

(b) Subleading muon

Figure 6.15: Results from July 2016: The distribution of significance of the absolute value of the transverse impact parameter with respect to the beam line for the leading (a) and the subleading (b) muons after the dilepton search event selection (except the d_0 criterion), showing the stacked sum of all expected backgrounds. The MC expectation is normalized to data in the invariant mass region 80-120 GeV [112].

(a) and z_0^{BL} (b) cut efficiencies as functions of the p_T of the leading and subleading muons, showing that these impact parameter cuts have a very high efficiency on both the DY events and the SM backgrounds.

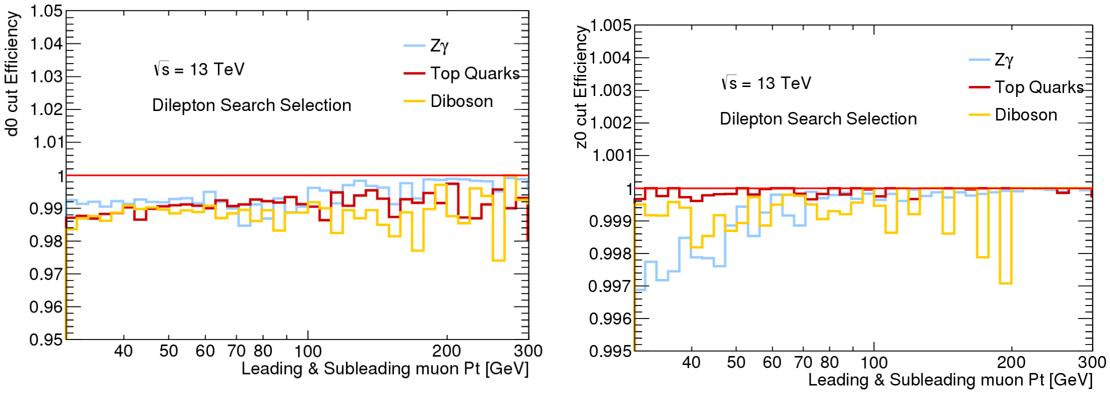

(a) Transverse impact parameter.

(b) Longitudinal impact parameter.

Figure 6.16: Results from July 2016: The efficiencies of the cuts on muon $|d_0^{\mathrm{BL,BS}}|$ (a) and $|z_0^{\mathrm{BL}} \cdot \sin\theta|$ (b) as functions of the leading and subleading muon transverse momentum p_T [112].

6.3.3 Muon channel mass deficit study

When looking at the dimuon invariant mass distribution in Figure 6.7 we see a rather large dip in the data over MC ratio plot between 300 and 500 GeV. Investigations were performed to decide whether this was a problem with MC modelling or a statistical downward fluctutation of data.

6.3.3.1 Muon kinematics for the region 300 GeV$<$ M$_{\mu\mu}$ $<$ 500 GeV

We plot several muon kinematic variables for events only in the dimuon invariant mass region between 300 and 500 GeV, for both the high p_T and medium[3] muon working points to assess if there is a problem with the high p_T working point specifically. Also to assess whether there was a problem with the efficiency scale factors (isolation, trigger, and reconstruction), muon kinematic distributions are made both with and without these scale factors.

Figure 6.17 shows muon kinematic distributions for both the leading and subleading muons, with and without the efficiency scale factors, using the high p_T working point. Figure 6.18 (6.19) displays the same distributions for the leading (subleading) muon. Figure 6.20 shows the muon kinematic distributions for the leading and subleading muon, with and without the efficiency scale factors, for the medium working point, while Figure 6.21 (6.22) shows the same distributions for the leading (subleading) muon.

To conclude; the efficiency scale factors have very little impact on the data/MC agreement, both for the high p_T and medium working points. No obvious trends which could point towards an issue are visible when looking at the muon η and ϕ distributions, and the same

---

[3] As mentioned before, the high p_T working point was developed for the Z' and W' analyses, maximizing momentum resolution for high p_T muons, while the medium working point is the default working points for muon analyses in general.

kind of deficit is seen for both the high p_T and medium working points. Looking at the muon p_T distributions we see a deficit in the region between 150 and 250 GeV, and we investigate this region further in the following.

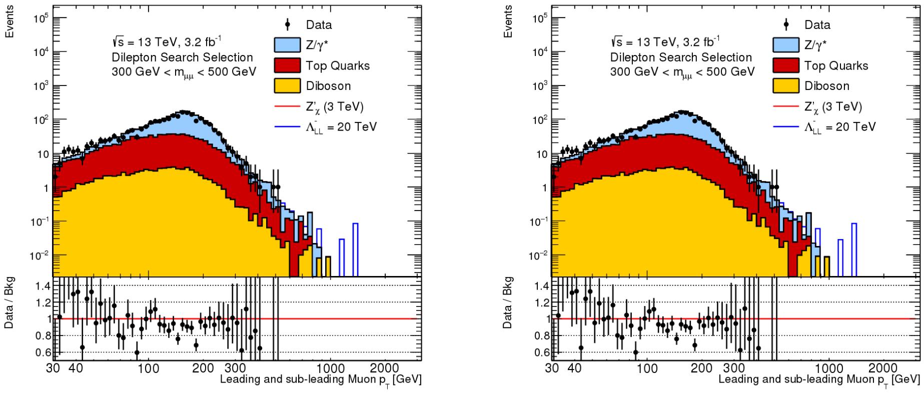

(a) Leading and subleading muon p_T

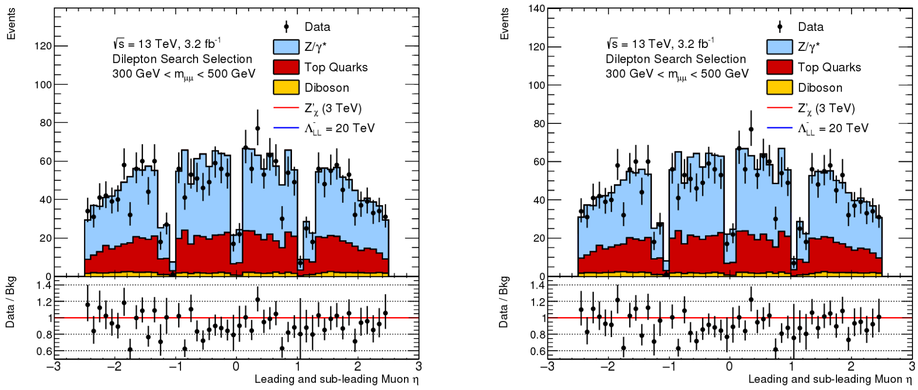

(b) Leading and subleading muon η

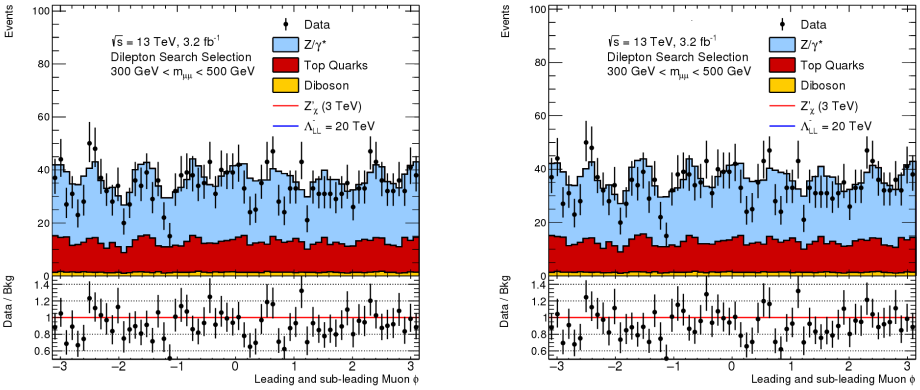

(c) Leading and subleading muon ϕ

Figure 6.17: Results from July 2016: Muon kinematic distributions for dimuon pairs with invariant mass between 300 and 500 GeV, using the high p_T working point. The left-hand side shows the distributions with all efficiency scale factors applied, while the right-hand sides shows the same distributions without the efficiency scale factors applied. The normalization is the same as for the nominal analysis [112].

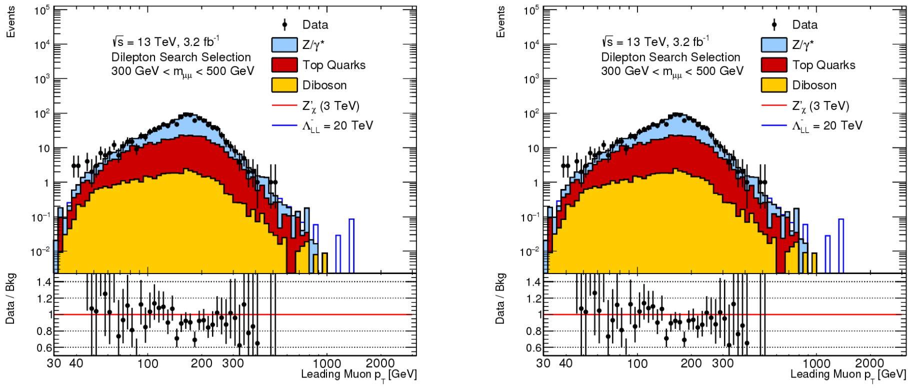

(a) Leading muon p_T

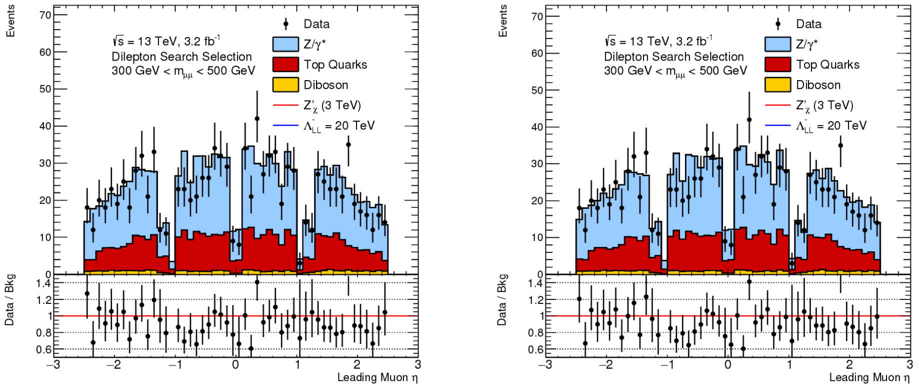

(b) Leading muon η

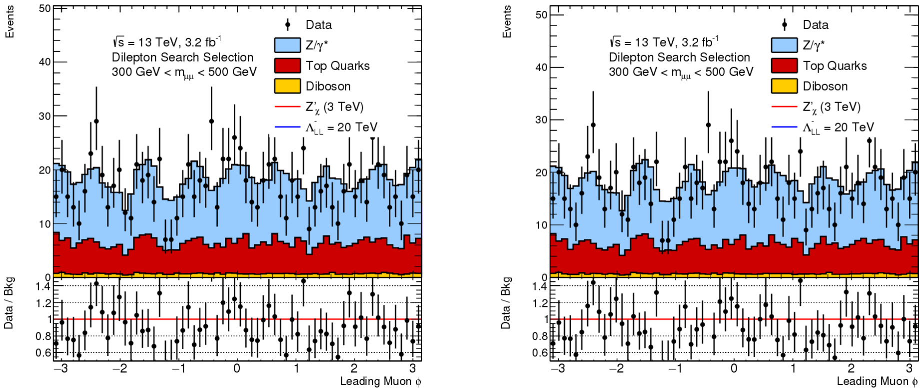

(c) Leading muon ϕ

Figure 6.18: Results from July 2016: Muon kinematic distributions for dimuon pairs with invariant mass between 300 and 500 GeV (showing only the leading muon kinematics), using the high p_T working point. The left-hand side shows the distributions with all efficiency scale factors applied, while the right-hand sides shows the same distributions without the efficiency scale factors applied. The normalization is the same as for the nominal analysis [112].

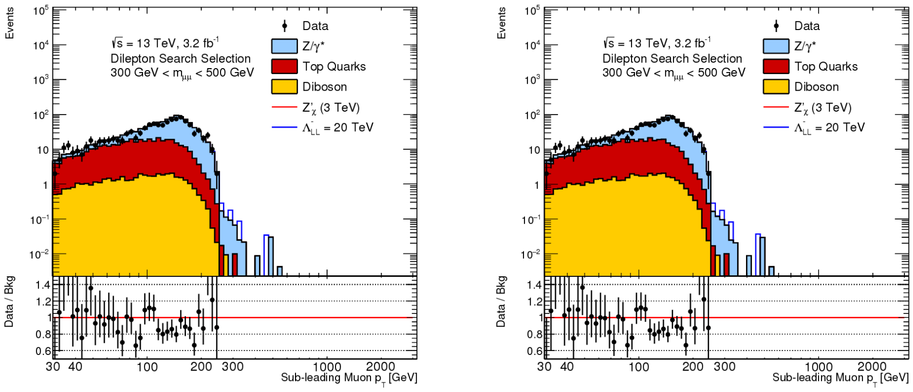

(a) Subleading muon p_T

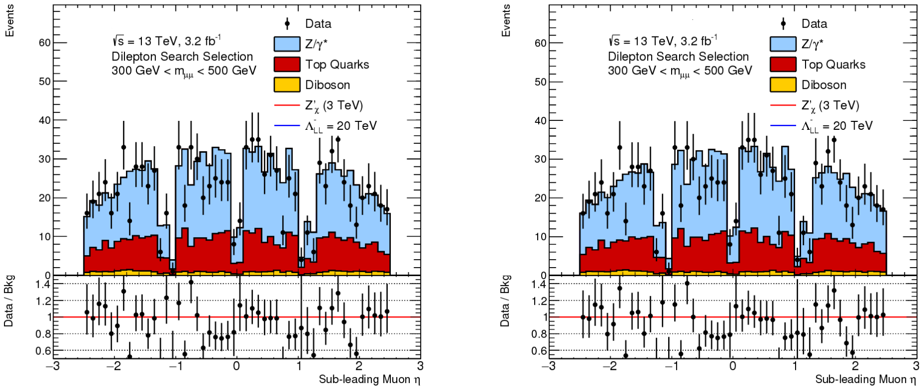

(b) Subleading muon η

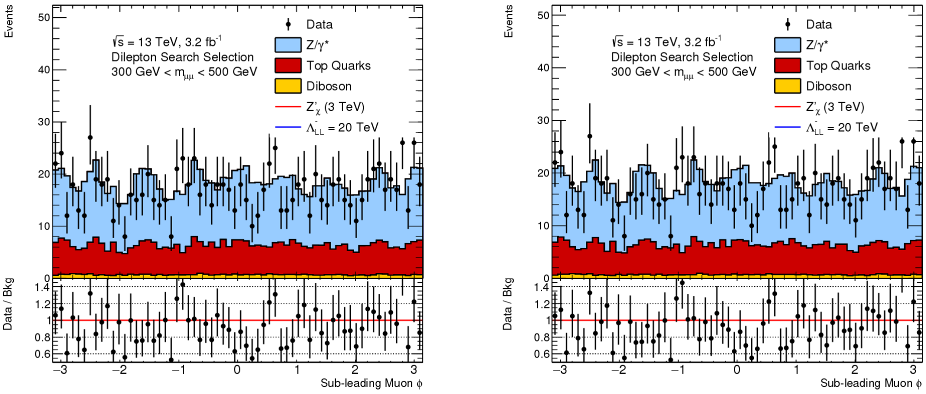

(c) Subleading muon ϕ

Figure 6.19: Results from July 2016: Muon kinematic distributions for dimuon pairs with invariant mass between 300 and 500 GeV (showing only the subleading muon kinematics), using the high p_T working point. The left-hand side shows the distributions with all efficiency scale factors applied, while the right-hand sides shows the same distributions without the efficiency scale factors applied. The normalization is the same as for the nominal analysis [112].

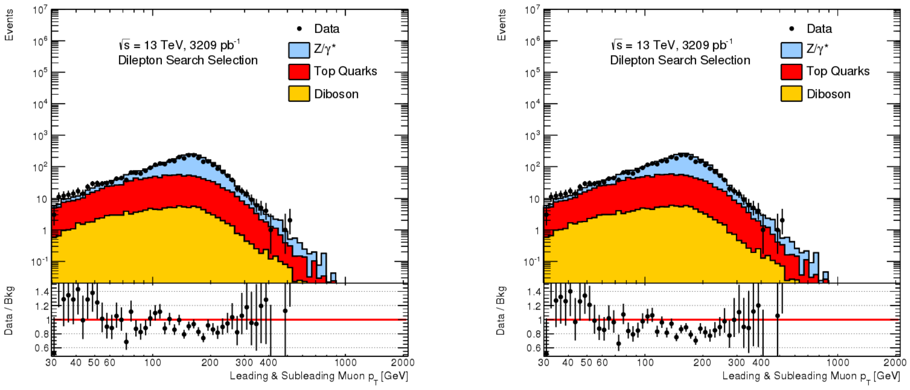

(a) Leading and subleading muon p_T

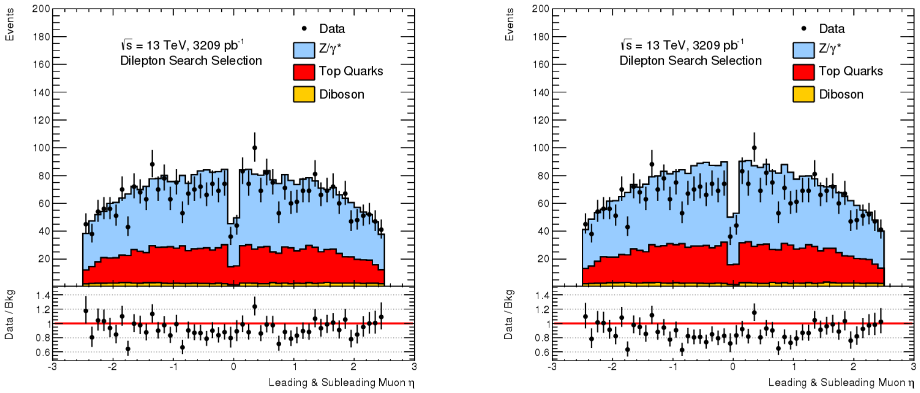

(b) Leading and subleading muon η

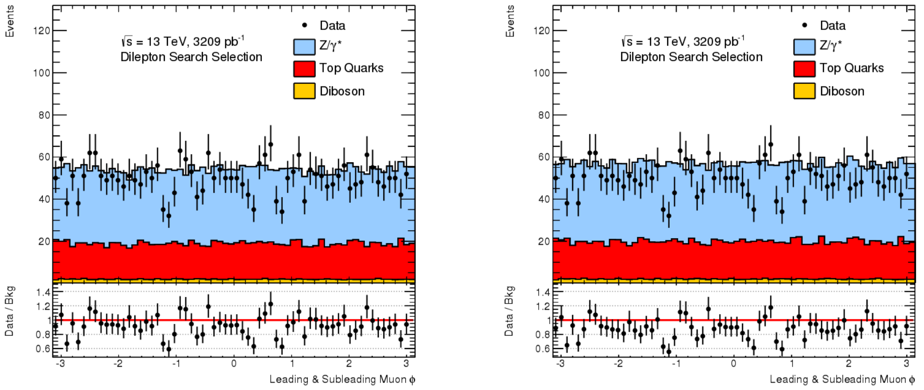

(c) Leading and subleading muon ϕ

Figure 6.20: Results from July 2016: Muon kinematic distributions for dimuon pairs with invariant mass between 300 and 500 GeV, using the medium working point. The left-hand side shows the distributions with all efficiency scale factors applied, while the right-hand sides shows the same distributions without the efficiency scale factors applied. The normalization is the same as for the nominal analysis [112].

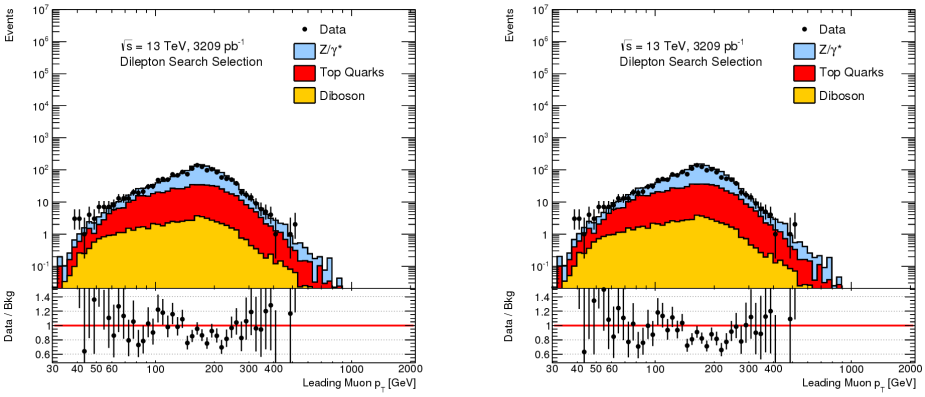

(a) Leading muon p_T

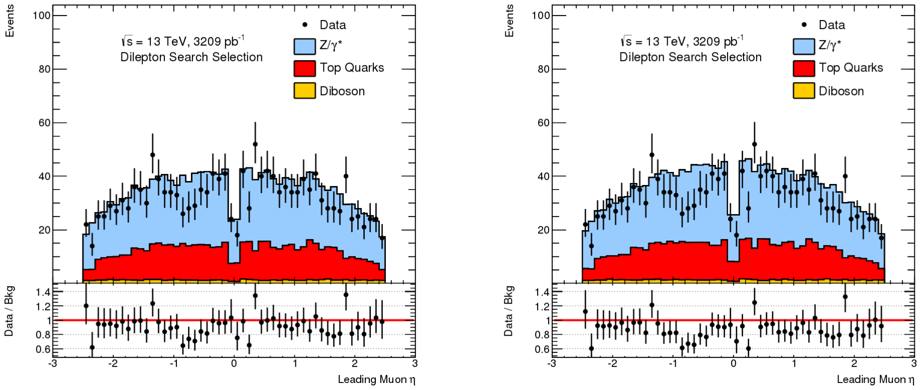

(b) Leading muon η

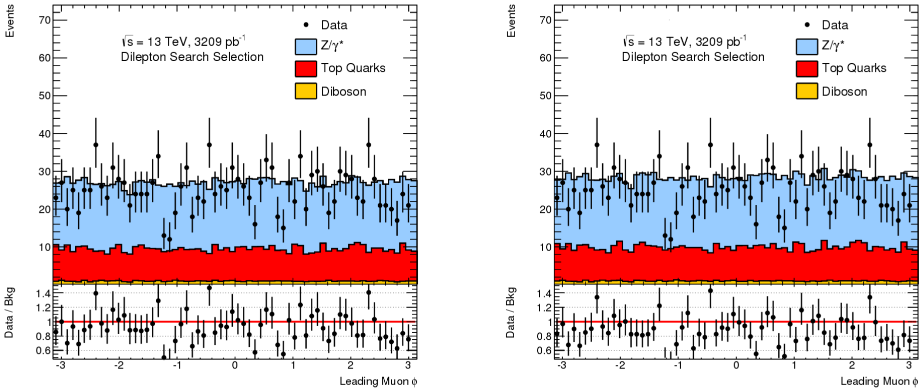

(c) Leading muon ϕ

Figure 6.21: Results from July 2016: Muon kinematic distributions for dimuon pairs with invariant mass between 300 and 500 GeV (showing only the leading muon kinematics), using the medium working point. The left-hand side shows the distributions with all efficiency scale factors applied, while the right-hand sides shows the same distributions without the efficiency scale factors applied. The normalization is the same as for the nominal analysis [112].

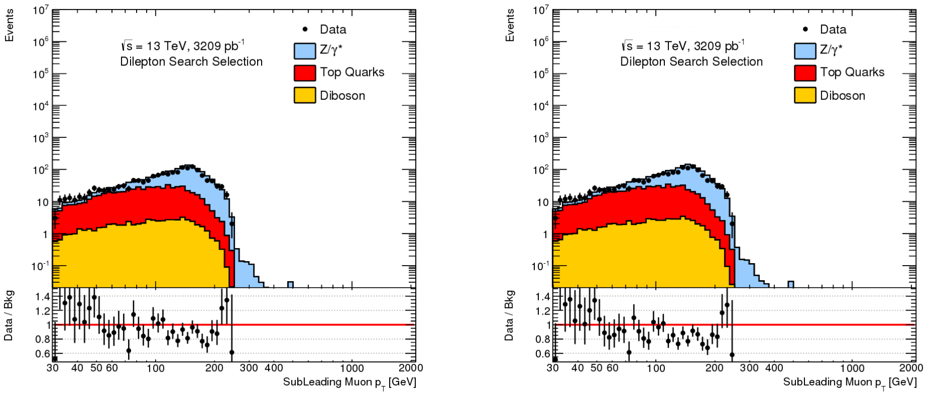

(a) Subleading muon p_T

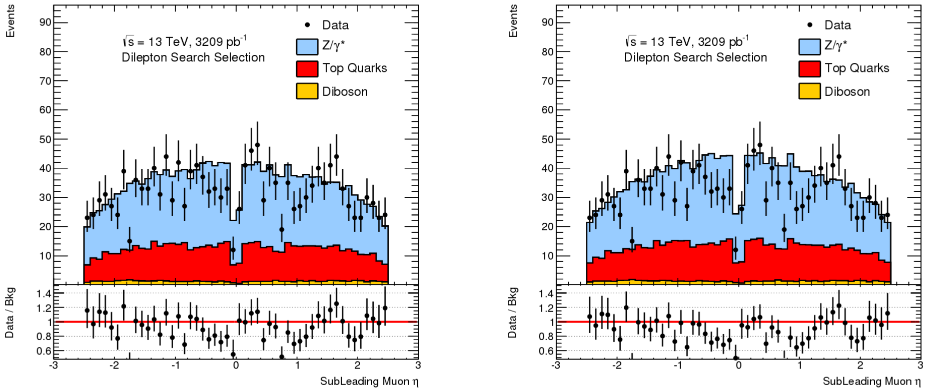

(b) Subleading muon η

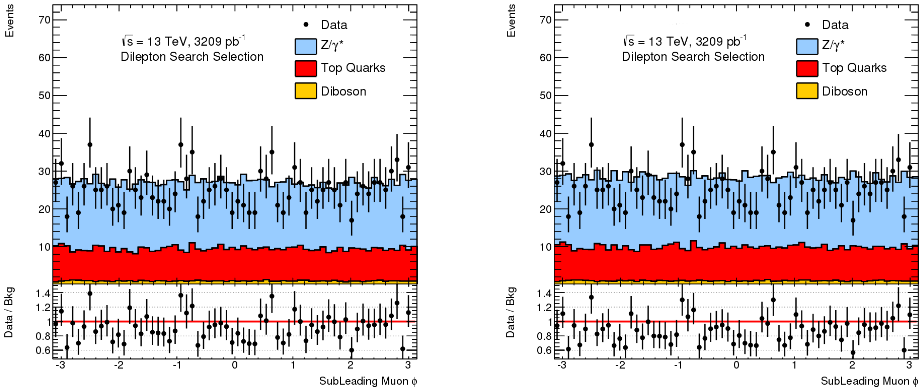

(c) Subleading muon ϕ

Figure 6.22: Results from July 2016: Muon kinematic distributions for dimuon pairs with invariant mass between 300 and 500 GeV (showing only the subleading muon kinematics), using the medium working point. The left-hand side shows the distributions with all efficiency scale factors applied, while the right-hand sides shows the same distributions without the efficiency scale factors applied. The normalization is the same as for the nominal analysis [112].

6.3.3.2 Muon kinematics for the region 150 GeV$< p_T <$ 250 GeV

Muon kinematic variables for events where both muons are in the p_T range between 150 and 250 GeV were further studied. Figure 6.23 shows muon kinematic distributions for both the leading and subleading muon, with and without the efficiency scale factors for the high p_T working point, and Figure 6.24 (6.25) shows the same distribution but for the leading (subleading) muon. Figure 6.26 shows the muon kinematic distributions for the leading and subleading muons with and without the efficiency scale factors, for the medium working point, while Figure 6.27 (6.28) shows the same distributions for the leading (subleading) muons.

As before we see that the efficiency scale factors do not have a large impact on the agreement, with similar results for both the medium and high p_T working points. The kinematic distributions do not display any problematic behaviour. If there was a problem with the measurement of the transverse momentum of the muons in a specific range, between 150 GeV and 250 GeV, we would expect to see a data over MC ratio away from unity when using only these muons in the kinematic distributions.

6.3.3.3 Conclusion

No problematic behaviour was uncovered in the data. The observed number of events in this region is 1083, while the expected number is 1183 ± 32, giving a -2.1σ deficit, which is concluded to be within an acceptable level of agreement to the SM prediction. Time would also show that this was indeed not a physical effect, as the “deficit” had gone away by the October 2017 publication using 36 fb^{-1} of data, as can be seen in Figure 6.29.

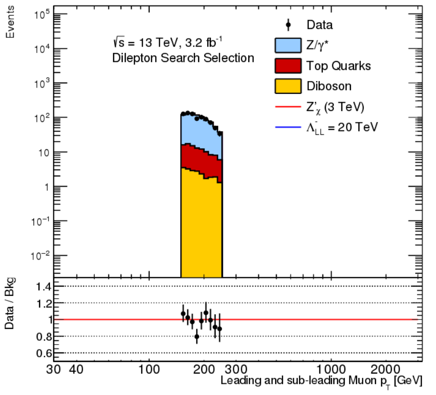

(a) Leading and subleading muon p_T

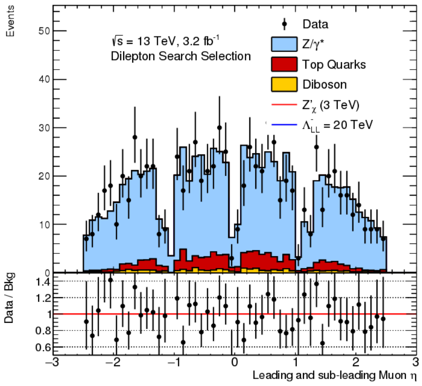

(b) Leading and subleading muon η

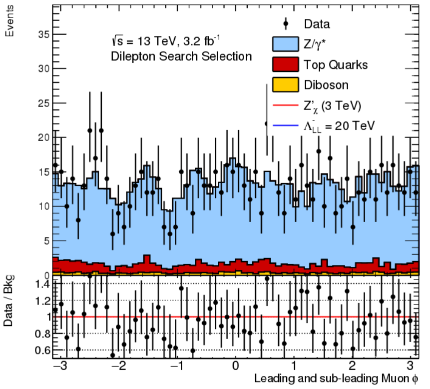

(c) Leading and subleading muon ϕ

Figure 6.23: Results from July 2016: Muon kinematic distributions for muons with p_T between 150 and 250 GeV, using the high p_T working point. The left-hand side shows the distributions with all efficiency scale factors applied, while the right-hand sides shows the same distributions without the efficiency scale factors applied. The normalization is the same as for the nominal analysis [112].

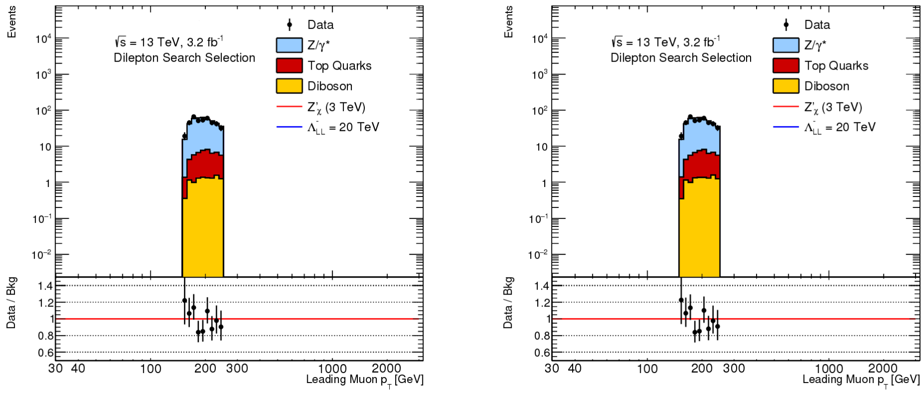

(a) Leading muon p_T

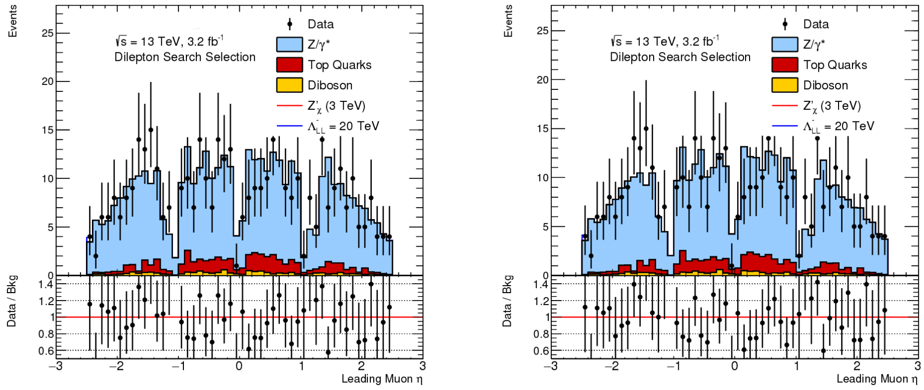

(b) Leading muon η

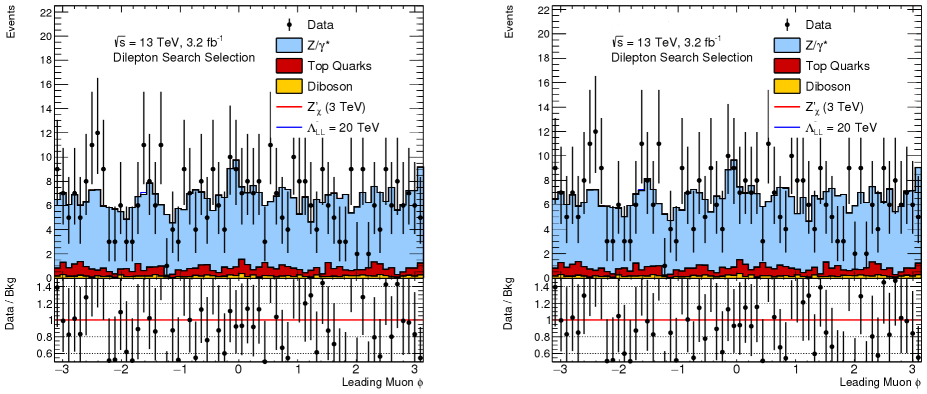

(c) Leading muon ϕ

Figure 6.24: Results from July 2016: Muon kinematic distributions for muons with p_T between 150 and 250 GeV (showing only the leading muon kinematics), using the high p_T working point. The left-hand side shows the distributions with all efficiency scale factors applied, while the right-hand sides shows the same distributions without the efficiency scale factors applied. The normalization is the same as for the nominal analysis [112].

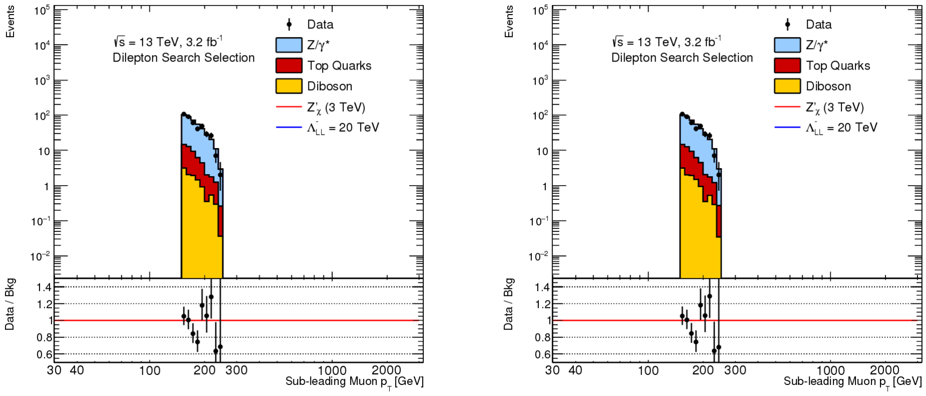

(a) Subleading muon p_T

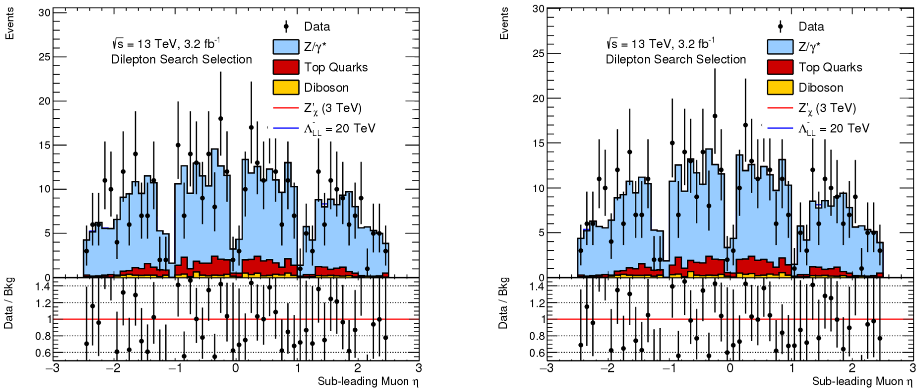

(b) Subleading muon η

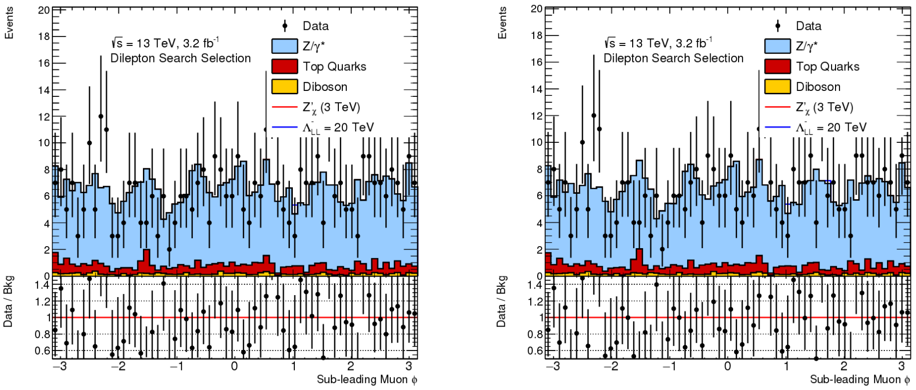

(c) Subleading muon ϕ

Figure 6.25: Results from July 2016: Muon kinematic distributions for muons with p_T between 150 and 250 GeV (showing only the subleading muon kinematics), using the high p_T working point. The left-hand side shows the distributions with all efficiency scale factors applied, while the right-hand sides shows the same distributions without the efficiency scale factors applied. The normalization is the same as for the nominal analysis [112].

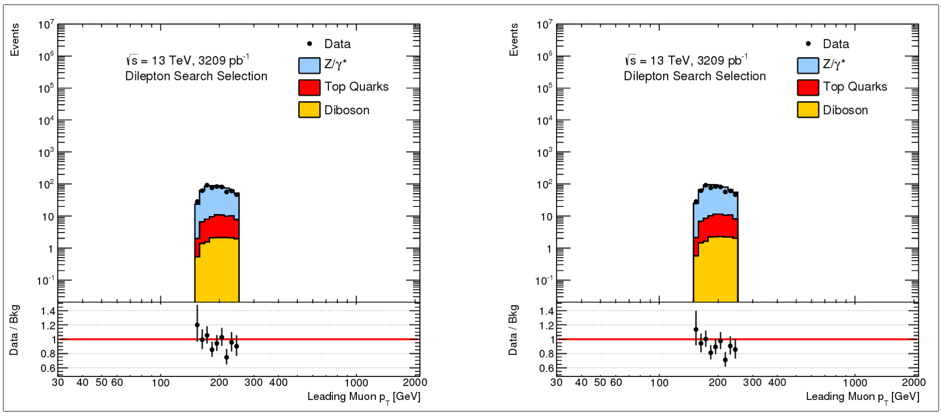

(a) Leading and subleading muon p_T

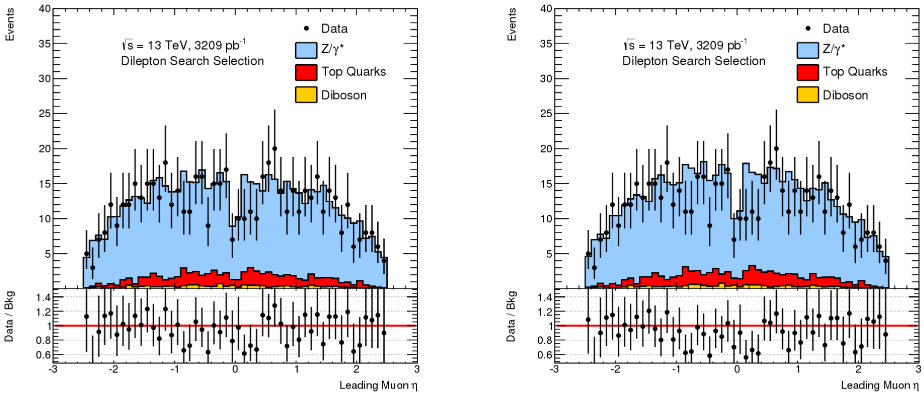

(b) Leading and subleading muon η

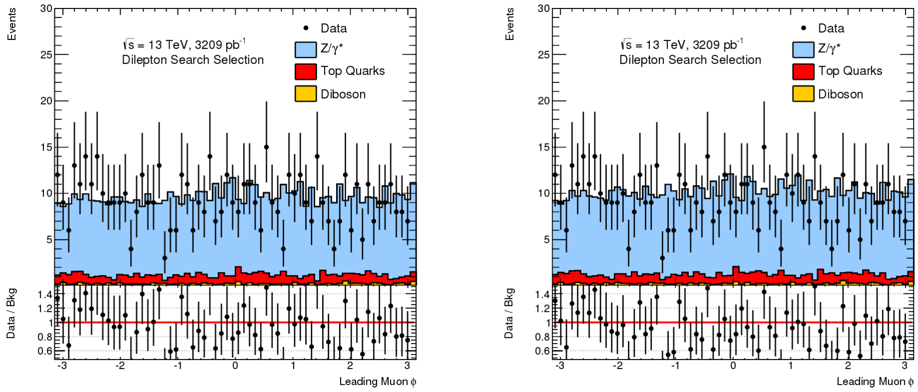

(c) Leading and subleading muon ϕ

Figure 6.26: Results from July 2016: Muon kinematic distributions for muons with p_T between 150 and 250 GeV, using the medium working point. The left-hand side shows the distributions with all efficiency scale factors applied, while the right-hand sides shows the same distributions without the efficiency scale factors applied. The normalization is the same as for the nominal analysis [112].

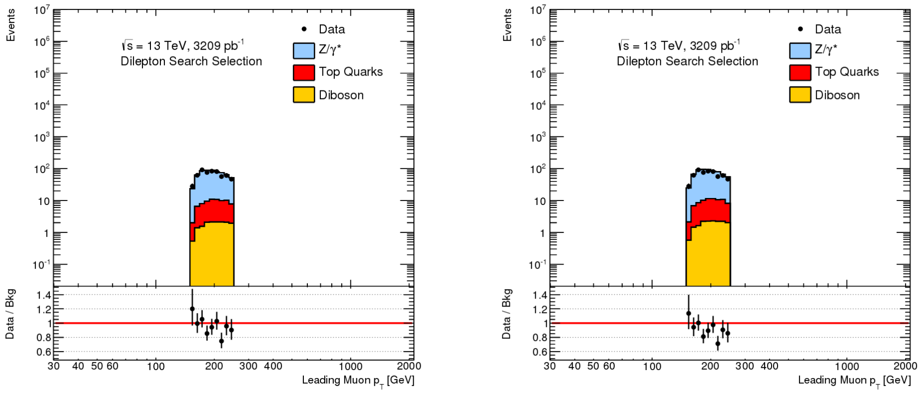

(a) Leading muon p_T

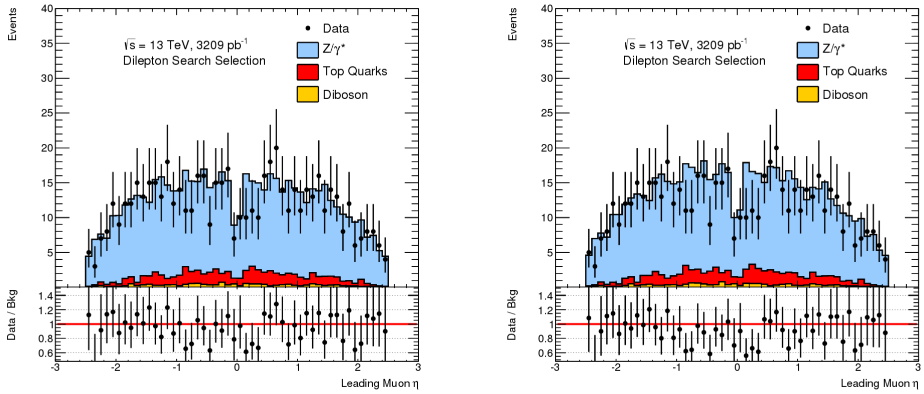

(b) Leading muon η

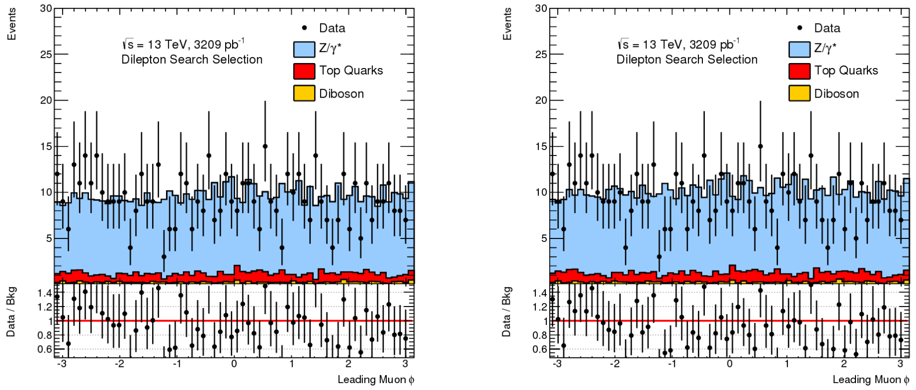

(c) Leading muon ϕ

Figure 6.27: Results from July 2016: Muon kinematic distributions for muons with p_T between 150 and 250 GeV (showing only the leading muon kinematics), using the medium working point. The left-hand side shows the distributions with all efficiency scale factors applied, while the right-hand sides shows the same distributions without the efficiency scale factors applied. The normalization is the same as for the nominal analysis [112].

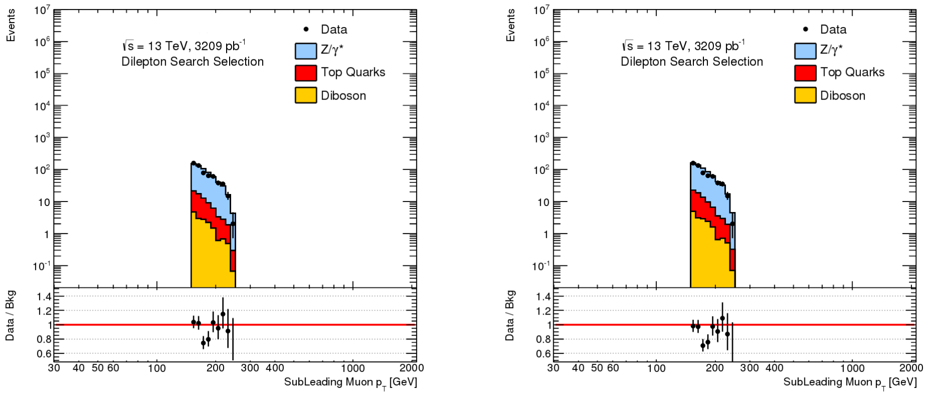

(a) Subleading muon p_T

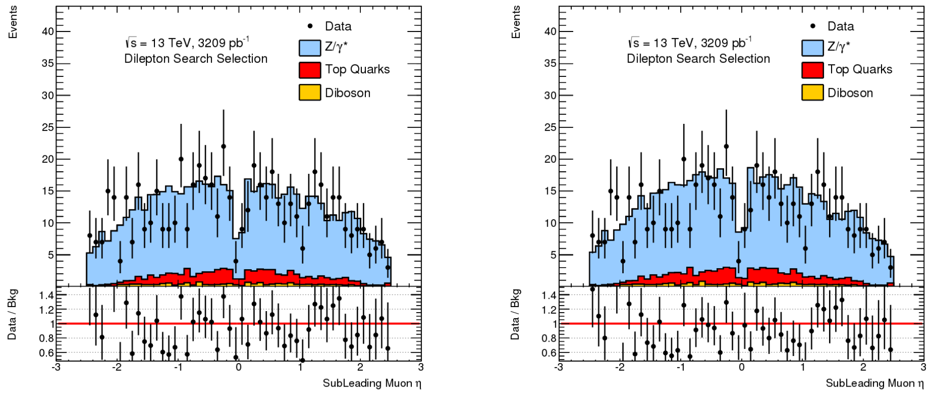

(b) Subleading muon η

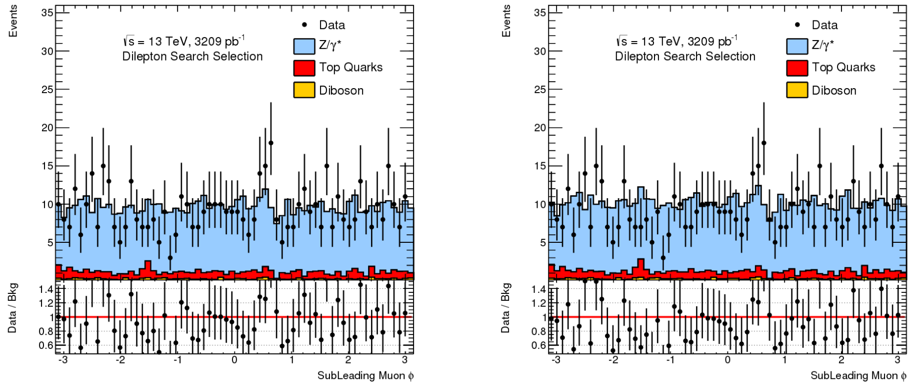

(c) Subleading muon ϕ

Figure 6.28: Results from July 2016: Muon kinematic distributions for muons with p_T between 150 and 250 GeV (showing only the subleading muon kinematics), using the medium working point. The left-hand side shows the distributions with all efficiency scale factors applied, while the right-hand sides shows the same distributions without the efficiency scale factors applied. The normalization is the same as for the nominal analysis [112].

6.4 October 2017 - Journal of High Energy Physics

In October 2017 new results from the dilepton group were published, this time in the Journal of High Energy Physics (JHEP) [23]. I contributed once again in general to the dimuon analysis, in particular the main dimuon analysis and the minimal Z' models, as detailed in the next subsections.

6.4.1 Updated results

The analysis strategy and statistical analysis still remained unchanged from the previous round, but the amount of data was tenfold, up from $3.2\,\mathrm{fb}^{-1}$ to $36.1\,\mathrm{fb}^{-1}$. Figure 6.29 shows the dimuon invariant mass after final selection. The middle panel shows the ratio of the data to the expected background, as before, with the green band as the total systematic uncertainty. However, a new panel has appeared. This is the expected background "post-fit" (as defined in Section 5.4.4). We see that this ratio is now much closer to the value 1.0 compared to the pre-fit ratio, which is typical when the systematic variations are sufficient to describe the variations in the data. The local p-value plot in Figure 6.30 does not reveal any signs of

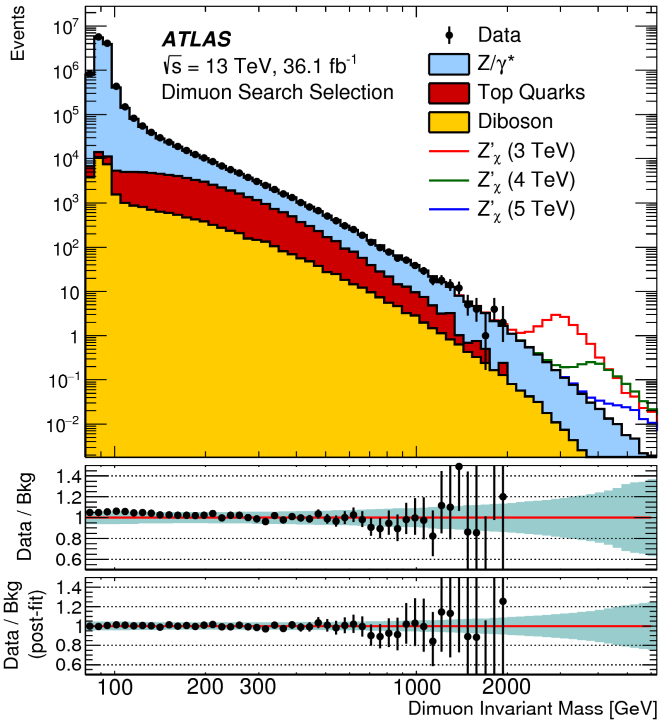

Figure 6.29: Results from October 2017 (JHEP): Dimuon invariant mass distribution after the dimuon event selection, showing the stacked sum of all expected backgrounds, for data and SM background estimates as well as their ratio [23]. Three selected signals are overlaid, Z'_χ with pole masses of 3, 4 and 5 TeV. The bin width of the distribution is constant in $\log(M_{ll})$. The middle panel shows the ratio of the data to the expected background. The green bands in the middle and the lower panels illustrates the total systematic uncertainty. The lower panel shows the ratio of the data to the adjusted expected background that results from the statistical analysis.

new physics. The most significant observed excess in the dimuon channel is at a mass of 481 GeV with a local p-value of 5.8%, corresponding to 1.6σ. The global p-value however is 91% (-1.3σ). Expected and observed upper limits on the Z' production cross-section times

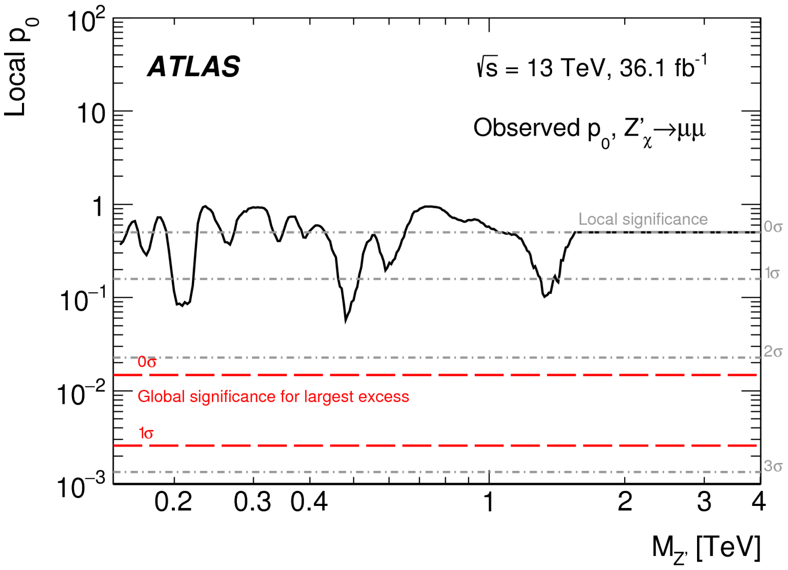

Figure 6.30: Results from October 2017 (JHEP): Local p-value as a function of the Z'_χ pole mass for the dimuon channel derived for Z'_χ signals with pole mass between 0.15 and 4.0 TeV for the dimuon channel [112]. The local and global significance levels are shown as dashed lines. Note that un-capped p-values are used for pole masses below 1.5 TeV, while capped p-values are used above. The difference between capped and un-capped p-values is described in Section 5.5.3.

branching ratio (σB) to dimuons are shown in Figure 6.31, with lower pole mass limits for various Z' scenarios (described in Section 2.3) as summarized in Table 6.3.

Model	Width [%]	θ_{E_6} [rad]	Lower limits on $M_{Z'}$ [TeV]					
			ee		$\mu\mu$		$\ell\ell$	
			Obs	Exp	Obs	Exp	Obs	Exp
Z'_{SSM}	3.0	-	4.3	4.3	4.0	3.9	4.5	4.5
Z'_χ	1.2	0.50 π	3.9	3.9	3.6	3.6	4.1	4.0
Z'_{S}	1.2	0.63 π	3.9	3.8	3.6	3.5	4.0	4.0
Z'_I	1.1	0.71 π	3.8	3.8	3.5	3.4	4.0	3.9
Z'_η	0.6	0.21 π	3.7	3.7	3.4	3.3	3.9	3.8
Z'_{N}	0.6	-0.08 π	3.6	3.6	3.4	3.3	3.8	3.8
Z'_ψ	0.5	0 π	3.6	3.6	3.3	3.2	3.8	3.7

Table 6.3: Results from October 2017 (JHEP): Observed and expected 95% C.L. lower mass limits in various Z' scenarios [112]. The widths are quoted as a percentage of the resonance mass. The variable θ_{E_6} is an angle related to the definition of the Z' in the various scenarios.

6.4.2 Minimal Z' models

The dilepton high-mass resonance search paper from July 2014 [1], using the full 2012 8 TeV dataset (20.5 fb^{-1}), included exclusion limits on minimal Z' models (briefly described in

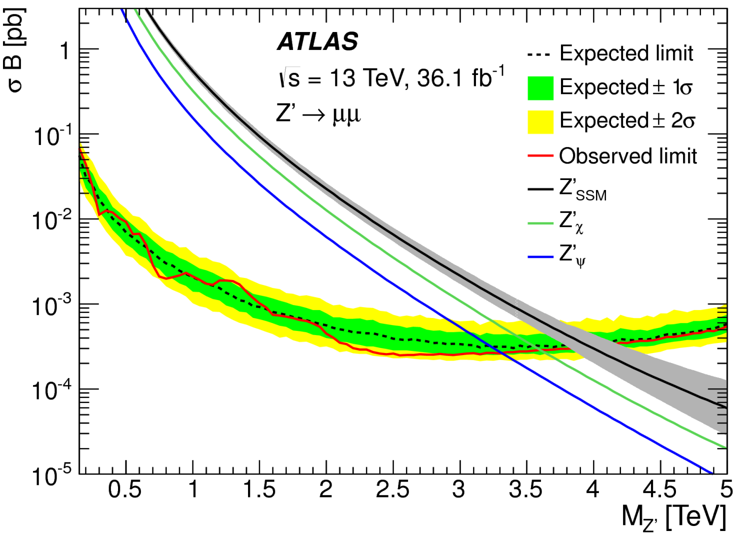

Figure 6.31: Results from October 2017 (JHEP): Upper 95% C.L. limits on the Z' production cross-section times branching ratio to two muons calculated for the Z'_χ, with theory lines for three different Z' models [112]. The theoretical uncertainty on the $Z'_{\rm SSM}$ is shown as a band for illustration purposes, but is not included in the σB limit calculation.

Section 2.3.0.3). The dilepton group decided to revive this for the 2017 publication, and I volunteered to work on it.

A lot of work went into reviving and validating the signal reweighting code used in the 2014 publication. As the minimal models include some of the regular Z' modes, like Z'_χ, I was able to compare the signal reweighting code used in the minimal Z' models to the signal samples created by the regular reweighting code used within the dilepton search group to set the regular cross-section exclusion limits. The two codes sprang from the same source, but diverged many years before. The most noticeable difference was that the Z' width in one case was based on scaling the Z^0 width (the regular code), while in the other case the Z' width was calculated theoretically from scratch (the minimal Z' models code). It actually turned out that there was a bug in the regular reweighting code, affecting the low mass region: The calculation of the width of a new Z' boson opens up to $t\bar{t}$ decay at two times the top qark mass, at around 350 GeV, and in the regular reweighting code, a missing factor in the calculated mass-dependent Z' width caused a rather abrupt step at this point. The dilepton group later adopted the minimal Z' models code to use for all reweighting.

6.4.2.1 Statistical framework

In Chapter 5.4 the statistical framework for the regular dimuon resonance search analysis is described. The statistical framework used in the case of minimal Z' models is somewhat different because the new hypothetical $Z'_{\rm Min}$ boson is considered together with the SM DY process, $q\bar{q} \to Z^0/\gamma/Z'_{\rm Min} \to \mu^+\mu^-$, to ensure that interference effects can be taken properly into account. In the regular statistical analysis, we consider a likelihood $\mathcal{L}$ (as defined in

Equation 5.2)

$$\mathcal{L}(\sigma, \boldsymbol{\theta}) = \prod_{k=1}^{N_{\text{chan}}} \prod_{l=1}^{N_{\text{bin}}} \frac{\lambda_{kl}^{n_{kl}}(\sigma, \boldsymbol{\theta}) e^{-\lambda_{kl}(\sigma, \boldsymbol{\theta})}}{n_{kl}!},$$

where the expectation value $\lambda_{kl}(\sigma, \boldsymbol{\theta})$ is a sum of the expected signal and background,

$$\lambda_{kl}(\sigma, \boldsymbol{\theta}) = s_{kl}(\sigma, \boldsymbol{\theta}) + b_{kl}(\boldsymbol{\theta}).$$

We remind the reader that k is the channel and l is the mass bin. The prior on the signal cross-section σ is flat.

The situation for the minimal Z' models is similar, but with a few important differences. Like before, the likelihood is a product of independent Poisson distributions,

$$\mathcal{L}(\gamma'^4, \boldsymbol{\theta}) = \prod_{k=1}^{N_{\text{chan}}} \prod_{l=1}^{N_{\text{bin}}} \frac{\lambda_{kl}^{n_{kl}}(\gamma'^4, \boldsymbol{\theta}) e^{-\lambda_{kl}(\gamma'^4, \boldsymbol{\theta})}}{n_{kl}!}, \tag{6.2}$$

but the expectation value $\lambda_{kl}(\gamma'^4, \boldsymbol{\theta})$ is now the sum of the expectation values of the process $q\bar{q} \to Z^0/\gamma/Z'_{\text{Min}} \to \mu^+\mu^-$ and the other backgrounds to the search ($t\bar{t}$ and diboson events),

$$\lambda_{kl}(\gamma'^4, \boldsymbol{\theta}) = \lambda_{\text{DY},kl}(\gamma'^4, \boldsymbol{\theta}) + \lambda_{\text{other},kl}(\boldsymbol{\theta}). \tag{6.3}$$

The parameter of interest is the γ' (defined in Equation (2.2)), which is one of the two effective coupling constants of the theory. The other effective coupling constant, θ_{Min}, is given a specific value that corresponds to a specific Z' theory. A flat prior is used on γ'^4, as the cross-section of the Z' is proportional to γ'^4 at leading order.

6.4.2.2 Z'_{Min} signal reweighting from SM Drell-Yan MC samples

In much the same way as explained in Section 4.5.2 the DY MC samples are reweighted to Z' samples, using the ratio of the differential cross-section of the Z'_{Min} over the one for the SM DY process for a given reconstructed invariant mass. The difference now is that we added a new dimension to the procedure: where we normally would define a small set of Z' models beforehand and then calculate the ratios for each, we now define a signal grid in the γ'^4 dimension (fixing the other parameter to a specific value, as mentioned before) and calculate the ratio for each of these. This is an important distinction, as it allows us to properly account for width effects in the limit setting, as the width of the Z' depends on the two effective coupling constants (γ' and θ_{Min}). Figure 6.32 shows the result of the rewighting procedure for two Z' pole masses, 130 GeV (a) and 2.5 TeV (b).

If we slice up the surface plots in Figure 6.32(a) parallel to the γ'^4-plane, we get curves like the ones in Figure 6.33. The curve in Figure 6.33(a) is on the Z' pole mass at dimuon invariant mass 130 GeV, and the curve in Figure 6.33(b) is away from the pole mass, the exact point is not important. These curves represent the $\lambda_{\text{DY},kl}$ in Equation (6.3). We note that when the reconstructed dimuon mass is away from the signal pole mass, γ'^4 is proportional to the cross-section (number of events), while when it is on the signal pole mass, then γ'^4 is not proportional to the cross-section.

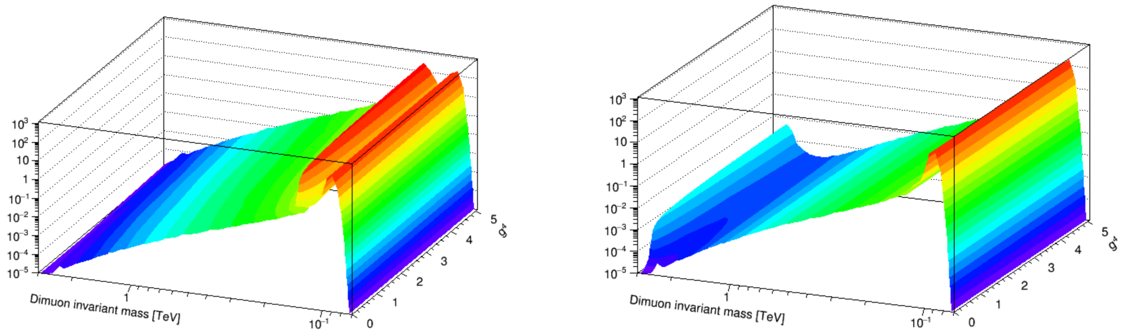

(a) Z'_{Min} pole mass 130 GeV surface plot

(b) Z'_{Min} pole mass 2.5 TeV surface plot

Figure 6.32: Surface plots for the Z'_{Min} with a mass of 130 GeV (a) and 2.5 TeV (b), with the one of the parameters of the theory γ'^4 (marked as g^4 in the plots) on the x-axis and the reconstructed invariant dimuon mass on the y-axis. Each slice in g^4 is scaled to the Z^0 peak, which was the procedure followed by the dilepton group at that point in time.

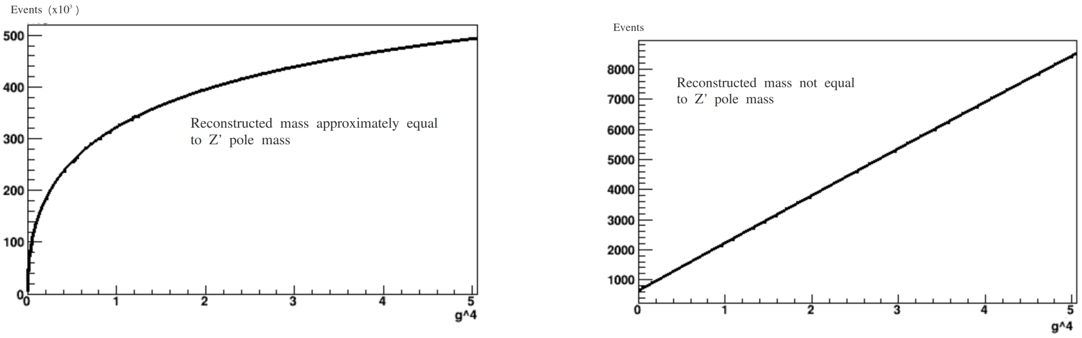

(a) Reconstructed dimuon mass at the Z'_{Min} pole mass.

(b) Reconstructed dimuon mass away from Z'_{Min} pole mass.

Figure 6.33: Curves that represent profiles of the surface plots in Figure 6.32(a) in a plane parallel to the γ'^4-plane.

As in Section 5.4.3, the Bayesian Analysis Toolkit was used to marginalize $p(\gamma'^4, \boldsymbol{\theta}|\boldsymbol{n})$ to get a posterior distribution for the parameter of interest, the coupling γ'^4 (for a specific value of θ_{Min}).

6.4.2.3 Published results

The results for the Z' minimal model analysis were published in July 2017 using 36 fb^{-1} of proton-proton collision data [23]. Figure 6.34 shows the exclusion limits set at 95% C.L. on the parameter γ' as a function of the Z'_{Min} boson mass in the dilepton channel. The two values of θ_{Min} yielding the minimum and maximum cross-sections are used to define a band of limits in the $(\gamma', M_{Z'_{\text{Min}}})$ plane. Lower mass limits on Z'_{Min} are set on three specific Z' models, as listed in Table 6.4. Comparing the numbers for the Z'_χ to the ones for Z'_χ in Table 6.3, we see that they lie around 200-300 GeV lower. This is due to the difference in priors - the regular σB analysis uses a flat prior on the cross-section σ of the Z', while the minimal model analysis uses a flat prior on γ'^4. It was checked that when fixating the width to the Z'_χ width, the results were identical. When the width is fixed, the cross-section is proportional to the γ'^4 and the two priors are equivalent. When the width is allowed to vary

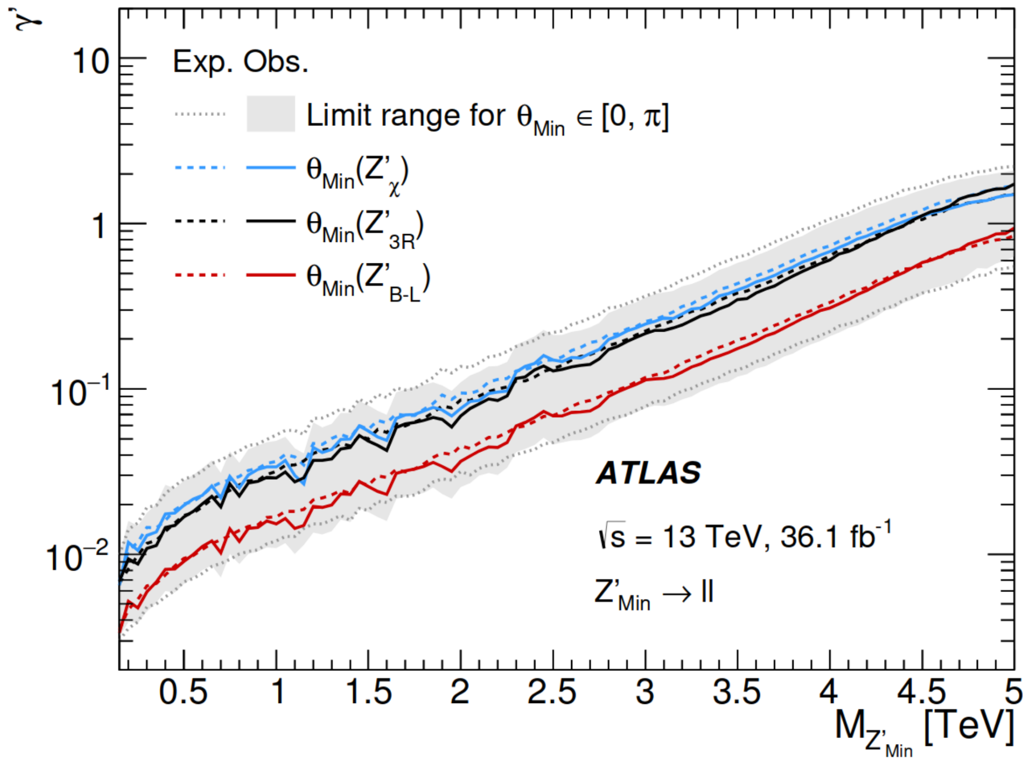

Figure 6.34: Results from October 2017 (JHEP): Expected (dotted and dashed lines) and observed (filled area and lines) exclusion limits set at 95% C.L. on the relative coupling strength γ' for the dilepton channel as a function of the Z'_{Min} mass [23]. Three representative values of the mixing angle θ_{Min} are selected and limit curves are shown for these ($Z'_{\text{B-L}}$, Z'_{3R} and Z'_χ). The region above each line is excluded. The grey band envelops all observed limit curves, which depends on the choice of $\theta_{\text{Min}} \in [0, \pi]$.

with the parameter γ',[4] the two priors are not equivalent, and there is a slight impact on the lower mass limits from this.

Model	Lower limits on $M_{Z'_{\mathrm{Min}}}$ [TeV]					
	ee		$\mu\mu$		ll	
	Obs	Exp	Obs	Exp	Obs	Exp
Z'_χ	3.7	3.7	3.4	3.3	3.9	3.8
Z'_{3R}	4.0	3.9	3.6	3.6	4.1	4.1
$Z'_{\mathrm{B-L}}$	4.0	4.0	3.6	3.6	4.2	4.1

Table 6.4: Lower mass limits on three specific minimal Z' models [23].

6.5 Summary

In this chapter, we reviewed the four publications that I personally contributed to in the years before the publication in 2019 (described in Section 5.5 using the full Run 2 dataset). During these years, I worked on the muon channel analysis, running the dimuon analysis and providing input for the statistical analysis. Also I revived, cleaned up and validated the code for setting exclusion limits on the minimal Z' models, which was used in both the dielectron and dimuon channel in the 2017 publication.

---

[4] And the parameter θ_{Min}, but this parameter is fixated to a specific value in the analysis.

Chapter 7

The fake background in the dimuon channel

In Chapter 5 we discussed in detail the full dimuon resonance search analysis, and in Chapter 6 we looked at related publications in the years between 2015 and 2018. We now turn our attention to a study that was performed as part of this thesis work, and also added to the additional material[1] [100] that accompanied the 2019 dilepton publication [120].

As discussed in Section 4.4.5, a data-driven method is needed to investigate the relative size of the W+jets and dijets background. This study is separated out from the main analysis chapters because the contribution was found to be negligible in the dimuon channel and therefore not included in the statistical analysis. Also, it was not included as a part of the dimuon background in the publications discussed in the two previous chapters.

In the following, we define a “real muon” as a prompt muon from for example leptonically decaying Z or W bosons and a “fake muon” as either a non-prompt muon, e.g. a real muon inside a jet or a wrongly reconstructed muon for example from energetic hadronic jets that punch through the calorimeters into the MS. A “real dimuon” or a “real muon pair” is a pair with two real muons, while a “fake dimuon” or a “fake muon pair” is either a real and a fake muon or two fake muons.

The fake background in the dimuon channel consists of events that contain fake dimuons. These fake dimuon events can originate from single top and $t\bar{t}$ events or diboson events. In addition there are large contributions from dijet and W+jets events, and a smaller contribution from the Z boson decaying leptonically in association with jets, where one lepton is not reconstructed. For the dijets, the two main contributors to the fake background are the heavy-flavor dijets, $c\bar{c}$ and $b\bar{b}$, because the b and c quarks can decay semi-leptonically, resulting in muons inside the jets. Figures 7.1(a) illustrates the main production channels for the heavy-flavor dijets and Figure 7.1(b) a probable production channel for the W boson produced in association with a jet. We expect the fake background in the dimuon channel to be negligible for high-p_{T} muons, but we need a measurement to confirm this. One possibility is to do a data-driven estimate of the fake background, as is done for the dielectron channel [23]. However, for the dielectron channel it is a different matter, as the fake background is non-negligible. We employ a less time and resource demanding method, because the goal here is

---

[1] Only available for members of the ATLAS Collaboration.

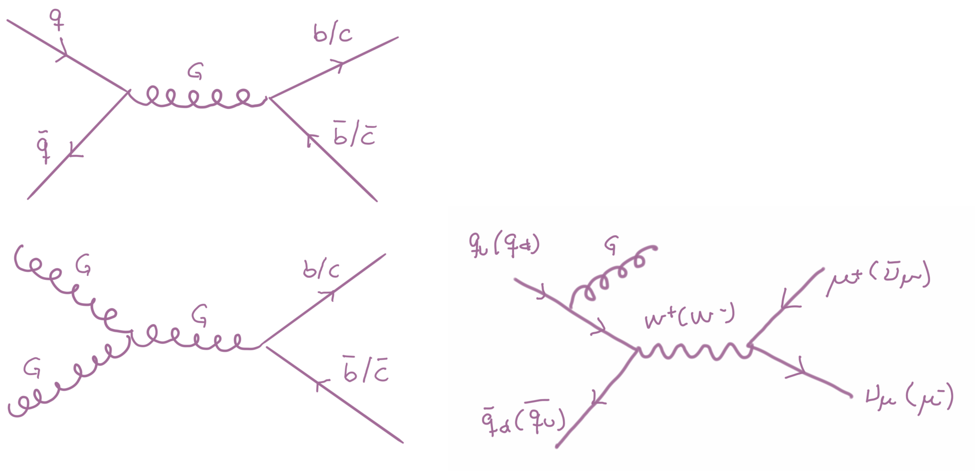

(a) $b\bar{b}$ and $c\bar{c}$ production. (b) W boson produced in association with a jet.

Figure 7.1: Feynman diagrams of $c\bar{c}$ and $b\bar{b}$ production (a) and W boson produced in association with a jet (b).

to confirm or refute the negligibility of the high-mass dimuon fake background.

7.1 MC samples

The samples used in this study are, in addition to the ones listed in Section 4.4,[2] dedicated fake-enriched samples, listed in Section B.3.

7.1.1 Dijets

There is one sample for each heavy-flavor dijet channel ($b\bar{b}$ and $c\bar{c}$) with requirements on at least one of the quarks at truth level ($p_{\mathrm{T}} > 15\,\mathrm{GeV}$ and $|\eta| < 4.5$) and at least one reconstructed muon in each event. These samples were made with PYTHIA 8 using the NNPDF 2.3 LO PDF set and the ATLAS A14 set of tuned parameters for parton showering and hadronization.

7.1.2 Top

The $t\bar{t}$ samples were generated with POWHEG BOX using the NNPDF 3.0 NLO PDF set, with PYTHIA 8 handling the parton showering with the NNPDF 2.3 LO PDF set and the ATLAS A14 set of parameter tunes (the same as the dilepton filtered $t\bar{t}$ sample described in Section 4.4.4). For both the $t\bar{t}$ MC samples a flat k-factor is applied, the value of which is 1.14 as in the case for the $t\bar{t}$ MC sample with a dilepton filter, described in Section 4.4.6.

---

[2] Not including the $t\bar{t}$ sample with dilepton filter, for this task we mainly use two other $t\bar{t}$ samples – one with a filter requiring at least one lepton and one with a filter requiring both top decays to be fully hadronic.

7.1.3 W boson in association with jets

The W+jets samples are generated with Sherpa (v2.2.1) using the NNPDF 3.0 PDF set, for the particle generation, parton showering and hadronization. The generation is performed separately for 0 to 4 jets at the matrix element level. The diagrams with 0, 1 or 2 jets are at the next-to-leading-order level, while the ones with 3 or 4 jets are at leading order. To get an adequate number of events over the full momentum (or mass) spectrum, these samples are generated in intervals of the transverse momentum of the W boson with b- and c-quark filters. For W bosons with transverse momentum above 500 GeV, there is no quark filter in the samples. A flat k-factor of 0.9702 is applied to all samples.

7.2 An outline of the QCD background estimation method

We now briefly describe the method to make it easier for the reader to follow the detailed description that follows directly after this section. Refer to Figure 7.2 for an overview of the different sets of selections in use.

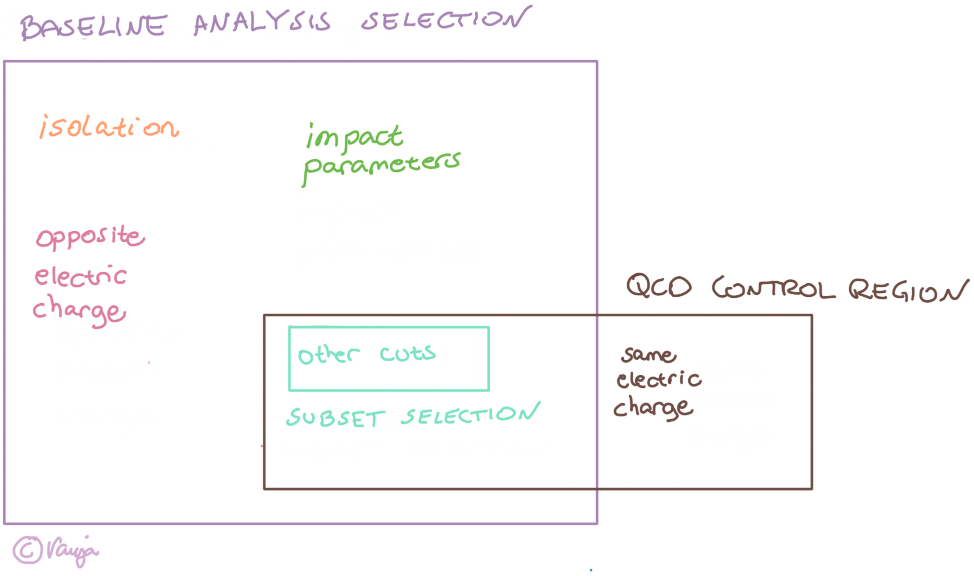

Figure 7.2: A schematic drawing showing the different selections (cuts) used in the estimation of the QCD background. The full baseline analysis selection is listed in Table 5.1.

We define a set of cuts that contain a subset of the set of baseline analysis cuts,[3] removing the cuts on the muon isolation, impact parameters and electric charge (further explained in Section 7.3). This subset should now contain both real and fake muon pairs. The muons are all of high quality due to the set of cuts ("other cuts") that are applied at this point, most

---

[3] A subset of the cuts, and a superset of the events, not to be confused with a subset of the events.

noticeably the high-p_T working point. We shall find here that dedicated hadronic dijet and W+jets samples are needed to describe the data in an intermediate invariant mass range.

The next step is to define a QCD-enriched region (a QCD control region (CR)) (as described in Section 7.4) by using the subset selection, and also requiring that the two leading muons have the *same* electric charge. We find again that data is well described by MC, only limited by too few MC events generated in the samples.

We now use the events in the QCD CR and require that they pass the cuts on muon isolation and the impact parameters, finding the efficiency of these cuts for fake dimuons, the “dimuon fake efficiency”.

The last step is combining the information from the invariant mass distribution in the subsets region with the dimuon fake efficiency measurement and estimating the amount of fake events left in the invariant mass distribution after the full set of analysis cuts, finding it to be negligible (Section 7.6).

We now continue on to the detailed description of this procedure.

7.3 A subset of full selection

We define the subset of the full selection using all requirements from Table 5.1 except isolation, $d_0^{\mathrm{BL}}(\sigma)$ and $\Delta z_0^{\mathrm{BL}} \cdot \sin\theta$ cuts and the opposite sign (opposite elctric charge) requirement. This is represented by the cyan-colored box marked “SUBSET SELECTION” in Figure 7.2. Figure 7.3(a) shows the dimuon invariant mass distribution in the subset region without MC samples for dijet and W+jets. There is an obvious mismatch between data and MC in mid-range masses, from about 100 GeV to about 500-600 GeV. When we add the dedicated dijet and W+jets MC samples, we get the result in Figure 7.3(b). Now we see that MC and data are in reasonable agreement. We conclude that there are non-negligible contributions to the background from dijet and W+jets processes, and that the dijet and W+jets processes

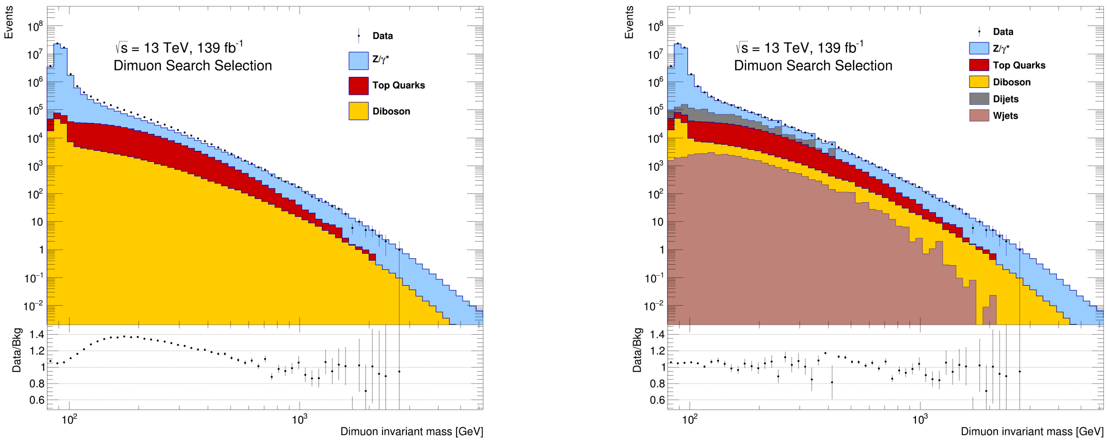

(a) Dimuon invariant mass distribution *without* dedicated QCD samples included.

(b) Dimuon invariant mass distribution *with* dedicated QCD samples included.

Figure 7.3: Dimuon invariant mass distribution after the subset selection without (a) and with (b) dedicated QCD samples included.

are sufficient to describe the high-mass (or high-p_T) fake background. The dijet samples suffer from lack of simulated data above a few hundred GeV and stops abruptly at around 400 GeV, but as we do not aim to estimate the fake background precisely, this is not regarded as a showstopper.

7.4 QCD control region

We now define a QCD control region (CR) by taking the events in the subset selection and requiring that the two leading muons have the *same* sign. This selection is represented by the dark brown-colored box marked “QCD CONTROL REGION” in Figure 7.2. The requirements are chosen to pick out high-quality muons in a QCD-enriched region.

Figure 7.4 shows the dimuon invariant mass distribution in the QCD control region. The dijet samples suffer from lack of simulated events at masses above about 200 GeV, but the data seems to continue on the path drawn by the stack of simulated data at lower masses, indicating that the missing pieces are the dijet samples only. We therefore conclude that the data and MC are roughly in agreement.

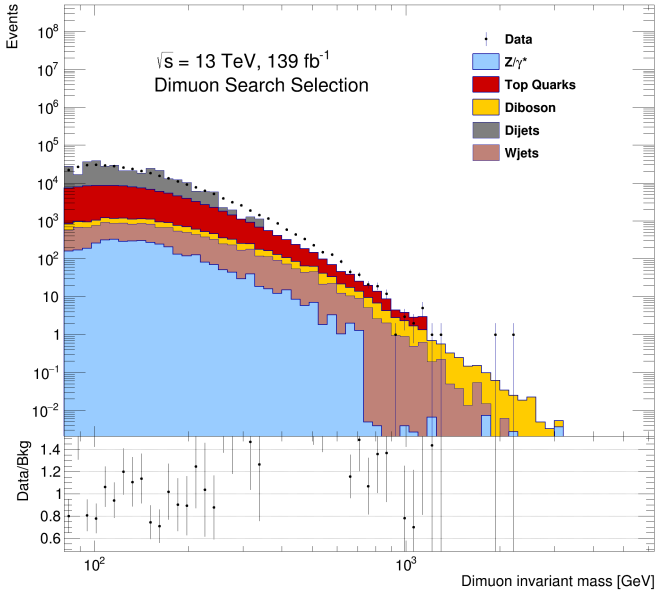

Figure 7.4: Data and MC in the QCD control region defined in Section 7.4.

7.4.1 QCD control region - composition of top and diboson backgrounds

We now want to estimate the dimuon fake efficiency of the impact parameter and isolation cuts. To get the best estimation of the dimuon fake efficiency, we ideally want the backgrounds to consist of fake muon pairs (with two fake muons or with one real muon and one fake muon) only. The DY background consists mostly of real dimuons (with two real muons), while the W+jets and dijets backgrounds are mostly fake dimuons (with two fake muons, or one real and one fake muon). The question now is what the mix is in the top and diboson backgrounds.

7.4.1.1 Fake/real composition of the top background

Figure 7.5(a) shows the full top background in the QCD control region decomposed into fully leptonic $t\bar{t}$, hadronic and semi-leptonic $t\bar{t}$, and single top components. The filled histograms are an estimate of the real contributions from the leptonic $t\bar{t}$ and Wt backgrounds, and how this is estimated will be explained shortly.

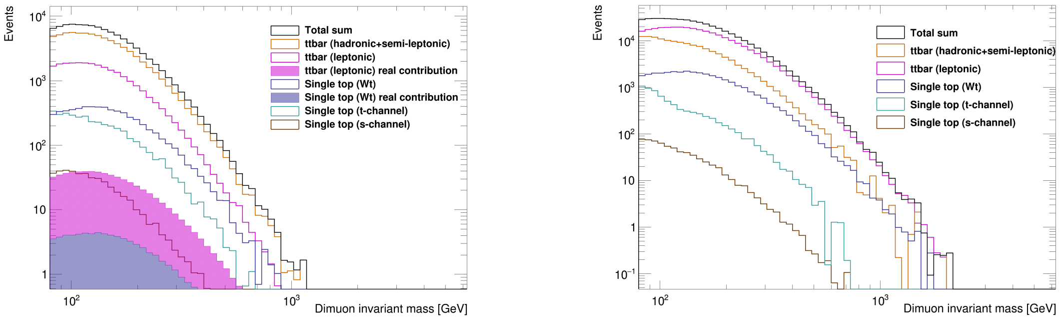

(a) QCD control region (with same sign requirement). The filled histograms contain the estimated real contribution of the named processes.

(b) Subset region (no requirement on the sign of the two muons).

Figure 7.5: The total top background decomposed into fully leptonic $t\bar{t}$, hadronic and semi-leptonic $t\bar{t}$, and single top components.

The s-channel and t-channel single top components (illustrated in Figure 4.13) contribute to the fake background. The fully leptonic $t\bar{t}$ (as illustrated in Figure 4.11) and the Wt associated single top production mode (as illustrated in Figure 4.12) contribute with both real and fake dimuon pairs, but the real component is thought to be low due to the two real muons in these types of events have opposite electrical charge and therefore do not pass the requirement of the QCD CR.

To investigate this further we take a look at the top background in the subset region. This is shown in Figure 7.5(b). We assume that most of the events in the fully leptonic $t\bar{t}$ and the Wt associated single top production mode components in the subset region are real muons due to the fact that we have required at least two reconstructed high-quality muons in the subset region. The charge misidentification probability for muons is very small, $< 0.1\%$ [95] throughout the whole p_{T} spectrum, which means that less than 0.2% of the real dimuon events[4] in the mentioned components of the $t\bar{t}$ background are left after requiring that the two leading muons in the events in the QCD CR have the same sign. The filled histograms in Figure 7.5(a) are calculated by scaling the dimuon invariant mass distributions in the subset region as shown in Figure 7.5(b) by the charge misidentification rate for the two muons (0.2%), and they represent the real contrbutions from the $t\bar{t}$ and Wt processes in the QCD CR. This means that by far most of the events from the dilepton and Wt associated single top production mode components of the top background in the QCD control region are fake dimuons, which is exactly what we hoped for.

---

[4] These are the events where one of the two muons are reconstructed with the wrong charge.

7.4.1.2 Fake/real composition of the diboson background

The diboson background in the QCD CR is shown in Figure 7.6, with its individual components. The two leading components, $WZ \to l\nu\mu\mu$ and $ZZ \to ll\mu\mu$ are composed of real muon pairs, as these components have respectivly three or four real muons,[5] thus enabling the combination of two real muons of the same sign to be picked out. The $WW \to \mu\nu\mu\nu$ and $WZ/ZZ \to qq\mu\mu$ components have two real muons of opposite charge, and the events passing the requirements for the QCD control region are either one real muon paired with one fake muon, or two real muons where one of them has been assigned the wrong charge. A similar analysis using the charge misidentification rate to estimate the real contribution in the QCD CR as was done for the top background could also be done for these two components, but as they are the smallest ones and because we already concluded that the two largest ones are real-dominated,[6] we decide this is not necessary, and conclude that the diboson background is composed of mostly real muon pairs, in contrast to the top background that in the QCD CR is composed mostly of fake muon pairs. Looking at the dimuon invariant mass in the QCD CR in Figure 7.4, we see that the diboson process is much smaller than the contribution from the top processes at lower masses, but has increasing relative importance approaching an invariant mass of approximately 1 TeV.

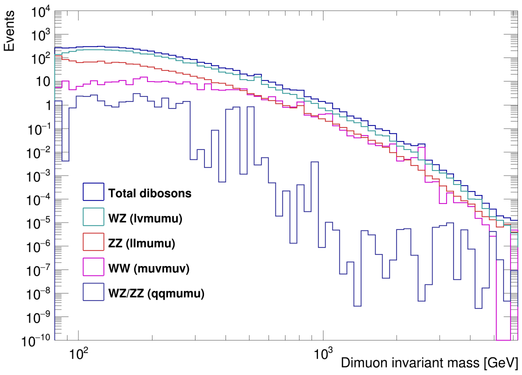

Figure 7.6: The total diboson background in the QCD control region, showing the four different components. Both the largest (WZ) and second largest (ZZ) components contribute with real muon pairs.

7.5 The dimuon fake efficiency

We now proceed by requiring that the events in the QCD CR (as shown in Figure 7.4) pass the regular analysis requirements on muon isolation and on the transverse and longitudinal impact parameters as described in Table 5.1. In Figure 7.7 we see the effect of the individual cuts in 7.7(a) - 7.7(c) and the effect of the combined cuts in 7.7(d). We see that isolation is the requirement that removes by far most events. We also note that the dijet MC contains too few events to describe data, creating the disagreement observed between data and MC. Although

---

[5] The ’l’ can also be an electron, but we have actively picked out the muons.

[6] We note that the WW component contributes the same amount to the total diboson background as the ZZ component at masses above 400 GeV, but as the main contribution is the WZ component over the whole mass range, and because the diboson contribution in the QCD CR in the mid-range masses is lower than the dijets and top background components (as shown in Figure 7.4), this does not change the arguments or the conclusion.

we no longer can rely on simulated data, we can use the real collision data to estimate the efficiency of these cuts on same sign muon pairs. Later we will use this information to estimate the amount of fake muon pairs in opposite sign events. We assume that the dimuon fake efficiency is independent of the charges of the muons.

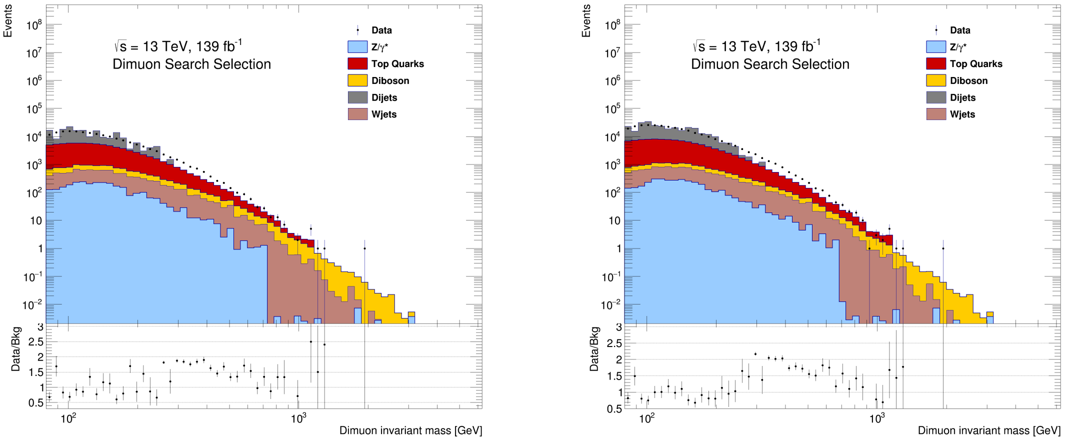

(a) With requirement on $d_0^{\mathrm{BL}}(\sigma)$.

(b) With requirement on $\Delta z_0^{\mathrm{BL}} \cdot \sin\theta$.

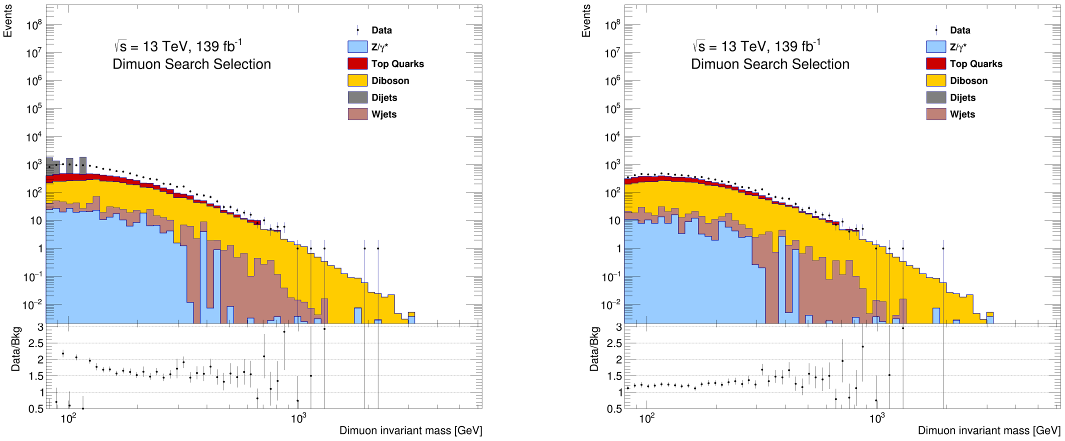

(c) With requirement on isolation.

(d) With all three requirements.

Figure 7.7: Applying three cuts to the QCD control region (Figure 7.4), isolation, transverse impact parameter with respect to the beam line, $d_0^{\mathrm{BL}}(\sigma)$, and longitudinal impact parameter with respect to the reconstructed primary vertex $\Delta z_0^{\mathrm{BL}} \cdot \sin\theta$, individually in subfigures 7.7(a) to 7.7(c) and combined in Figure 7.7(d).

Figure 7.8 displays the ratio defined by the number of events after the combined impact parameter and isolation cuts divided by the number of events before, in the QCD control region, as a function of the dimuon invariant mass. This is an estimate of the dimuon fake efficiency, i.e. the rate at which fake dimuon pairs pass the cuts. The estimate is conservative, as we know there is a non-negligible amount of real dimuons in the mix, most prominently from the diboson background, with increasing relative importance at higher masses. The efficiency goes up with increasing invariant mass, and we interpret this as an effect due to the increasing relative importance of the diboson background, consisting mostly of real dimuon pairs, at higher masses. In a more thorough study, we would subtract the real dimuons from

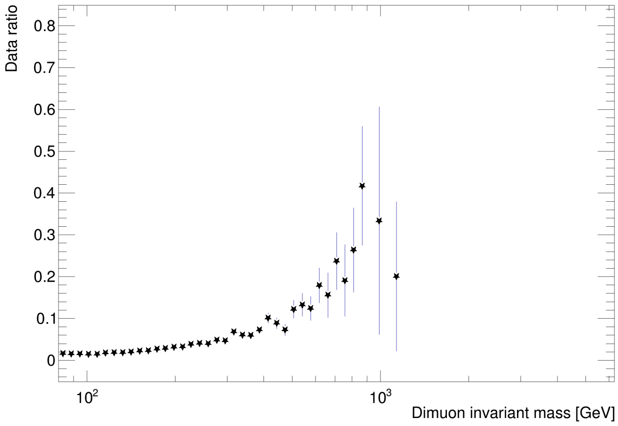

Figure 7.8: The efficiency of the combined $d_0^{\mathrm{BL}}(\sigma)$, $\Delta z_0^{\mathrm{BL}} \cdot \sin\theta$ and isolation cuts on the QCD CR events as a function of the dimuon invariant mass (dimuon fake efficiency).

this dimuon fake efficiency estimate, but as we will only make a statement about whether or not the fake background is negligible, we are satisfied with this somewhat rough, conservative estimate. In any case, we see that these three cuts are very efficient in removing fake dimuon events.

7.6 The negligibility of the QCD background

We can now produce a dimuon invariant mass distribution after all the baseline analysis cuts (illustrated schematically in Figure 7.2) with a rough estimate of the fake background included. To achieve this, we require that the dijets and W+jets dimuons in the subset region (as shown in Figure 7.3(b)) have opposite charge and multiply in the dimuon fake efficiency as shown in Figure 7.8, bin by bin in invariant mass. This leaves us with a conservative estimate of the fake background. In Figure 7.9 we see the final selection with this fake background estimate. We see, as expected, that the fake background contributes far less than the smallest background component included (dibosons).

If the plot leaves any reader feeling uneasy because of the obvious lack of dijet events at masses above a few hundred GeV, leaving room for suspicion of an increasing dijet importance, we would like to remind the reader that the QCD background is important only in the invariant mass range between 100 GeV and 500-600 GeV, as discussed in Section 7.3, and that there is no reason to think that the relative importance of the QCD background has increased between that distribution and the dimuon invariant mass distribution after all analysis cuts, but rather the opposite.

7.7 Summary

In this section, we used a simple method for confirming that the fake background in the dimuon channel is indeed negligible.

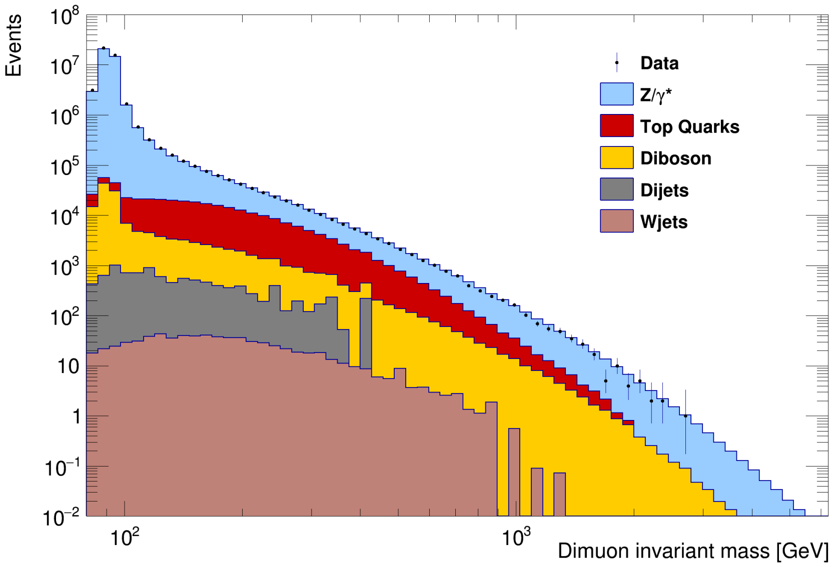

Figure 7.9: Dimuon invariant mass distribution after full selection (Table 5.1), including a conservative estimate of the fake background (dijets and W+jets).

Chapter 8

Particle physics outreach – bringing discoveries to the classroom

The experimental particle physics world is complicated, using a framework of mathematics and statistics, and knowledge specific to the field that is not accessible to most people. This is not unique to our field, but a more general statement about research. Because of this, researchers in every field of science have a responsibility to communicate discoveries, plans and prospects with the governments and politicians, the scientific community as a whole and the general public, including teachers and students. Not only to generate funds to enable the research to continue in the future, but also to recruit a new generation of researchers to ensure that the scientific field keeps evolving, and to share the enormous excitement we feel about our work. CERN does this in many ways, including but not limited to online communication and social media, exhibitions and teacher and student programs, and virtual visits as well as on-site visits. One such program is the International Masterclasses.

8.1 The International hands-on particle physics Masterclasses

The International hands-on particle physics Masterclasses is a yearly event where more than 13 000 high school students in 55 countries visit one of the 225 participating universities or research facilities in their vicinity and get to be particle physicists for one day [131]. This idea has been in development ever since the first particle physics masterclass in the UK in the mid 1990's. The masterclasses were named "Hands-on CERN" and used real data from the OPAL and DELPHI experiments at the Large Electron-Positron Collider (LEP). In 2005 the European Particle Physics Outreach Group (EPOG, now IPPOG – The International Particle Physics Outreach Group) extended the concept.

The concept kept evolving, and when LHC data became available, the Masterclasses were updated with this. The last masterclass with data from LEP was held in 2010, and the first masterclass with real data from LHC was arranged the same year [132] .

IPPOG [133] has 33 members: 26 countries, 6 experiments[1] and CERN as an international laboratory. According to their website "IPPOG is a network of scientists, science

---

[1] The ATLAS Collaboration, the LHCb Collaboration, the CMS Collaboration, the HAWC Collaboration, the Belle II Collaboration, and DESY.

educators and communication specialists working across the globe in science education and public outreach for particle physics. Particle physics is the science of matter, energy, space and time. IPPOG brings new discoveries in this exciting field to young people and conveys to the public that the beauty of nature is indeed becoming understandable from the interactions of its most fundamental parts – the elementary particles."

Among the several hands-on Particle Physics Masterclasses that are arranged these days, the Z-path is the most popular one. The Z-path measurements were developed to a large degree at the University of Oslo. We use data from the ATLAS detector, the invariant mass technique, an event display program and a result display program to allow the students to find interesting events by eye, look at their results in histograms, and explore the power of statistics by adding up the contribution from each pair of students, and even from the different institutes, to view the grand total.

In the following we focus on the description around the result display program, which was developed by me as part of my thesis work.

8.2 From a student's point of view – The Z-path

This section is based on the Norwegian program. Different countries and institutes might arrange their day differently.

Since the start, the interest has been increasing. 2018 is the record year, when more than 500 students and 30 teachers came to the University of Oslo to be particle physicists for a day. In the following, a typical Z-Path day is described.

8.2.1 Lectures

The students arrive in the morning and the first lecture starts at 10:00 am. There are two lectures in a row until lunch at 12:00. In these lectures, the students learn about particle accelerators and LHC and the ATLAS experiment, and about particle physics in general. After lunch, at 12:45, the students come back for a brief introduction to the actual measurements they are about to perform. The experimental session starts at about 13:30.

8.2.2 The experiment

We have developed a Norwegian web page, as pictured in Figure 8.1, for the students to refer to for instructions [131]. This page is not used a lot during the few intense hours of data analysis, but teachers at the different schools are welcome to use it in preparation of the day, or after the event.

Each group, consisting of 2 students, download their own set of unique events, 50 in total. Each event is viewed in an event display named HYPATIA (HYbrid Pupil's Analysis Tool for Interactions in ATLAS) [134]. An example is shown in Figure 8.2. It is possible to turn on or off a large number of different cuts. We have turned on a set of default cuts, and we usually advise them to tune the p_T cut a bit, while keeping it at a sensible level (e.g. 5 GeV).

Z-Sporet

Velkommen til Z-sporet! Her skal du lære om noen av partiklene, slik som Z- og Higgs-bosonet, og deres betydning for vår forståelse av naturen. Til å hjelpe deg med denne oppgaven skal du ta i bruk ekte ATLAS data fra The Large Hadron Collider (LHC) ved CERN.

Før vi begynner med denne oppgaven tar vi deg med på en reise inn til de minste strukturene menneskeheten kjenner: elementærpartiklene. Du får se hvordan disse kan produseres i proton-proton kollisjoner ved LHC, og lære hvordan du kan identifisere elementærpartiklene i ATLAS-detektoren. Deretter skal du utføre en virkelig fysikkmåling på ferske data fra ATLAS detektoren: identifisere Z- bosonet og andre lettere partikler og måle deres egenskaper! Du vil få muligheten til å lete etter Higgs-bosonet med lignende metoder som fysikere ved ATLAS bruker. Du vil da innse at du mestrer et redskap for å oppdage det ukjente!

Z-sporet

- Introduksjon av Z-bosonet
- Introduksjon av Higgs-bosonet
- Ny fysikk
- Partikkelidentifikasjon
- Event-identifikasjon
- Søk og oppdag med masserekonstruksjon
- Sett igang!

Opplysningssenter

- Forskning ved LHC
- Standardmodellen
- Mer om Z-bosonet
- Ekstra dimensjoner og gravitasjon
- Supersymmetri
- Massefart
- Egenspinn
- Energienheter
- Vektorer
- Histogrammer
- Radioaktivitet og W-bosonet
- Feynman-diagrammer

Figure 8.1: Welcome to the web page the Oslo group developed as part of the Z-path educational material [131].

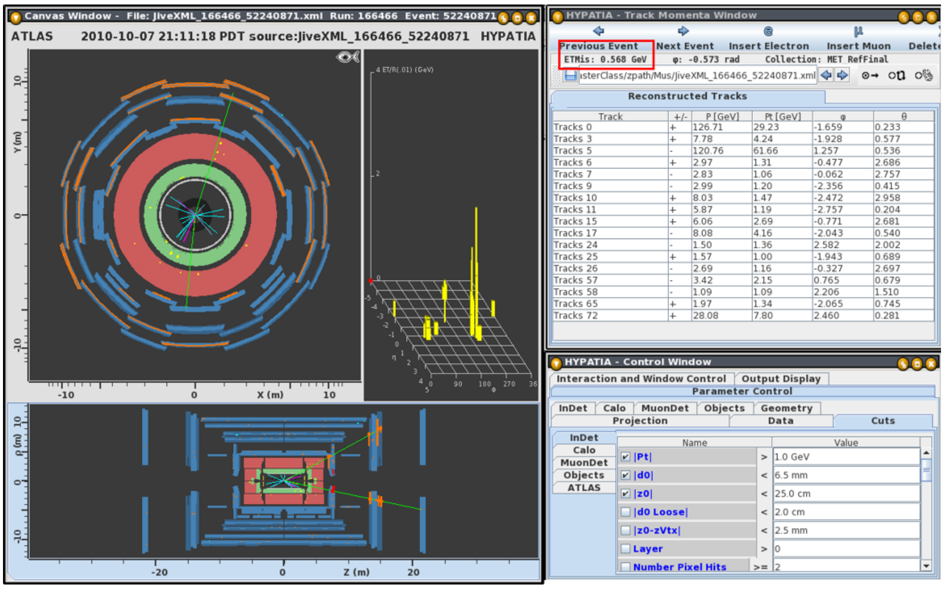

ETMis: 0.568 GeV φ: -0.573 rad Collection: MET RefFinal

asterClass/zpath/Mus/JiveXML_166466_52240871.xml

Track	+/-	P [GeV]	Pt [GeV]	φ	θ
Tracks 0	+	126.71	29.23	-1.659	0.233
Tracks 3	+	7.78	4.24	-1.928	0.577
Tracks 5	-	120.76	61.66	1.257	0.536
Tracks 6	+	2.97	1.31	-0.477	2.686
Tracks 7	-	2.83	1.06	-0.062	2.757
Tracks 9	-	2.99	1.20	-2.356	0.415
Tracks 10	+	8.03	1.47	-2.472	2.958
Tracks 11	+	5.87	1.19	-2.757	0.204
Tracks 15	+	6.06	2.69	-0.771	2.681
Tracks 17	-	8.08	4.16	-2.043	0.540
Tracks 24	-	1.50	1.36	2.582	2.002
Tracks 25	+	1.57	1.00	-1.943	0.689
Tracks 26	-	2.69	1.16	-0.327	2.697
Tracks 57	-	3.42	2.15	0.765	0.679
Tracks 58	-	1.09	1.09	2.206	1.510
Tracks 65	+	1.97	1.34	-2.065	0.745
Tracks 72	+	28.08	7.80	2.460	0.281

Name		Value
☑ |Pt|	>	1.0 GeV
☑ |d0|	<	6.5 mm
☑ |z0|	<	25.0 cm
☐ |d0 Loose|	<	2.0 cm
☐ |z0-zVtx|	<	2.5 mm
☐ Layer	>	0
☐ Number Pixel Hits	>=	2

Figure 8.2: An event viewed in the event display HYPATIA.

In each event, they find either two electrons, two muons, two photons, four muons, four electrons or two muons and two electrons. There are no background events in the sample.[2] When they find particles they think are in one of the categories of interest, they mark them and add them to the invariant mass table. The mass is automatically calculated. Only pairs of leptons with opposite electric charges are accepted.

Usually the majority of the students make it through the whole set of 50 events, and some do not. Either way, every pair of students upload their results in OPloT [135], the Oslo Plotting Tool.

8.2.3 Local discussion of results

The students get a 15 minute break before coming back to the lecture room to discuss the results and to prepare for the video conference. At this point in time, the students seem to feel somewhat exhausted, and thus we come to one of the high-points of the afternoon – the bun tossing. This ensures that the bags of buns are delivered to the students in the shortest possible time, while invigorating the cheering students, as illustrated in Figure 8.3.

Figure 8.3: Eager students and an airborne pack of buns.

Figure 8.4(a) shows the results from one of the groups in Oslo. We see three histograms. Dilepton invariant mass on top, further separated into dielectrons and dimuons in two colors of blue (stacked histograms), on a logarithmic axis. Four-lepton invariant mass is in the middle, on a linear scale. Diphoton invariant mass is on the bottom, also on a linear scale. We see that there are a few gatherings of events, but the total number of events is low. Because all the student pairs were given unique datasets to analyze, it is possible to combine the results from every group into a result for the institute, as shown in Figure 8.4(b). In the lower right corner we see the expected number of events and the number found by the students, divided into the three different channels, and the combined number of events. This is a typical result: A large fraction of the dilepton and diphoton events are found, and too many four-lepton events are identified.

---

[2] Even so there are always at least a handful of events that do not seem to be signal events, even when examined by one of the expert tutors. This is a part of the full particle physicist-experience.

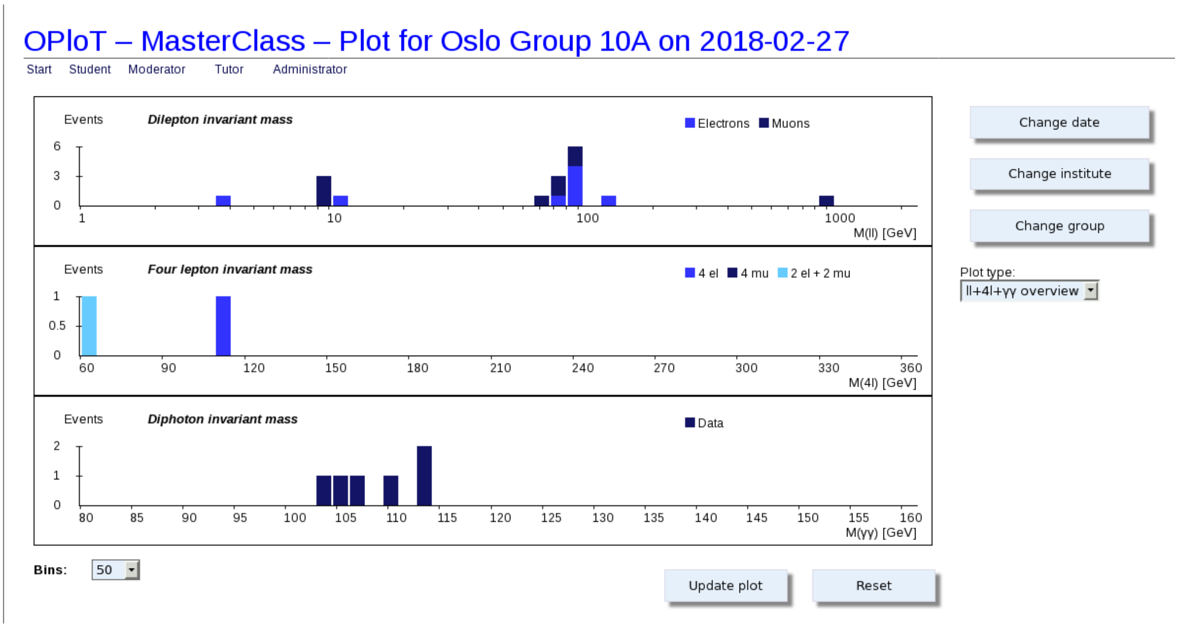

OPloT – MasterClass – Plot for Oslo Group 10A on 2018-02-27

Plot type: ll+4l+γγ overview

Bins: 50

(a) The results from one group in Oslo on February 27, 2018.

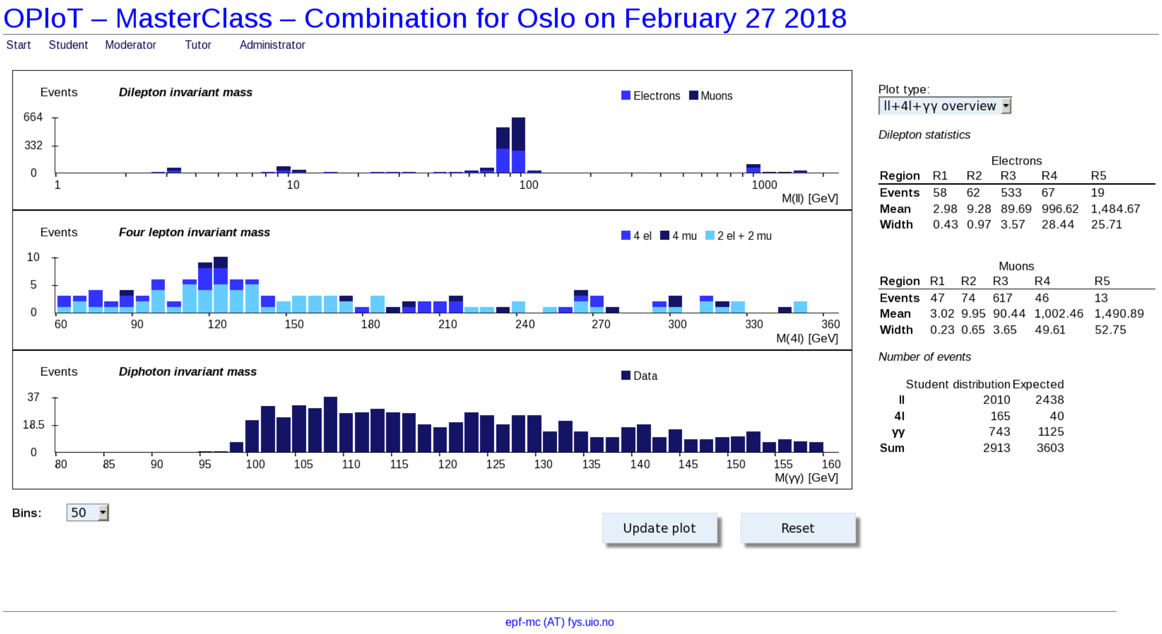

OPloT – MasterClass – Combination for Oslo on February 27 2018

Plot type: ll+4l+γγ overview

Dilepton statistics

Electrons

Region	R1	R2	R3	R4	R5
Events	58	62	533	67	19
Mean	2.98	9.28	89.69	996.62	1,484.67
Width	0.43	0.97	3.57	28.44	25.71

Muons

Region	R1	R2	R3	R4	R5
Events	47	74	617	46	13
Mean	3.02	9.95	90.44	1,002.46	1,490.89
Width	0.23	0.65	3.65	49.61	52.75

Number of events

	Student distribution	Expected
ll	2010	2438
4l	165	40
γγ	743	1125
Sum	2913	3603

Bins: 50

epf-mc (AT) fys.uio.no

(b) The combined result from all the groups in Oslo on February 27, 2018.

Figure 8.4: Results from the Oslo Masterclass on February 27, 2018, for a single group (top) and for the whole institute combined (bottom).

Now we look at the three different channels separately, for all the groups combined.

8.2.3.1 Dilepton events

It is possible to choose between linear and logarithmic x-axis, and also what parts of the x-axis to show, in addition to the number of bins. Usually though we keep to the default, which is shown in Figure 8.5. The tables to the right in the figure show the five predefined regions R1 to R5, displaying the number of events within that region together with the mean and the width. The mean value is calculated within each region, as the sample mean,

$$\bar{x} = \frac{1}{N} \sum_{i=1}^{N} x_i,$$

where x_i are the observed invariant masses of the N events within a region. The width is calculated as the standard deviation of the sample,

$$s_N = \sqrt{\frac{1}{N} \sum_{i=1}^{N} (x_i - \bar{x})^2}.$$

At the bottom it is possible to redefine the regions R1 to R5 if necessary.

The observant student or reader might notice that there is a difference in width for dielectrons and dimuons at high mass, well above the Z^0 peak, which reflects the real difference in the precision of the electron and muon energy/momentum measurements at high p_{T}.

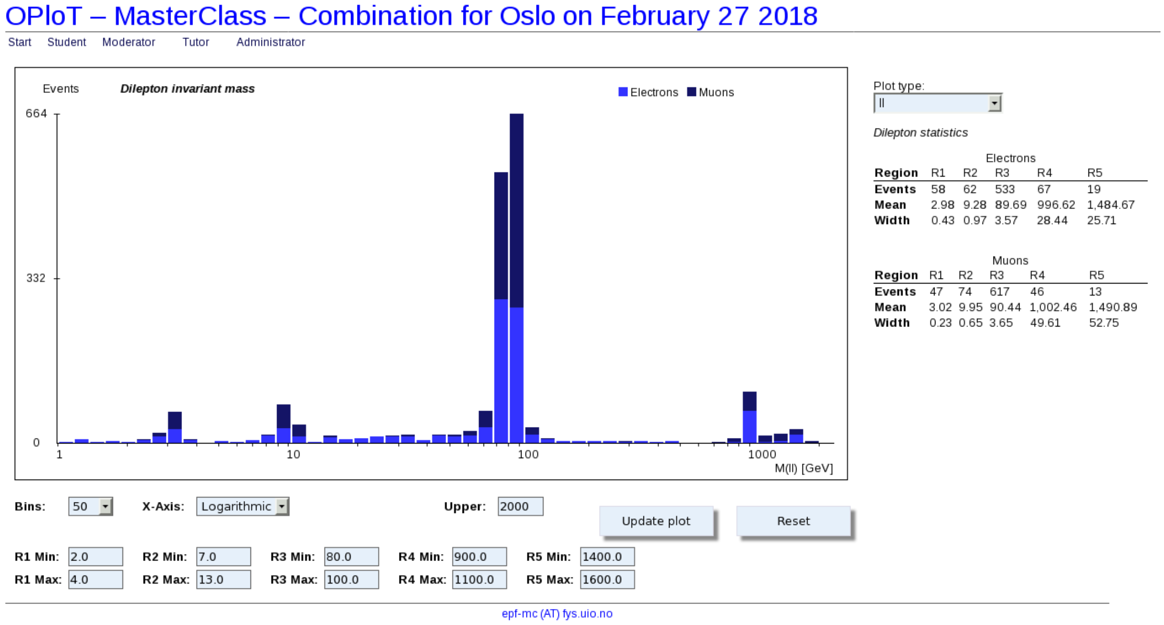

Plot type: ll

Dilepton statistics

Electrons

Region	R1	R2	R3	R4	R5
Events	58	62	533	67	19
Mean	2.98	9.28	89.69	996.62	1,484.67
Width	0.43	0.97	3.57	28.44	25.71

Muons

Region	R1	R2	R3	R4	R5
Events	47	74	617	46	13
Mean	3.02	9.95	90.44	1,002.46	1,490.89
Width	0.23	0.65	3.65	49.61	52.75

Bins: 50 **X-Axis:** Logarithmic **Upper:** 2000

R1 Min:	2.0	**R2 Min:**	7.0	**R3 Min:**	80.0	**R4 Min:**	900.0	**R5 Min:**	1400.0
R1 Max:	4.0	**R2 Max:**	13.0	**R3 Max:**	100.0	**R4 Max:**	1100.0	**R5 Max:**	1600.0

Figure 8.5: The dilepton invariant mass distribution using data from all the groups in Oslo on February 27, 2018.

There are four prominent clusters of events visible at approximately 3 GeV, 10 GeV, 90 GeV and 1 to 2 TeV. In general the students understand that these represent particles with a certain mass decaying into two electron or two muons. Usually they remember the name of the particle at around 90 GeV, the Z boson with mass 91 GeV. In addition to this, we see the J/Ψ at 3 GeV and the Upsilon (ϒ) meson at 10 GeV.[3] In between these particles we see a background, which originates from leptons that did not come from the same decay, often referred to as the "combinatorial background". But what is that bump at and above 1 TeV? Usually, during the practical computer exercise earlier in the day, we get questions from some of the more observant students who wonder why their particle pair has such a high mass. Has anyone ever heard of a particle with a mass that high? So this is the time to reveal that, no, no such particle has *actually* been observed, we imported simulated events from a Z' with mass 1 TeV. The students are usually quite amused by this revelation after considering the possibility of them finding something new in our data. But, as we point out, this is one of the ways we *can* find new particles, and *have* found particles in the past. Just by spending a couple of hours in lectures, a large class of high school students can perform an actual analysis.[4]

8.2.3.2 Four-lepton events

We now continue to the four lepton invariant mass distribution, see Figure 8.6(b). The events that are actually four lepton events (40 in total) in the whole sample are shown in Figure 8.6(a), while all the four lepton events as identified by the students are shown in Figure 8.6(b). It is easily seen by visual comparison of the two figures that there are only a handful of extra events with four muons (the darkest blue), a bit more of the events containing four electrons (the middle blue) and a lot more of the events containing two electrons and two muons (the lightest blue). In these cases, the students have probably correctly identified the muon pair first, and then added an "electron pair" that was not really connected to the two muons in any way. This is because the muons are easily identified, while the students struggle quite a bit to properly identify electrons. The revealing of the expected distribution always ensures a good laugh in the audience.

At this point, we might ask the students a question like "Did any of you see an event that you think was a Higgs boson decaying?" Usually one of the braver students raises his or hers hand and answers that "Yes, *we* did". Probably they tell us that they remembered that the mass of the Higgs boson was around 125 GeV and that they found a four lepton event with that invariant mass. We then tell them that yes, indeed, in that sample of 40 events,[5] there is one good Higgs boson candidate, and that they just might have seen a real Higgs boson event. The other event at around 125 GeV was a $Z^0 + J/\psi- > 4l$ candidate.

In the plot in Figure 8.6(b) there seems to be a wide excess around the Higgs boson mass at 125 GeV, between about 50 GeV and 200 GeV, but this is probably a Z^0 boson decaying to two muons (which is easily identified) paired with two random electrons. All

---

[3] The most precise values measured for these particles are 3096.900 ± 0.006 MeV for the J/Ψ and 9460 ± 0.26 MeV for the Upsilon meson [16], but our precision is much lower.

[4] Of course we have preselected the events and are displaying a portion of the data that is highly enriched with interesting events, but even so the point stands.

[5] All the groups have 2 or 3 real four lepton events in the bunch of 50 events. There are a total of 40 real four lepton events, which means that all of these are seen in many groups. OPloT automatically checks for and removes duplicate entries.

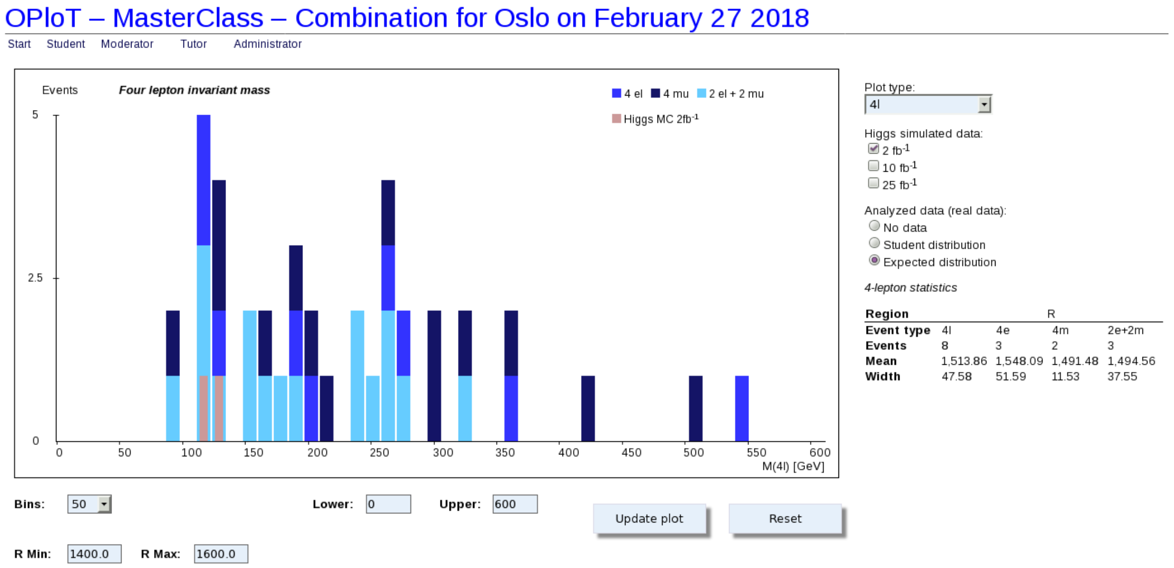

Plot type: 4l

Higgs simulated data:
☑ 2 fb^{-1}
☐ 10 fb^{-1}
☐ 25 fb^{-1}

Analyzed data (real data):
○ No data
○ Student distribution
● Expected distribution

4-lepton statistics

Region	R			
Event type	4l	4e	4m	2e+2m
Events	8	3	2	3
Mean	1,513.86	1,548.09	1,491.48	1,494.56
Width	47.58	51.59	11.53	37.55

Bins: 50 **Lower:** 0 **Upper:** 600

R Min: 1400.0 **R Max:** 1600.0

(a) The four lepton invariant mass distribution on a linear scale between 0 and 600 GeV, using only the actual four lepton events. Note the difference in the scale of t he y-axis. Plotted is also the expected number of events using $2\,\mathrm{fb}^{-1}$ of Higgs boson MC.

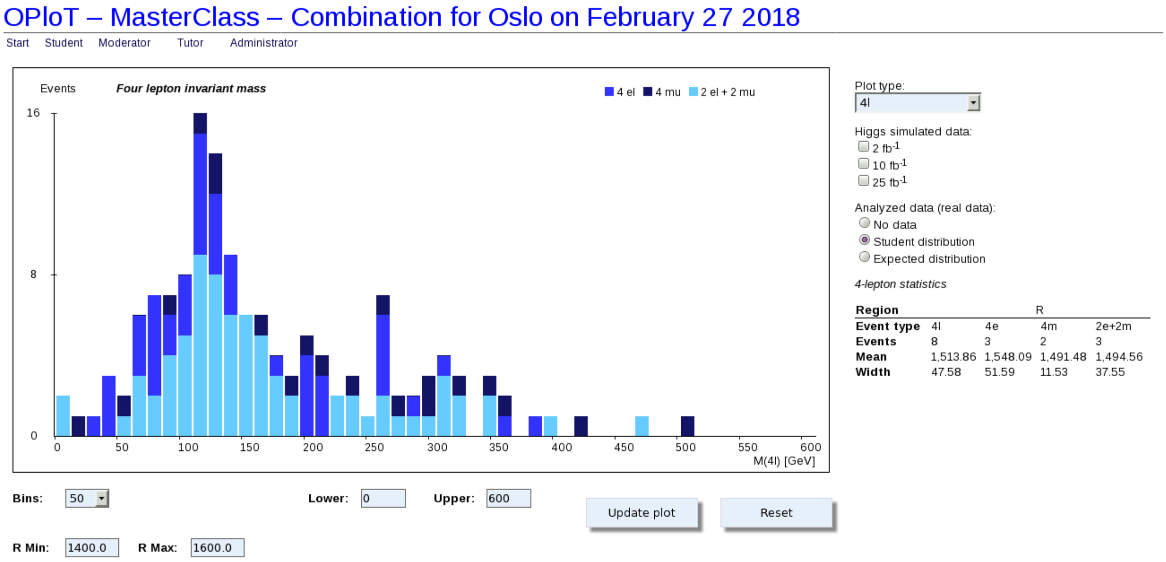

Plot type: 4l

Higgs simulated data:
☐ 2 fb^{-1}
☐ 10 fb^{-1}
☐ 25 fb^{-1}

Analyzed data (real data):
○ No data
● Student distribution
○ Expected distribution

4-lepton statistics

Region	R			
Event type	4l	4e	4m	2e+2m
Events	8	3	2	3
Mean	1,513.86	1,548.09	1,491.48	1,494.56
Width	47.58	51.59	11.53	37.55

Bins: 50 **Lower:** 0 **Upper:** 600

R Min: 1400.0 **R Max:** 1600.0

(b) The four lepton invariant mass distribution on a linear scale between 0 and 600 GeV.

Figure 8.6: Results for all groups in Oslo on February 27, 2018.

four-muon events enter the dilepton distribution as two separate dilepton events. There is a clearly visible dielectron background in Figure 8.5 between the Upsilon meson and the Z^0 boson. Many of these are probably from the four lepton events with two muons from the Z^0 boson at about 91 GeV and two unrelated electrons with some mass. This explains why the broad excess is a bit above the Z^0 mass.

Continuing the discussion, we venture into the topic of statistics again. Is it possible to discover the Higgs boson in the four-lepton channel with the amount of data the students went through today? To answer this we add Higgs boson MC corresponding to the amount of data that is in the total dataset available to the students – $2\,\mathrm{fb}^{-1}$ – displayed as the red/brown histogram in Figure 8.6(a). We expect two events from the Higgs boson and 40 events from background. The background suffers from large statistical fluctuations and is not smooth. The signal is swamped by background and impossible to see. We also added the possibility to add Higgs boson MC corresponding to 10 fb^{-1} and 25 fb^{-1}, and maybe some institutes use this, but we do not.

8.2.3.3 Diphoton events

Figure 8.7(a) shows the student distribution and Figure 8.7(b) shows the expected distribution[6]. The distributions look quite similar, but as can be seen from Figure 8.4(b) (bottom right corner) the students found about 2/3 of the true diphoton events.

On the right hand side, almost on top, there is an option to overlay signal and background simulated data, see Figure 8.8. "No data" is selected as the default. The next point reads "$0.2027\,\mathrm{fb}^{-1}$", and this number is an estimate of the amount of data that is analyzed at our institute on that particular day.[7] Thus Oslo analyzed about 10% of the total amount of data available. We point out to the students that the background is far from smooth and that the signal would drown in the statistical fluctuations of the background.

But then the question becomes – how much data *is* needed to discover the Standard Model Higgs boson in the diphoton channel? In figures 8.9(a)-8.9(c) we see the simulated diphoton invariant mass distribution for 2 fb^{-1}, 10 fb^{-1} and 25 fb^{-1}. Note that the background seems to get smoother with increasing amount of data. In the case of 2 and 10 fb^{-1}, the background (displayed in green) statistical fluctuations are larger or as large as the size of the signal (displayed in brown), while in the case of 25 fb^{-1} we see the signal on top of a smooth background.

8.2.3.4 Overview at high mass

We now take a look at the second of the two overview displays. This one allows us to view all the three plots on the same mass scale, see Figure 8.10. If we look at the dilepton events first, at the top, we see the Z' (simulation) at 1 TeV, but what is that at 1.5 TeV? We must consult the other two distributions. We see quite a few events in the four lepton distribution. The events around 1 TeV are in reality dilepton events from the 1 TeV Z' which are wrongly

---

[6] The expected distribution is based on the assumption that all the student groups got through all 50 events. This is not completely true, but not very far off based on my experience.

[7] Again, this estimate is based on the assumption that all groups analyzed all their events.

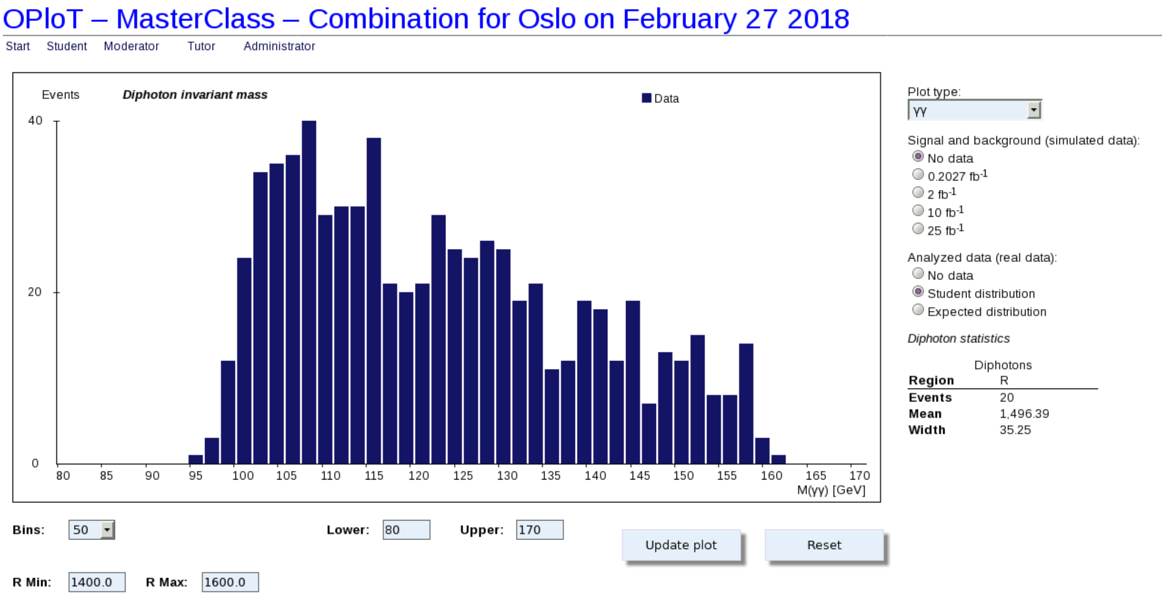
OPloT – MasterClass – Combination for Oslo on February 27 2018

Plot type: γγ

Signal and background (simulated data):
● No data
○ 0.2027 fb^{-1}
○ 2 fb^{-1}
○ 10 fb^{-1}
○ 25 fb^{-1}

Analyzed data (real data):
○ No data
● Student distribution
○ Expected distribution

Diphoton statistics

	Diphotons
Region	R
Events	20
Mean	1,496.39
Width	35.25

Bins: 50
Lower: 80
Upper: 170
R Min: 1400.0
R Max: 1600.0

(a) The events found by the students.

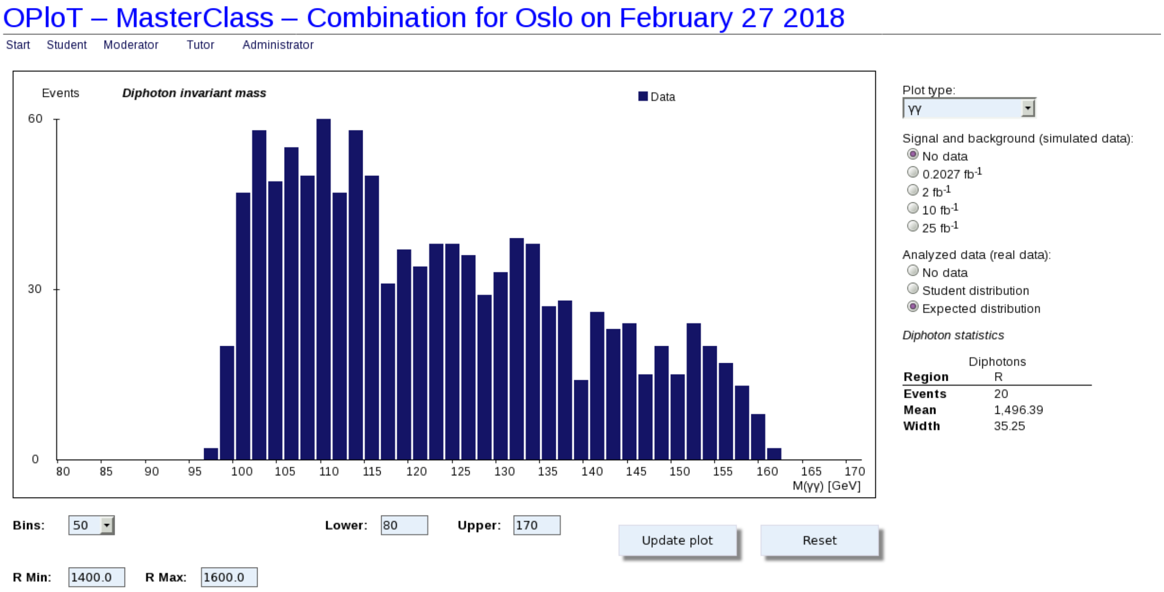
OPloT – MasterClass – Combination for Oslo on February 27 2018

Plot type: γγ

Signal and background (simulated data):
● No data
○ 0.2027 fb^{-1}
○ 2 fb^{-1}
○ 10 fb^{-1}
○ 25 fb^{-1}

Analyzed data (real data):
○ No data
○ Student distribution
● Expected distribution

Diphoton statistics

	Diphotons
Region	R
Events	20
Mean	1,496.39
Width	35.25

Bins: 50
Lower: 80
Upper: 170
R Min: 1400.0
R Max: 1600.0

(b) The expected distribution of events.

Figure 8.7: Results in the diphoton channel, showing the number of events as function of the diphoton invariant mass on a linear scale. The result is for all groups in Oslo on February 27, 2018.

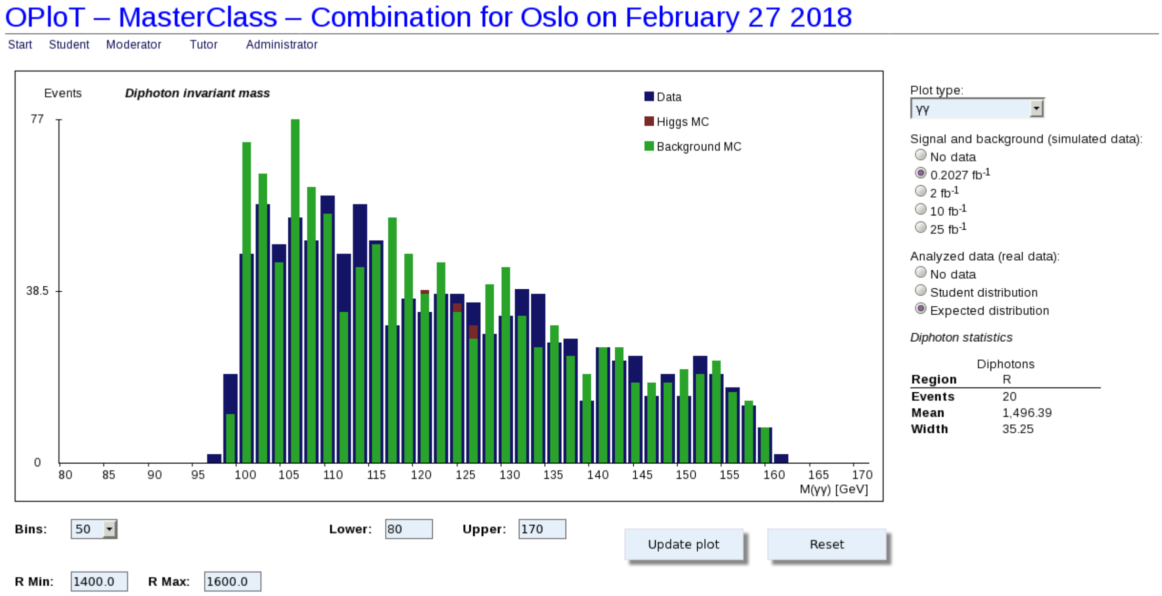

OPloT – MasterClass – Combination for Oslo on February 27 2018

Plot type: γγ

Signal and background (simulated data):
○ No data
● 0.2027 fb^{-1}
○ 2 fb^{-1}
○ 10 fb^{-1}
○ 25 fb^{-1}

Analyzed data (real data):
○ No data
○ Student distribution
● Expected distribution

Diphoton statistics

	Diphotons
Region	R
Events	20
Mean	1,496.39
Width	35.25

Bins: 50
Lower: 80
Upper: 170
R Min: 1400.0
R Max: 1600.0

Figure 8.8: The diphoton invariant mass distribution (blue) with signal (brown) and background MC (green) overlaid for all groups in Oslo on February 27, 2018, using the true diphoton distribution for $0.2\,\mathrm{fb}^1$ (the amount of data analyzed by the Oslo students).

paired with uncorrelated electrons or muons.[8] Between 1.4 TeV and 1.7 TeV we see 10 four lepton events. Consulting the diphoton distribution on the bottom we see a nice bump containing about 20 events at 1.5 TeV. So it seems this 1.5 TeV particle decays to dileptons and diphotons. The Z' at 1 TeV does not decay to diphotons,[9] so it can not be another Z' boson at 1.5 TeV. What can it be, we ask the students, what type of particle can this be? We reveal that this also is simulated data that we put into the mix, and that this time it was a graviton excitation with spin 2. If any of these two high-mass resonances were to show up in the real data, then we would attempt to make a measurement of the spin of the particle, using knowledge about how the different particles decay. This was briefly discussed in the lectures the same morning, how angular distributions for particles with different spins look.

8.2.4 Video conference with CERN

In the last hour of the day we have a video conference with CERN. At CERN there is a whole team of moderators consisting of researchers and students working at CERN volunteering for this. They look at the results from all the institutes participating on that day, up to five different institutes, and discuss the separate results with the students. They also do a statistical combination of the results from all the institutes on that day, which is possible because all groups of students look at different sets of events.[10] In Figure 8.11 we see two overviews of the different distributions. The results look similar to before, but with a lot

---

[8] We know this because we made the mix of events, and there are no particles with mass around 1 TeV that decay to four leptons in the mix.

[9] This is known as the Landau-Yang theorem – a massive spin 1 boson can not decay to two photons.

[10] Except for the four lepton events, 40 in total for the whole 2 fb^{-1} of data, but this is handled automatically in OPloT, removing duplicate events.

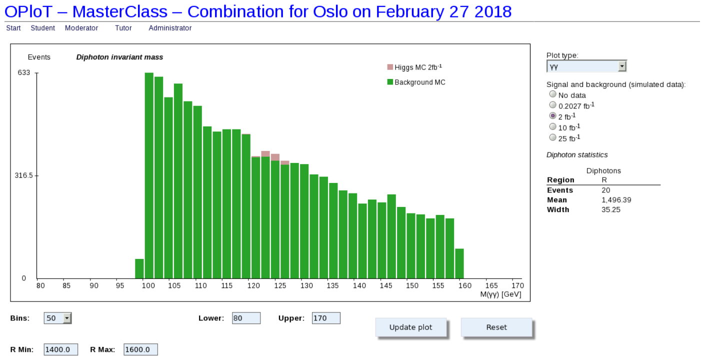

OPloT – MasterClass – Combination for Oslo on February 27 2018

Plot type: γγ

Signal and background (simulated data):
○ No data
○ 0.2027 fb⁻¹
● 2 fb⁻¹
○ 10 fb⁻¹
○ 25 fb⁻¹

Diphoton statistics

	Diphotons
Region	R
Events	20
Mean	1,496.39
Width	35.25

Bins: 50
Lower: 80
Upper: 170
R Min: 1400.0
R Max: 1600.0

(a) 2 fb^{-1}

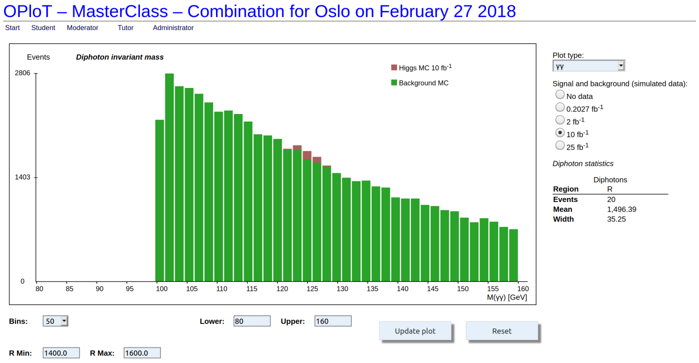

OPloT – MasterClass – Combination for Oslo on February 27 2018

Plot type: γγ

Signal and background (simulated data):
○ No data
○ 0.2027 fb⁻¹
○ 2 fb⁻¹
● 10 fb⁻¹
○ 25 fb⁻¹

Diphoton statistics

	Diphotons
Region	R
Events	20
Mean	1,496.39
Width	35.25

Bins: 50
Lower: 80
Upper: 160
R Min: 1400.0
R Max: 1600.0

(b) 10 fb^{-1}

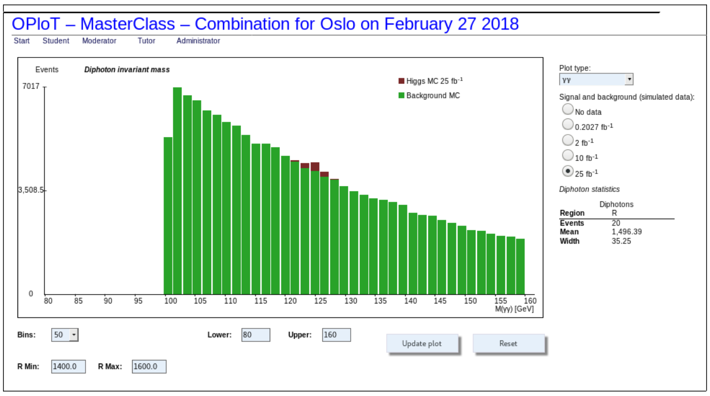

OPloT – MasterClass – Combination for Oslo on February 27 2018

Plot type: γγ

Signal and background (simulated data):
○ No data
○ 0.2027 fb⁻¹
○ 2 fb⁻¹
○ 10 fb⁻¹
● 25 fb⁻¹

Diphoton statistics

	Diphotons
Region	R
Events	20
Mean	1,496.39
Width	35.25

Bins: 50
Lower: 80
Upper: 160
R Min: 1400.0
R Max: 1600.0

(c) 25 fb^{-1}

Figure 8.9: Simulated data of the expected background (green) and the expected signal from the Standard Model Higgs boson (brown) for integrated luminosities of 2 fb^{-1}, 10 fb^{-1} and 25 fb^{-1}.

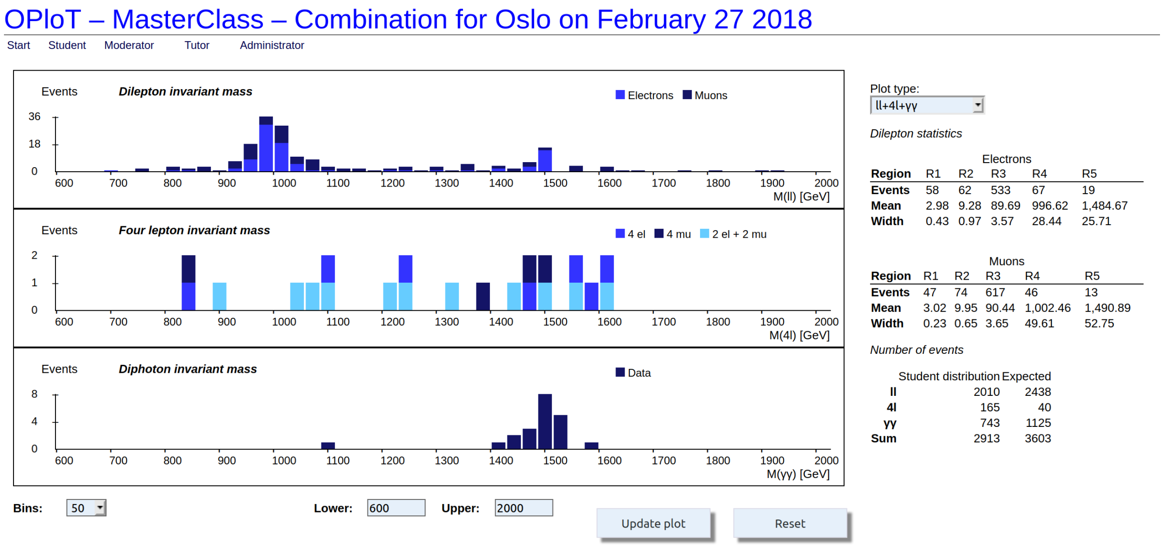

OPloT – MasterClass – Combination for Oslo on February 27 2018

Plot type: ll+4l+γγ

Dilepton statistics

Electrons

Region	R1	R2	R3	R4	R5
Events	58	62	533	67	19
Mean	2.98	9.28	89.69	996.62	1,484.67
Width	0.43	0.97	3.57	28.44	25.71

Muons

Region	R1	R2	R3	R4	R5
Events	47	74	617	46	13
Mean	3.02	9.95	90.44	1,002.46	1,490.89
Width	0.23	0.65	3.65	49.61	52.75

Number of events

	Student distribution	Expected
ll	2010	2438
4l	165	40
γγ	743	1125
Sum	2913	3603

Bins: 50

Lower: 600 **Upper:** 2000

Figure 8.10: This overview display allows us to set the mass scale. In the figure we show the high mass area, between 600 GeV and 2 TeV.

more events.

Different moderators have different approaches, and the suggested approach has varied through the years. Usually one or several students at all institutes on that day make a statement about their findings and can also ask several questions, about working at CERN, life as a researcher, about physics, or anything really.

The last ten minutes are dedicated to a quiz about particle physics, which usually ensures that the students, tired after a long day, wake up and join the friendly competition. After this, the students are free to go home and process all the new knowledge they acquired during the day.

8.3 OPloT – a brief history and a technical note

OPloT first light in 2011. The first time I saw it, it looked very much like the OPloT test version,[11] see Figure 8.12.

This skeleton code was written in PHP (Hypertext Preprocessor) code embedded into HTML (Hypertext Markup Language) code. PHP is a server-side scripting language, while HTML is the standard language for creating web pages. The look of the web page, colors and fonts for examples, are controlled by CSS (Cascading Style Sheets).

The development from skeleton code to finished product was done by me. Suggestions for improvements came from the whole Oslo team.

OPloT was first used in the 2012 Masterclasses, and already then it had much of its current form and functionality. During the next years we added bits and pieces and improved on current functionality. Since then the only improvements have been in internal structure to account for the ever-increasing amount of analyzed data from eager students.

---

[11] `http://cernmasterclass.uio.no/testOPloT.php`

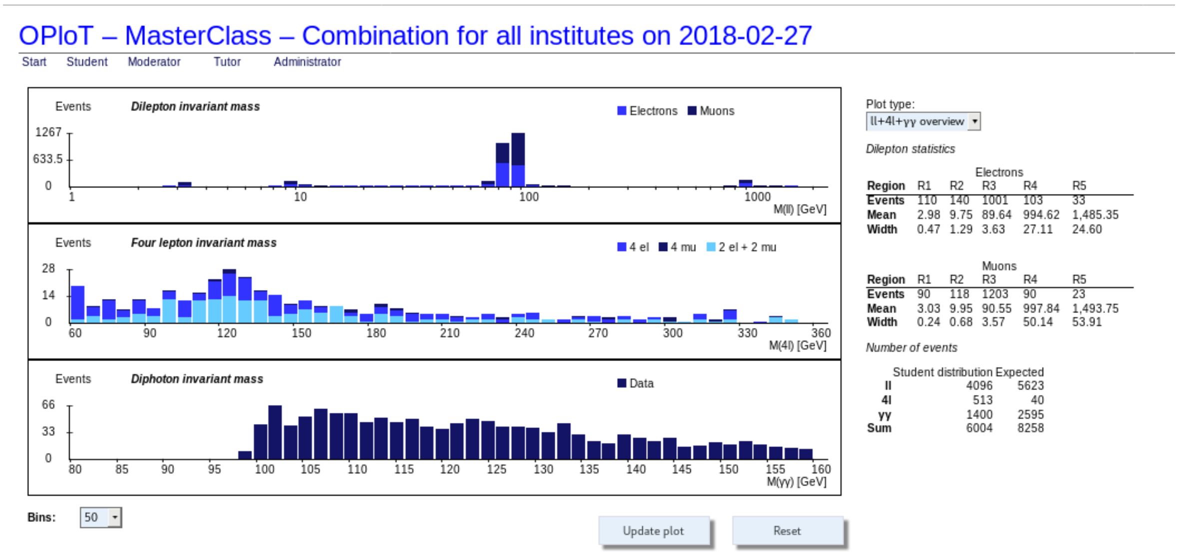

OPloT – MasterClass – Combination for all institutes on 2018-02-27

Plot type: ll+4l+γγ overview

Bins: 50

Dilepton statistics

Electrons

Region	R1	R2	R3	R4	R5
Events	110	140	1001	103	33
Mean	2.98	9.75	89.64	994.62	1,485.35
Width	0.47	1.29	3.63	27.11	24.60

Muons

Region	R1	R2	R3	R4	R5
Events	90	118	1203	90	23
Mean	3.03	9.95	90.55	997.84	1,493.75
Width	0.24	0.68	3.57	50.14	53.91

Number of events

	Student distribution	Expected
ll	4096	5623
4l	513	40
γγ	1400	2595
Sum	6004	8258

(a) An overview of the three distributions with mass range set differently for the three.

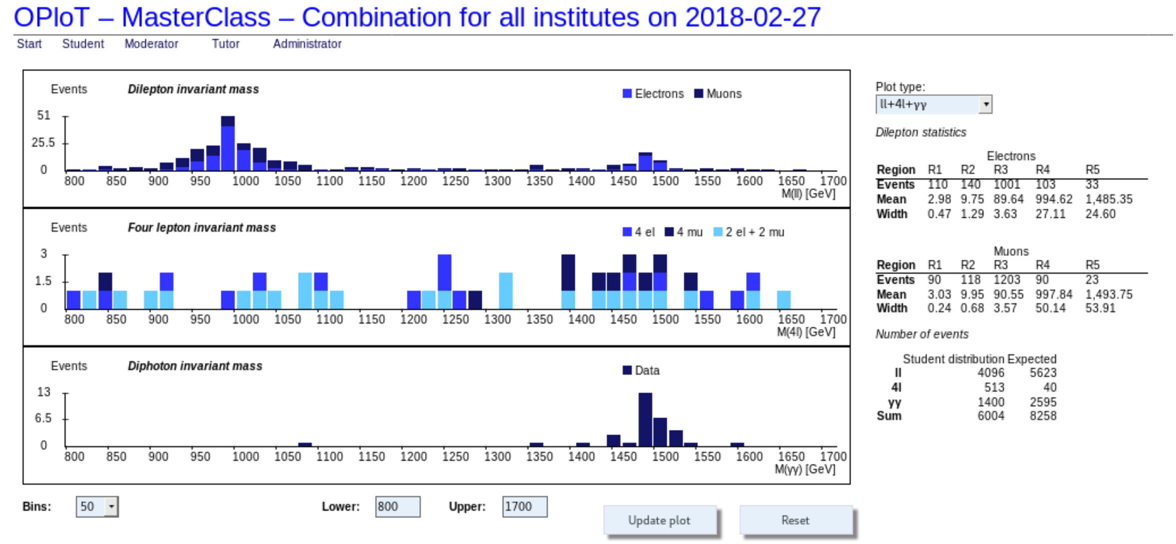

OPloT – MasterClass – Combination for all institutes on 2018-02-27

Plot type: ll+4l+γγ

Bins: 50

Lower: 800

Upper: 1700

Dilepton statistics

Electrons

Region	R1	R2	R3	R4	R5
Events	110	140	1001	103	33
Mean	2.98	9.75	89.64	994.62	1,485.35
Width	0.47	1.29	3.63	27.11	24.60

Muons

Region	R1	R2	R3	R4	R5
Events	90	118	1203	90	23
Mean	3.03	9.95	90.55	997.84	1,493.75
Width	0.24	0.68	3.57	50.14	53.91

Number of events

	Student distribution	Expected
ll	4096	5623
4l	513	40
γγ	1400	2595
Sum	6004	8258

(b) An overview of the three distributions at high mass, between 800 GeV and 1.7 TeV.

Figure 8.11: An overview of the combined result from all five institutes on February 27, 2018. The three distributions are the dilepton invariant mass on top, four lepton invariant mass in the middle and diphoton invariant mass on the bottom.

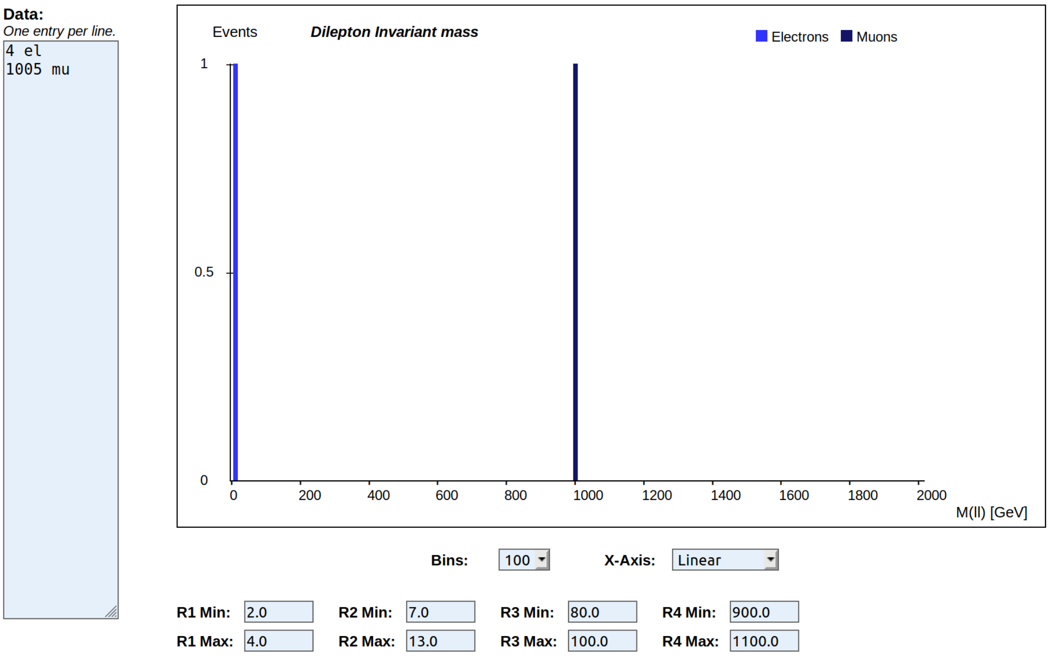

Data:
One entry per line.

```
4 el
1005 mu
```

Bins: 100 **X-Axis:** Linear

R1 Min: 2.0 **R2 Min:** 7.0 **R3 Min:** 80.0 **R4 Min:** 900.0
R1 Max: 4.0 **R2 Max:** 13.0 **R3 Max:** 100.0 **R4 Max:** 1100.0

Figure 8.12: The Oslo Plotting Tool (OPloT) as it was in 2011. At this point in time it had never been used in a Masterclass, it served only as an example program.

8.4 Summary

In this chapter we took a deep dive into one of the outreach programs offered at CERN, the Z-Path. We went through what the students do during the day, focusing on the OPloT and its features. We also briefly looked at the history of the Masterclasses, and the development of OPloT.

In the two years following, we had almost 400 students in Oslo in 2019, and in 2020 the Masterclasses were canceled due to the global COVID-19 outbreak.

Chapter 9

Conlusion and outlook

We started this search with the hope of finding something new, something that would shed light on the underlying theory that governs the Universe, but in the end we observed nothing beyond the expectation. The prime search variable, the dimuon invariant mass, showed that the collision data is well described by the simulated data that represents the Standard Model expectations. Upper exclusion limits on the production cross-section is set for three different Z' models, the Sequential Standard Model Z'_{SSM} and two theories motivated by Grand Unified Theories, Z'_{ψ} and Z'_{χ}. The observed lower mass limits are set at 3.8 TeV, 4.1 TeV and 4.4 TeV for Z'_{ψ}, Z'_{χ} and Z'_{SSM} respectively. The exclusion limits on these three theories are in good agreement with the latest dilepton search publication from the ATLAS Collaboration [120], and with the latest publication from the CMS Collaboration [124] which included only Z'_{ψ} and Z'_{SSM}.

At the present time, there are no collisions at the LHC. After the completion of Run 2 at the end of 2018, we entered a phase knows as *Long Shutdown 2 (LS2)* [136]. The ATLAS detector will undergo general maintenance, and an upgrade. One of the key upgrades are the New Small Wheels (NSW) that will replace the innermost sections of the ATLAS end-cap Muon Spectrometer [137]. This will allow the Muon Spectrometer to deal adequately with the higher collision rates that are planned for the future. The ATLAS Liquid Argon (LAr) calorimeter (the hadronic calorimeter) will be upgraded with new electronics and cabling, which will greatly improve the resolution of the sub-detector and enable much better abilities to separate hadronic jets from electrons and photons. The ATLAS trigger and data-acquisition system will be updated with new electronics, which will further improve the overall performance. The center-of-mass energy will most probably be 14 TeV [138].

The startup of Run 3 was planned at the start of the year 2021, but has been postponed due to the worldwide pandemic outbreak of COVID-19. The first test beams are set to circulate at the end of September 2021, followed by the gradual restart of the rest of the LHC complex [139]. The progress of the maintenance and upgrades in each of main LHC experiments were also delayed due to COVID-19, and Run 3 of the LHC will therefore probably not start until March 2020. Total amount of data collected at the ATLAS experiment during Run 3, that will last for 4 years until the end of 2024, is expected to be 300 fb^{-1}.

Long Shutdown 3 (LS3) will start at the beginning of 2025 [139]. During LS3, both the accelerator and the detectors will undergo major upgrades. The improved accelerator is known as the High Luminosity LHC (HL-LHC), and is set to be operational by the end of 2027 [140][141]. Run 4 will last up to a decade [142]. During this time we will collect 3000 fb^{-1}, 10 times more data than we expect to gather in Run 3, at 14 TeV center-of-mass energy.

Studies have been performed to investigate the prospects for new neutral heavy gauge bosons Z' in the dilepton final state at the HL-LHC [143]. The analyses are based on generator-level information, with parameterizations of the detector responses applied to estimate the effect at the upgraded ATLAS detector. The event selection and the statistical analysis is similar to what is described in Chapter 5 of this thesis. At 14 TeV center-of-mass energy, with 3000 fb^{-1} of data, the discovery reach in the dimuon (dilepton) channel is calculated to be 5.0 TeV (5.7 TeV) for the Z'_{ψ} and 5.7 TeV (6.4 TeV) for the Z'_{SSM}. In the event that no excess above the Standard Model background is observed, lower exclusion limit on the signal mass can be set in the dimuon (dilepton) channel at 5.2 TeV (5.8 TeV) for the Z'_{ψ} and 5.8 TeV (6.5 TeV) for the Z'_{SSM}.

The planning for the future beyond HL-LHC started already many years ago. Several possibilities are explored, one of them is the High Energy LHC (HE-LHC) [144]. The HE-LHC is a proton-proton collider, designed to operate at a centre-of-mass energy 27 TeV. It can use the current LHC tunnel, and the vastly improved magnets can generate a 16 T magnetic flux density field, the double of what is achieved today. During 20 years of operation, the amount of data that can be collected is of the order of 15 ab^{-1}.

The readers of this work might reach this end-point in the thesis with the feeling that not much has been achieved, and in that case, a few words about this is of the utmost importance. Reaching a conclusion that in the end nothing was discovered is not a worthless statement. The number of possible theories that can describe Nature is vast, and the probability to stumble upon the Ultimate Theory of Nature at once is miniscule. There is a large network of theories spanning out the theoretical space, and it requires a huge effort from mankind to explore all the options until the final solution is found. The question is not if, but when, this will happen. Even though my own personal experimental particle physics adventure ends here, I sincerely hope that I will live to see the answer.

Appendix A

Qualification task

The ATLAS collaboration has about 2900 authors,[1] including more than 1000 Ph.D. students. To qualify as an ATLAS author, new members must[2]

- Have been a Qualifying ATLAS Member for at least one year.
- Not be an author of another major LHC collaboration at the time of finalizing the qualification work and being eligible to become an Active ATLAS Author.
- Complete a qualifying task, defined by a Project Leader or Activity Coordinator taking into account the special skills and availability of the person and corresponding to a work load of about 80 full working days. Normally the task should be completed within one year.

I did my qualification task within the Monte Carlo Production Group doing three independent tasks:

1. Writing and testing a script that splits up large files from event generation on High Performance Computers (HPCs) to enable simulation and reconstruction in smaller bunches as described in Section A.2).
2. Validating a set of samples made on HPCs as described in Section A.3.
3. Investigating the observed difference between two generators, Herwig and PYTHIA 6, in the showering of a $t\bar{t}$ sample as described in Section A.4.

Before diving into the specifics of the three tasks, we will briefly visit the topic of supercomputers and their use in MC simulation.

A.1 Supercomputers and High Performance Computing

A supercomputer (or a High Performance Computer, abbreviated HPC) is a computer consisting of a high number of individual cores (CPUs) connected to one another. Each separate

---

[1] May 2018

[2] From the ATLAS Authorship Policy, Version 7.8

CPU doesn't need to be extremely fast, and the amount of memory per core can be quite low, but these supercomputers can perform exceptionally many floating-point operations per second (flops) and they play an important role in the field of computational science. They are the primary choice of computational force in various fields, including quantum mechanics, climate research and weather forecasting. Running any of these computations require a large fraction of the supercomputer at a time, which means that the computer might be considered as fully occupied when there are a number of free CPUs. When a task is finished, the supercomputer is emptied. This might take quite some time, and in the wake of this many CPUs are idle. As it does not look good to have a very expensive supercomputer being partially idle a large portion of the time, the supercomputing facilities are searching for small jobs to fill the empty voids. This is where the ATLAS MC generation enters - we have small tasks that are well suited for running on supercomputers.

A.1.1 Event generation on HPCs

Event generation is a perfect candidate for filling the void on HPCs running large tasks:

- The event generation procedure is easily chopped into smaller, statistically independent jobs.
- No input data is needed to run the jobs.
- The job, including the output, takes up little disk space.
- They are really fast.

There has also been efforts to do simulation and reconstruction on HPCs, but the challenge with this is that the ATLAS software and databases use a lot of disk space, which is something the supercomputers do not have. An idea is to send one event at at time to the HPC for simulation/reconstruction.

A.2 Dividing input files into smaller bunches

Some time before my qualification task was defined, an American ATLAS physicist and his colleagues generated a number of ALPGEN [145] samples on a supercomputer.[3] ALPGEN is a tree-level matrix element calculator for a fixed number of partons ("legs") in the final-state. It outputs one sample for each number of legs. The sample in question was the Z^0 boson decaying to dileptons, with 0 to 5 jets ("ZeeNpX"), e.g. ZeeNp1 includes Z^0 to dielectrons plus one parton. The showering of the partons is performed by another generator, e.g. PYTHIA 8 [63] or Herwig 7.0 [64], at a later time (consult Section 4.2.2 for more information on the parton showering procedure).

---

[3] Intrepid (163k cores, 80 TB of RAM, peak performance 557 teraflops) and Challenger (4096 cores, 2 TB of RAM, peak performance 13.9 teraflops) at the Argonne National Laboratory.

The samples (event generation) that are produced on supercomputers are combined into huge files. The reason for this is that DQ2 [146], the implementation of the ATLAS Distributed Data Management system (the DDM) responsible for e.g. the data transferal,[4] uses an equal amount of time to transfer files of all sizes,[5] and because of the slow connection between the HPCs and the surrounding world transferring many small files would take too long. For the detector simulation and reconstruction it is most efficient to run over a small number of events at a time, and run this in parallel. Because of this, the input files from the HPCs (the generated events) must be divided into smaller files. This task made up a large part of my qualification work.

A.2.1 Technical implementation

A function called Generate_tf.py is a portal to many Athena[6] tools, including event generation and showering of events. The following description follows the number scheme found in Figure A.1:

1. The job is defined in a so-called job options file, specifying e.g. the physical process, the event generator and the number of events to generate.

2. When running Generate_tf.py to shower events, Athena links the .events file (which is the large output file from the supercomputer) to a file called alpgen.unw_events.

3. All the events in alpgen.unw_events are run over by default.

4. The python script I wrote, reduceEventFile.py(N,M), starts on event number N and the number of requested events is M.

5. Events before N and after $\frac{M\times(1+\text{buffer})}{e}+N$ is cut out of alpgen.unw_events and saved as the new alpgen.unw_events. See Section A.2.1.1 for an explanation of the expression in this point.

6. alpgen.unw_events (now containing only a part of the total number of events in the generated dataset) is then showered in e.g. PYTHIA 6.

---

[4] DQ2 is outdated and today we use a tool called Rucio.

[5] This might seem odd, but the reason is that the transferal time is dominated by the time it takes to initiate the data transmission.

[6] A C++ control framework in which ATLAS data processing and analyses are performed.

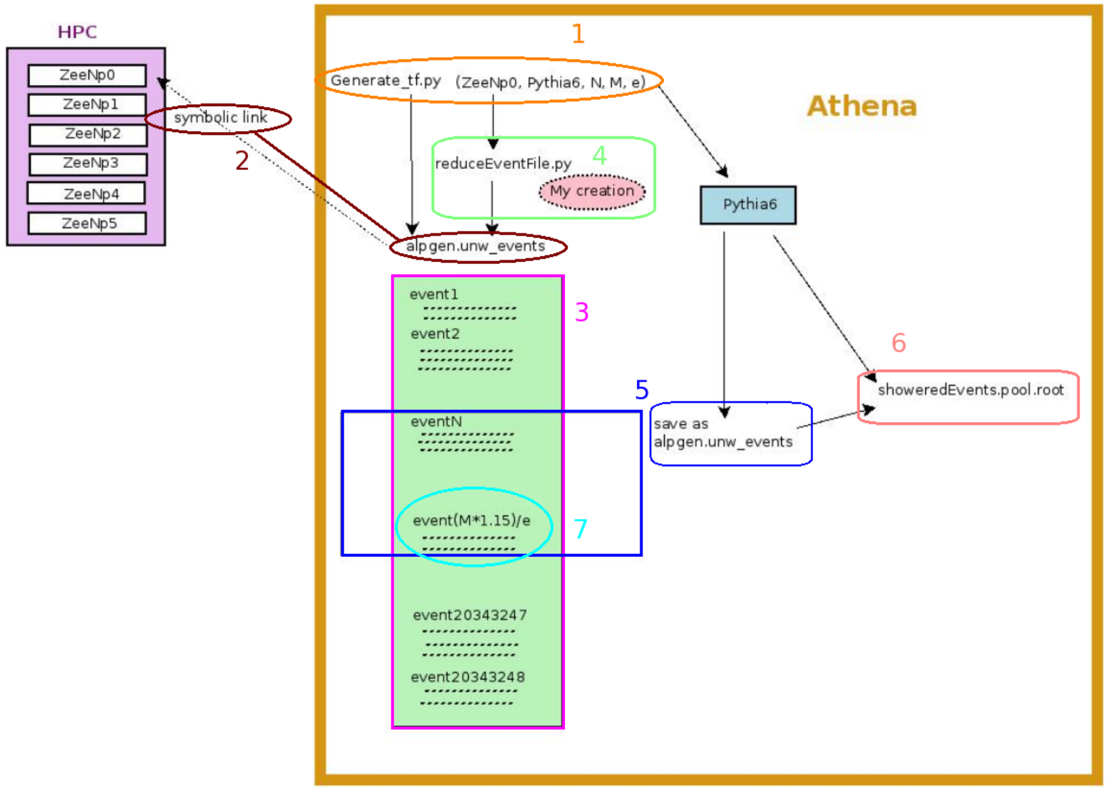

Figure A.1: An overview of the program flow starting with the finished generated events and ending with M showered events. The numbering is explained in Section A.2.1.

A.2.1.1 MLM matching efficiency

The datasets were made by the event generator ALPGEN. As stated earlier, in Section A.1, the physical process in question is a Z^0 boson decaying to dileptons in association with jets. ALPGEN produces these as $Z^0 \rightarrow l^+l^-$ (with l as electrons, muons or taus) with 0 to 5 and more hard partons, separated into 6 datasets. When these events are showered by e.g. Herwig or PYTHIA, there are two demands that need to be fulfilled:

1. There must be a hard jet in the showered sample corresponding to each parton produced by ALPGEN.[7]

2. There must be no other hard jets, as this corresponds to another sample (this is not used for the sample with 5 partons, as this sample includes 5 partons and above).

The events that do not obey these rules are simply thrown away. The efficiency of this selection is called the MLM matching efficiency.[8] The exact size of the MLM matching efficiency, $\hat{e}_{\mathrm{MLM}}$, must be assessed for each dataset by running over a sample. When asking the showering generator to output M events, it needs to run over $\frac{M}{\hat{e}_{\mathrm{MLM}}}$ events. To account for the uncertainty in the MLM matching efficiency one can add a buffer, $\frac{M\times(1+\mathrm{buffer})}{\hat{e}_{\mathrm{MLM}}}$. Obviously this buffer should not be set too high, as the extra events are thrown away.

A.3 Validating the HPC samples

These samples discussed in the previous section were already validated on a matrix-element level, comparing the samples made on the HPCs to the same samples from official ATLAS production, still it was possible that machine-dependent differences in architecture could show up in these samples after the showering. As part of my qualification work, I showered the samples made on the HPCs in PYTHIA 6 [62] and compared them to two official ATLAS samples. This also served as a validation of the splitter script that I wrote earlier, as described in the previous section.

The comparison was done using the Rivet toolkit (Robust Independent Validation of Experiment and Theory) [147]. Rivet is a framework containing a large, growing set of experimental analyses and is often used when e.g. validating and tuning MC generators. This means that a large variety of plots are available with little effort. A few example plots made using Rivet[9] are displayed in Figure A.2. Based on these, and more, it was decided that the showered samples should be considered validated as the various kinematic variables showed no significant differences.

---

[7] The exact definition of jet and how close it needs to be to correspond to a parton produced by ALPGEN is described in the documentation in each showering generator.

[8] Named after the creator of ALPGEN, M. L. Mangano.

[9] For an expert reader: The analyses used was MC_ZJETS [148] and MC_ZINC [149]

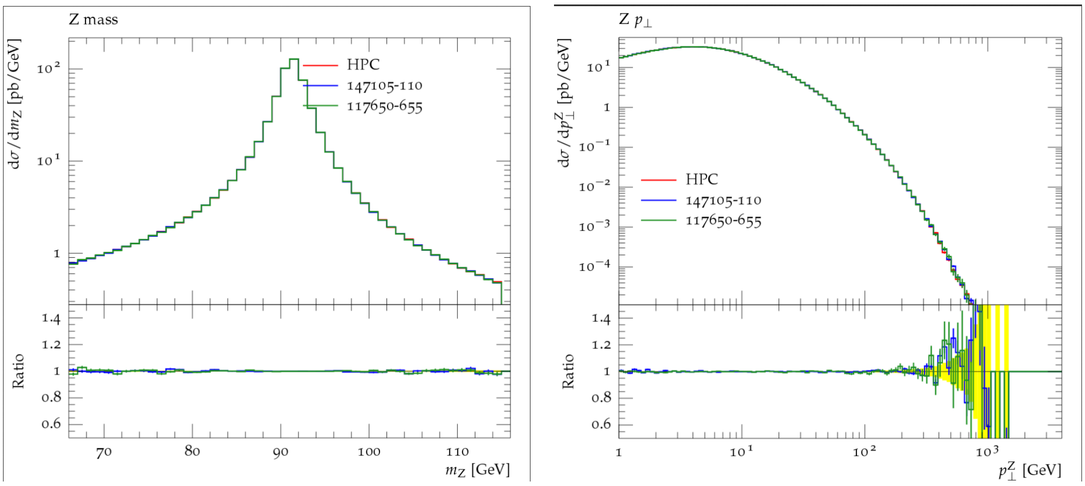

(a) Mass of the Z^0 boson.

(b) Z^0 transverse momentum.

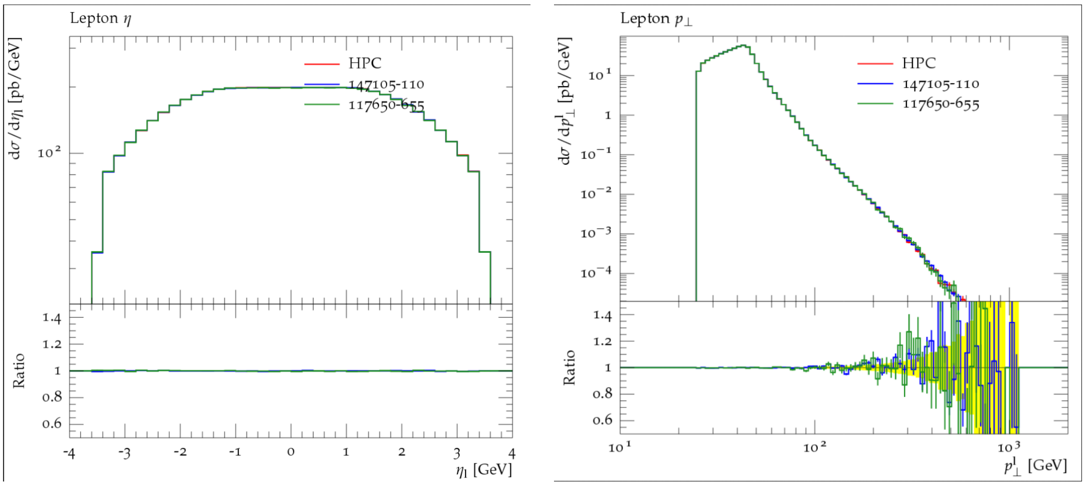

(c) Lepton pseudorapidity.

(d) Lepton transverse momentum.

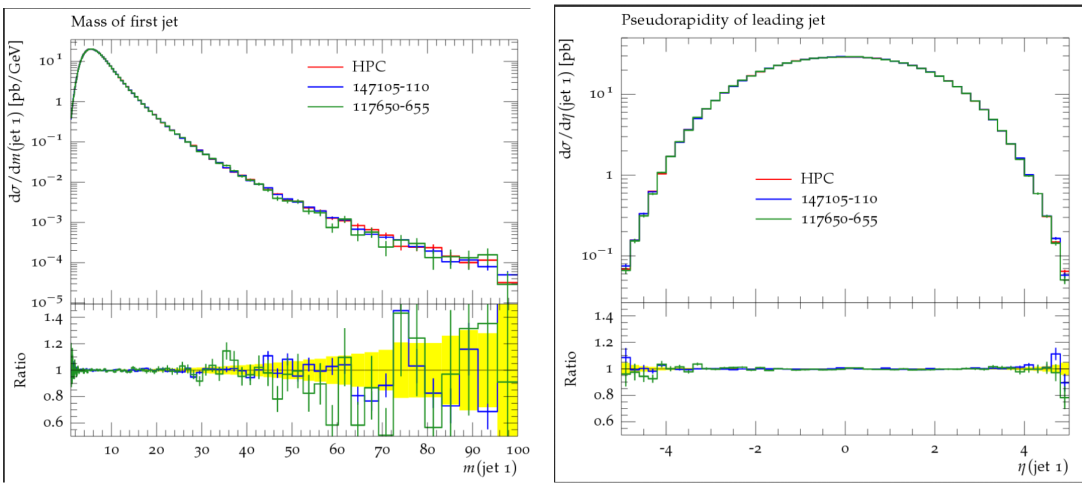

(e) Mass of the leading jet.

(f) Pseudorapidity of the leading jet.

Figure A.2: The figures display six out of many of the plots made using Rivet comparing a ALPGEN ZeeNpX made on a supercomputer to two official ATLAS productions.

A.4 TTbar datasets and observed differences between PYTHIA 6 and Herwig

Somewhat unrelated to the rest of my task, the last part was to investigate some observed differences between two MC samples. The samples were both generated with ALPGEN, but with different PDFs - CTEQ5L [150] and CTEQ6L1 [81]. The former was then showered in PYTHIA 6 and the latter in Herwig. The question then was whether the observed difference was caused by differences in PYTHIA 6 and Herwig or by the different PDFs.

A.4.1 Comparing ALPGEN $t\bar{t}$ samples with different PDFs

To find out, I received an ALPGEN $t\bar{t}$ sample produced with the CTEQ6L1 PDF. I showered them in PYTHIA 6 and ran them through Rivet.[10] In Figure A.3 we see the mass of the leading jet in Figure A.3(a) and the jet multiplicity in A.3(b). The red line is the ALPGEN $t\bar{t}$ sample using the CTEQ6L1 PDF showered with Herwig, the blue line with PYTHIA 6 and the green line is the sample with the CTEQ5L PDF showered in PYTHIA 6. We see that the two samples showered in PYTHIA 6 agree well with each other despite the difference in PDFs. The sample that is showered in Herwig differs from both PYTHIA 6 lines. In light of the similarities in the PYTHIA 6 results despite of the change of PDF, we conclude that the difference between Herwig and PYTHIA 6 is not covered by changing the PDF. It seems there are differences in the generators that cause the observed differences in the kinematic variables.

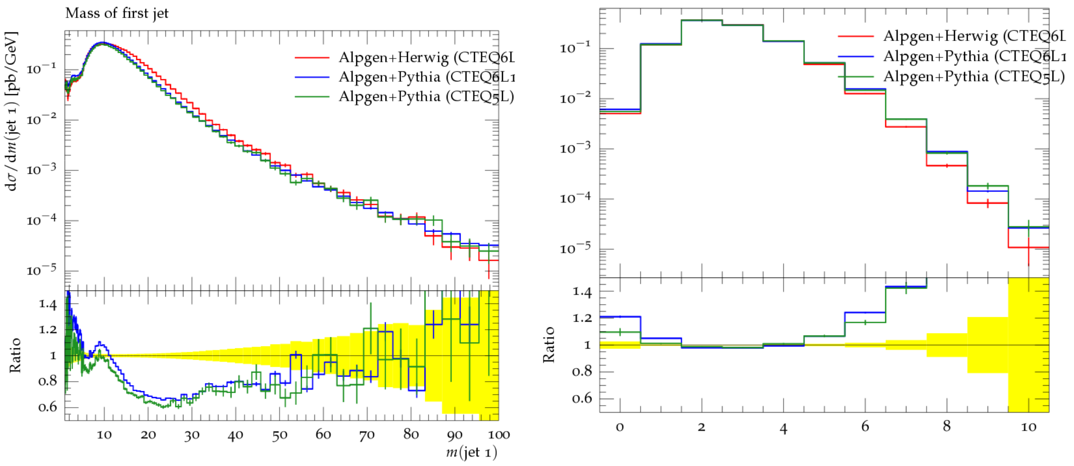

(a) Mass of first jet

(b) Jet multiplicity

Figure A.3: Distribution of the invariant mass of the leading jet and the jet multiplicity, (number of jets in the event), comparing samples prepared in ALPGEN using different PDFs and showered in Herwig or PYTHIA 6. The bottom panel shows the ratio of the green and blue lines to the red line.

---

[10] For an expert reader: the analyses used was MC_JETS [151], MC_TTBAR [152], MC_WJETS [153] and ATLAS_2012_I1094568 [154].

A.4.2 Comparing ALPGEN $t\bar{t}$ samples with different generator input variables

To investigate further, I was asked to do the following comparisons:

- ALPGEN dataset with PYTHIA 6 style inputs compared to ALPGEN dataset with Herwig style inputs, both showered with PYTHIA 6.
- ALPGEN dataset with PYTHIA 6 style inputs compared to ALPGEN dataset with Herwig style inputs, both showered with Herwig.

The inputs in question is the generated events from ALPGEN, where ALPGEN has been given values of different parameters tuned for either Herwig or PYTHIA 6. These were compared to each other and also to a published ATLAS analysis [155] measuring the additional jet activity in dileptonic $t\bar{t}$ events. Figure A.4 shows a few representative Rivet plots. The two top plots show the gap fraction as a function of Q_0, and the two bottom plots show the gap fraction as a function of Q_{sum}. The gap fraction $f(Q_0)$ is defined as $f(Q_0) = \frac{n(Q_0)}{N}$, where N is the number of selected $t\bar{t}$ events (details about the analysis can be found in [155]) and $n(Q_0)$ is the subset of these events that do not contain any jets with transverse momentum p_{T} above a threshold Q_0 in a central rapidity interval, except for the two b-jets from the $t\bar{t}$ decay. An alternate definition of the gap fraction is used to probe jet activity beyond the leading additional jet, $f(Q_{\mathrm{sum}}) = \frac{n(Q_{\mathrm{sum}})}{N}$, where $n(Q_{\mathrm{sum}})$ is the number of $t\bar{t}$ events where the scalar sum of the transverse momenta of the additional jets in a given rapidity interval is less than Q_{sum}. In Figure A.4(a) and (c) we see that using Herwig with Herwig style inputs gives a better fit to the data analysis than using Herwig with the PYTHIA style inputs. In (b) and (d) we see that using PYTHIA with Herwig style inputs gives a better fit to the data than using Pythia with the Pythia style inputs.

We conclude from this that the PYTHIA 6 style inputs are non-optimal and need tuning. The experts in the MC Production Group suspected the value of the QCD scale Λ_{QCD} could be the key, as Herwig used the value 0.18 and PYTHIA 6 used the value 0.26.

A.5 Summary

In this chapter, we reviewed the requirements for ATLAS Ph.D. students to be registered as official authors, and discussed the work I performed, consisting of three separate tasks.

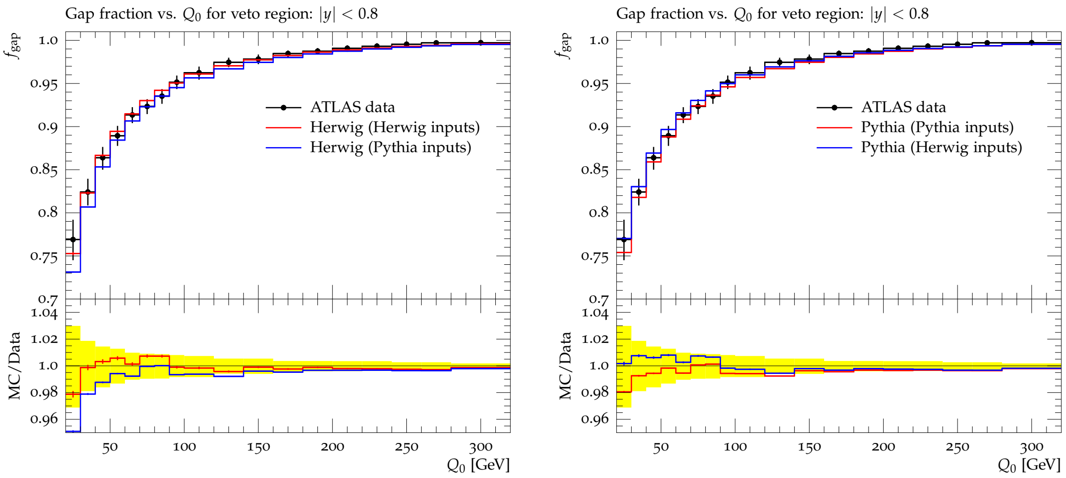

(a) Showered in Herwig.

(b) Showered in PYTHIA 6.

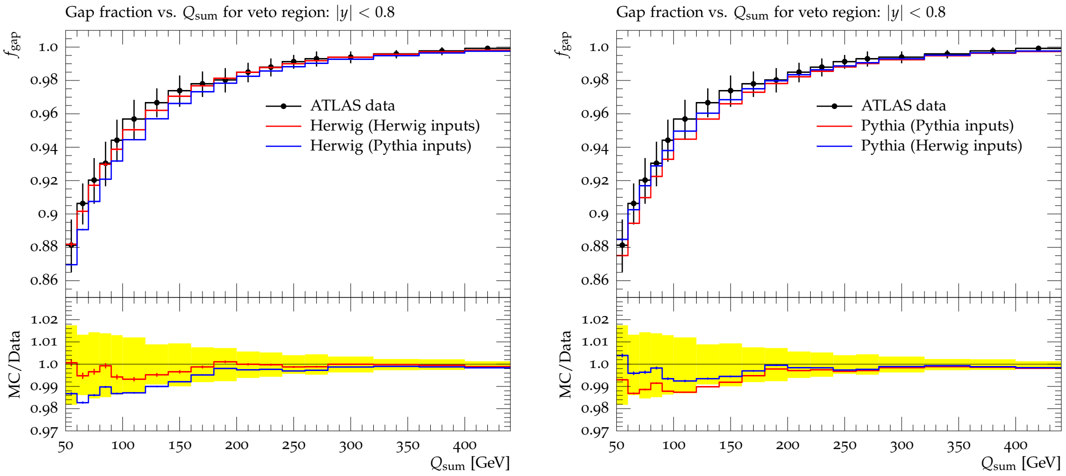

(c) Showered in Herwig.

(d) Showered in PYTHIA 6.

Figure A.4: Distributions of the gap fraction as a function of Q_0, comparing results from a published ATLAS analysis [154] to ALPGEN $t\bar{t}$ events showered in Herwig (left column) and PYTHIA 6 (right column) using either Herwig or PYTHIA 6 style inputs. The bottom panel shows the ratio of the green and blue lines to the ATLAS data analysis.

Appendix B

Additional information on MC samples

B.1 Background processes

Tables B.1, B.2 and B.3 lists relevant information about the MC samples used to model the SM background in the dimuon search performed in this thesis work, in Sections 4 and 5.

Process	**Filter**	$N_{\text{events}}^{\text{mc16a}}$	$N_{\text{events}}^{\text{mc16d}}$	$N_{\text{events}}^{\text{mc16e}}$	σ_{gen}
$Z \to \mu^+\mu^-$	$m_{\mu\mu} > 60\,\text{GeV}$	$7.89 \cdot 10^7$	$8.09 \cdot 10^7$	$1.43 \cdot 10^8$	1.90 nb
$Z \to \mu^+\mu^-$	$120\,\text{GeV} < m_{\mu\mu} < 180\,\text{GeV}$	$5.00 \cdot 10^5$	$1.49 \cdot 10^6$	$3.32 \cdot 10^6$	17.5 pb
$Z \to \mu^+\mu^-$	$180\,\text{GeV} < m_{\mu\mu} < 250\,\text{GeV}$	$2.50 \cdot 10^5$	$8.98 \cdot 10^5$	$1.90 \cdot 10^6$	2.92 pb
$Z \to \mu^+\mu^-$	$250\,\text{GeV} < m_{\mu\mu} < 400\,\text{GeV}$	$1.50 \cdot 10^4$	$1.20 \cdot 10^6$	$2.25 \cdot 10^6$	1.08 pb
$Z \to \mu^+\mu^-$	$400\,\text{GeV} < m_{\mu\mu} < 600\,\text{GeV}$	$1.00 \cdot 10^5$	$9.00 \cdot 10^5$	$1.66 \cdot 10^5$	0.196 pb
$Z \to \mu^+\mu^-$	$600\,\text{GeV} < m_{\mu\mu} < 800\,\text{GeV}$	$1.00 \cdot 10^5$	$4.95 \cdot 10^5$	$1.00 \cdot 10^6$	37.4 fb
$Z \to \mu^+\mu^-$	$800\,\text{GeV} < m_{\mu\mu} < 1000\,\text{GeV}$	$5.00 \cdot 10^4$	$2.50 \cdot 10^5$	$4.95 \cdot 10^5$	10.6 fb
$Z \to \mu^+\mu^-$	$1000\,\text{GeV} < m_{\mu\mu} < 1250\,\text{GeV}$	$5.00 \cdot 10^4$	$1.00 \cdot 10^5$	$2.50 \cdot 10^5$	4.26 fb
$Z \to \mu^+\mu^-$	$1250\,\text{GeV} < m_{\mu\mu} < 1500\,\text{GeV}$	$5.00 \cdot 10^4$	$5.00 \cdot 10^4$	$1.70 \cdot 10^5$	1.42 fb
$Z \to \mu^+\mu^-$	$1500\,\text{GeV} < m_{\mu\mu} < 1750\,\text{GeV}$	$5.00 \cdot 10^4$	$5.00 \cdot 10^4$	$1.70 \cdot 10^5$	0.545 fb
$Z \to \mu^+\mu^-$	$1750\,\text{GeV} < m_{\mu\mu} < 2000\,\text{GeV}$	$5.00 \cdot 10^4$	$5.00 \cdot 10^4$	$1.70 \cdot 10^5$	0.230 fb
$Z \to \mu^+\mu^-$	$2000\,\text{GeV} < m_{\mu\mu} < 2250\,\text{GeV}$	$5.00 \cdot 10^4$	$5.00 \cdot 10^4$	$1.70 \cdot 10^5$	0.104 fb
$Z \to \mu^+\mu^-$	$2250\,\text{GeV} < m_{\mu\mu} < 2500\,\text{GeV}$	$5.00 \cdot 10^4$	$5.00 \cdot 10^4$	$1.70 \cdot 10^5$	49.4 ab
$Z \to \mu^+\mu^-$	$2500\,\text{GeV} < m_{\mu\mu} < 2750\,\text{GeV}$	$5.00 \cdot 10^4$	$5.00 \cdot 10^4$	$1.70 \cdot 10^5$	24.5 ab
$Z \to \mu^+\mu^-$	$2750\,\text{GeV} < m_{\mu\mu} < 3000\,\text{GeV}$	$5.00 \cdot 10^4$	$5.00 \cdot 10^4$	$1.70 \cdot 10^5$	12.5 ab
$Z \to \mu^+\mu^-$	$3000\,\text{GeV} < m_{\mu\mu} < 3500\,\text{GeV}$	$5.00 \cdot 10^4$	$5.00 \cdot 10^4$	$1.70 \cdot 10^5$	10.0 ab
$Z \to \mu^+\mu^-$	$3500\,\text{GeV} < m_{\mu\mu} < 4000\,\text{GeV}$	$5.00 \cdot 10^4$	$5.00 \cdot 10^4$	$1.70 \cdot 10^5$	2.93 ab
$Z \to \mu^+\mu^-$	$4000\,\text{GeV} < m_{\mu\mu} < 4500\,\text{GeV}$	$5.00 \cdot 10^4$	$5.00 \cdot 10^4$	$1.70 \cdot 10^5$	0.898 ab
$Z \to \mu^+\mu^-$	$4500\,\text{GeV} < m_{\mu\mu} < 5000\,\text{GeV}$	$5.00 \cdot 10^4$	$5.00 \cdot 10^4$	$1.70 \cdot 10^5$	0.281 ab
$Z \to \mu^+\mu^-$	$m_{\mu\mu} > 5000\,\text{GeV}$	$5.00 \cdot 10^4$	$5.00 \cdot 10^4$	$1.70 \cdot 10^5$	0.126 ab
$Z \to \tau^+\tau^-$	$m_{\tau^+\tau^-} > 60\,\text{GeV}$	$3.95 \cdot 10^7$	$3.71 \cdot 10^7$	$3.90 \cdot 10^7$	1.90 nb
$Z \to \tau^+\tau^-$	$120\,\text{GeV} < m_{\mu\mu} < 180\,\text{GeV}$	$4.50 \cdot 10^5$	$4.50 \cdot 10^5$	$7.50 \cdot 10^5$	17.5 pb
$Z \to \tau^+\tau^-$	$180\,\text{GeV} < m_{\tau\tau} < 250\,\text{GeV}$	$2.73 \cdot 10^5$	$4.50 \cdot 10^5$	$7.50 \cdot 10^5$	2.92 pb
$Z \to \tau^+\tau^-$	$250\,\text{GeV} < m_{\tau\tau} < 400\,\text{GeV}$	$4.50 \cdot 10^5$	$4.50 \cdot 10^5$	$7.50 \cdot 10^5$	1.08 pb
$Z \to \tau^+\tau^-$	$400\,\text{GeV} < m_{\tau\tau} < 600\,\text{GeV}$	$4.50 \cdot 10^5$	$4.50 \cdot 10^5$	$7.50 \cdot 10^5$	0.196 pb
$Z \to \tau^+\tau^-$	$600\,\text{GeV} < m_{\tau\tau} < 800\,\text{GeV}$	$4.50 \cdot 10^5$	$4.50 \cdot 10^5$	$7.50 \cdot 10^5$	37.4 fb
$Z \to \tau^+\tau^-$	$800\,\text{GeV} < m_{\tau\tau} < 1000\,\text{GeV}$	$4.50 \cdot 10^5$	$4.50 \cdot 10^5$	$7.50 \cdot 10^5$	10.6 fb
$Z \to \tau^+\tau^-$	$1000\,\text{GeV} < m_{\tau\tau} < 1250\,\text{GeV}$	$4.50 \cdot 10^5$	$4.50 \cdot 10^5$	$7.50 \cdot 10^5$	4.26 fb
$Z \to \tau^+\tau^-$	$1250\,\text{GeV} < m_{\tau\tau} < 1500\,\text{GeV}$	$4.50 \cdot 10^5$	$4.50 \cdot 10^5$	$7.49 \cdot 10^5$	1.42 fb
$Z \to \tau^+\tau^-$	$1500\,\text{GeV} < m_{\tau\tau} < 1750\,\text{GeV}$	$3.50 \cdot 10^5$	$3.50 \cdot 10^5$	$5.88 \cdot 10^5$	0.545 fb
$Z \to \tau^+\tau^-$	$1750\,\text{GeV} < m_{\tau\tau} < 2000\,\text{GeV}$	$2.35 \cdot 10^5$	$2.35 \cdot 10^5$	$4.00 \cdot 10^5$	0.230 fb
$Z \to \tau^+\tau^-$	$2000\,\text{GeV} < m_{\tau\tau} < 2250\,\text{GeV}$	$4.50 \cdot 10^5$	$4.50 \cdot 10^5$	$7.50 \cdot 10^5$	0.104 fb
$Z \to \tau^+\tau^-$	$2250\,\text{GeV} < m_{\tau\tau} < 2500\,\text{GeV}$	$3.50 \cdot 10^5$	$3.50 \cdot 10^5$	$5.90 \cdot 10^5$	49.4 ab
$Z \to \tau^+\tau^-$	$2500\,\text{GeV} < m_{\tau\tau} < 2750\,\text{GeV}$	$3.50 \cdot 10^5$	$3.50 \cdot 10^5$	$5.90 \cdot 10^5$	24.5 ab
$Z \to \tau^+\tau^-$	$2750\,\text{GeV} < m_{\tau\tau} < 3000\,\text{GeV}$	$3.50 \cdot 10^5$	$3.50 \cdot 10^5$	$5.90 \cdot 10^5$	12.5 ab
$Z \to \tau^+\tau^-$	$3000\,\text{GeV} < m_{\tau\tau} < 3500\,\text{GeV}$	$3.50 \cdot 10^5$	$3.50 \cdot 10^5$	$5.90 \cdot 10^5$	10.0 ab
$Z \to \tau^+\tau^-$	$3500\,\text{GeV} < m_{\tau\tau} < 4000\,\text{GeV}$	$5.00 \cdot 10^4$	$4.00 \cdot 10^5$	$6.70 \cdot 10^5$	2.93 ab
$Z \to \tau^+\tau^-$	$4000\,\text{GeV} < m_{\tau\tau} < 4500\,\text{GeV}$	$3.15 \cdot 10^5$	$3.15 \cdot 10^5$	$5.40 \cdot 10^5$	0.898 ab
$Z \to \tau^+\tau^-$	$4500\,\text{GeV} < m_{\tau\tau} < 5000\,\text{GeV}$	$3.50 \cdot 10^5$	$3.50 \cdot 10^5$	$5.90 \cdot 10^5$	0.281 ab
$Z \to \tau^+\tau^-$	$m_{\tau\tau} > 5000\,\text{GeV}$	$3.50 \cdot 10^5$	$3.50 \cdot 10^5$	$5.90 \cdot 10^5$	0.126 ab

Table B.1: MC samples used to describe the Drell-Yan background in the dimuon channel. The filter column describes a generator level cut. The three columns labeled N_{events} describe how many events are generated for the mc16a, mc16d and mc16e campaigns. The last column labeled σ_{gen} gives the generator level cross-section for the process. All samples are generated with POWHEG BOX [79] matrix-element calculations at next-to-leading order (NLO) in perturbative QCD (pQCD) using the CT10 [80] NLO PDFs, with PYTHIA 8 [63] handling the parton showers, hadronization and underlying event, using the CTEQ6L1 [81] PDF set.

Process	**Filter**	$N_{\text{events}}^{\text{mc16a}}$	$N_{\text{events}}^{\text{mc16d}}$	$N_{\text{events}}^{\text{mc16e}}$	σ_{gen}
$VV \to \mu\nu\mu\nu$	$50\,\text{GeV} < m_{VV} < 150\,\text{GeV}$	$2.00 \cdot 10^5$	$2.51 \cdot 10^5$	$2.00 \cdot 10^5$	0.829 pb
$VV \to \mu\nu\mu\nu$	$150\,\text{GeV} < m_{VV} < 500\,\text{GeV}$	$5.00 \cdot 10^4$	$6.30 \cdot 10^4$	$5.00 \cdot 10^4$	0.232 pb
$VV \to \mu\nu\mu\nu$	$500\,\text{GeV} < m_{VV} < 1000\,\text{GeV}$	$5.00 \cdot 10^4$	$6.30 \cdot 10^4$	$5.00 \cdot 10^4$	11.8 fb
$VV \to \mu\nu\mu\nu$	$1000\,\text{GeV} < m_{VV} < 2000\,\text{GeV}$	$5.00 \cdot 10^4$	$6.30 \cdot 10^4$	$5.00 \cdot 10^4$	1.45 fb
$VV \to \mu\nu\mu\nu$	$2000\,\text{GeV} < m_{VV} < 3000\,\text{GeV}$	$5.00 \cdot 10^4$	$6.30 \cdot 10^4$	$4.90 \cdot 10^4$	0.128 fb
$VV \to \mu\nu\mu\nu$	$3000\,\text{GeV} < m_{VV} < 4000\,\text{GeV}$	$5.00 \cdot 10^4$	$6.00 \cdot 10^4$	$5.00 \cdot 10^4$	27.8 ab
$VV \to \mu\nu\mu\nu$	$4000\,\text{GeV} < m_{VV} < 5000\,\text{GeV}$	$5.00 \cdot 10^4$	$6.30 \cdot 10^4$	$5.00 \cdot 10^4$	6.45 ab
$VV \to \mu\nu\mu\nu$	$m_{VV} > 5000\,\text{GeV}$	$5.00 \cdot 10^4$	$6.30 \cdot 10^4$	$5.00 \cdot 10^4$	1.41 ab
$VV \to ll\mu\mu$	$50\,\text{GeV} < m_{VV} < 150\,\text{GeV}$	$2.00 \cdot 10^5$	$2.51 \cdot 10^5$	$2.00 \cdot 10^5$	1.22 pb
$VV \to ll\mu\mu$	$150\,\text{GeV} < m_{VV} < 500\,\text{GeV}$	$5.00 \cdot 10^4$	$5.00 \cdot 10^4$	$4.90 \cdot 10^4$	21.1 fb
$VV \to ll\mu\mu$	$500\,\text{GeV} < m_{VV} < 1000\,\text{GeV}$	$5.00 \cdot 10^4$	$6.30 \cdot 10^4$	$5.00 \cdot 10^4$	0.726 fb
$VV \to ll\mu\mu$	$1000\,\text{GeV} < m_{VV} < 2000\,\text{GeV}$	$5.00 \cdot 10^4$	$6.05 \cdot 10^4$	$4.95 \cdot 10^4$	64.4 ab
$VV \to ll\mu\mu$	$2000\,\text{GeV} < m_{VV} < 3000\,\text{GeV}$	$5.00 \cdot 10^4$	$6.30 \cdot 10^4$	$5.00 \cdot 10^4$	1.54 ab
$VV \to ll\mu\mu$	$3000\,\text{GeV} < m_{VV} < 4000\,\text{GeV}$	$5.00 \cdot 10^4$	$6.30 \cdot 10^4$	$4.90 \cdot 10^4$	94.6 zb
$VV \to ll\mu\mu$	$4000\,\text{GeV} < m_{VV} < 5000\,\text{GeV}$	$5.00 \cdot 10^4$	$6.10 \cdot 10^4$	$8.00 \cdot 10^4$	7.66 zb
$VV \to ll\mu\mu$	$m_{VV} > 5000\,\text{GeV}$	$4.85 \cdot 10^4$	$5.95 \cdot 10^4$	$5.00 \cdot 10^4$	0.697 zb
$VV \to l\nu\mu\mu$	$50\,\text{GeV} < m_{VV} < 150\,\text{GeV}$	$2.00 \cdot 10^5$	$2.50 \cdot 10^5$	$2.00 \cdot 10^5$	0.925 pb
$VV \to l\nu\mu\mu$	$150\,\text{GeV} < m_{VV} < 500\,\text{GeV}$	$5.00 \cdot 10^4$	$6.30 \cdot 10^4$	$5.00 \cdot 10^4$	0.117 pb
$VV \to l\nu\mu\mu$	$500\,\text{GeV} < m_{VV} < 1000\,\text{GeV}$	$5.00 \cdot 10^4$	$6.30 \cdot 10^4$	$5.00 \cdot 10^4$	14.1 fb
$VV \to l\nu\mu\mu$	$1000\,\text{GeV} < m_{VV} < 2000\,\text{GeV}$	$5.00 \cdot 10^4$	$6.30 \cdot 10^4$	$5.00 \cdot 10^4$	0.334 fb
$VV \to l\nu\mu\mu$	$2000\,\text{GeV} < m_{VV} < 3000\,\text{GeV}$	$5.00 \cdot 10^4$	$6.30 \cdot 10^4$	$4.90 \cdot 10^4$	7.97 ab
$VV \to l\nu\mu\mu$	$3000\,\text{GeV} < m_{VV} < 4000\,\text{GeV}$	$4.95 \cdot 10^4$	$6.15 \cdot 10^4$	$4.90 \cdot 10^4$	0.407 ab
$VV \to l\nu\mu\mu$	$4000\,\text{GeV} < m_{VV} < 5000\,\text{GeV}$	$4.95 \cdot 10^4$	$6.20 \cdot 10^4$	$4.80 \cdot 10^4$	23.9 zb
$VV \to l\nu\mu\mu$	$m_{VV} > 5000\,\text{GeV}$	$4.75 \cdot 10^4$	$5.60 \cdot 10^4$	$4.40 \cdot 10^4$	1.81 zb
$VV \to qq\mu\mu$	$50\,\text{GeV} < m_{VV} < 150\,\text{GeV}$	$2.00 \cdot 10^5$	$2.51 \cdot 10^5$	$2.00 \cdot 10^5$	5.70 pb
$VV \to qq\mu\mu$	$150\,\text{GeV} < m_{VV} < 500\,\text{GeV}$	$5.00 \cdot 10^4$	$6.30 \cdot 10^4$	$5.00 \cdot 10^4$	0.173 pb
$VV \to qq\mu\mu$	$500\,\text{GeV} < m_{VV} < 1000\,\text{GeV}$	$5.00 \cdot 10^4$	$6.30 \cdot 10^4$	$5.00 \cdot 10^4$	4.09 fb
$VV \to qq\mu\mu$	$1000\,\text{GeV} < m_{VV} < 2000\,\text{GeV}$	$5.00 \cdot 10^4$	$6.30 \cdot 10^4$	$5.00 \cdot 10^4$	0.312 fb
$VV \to qq\mu\mu$	$2000\,\text{GeV} < m_{VV} < 3000\,\text{GeV}$	$5.00 \cdot 10^4$	$6.30 \cdot 10^4$	$4.90 \cdot 10^4$	10.1 ab
$VV \to qq\mu\mu$	$3000\,\text{GeV} < m_{VV} < 4000\,\text{GeV}$	$5.00 \cdot 10^4$	$6.30 \cdot 10^4$	$5.00 \cdot 10^4$	0.663 ab
$VV \to qq\mu\mu$	$4000\,\text{GeV} < m_{VV} < 4000\,\text{GeV}$	$5.00 \cdot 10^4$	$6.30 \cdot 10^4$	$5.00 \cdot 10^4$	54.1 zb
$VV \to qq\mu\mu$	$m_{VV} > 5000\,\text{GeV}$	$5.00 \cdot 10^4$	$6.30 \cdot 10^4$	$5.00 \cdot 10^4$	4.82 zb

Table B.2: MC samples used to describe the leptonic part of the diboson background in the dimuon channel. The symbol V is used to denote either a Z boson or a W boson. The filter column describes a generator level cut. The three columns labeled N_{events} describe how many events are generated for the mc16a, mc16d and mc16e campaigns. The last column labeled σ_{gen} gives the generator level cross-section for the process. All the samples are generated with Sherpa[66][82] using the NLO CT10[80] parton distribution function.

Process	**Filter**	**Filter eff.**	$N_{\text{events}}^{\text{mc16a}}$	$N_{\text{events}}^{\text{mc16d}}$	$N_{\text{events}}^{\text{mc16e}}$	σ_{gen}
$t\bar{t}$	ll	0.105	$2.00 \cdot 10^7$	$2.49 \cdot 10^7$	$3.31 \cdot 10^7$	0.730 nb
Wt, t-channel	ll	1.0	$1.00 \cdot 10^6$	$1.25 \cdot 10^6$	$1.66 \cdot 10^6$	3.99 pb
$W\bar{t}$, t-channel	ll	1.0	$1.00 \cdot 10^6$	$1.25 \cdot 10^6$	$1.65 \cdot 10^6$	3.99 pb
Single t, t-channel	ll	1.0	$4.79 \cdot 10^6$	$6.62 \cdot 10^6$	$8.29 \cdot 10^6$	37.00 pb
Single $\bar{t}$, t-channel	ll	1.0	$4.76 \cdot 10^6$	$5.97 \cdot 10^6$	$8.30 \cdot 10^6$	22.2 pb
Single t, s-channel	ll	1.0	$2.00 \cdot 10^6$	$2.50 \cdot 10^6$	$3.31 \cdot 10^6$	2.03 pb
Single $\bar{t}$, s-channel	ll	1.0	$2.00 \cdot 10^6$	$2.50 \cdot 10^6$	$3.32 \cdot 10^6$	1.27 pb

Table B.3: MC samples used to describe the leptonic part of the top background in the dimuon channel. The filter column describes a generator level cut, with a corresponding filter efficiency. The three columns labeled N_{events} describe how many events are generated for the mc16a, mc16d and mc16e campaigns. The last column labeled σ_{gen} gives the generator level cross-section for the process. All samples were made with POWHEG BOX using the NNPDF3.0 NLO [84] PDF set, with PYTHIA 8 handling the parton showering, using the NNPDF2.3 LO [85] PDF set and the ATLAS A14 [86] set of tuned parameters for parton showering and hadronization. For the $W + t$ samples, the event generation used the DR scheme [87] to subtract $t\bar{t}$ terms from the $W + t$ production.

B.2 Signal processes

Table B.4 list relevant information on the four dedicated Z'_χ samples used in the dimuon resonance search performed in this thesis work, Section 5, while Table B.5 list relevant information on the LO DY samples used for reweighting to several different Z' boson in various scenarions, used in the statistical analysis.

Process	$N_{\text{events}}^{\text{mc16a}}$	$N_{\text{events}}^{\text{mc16d}}$	$N_{\text{events}}^{\text{mc16e}}$	σ_{gen}
$Z' \to \mu\mu$ 2 TeV	$1.00 \cdot 10^6$	$1.00 \cdot 10^6$	$1.66 \cdot 10^6$	8.880 fb
$Z' \to \mu\mu$ 3 TeV	$1.00 \cdot 10^6$	$1.00 \cdot 10^6$	$1.66 \cdot 10^6$	0.803 fb
$Z' \to \mu\mu$ 4 TeV	$1.00 \cdot 10^6$	$9.4 \cdot 10^5$	$1.66 \cdot 10^6$	0.103 fb
$Z' \to \mu\mu$ 5 TeV	$3.35 \cdot 10^5$	$9.66 \cdot 10^5$	$1.66 \cdot 10^6$	18.3 ab

Table B.4: MC samples used to describe the signal processes (Z'_χ) with dedicated samples in the dimuon channel at four different masses. The three columns labeled N_{events} describe how many events are generated for the mc16a, mc16d and mc16e campaigns. The last column labeled σ_{gen} gives the generator level cross-section for the process. All samples are generated with PYTHIA 8 at leading order using the NNPDF2.3 PDF set and the ATLAS A14 set of tuned parameters for parton showering and hadronization.

Process	**Filter**	$N_{\text{events}}^{\text{mc16a}}$	$N_{\text{events}}^{\text{mc16d}}$	$N_{\text{events}}^{\text{mc16e}}$	σ_{gen}
$\gamma/Z^0 \to \mu^+\mu^-$	70 GeV < $m_{\mu\mu}$ < 120 GeV	$1.25 \cdot 10^6$	$3.15 \cdot 10^5$	$2.49 \cdot 10^5$	1.43 nb
	120 GeV < $m_{\mu\mu}$ < 180 GeV	$1.25 \cdot 10^6$	$1.57 \cdot 10^6$	$2.50 \cdot 10^5$	13.8 pb
	180 GeV < $m_{\mu\mu}$ < 250 GeV	$1.25 \cdot 10^6$	$1.57 \cdot 10^6$	$2.25 \cdot 10^5$	2.33 pb
	250 GeV < $m_{\mu\mu}$ < 400 GeV	$1.40 \cdot 10^6$	$1.75 \cdot 10^6$	$1.49 \cdot 10^5$	0.867 pb
	400 GeV < $m_{\mu\mu}$ < 600 GeV	$1.35 \cdot 10^6$	$1.69 \cdot 10^6$	$1.00 \cdot 10^5$	0.156 pb
	600 GeV < $m_{\mu\mu}$ < 800 GeV	$1.30 \cdot 10^6$	$1.63 \cdot 10^6$	$4.90 \cdot 10^4$	29.6 fb
	800 GeV < $m_{\mu\mu}$ < 1000 GeV	$1.05 \cdot 10^6$	$1.32 \cdot 10^6$	$5.00 \cdot 10^4$	8.33 fb
	1000 GeV < $m_{\mu\mu}$ < 1250 GeV	$1.05 \cdot 10^6$	$1.32 \cdot 10^6$	$5.00 \cdot 10^4$	3.31 fb
	1250 GeV < $m_{\mu\mu}$ < 1500 GeV	$1.05 \cdot 10^6$	$1.32 \cdot 10^6$	$5.00 \cdot 10^4$	1.10 fb
	1500 GeV < $m_{\mu\mu}$ < 1750 GeV	$1.05 \cdot 10^6$	$1.32 \cdot 10^6$	$5.00 \cdot 10^4$	0.418 fb
	1750 GeV < $m_{\mu\mu}$ < 2000 GeV	$1.05 \cdot 10^6$	$1.32 \cdot 10^6$	$5.00 \cdot 10^4$	0.176 fb
	2000 GeV < $m_{\mu\mu}$ < 2250 GeV	$5.50 \cdot 10^5$	$6.90 \cdot 10^5$	$5.00 \cdot 10^4$	79.8 ab
	2250 GeV < $m_{\mu\mu}$ < 2500 GeV	$5.50 \cdot 10^5$	$6.90 \cdot 10^5$	$5.00 \cdot 10^4$	38.2 ab
	2500 GeV < $m_{\mu\mu}$ < 2750 GeV	$5.50 \cdot 10^5$	$6.90 \cdot 10^5$	$5.00 \cdot 10^4$	19.1 ab
	2750 GeV < $m_{\mu\mu}$ < 3000 GeV	$5.50 \cdot 10^5$	$6.90 \cdot 10^5$	$4.90 \cdot 10^4$	9.86 ab
	3000 GeV < $m_{\mu\mu}$ < 3500 GeV	$3.00 \cdot 10^5$	$3.80 \cdot 10^5$	$5.00 \cdot 10^4$	8.06 ab
	3500 GeV < $m_{\mu\mu}$ < 4000 GeV	$3.00 \cdot 10^5$	$3.80 \cdot 10^5$	$5.00 \cdot 10^4$	2.42 ab
	4000 GeV < $m_{\mu\mu}$ < 4500 GeV	$3.00 \cdot 10^5$	$3.80 \cdot 10^5$	$5.00 \cdot 10^4$	0.757 ab
	4500 GeV < $m_{\mu\mu}$ < 5000 GeV	$3.00 \cdot 10^5$	$3.80 \cdot 10^5$	$5.00 \cdot 10^4$	0.243 ab
	$m_{\mu\mu}$ > 5000 GeV	$3.00 \cdot 10^5$	$3.80 \cdot 10^5$	$5 \cdot 10^4$	0.117 ab

Table B.5: LO Drell-Yan MC samples, used in a reweighting procedure creating signal samples within a range of selected signal hypotheses. The three columns labeled N_{events} describe how many events are generated for the mc16a, mc16d and for mc16e campaigns. The last column labeled σ_{gen} gives the generator level cross-section for the process. All samples are generated with PYTHIA 8 at leading order using the NNPDF2.3 PDF set and the ATLAS A14 set of tuned parameters for parton showering and hadronization.

B.3 The fake background

Tables B.6 and B.7 lists relevant information on the MC samples used in the study of the dimuon fake bacground performed in Chapter 7.

Process	**Filter**	**Filter efficiency**	$N_{\text{events}}^{\text{mc16a}}$	$N_{\text{events}}^{\text{mc16d}}$	$N_{\text{events}}^{\text{mc16e}}$	σ_{gen}
$W \to \mu\nu$	$N_b \geq 1, p_{\text{T}}^W \epsilon \langle 0, 70 \rangle$ GeV	0.0446	$1.75 \cdot 10^7$	$4.36 \cdot 10^6$	$2.88 \cdot 10^7$	19.01 nb
$W \to \mu\nu$	$N_c \geq 1, p_{\text{T}}^W \epsilon \langle 0, 70 \rangle$ GeV	0.131	$9.99 \cdot 10^6$	$2.50 \cdot 10^6$	$1.66 \cdot 10^7$	19.01 nb
$W \to \mu\nu$	$N_b \geq 1, p_{\text{T}}^W \epsilon \langle 70, 140 \rangle$ GeV	0.0847	$1.99 \cdot 10^7$	$2.48 \cdot 10^7$	$1.34 \cdot 10^7$	0.944 nb
$W \to \mu\nu$	$N_c \geq 1, p_{\text{T}}^W \epsilon \langle 70, 140 \rangle$ GeV	0.243	$9.98 \cdot 10^6$	$9.97 \cdot 10^6$	$1.65 \cdot 10^7$	0.945 nb
$W \to \mu\nu$	$N_b \geq 1, p_{\text{T}}^W \epsilon \langle 140, 280 \rangle$ GeV	0.111	$2.50 \cdot 10^7$	$2.62 \cdot 10^7$	$4.15 \cdot 10^7$	0.340 nb
$W \to \mu\nu$	$N_c \geq 1, p_{\text{T}}^W \epsilon \langle 140, 280 \rangle$ GeV	0.293	$7.50 \cdot 10^6$	$1.87 \cdot 10^6$	$2.24 \cdot 10^7$	0.340 nb
$W \to \mu\nu$	$N_b \geq 1, p_{\text{T}}^W \epsilon \langle 280, 500 \rangle$ GeV	0.125	$2.94 \cdot 10^6$	$3.00 \cdot 10^6$	$4.98 \cdot 10^6$	72.1 pb
$W \to \mu\nu$	$N_c \geq 1, p_{\text{T}}^W \epsilon \langle 280, 500 \rangle$ GeV	0.320	$2.99 \cdot 10^6$	$7.49 \cdot 10^5$	$4.99 \cdot 10^7$	72.1 pb
$W \to \tau\nu$	$N_b \geq 1, p_{\text{T}}^W \epsilon \langle 0, 70 \rangle$ GeV	0.0451	$1.75 \cdot 10^7$	$2.18 \cdot 10^7$	$2.90 \cdot 10^7$	19.01 nb
$W \to \tau\nu$	$N_c \geq 1, p_{\text{T}}^W \epsilon \langle 0, 70 \rangle$ GeV	0.132	$9.99 \cdot 10^6$	$1.24 \cdot 10^7$	$1.66 \cdot 10^7$	19.01 nb
$W \to \tau\nu$	$N_b \geq 1, p_{\text{T}}^W \epsilon \langle 70, 140 \rangle$ GeV	0.0839	$1.00 \cdot 10^7$	$9.98 \cdot 10^6$	$2.49 \cdot 10^7$	0.946 nb
$W \to \tau\nu$	$N_c \geq 1, p_{\text{T}}^W \epsilon \langle 70, 140 \rangle$ GeV	0.242	$1.00 \cdot 10^7$	$1.23 \cdot 10^7$	$1.66 \cdot 10^7$	0.946 nb
$W \to \tau\nu$	$N_b \geq 1, p_{\text{T}}^W \epsilon \langle 140, 280 \rangle$ GeV	0.106	$2.50 \cdot 10^7$	$3.18 \cdot 10^7$	$4.17 \cdot 10^7$	0.339 nb
$W \to \tau\nu$	$N_c \geq 1, p_{\text{T}}^W \epsilon \langle 140, 280 \rangle$ GeV	0.283	$7.50 \cdot 10^6$	$1.88 \cdot 10^6$	$1.24 \cdot 10^7$	0.340 nb
$W \to \tau\nu$	$N_b \geq 1, p_{\text{T}}^W \epsilon \langle 280, 500 \rangle$ GeV	0.136	$3.00 \cdot 10^6$	$2.99 \cdot 10^6$	$4.98 \cdot 10^6$	71.9 pb
$W \to \tau\nu$	$N_c \geq 1, p_{\text{T}}^W \epsilon \langle 280, 500 \rangle$ GeV	0.318	$3.00 \cdot 10^6$	$3.00 \cdot 10^6$	$7.49 \cdot 10^6$	72.0 pb
$W \to \mu\nu$	$p_{\text{T}}^W \epsilon \langle 500, 1000 \rangle$ GeV	-	$3.97 \cdot 10^6$	$3.83 \cdot 10^6$	$6.57 \cdot 10^6$	0.399 pb
$W \to \tau\nu$	$p_{\text{T}}^W \epsilon \langle 500, 1000 \rangle$ GeV	-	$3.96 \cdot 10^6$	$3.92 \cdot 10^6$	$6.50 \cdot 10^6$	0.401 pb
$W \to \mu\nu$	$p_{\text{T}}^W > 1000\,\text{GeV}$	-	$4.00 \cdot 10^6$	$3.99 \cdot 10^6$	$6.64 \cdot 10^6$	7.88 fb
$W \to \tau\nu$	$p_{\text{T}}^W > 1000\,\text{GeV}$	-	$4.00 \cdot 10^6$	$3.92 \cdot 10^6$	$3.99 \cdot 10^6$	7.78 fb

Table B.6: MC samples used to describe the W+jets contribution of the fake background in the dimuon channel. The filter column describes a generator level cut, with a corresponding filter efficiency. The three columns labeled N_{events} describe how many events are generated for the mc16a, mc16d and mc16e campaigns. Sherpa 2.2.1 is used to generate all the listed samples, using the NNPDF 3.0 PDF set at NNLO. The last column labeled σ_{gen} gives the generator level cross-section for the process. The meaning of the shorthand notation is the following: $N_b >= 1$ ($N_c >= 1$) is at least one bottom (charm) quark, p_{T}^W is the transverse momentum of the W boson.

Process	**Filter**	**Filter efficiency**	**Generator**	$N_{\text{events}}^{\text{mc16a}}$	$N_{\text{events}}^{\text{mc16d}}$	$N_{\text{events}}^{\text{mc16e}}$	σ_{gen}
$b\bar{b}$	$p_{\text{T}}^b > 15\,\text{GeV}, N_\mu >= 1$	-	PYTHIA 8	$4.86 \cdot 10^6$	$5.00 \cdot 10^6$	$8.29 \cdot 10^6$	0.188 μb
$c\bar{c}$	$p_{\text{T}}^c > 15\,\text{GeV}, N_\mu >= 1$	-	PYTHIA 8	$5.00 \cdot 10^6$	$4.52 \cdot 10^6$	$8.30 \cdot 10^6$	58.5 nb
$t\bar{t}$	Fully hadronic	0.456	POWHEG + PYTHIA 8	$2.00 \cdot 10^7$	$2.47 \cdot 10^7$	$4.53 \cdot 10^7$	0.730 nb
$t\bar{t}$	At least one lepton	0.544	POWHEG + PYTHIA 8	$6.04 \cdot 10^7$	$7.45 \cdot 10^7$	$9.89 \cdot 10^7$	0.730 nb

Table B.7: MC samples used to describe the fake background in the dimuon channel (dijets ($b\bar{b}$, $c\bar{c}$), W+jets and $t\bar{t}$). The filter column describes a generator level cut, with a corresponding filter efficiency. The three columns labeled N_{events} describe how many events are generated for the mc16a, mc16d and mc16e campaigns. All samples are generatated using the the NNPDF 2.3 PDF set at LO. The last column labeled σ_{gen} gives the generator level cross-section for the process. The meaning of the shorthand notation is the following: p_{T}^b (p_{T}^c) is the transverse momentum of the bottom (charm) quark, $N_\mu >= 1$ is at least one real muon.

Bibliography

[1] Georges Aad et al. Search for high-mass dilepton resonances in pp collisions at $\sqrt{s} = 8$ TeV with the ATLAS detector. *Phys. Rev.*, D90(5):052005, 2014. `http://inspirehep.net/record/1296830`.

[2] Paul A.M. Dirac. Quantum theory of emission and absorption of radiation. *Proc. Roy. Soc. Lond. A*, A114:243, 1927. `https://inspirehep.net/literature/42586`.

[3] R. P. Feynman. Space-time approach to quantum electrodynamics. *Phys. Rev.*, 76:769–789, September 1949. `https://link.aps.org/doi/10.1103/PhysRev.76.769`.

[4] R. P. Feynman. Mathematical formulation of the quantum theory of electromagnetic interaction. *Phys. Rev.*, 80:440–457, November 1950. `https://link.aps.org/doi/10.1103/PhysRev.80.440`.

[5] S. Tomonaga. On a relativistically invariant formulation of the quantum theory of wave fields. *Prog. Theor. Phys.*, 1:27–42, 1946. `http://inspirehep.net/record/45283`.

[6] Julian Schwinger. Quantum electrodynamics. i. a covariant formulation. *Phys. Rev.*, 74:1439–1461, November 1948. `https://link.aps.org/doi/10.1103/PhysRev.74.1439`.

[7] Julian Schwinger. On quantum-electrodynamics and the magnetic moment of the electron. *Phys. Rev.*, 73:416–417, February 1948. `https://link.aps.org/doi/10.1103/PhysRev.73.416`.

[8] The Nobel Prize in Physics 2004. `https://www.nobelprize.org/nobel_prizes/physics/laureates/2004/`. Nobelprize.org. Nobel Media AB 2014.

[9] Sheldon L. Glashow. The renormalizability of vector meson interactions. *Nuclear Physics*, 10(Supplement C):107 – 117, 1959. `http://www.sciencedirect.com/science/article/pii/0029558259901968`.

[10] Abdus Salam and J. C. Ward. Weak and electromagnetic interactions. *Il Nuovo Cimento (1955-1965)*, 11(4):568–577, February 1959. `https://doi.org/10.1007/BF02726525`.

[11] Steven Weinberg. A model of leptons. *Phys. Rev. Lett.*, 19:1264–1266, November 1967. `https://link.aps.org/doi/10.1103/PhysRevLett.19.1264`.

[12] Abdus Salam. Elementary particle physics relativistic groups and analyticity. *N. Svartholm ed., Eighth Nobel Symposium Stockholm: Almquvist and Wiksell, Stockholm Sweden (1968) pg. 367.*

[13] The Nobel Prize in Physics 1979. `https://www.nobelprize.org/prizes/physics/1979/press-release/`. Nobelprize.org. Nobel Media AB 2014.

[14] G. 't Hooft and M. Veltman. Regularization and renormalization of gauge fields. *Nuclear Physics B*, 44(1):189 – 213, 1972. `http://www.sciencedirect.com/science/article/pii/0550321372902799`.

[15] The Nobel Prize in Physics 1999. `https://www.nobelprize.org/prizes/physics/1999/summary/`. Nobelprize.org. Nobel Media AB 2019.

[16] M. Tanabashi et al. Review of particle physics. *Phys. Rev. D*, 98:030001, August 2018. `https://link.aps.org/doi/10.1103/PhysRevD.98.030001`.

[17] F. Mandl and G. Shaw. *Quantum field theory*. Wiley, Second Edition edition, 2010.

[18] William Thomson, Baron Kelvin. *Baltimore Lectures on Molecular Dynamics and the Wave Theory of Light*. Cambridge Library Collection - Physical Sciences. Cambridge University Press, 2010.

[19] The matter-antimatter asymmetry problem. `https://home.cern/science/physics/matter-antimatter-asymmetry-problem`. "Copyright ©2020 CERN".

[20] Guy Coughlan, J. Doo, and B. Gripaios. *The Ideas of Particle Physics - An Introduction for Scientists*. 1994. Third Edition.

[21] H. Georgi and S. L. Glashow. Unity of All Elementary Particle Forces. *Phys. Rev. Lett.*, 32:438–441, 1974. `http://inspirehep.net/record/92111`.

[22] Paul Langacker. The Physics of Heavy Z' Gauge Bosons. *Rev. Mod. Phys.*, 81:1199–1228, 2009. `https://arxiv.org/abs/0801.1345`.

[23] Morad Aaboud et al. Search for new high-mass phenomena in the dilepton final state using 36 fb^{-1} of proton-proton collision data at $\sqrt{s} = 13$ TeV with the ATLAS detector. *JHEP*, 10:182, 2017. `http://inspirehep.net/record/1609250`.

[24] Ennio Salvioni, Giovanni Villadoro, and Fabio Zwirner. Minimal Z-prime models: Present bounds and early LHC reach. *JHEP*, 11:068, 2009. `http://inspirehep.net/record/830532`.

[25] Our Member States. `https://home.cern/about/who-we-are/our-governance/member-states`. "Copyright ©2020 CERN".

[26] CERN Annual report 2018. 2019. `https://cds.cern.ch/record/2671714`.

[27] Facts and figures about the LHC. `https://home.cern/resources/faqs/facts-and-figures-about-lhc`. Copyright ©2020 CERN.

[28] Jean-Luc Caron. LHC Layout. Schema general du LHC. `https://cds.cern.ch/record/841573`, September 1997.

[29] Esma Mobs. The CERN accelerator complex. Complexe des accélérateurs du CERN. July 2016. `https://cds.cern.ch/record/2197559`.

[30] Gerfried J Wiener, Julia Woithe, Alexander Brown, and Konrad Jende. Introducing the LHC in the classroom: an overview of education resources available. *Physics Education*, 51(3):035001, feb 2016. `https://doi.org/10.1088%2F0031-9120%2F51%2F3%2F035001`.

[31] Pulling together: Superconducting electromagnets. `https://home.cern/science/engineering/pulling-together-superconducting-electromagnets`. Copyright ©2019 CERN.

[32] Accelerating: Radiofrequency cavities. `https://home.cern/science/engineering/accelerating-radiofrequency-cavities`. Copyright ©2020 CERN.

[33] The ATLAS Collaboration. The ATLAS Experiment at the CERN Large Hadron Collider. *Journal of Instrumentation*, 3(08):S08003, 2008. `http://stacks.iop.org/1748-0221/3/i=08/a=S08003`.

[34] A. Airapetian et al. ATLAS: Detector and physics performance technical design report. Volume 1. 1999. `http://inspirehep.net/record/511648`.

[35] ATLAS: At the crossroads of art and science. `https://newatlas.com/cern-lhc-atlas-mural/28871/`. August 31, 2013.

[36] Sébastien Rettie. Muon identification and performance in the ATLAS experiment. *PoS*, DIS2018:097, 2018. `http://inspirehep.net/record/1705539`.

[37] Dr C. N. Booth. Measurement in a Magnetic Field. `http://cbooth.staff.shef.ac.uk/phy6040det/magfield.html`.

[38] Magnar Kopangen Bugge. *Search for new charged bosons and dark matter in final states with one lepton and missing transverse energy with the ATLAS detector at the LHC*. PhD thesis, Oslo U., Oslo, 2015-01-30. `http://inspirehep.net/record/1381329/`.

[39] Antonio Salvucci. Measurement of muon momentum resolution of the ATLAS detector. *EPJ Web Conf.*, 28:12039, 2012. `https://inspirehep.net/search?p=find+eprint+1201.4704`.

[40] Georges Aad et al. Muon reconstruction performance of the ATLAS detector in proton–proton collision data at $\sqrt{s}$ =13 TeV. *Eur. Phys. J.*, C76(5):292, 2016. `http://inspirehep.net/record/1429662`.

[41] M. Backhaus. The upgraded pixel detector of the atlas experiment for run 2 at the large hadron collider. *Nuclear Instruments and Methods in Physics Research Section A: Accelerators, Spectrometers, Detectors and Associated Equipment*, 831:65 – 70, 2016. `http://www.sciencedirect.com/science/article/pii/S0168900216303837`.

[42] Giulia Ripellino. The alignment of the ATLAS Inner Detector in Run-2. *PoS*, LHCP2016:196, 2016. `http://inspirehep.net/record/1589614`.

[43] W. R. Leo. *Techniques for Nuclear and Particle Physics Experiments: A How to Approach*. 1994. Second Revised Edition.

[44] The ATLAS collaboration. Operation and performance of the ATLAS semiconductor tracker. *Journal of Instrumentation*, 9(08):P08009–P08009, aug 2014. `https://doi.org/10.1088%2F1748-0221%2F9%2F08%2Fp08009`.

[45] V. A. Mitsou. The ATLAS Transition Radiation Tracker. November 2003. `https://inspirehep.net/search?p=find+eprint+hep-ex/0311058`.

[46] Bartosz Mindur. ATLAS Transition Radiation Tracker (TRT): Straw tubes for tracking and particle identification at the Large Hadron Collider. *Nucl. Instrum. Meth.*, A845:257–261, 2017. `http://inspirehep.net/record/1513538`.

[47] The ATLAS Collaboration. ATLAS liquid-argon calorimeter: Technical Design Report. 1996. `http://cds.cern.ch/record/331061` ***Internal ATLAS note***.

[48] K Nakamura and. Review of particle physics. *Journal of Physics G: Nuclear and Particle Physics*, 37(7A):075021, July 2010. `https://doi.org/10.1088%2F0954-3899%2F37%2F7a%2F075021`.

[49] E. Solfaroli Camillocci. Calibration and Performance of the precision chambers of the ATLAS muon spectrometer. `http://inspirehep.net/record/1196854`.

[50] ATLAS Collaboration. Commissioning of the ATLAS Muon Spectrometer with Cosmic Rays. *Eur. Phys. J. C*, 70(arXiv:1006.4384. CERN-PH-EP-2010-045):875–916. 58 p, August 2010. `https://cds.cern.ch/record/1275998`.

[51] Georges Aad et al. Resolution of the ATLAS muon spectrometer monitored drift tubes in LHC Run 2. *JINST*, 14(09):P09011, 2019. `https://inspirehep.net/literature/1741997`.

[52] Giordano Cattani. Performance of the ATLAS resistive plate chambers. *Nucl. Instrum. Meth.*, A661:S6–S9, 2012. `http://inspirehep.net/record/1094454`.

[53] A Ruiz Martínez and. The run-2 ATLAS trigger system. *Journal of Physics: Conference Series*, 762:012003, October 2016. `https://doi.org/10.1088%2F1742-6596%2F762%2F1%2F012003`.

[54] LHC Design Report Vol.1: The LHC Main Ring. June 2004. `https://inspirehep.net/literature/656250`.

[55] The ATLAS Collaboration. Rapidity gap cross sections measured with the atlas detector in pp collisions at $\sqrt{s} = 7$ tev. *The European Physical Journal C*, 72(3):1926, March 2012. `https://doi.org/10.1140/epjc/s10052-012-1926-0`.

[56] Jan Welti. *Inelastic, non-diffractive and diffractive proton-proton cross-section measurements at the LHC*. PhD thesis, U. Helsinki (main), 2017. `https://inspirehep.net/literature/1761222`.

[57] J M Campbell, J W Huston, and W J Stirling. Hard interactions of quarks and gluons: a primer for LHC physics. *Reports on Progress in Physics*, 70(1):89–193, December 2006. `https://doi.org/10.1088%2F0034-4885%2F70%2F1%2Fr02`.

[58] A. D. Martin, W. J. Stirling, R. S. Thorne, and G. Watt. Parton distributions for the LHC. *Eur. Phys. J.*, C63:189–285, 2009. `http://inspirehep.net/record/810127`.

[59] Gabriella Sciolla, Massimiliano Bellomo, Giacomo Artoni, Gaetano Barone, Kevin Michael Loew, Maximilian Goblirsch-Kolb, Nicolas Maximilian Koehler, Stefano Zambito, and Federico Sforza. Early performance plots for muon reconstruction at Run-II: MCP group . (ATL-COM-MUON-2015-029), June 2015. `https://cds.cern.ch/record/2027688` ***Internal ATLAS note***.

[60] M. A. Dobbs et al. Les Houches guidebook to Monte Carlo generators for hadron collider physics. In *Physics at TeV colliders. Proceedings, Workshop, Les Houches, France, May 26-June 3, 2003*, pages 411–459. `http://inspirehep.net/record/645707`.

[61] Andy Buckley et al. General-purpose event generators for LHC physics. *Phys. Rept.*, 504:145–233, 2011. `http://inspirehep.net/record/884202`.

[62] Torbjorn Sjostrand, Stephen Mrenna, and Peter Z. Skands. PYTHIA 6.4 Physics and Manual. *JHEP*, 05:026, 2006. `http://inspirehep.net/record/712925/`.

[63] Torbjorn Sjostrand. PYTHIA 8 Status Report. In *Proceedings, HERA and the LHC Workshop Series on the implications of HERA for LHC physics: 2006-2008*, pages 726–732, 2008. `http://inspirehep.net/record/794180`.

[64] M. Bahr et al. Herwig++ Physics and Manual. *Eur. Phys. J.*, C58:639–707, 2008. `http://inspirehep.net/record/780833/`.

[65] B. Andersson, G. Gustafson, G. Ingelman, and T. Sjöstrand. Parton fragmentation and string dynamics. *Physics Reports*, 97(2):31 – 145, 1983. `http://www.sciencedirect.com/science/article/pii/0370157383900807`.

[66] T. Gleisberg, Stefan. Hoeche, F. Krauss, M. Schonherr, S. Schumann, F. Siegert, and J. Winter. Event generation with SHERPA 1.1. *JHEP*, 02:007, 2009. `http://inspirehep.net/record/803708`.

[67] Stefano Catani, Stefan Dittmaier, Michael H. Seymour, and Zoltan Trocsanyi. The Dipole formalism for next-to-leading order QCD calculations with massive partons. *Nucl. Phys.*, B627:189–265, 2002. `http://inspirehep.net/record/581476`.

[68] Piotr Golonka and Zbigniew Was. PHOTOS Monte Carlo: A Precision tool for QED corrections in Z and W decays. *Eur. Phys. J.*, C45:97–107, 2006. `http://inspirehep.net/record/684121`.

[69] Pierre Artoisenet, Rikkert Frederix, Olivier Mattelaer, and Robbert Rietkerk. Automatic spin-entangled decays of heavy resonances in Monte Carlo simulations. *JHEP*, 03:015, 2013. `http://inspirehep.net/record/1207464`.

[70] G. Aad et al. The ATLAS Simulation Infrastructure. *Eur. Phys. J.*, C70:823–874, 2010. `http://inspirehep.net/record/856179/`.

[71] Wolfgang Lukas. Fast simulation for ATLAS: Atlfast-II and ISF. *Journal of Physics: Conference Series*, 396(2):022031, dec 2012. `http://inspirehep.net/record/1197050`.

[72] S. Agostinelli et al. GEANT4: A Simulation toolkit. *Nucl. Instrum. Meth.*, A506:250–303, 2003.

[73] Takashi Yamanaka. The ATLAS calorimeter simulation FastCaloSim. *J. Phys. Conf. Ser.*, 331:032053, 2011. `http://inspirehep.net/record/1092858`.

[74] Jörg Mechnich and. FATRAS - the ATLAS fast track simulation project. *Journal of Physics: Conference Series*, 331(3):032046, dec 2011. `http://inspirehep.net/record/1117095/`.

[75] Identification of very-low transverse momentum muons in the ATLAS experiment. (ATL-PHYS-PUB-2020-002), February 2020. `http://cds.cern.ch/record/2710574`.

[76] KyungEon Choi. Tracking and Vertexing with the ATLAS Inner Detector in the LHC Run-2. *Springer Proc. Phys.*, 213:400–403, 2018. `http://inspirehep.net/record/1687304`.

[77] The ATLAS Collaboration. A neural network clustering algorithm for the atlas silicon pixel detector. *JINST*, 9(09):P09009, 2014. `http://stacks.iop.org/1748-0221/9/i=09/a=P09009`.

[78] Muon reconstruction performance in early $\sqrt{s}$=13 TeV data. (ATL-PHYS-PUB-2015-037), August 2015. `https://cds.cern.ch/record/2047831`.

[79] Simone Alioli, Paolo Nason, Carlo Oleari, and Emanuele Re. A general framework for implementing NLO calculations in shower Monte Carlo programs: the POWHEG BOX. *JHEP*, 06:043, 2010. `http://inspirehep.net/record/845712/`.

[80] Hung-Liang Lai, Marco Guzzi, Joey Huston, Zhao Li, Pavel M. Nadolsky, Jon Pumplin, and C. P. Yuan. New parton distributions for collider physics. *Phys. Rev.*, D82:074024, 2010. `http://inspirehep.net/record/861245`.

[81] J. Pumplin, D. R. Stump, J. Huston, H. L. Lai, Pavel M. Nadolsky, and W. K. Tung. New generation of parton distributions with uncertainties from global QCD analysis. *JHEP*, 07:012, 2002. `http://inspirehep.net/record/581996`.

[82] Sherpa Manual Version 2.1.1. `https://sherpa.hepforge.org/doc/SHERPA-MC-2.1.1.html`. June 2014.

[83] Multi-Boson Simulation for 13 TeV ATLAS Analyses. (ATL-PHYS-PUB-2016-002), Jan 2016. `https://cds.cern.ch/record/2119986`.

[84] Richard D. Ball et al. Parton distributions for the LHC Run II. *JHEP*, 04:040, 2015. `http://inspirehep.net/record/1325552`.

[85] Richard D. Ball et al. Parton distributions with LHC data. *Nucl. Phys.*, B867:244–289, 2013. `http://inspirehep.net/record/1121392`.

[86] ATLAS Run 1 Pythia8 tunes. (ATL-PHYS-PUB-2014-021), November 2014. `https://cds.cern.ch/record/1966419`.

[87] Stefano Frixione, Eric Laenen, Patrick Motylinski, Bryan R. Webber, and Chris D. White. Single-top hadroproduction in association with a W boson. *JHEP*, 07:029, 2008. `http://inspirehep.net/record/786266`.

[88] Sayipjamal Dulat, Tie-Jiun Hou, Jun Gao, Marco Guzzi, Joey Huston, Pavel Nadolsky, Jon Pumplin, Carl Schmidt, Daniel Stump, and C. P. Yuan. New parton distribution functions from a global analysis of quantum chromodynamics. *Phys. Rev.*, D93(3):033006, 2016. `http://inspirehep.net/record/1377752`.

[89] Vrap. `http://www.slac.stanford.edu/~lance/Vrap/`.

[90] Sergey G. Bondarenko and Andrey A. Sapronov. NLO EW and QCD proton-proton cross section calculations with mcsanc-v1.01. *Comput. Phys. Commun.*, 184:2343–2350, 2013. `http://inspirehep.net/record/1211201`.

[91] A. D. Martin, R. G. Roberts, W. J. Stirling, and R. S. Thorne. Parton distributions incorporating QED contributions. *Eur. Phys. J.*, C39:155–161, 2005. `http://inspirehep.net/record/663449/`.

[92] Michal Czakon and Alexander Mitov. Top++: A Program for the Calculation of the Top-Pair Cross-Section at Hadron Colliders. *Comput. Phys. Commun.*, 185:2930, 2014. `http://inspirehep.net/record/1082926`.

[93] Morad Aaboud et al. Measurement of the $t\bar{t}$ production cross-section using $e\mu$ events with b-tagged jets in pp collisions at $\sqrt{s}$=13 TeV with the ATLAS detector. *Phys. Lett.*, B761:136–157, 2016. [Erratum: Phys. Lett.B772,879(2017)] `http://inspirehep.net/record/1468168`.

[94] Christopher Willis. The LPXSignalReweightingTool: A Package for Signal Template Reweighting in High-Energy Physics Analysis. (ATL-COM-PHYS-2016-912), July 2016. `https://cds.cern.ch/record/2199258` ***Internal ATLAS note***.

[95] Markus Zinser, Deshan Kavishka Abhayasinghe, Giacomo Artoni, Tracey Berry, Raymond Brock, Magnar Kopangen Bugge, Marc Cano Bret, James Catmore, Mihail Chizhov, Tiesheng Dai, Etienne Dreyer, Peter Johannes Falke, Oleg Fedin, Wojtek Fedorko, Wojciech Fedorko, Francesco Giuli, Daniel Hayden, Simen Hellesund, Noam Hod, Tetiana Hryn'ova, Elham E Khoda, Uta Klein, Mikhail Levchenko, Yanlin Liu, Victor Maleev, Paolo Mastrandrea, Vanja Morisbak, Farid Ould-Saada, Vojtech Pleskot, Sebastien Rettie, Simon Schmitz, Bernd Stelzer, Oliver Stelzer-Chilton, Heberth Torres, Christopher Willis, Stephane Willocq, Ivan Yeletskikh, Zhengguo Zhao, and Bing Zhou. Search for new high-mass resonances in the dilepton final state using proton-proton collisions at $\sqrt{s}$ = 13 TeV with the ATLAS detector. (ATL-COM-PHYS-2016-1404), September 2016. `https://cds.cern.ch/record/2217641` ***Internal ATLAS note***.

[96] Morad Aaboud et al. Luminosity determination in pp collisions at $\sqrt{s}$ = 8 TeV using the ATLAS detector at the LHC. *Eur. Phys. J.*, C76(12):653, 2016. `http://inspirehep.net/record/1481187`.

[97] ATLAS Experiment - Public results. `https://twiki.cern.ch/twiki/bin/view/AtlasPublic/LuminosityPublicResultsRun2`. Revision r60 - Date 2018-11-25.

[98] Morad Aaboud et al. Performance of the ATLAS Trigger System in 2015. *Eur. Phys. J.*, C77(5):317, 2017. `http://inspirehep.net/record/1500696`.

[99] MuonSelectionTool in Rel. 21. `https://twiki.cern.ch/twiki/bin/view/Atlas/MuonSelectionToolR21`. Topic revision: r6 - 2018-02-16.

[100] Deshan Kavishka Abhayasinghe, Tracey Berry, Magnar Kopangen Bugge, Etienne Dreyer, Peter Johannes Falke, Daniel Hayden, Simen Hellesund, Noam Tal Hod, Tetiana Hryn'ova, Uta Klein, Sean Dean Lawlor, Bing Li, Paolo Mastrandrea, Vanja Morisbak, Farid Ould-Saada, Sebastien Rettie, Stefano Rosati, Bernd Stelzer, Oliver Stelzer-Chilton, Damiano Vannicola, Aaron White, and Bing Zhou. Search for new high-mass phenomena in the dilepton final state using the full Run-2 proton-proton

collision dataset at $\sqrt{s}$ =13 TeV with the ATLAS detector. (ATL-COM-PHYS-2018-759), June 2018. `https://cds.cern.ch/record/2622420` ***Internal ATLAS note***.

[101] Magnar Kopangen Bugge, James Catmore, Daniel Hayden, Uta Klein, Farid Ould-Saada, Michael William O'Keefe, Kyungeon Choi, and Stephane Willocq. Search for new particles in the charged lepton plus missing transverse energy final state using pp collisions at $\sqrt{s}$ = 13 TeV in the ATLAS detector. (ATL-COM-PHYS-2018-1407), September 2018. `https://cds.cern.ch/record/2640567` ***Internal ATLAS note***.

[102] Morad Aaboud et al. Search for high-mass new phenomena in the dilepton final state using proton-proton collisions at $\sqrt{s} = 13$ TeV with the ATLAS detector. *Phys. Lett.*, B761:372–392, 2016. `https://inspirehep.net/record/1475476`.

[103] Atlantis Event Display. `http://atlantis.web.cern.ch/atlantis/`. 2015.

[104] MC16CampaignOverview. `https://twiki.cern.ch/twiki/bin/view/AtlasProtected/MC16CampaignOverview`. Topic revision: r5 - 2017-11-07.

[105] Georges Aad et al. Measurement of the muon reconstruction performance of the ATLAS detector using 2011 and 2012 LHC proton–proton collision data. *Eur. Phys. J.*, C74(11):3130, 2014. `http://inspirehep.net/record/1306491`.

[106] Luminosity for physics. `https://twiki.cern.ch/twiki/bin/viewauth/Atlas/LuminosityForPhysics`. Topic revision: r66 - 2019-07-31.

[107] Charalampos Anastasiou, Lance J. Dixon, Kirill Melnikov, and Frank Petriello. High precision QCD at hadron colliders: Electroweak gauge boson rapidity distributions at NNLO. *Phys. Rev.*, D69:094008, 2004. `http://inspirehep.net/record/635943/`.

[108] Jon Butterworth et al. PDF4LHC recommendations for LHC Run II. *J. Phys.*, G43:023001, 2016. `http://inspirehep.net/record/1397826/`.

[109] Patrick Motylinski, Lucian Harland-Lang, Alan D. Martin, and Robert S. Thorne. Updates of PDFs for the 2nd LHC run. *Nucl. Part. Phys. Proc.*, 273-275:2136–2141, 2016. `http://inspirehep.net/record/1466669`.

[110] S. Alekhin, J. Blumlein, and S. Moch. The ABM parton distributions tuned to LHC data. *Phys. Rev.*, D89(5):054028, 2014. `http://inspirehep.net/record/1258127`.

[111] Pedro Jimenez-Delgado and Ewald Reya. Delineating parton distributions and the strong coupling. *Phys. Rev.*, D89(7):074049, 2014. `http://inspirehep.net/record/1284991/`.

[112] Giacomo Artoni, Tracey Berry, Marc Cano Bret, Raymond Brock, James Catmore, Mihail Chizhov, Tiesheng Dai, Etienne Dreyer, Frank Ellinghaus, Oleg Fedin, Francesco Giuli, Daniel Hayden, Hannah Herde, Holger Herr, Noam Hod, Tetiana Hryn'ova, Uta Klein, Mikhail Levchenko, Yanlin Liu, Victor Maleev, Vanja Morisbak, Farid Ould-Saada, Graham Savage, Simon Schmitz, Gabriella Sciolla, Bernd Stelzer, Oliver Stelzer-Chilton, Heberth Torres, Christopher Willis, Stephane Willocq, Yusheng Wu, Ivan Yeletskikh, Zhengguo Zhao, Bing Zhou, Markus Zinser, Sebastien Rettie, Paolo Mastrandrea, Joseph Reichert, Jannicke Pearkes, Daniela Bortoletto, Ian Peter Joseph Shipsey, and Wojciech Fedorko. Search for high-mass new phenomena in the dilepton final state using proton-proton collisions at $\sqrt{s}$ = 13 TeV with the ATLAS detector. (ATL-COM-PHYS-2015-526), June 2015. `https://cds.cern.ch/record/2025566` ***Internal ATLAS note***.

[113] Magnar Kopangen Bugge, Alexey Ezhilov, Victor Solovyev, Holger Herr, Ellis Fawn Kay, Farid Ould-Saada, James Catmore, Monika Wielers, Uta Klein, Daniel Hayden, Frank Ellinghaus, Saminder Dhaliwal, Markus Zinser, Else Lytken, Yosuke Takubo, Oleksandr Viazlo, Kelsey O'connor, Heberth Torres, Joseph Reichert, Nikolaos Tsirintanis, Oleg Fedin, Paul Gessinger-Befurt, Graham Richard Lee, Julie Kirk, and Mihail Chizhov. Search for new particles in the charged lepton plus missing transverse energy final state using pp collisions at $\sqrt{s} = 13$ TeV in the ATLAS detector. (ATL-COM-PHYS-2016-1405), September 2016. `https://cds.cern.ch/record/2217650` ***Internal ATLAS note***.

[114] Glen Cowan, Kyle Cranmer, Eilam Gross, and Ofer Vitells. Asymptotic formulae for likelihood-based tests of new physics. *Eur. Phys. J.*, C71:1554, 2011. [Erratum: Eur. Phys. J.C73,2501(2013)] `http://inspirehep.net/record/860907`.

[115] Luc Demortier. 5 bayesian treatments of systematic uncertainties. `http://citeseerx.ist.psu.edu/viewdoc/summary?doi=10.1.1.205.7146`.

[116] ATLAS statistics forum. Frequentist limit recommendation. `https://twiki.cern.ch/twiki/pub/AtlasProtected/StatisticsTools/Frequentist_Limit_Recommendation.pdf`, 2011.

[117] S. S. Wilks. The large-sample distribution of the likelihood ratio for testing composite hypotheses. *Ann. Math. Statist.*, 9(1):60–62, 03 1938. `https://doi.org/10.1214/aoms/1177732360`.

[118] Frederik Beaujean, Allen Caldwell, Daniel Kollár, and Kevin Kröninger. BAT – the bayesian analysis toolkit. *Journal of Physics: Conference Series*, 331(7):072040, December 2011. `http://inspirehep.net/record/1089578`.

[119] Damiano Vannicola. Uncertainty on q/p criteria using full run 2. Technical Report ATL-COM-PHYS-2019-1000, CERN, Geneva, August 2019. `https://cds.cern.ch/record/2685294`.

[120] G. Aad and al. Search for high-mass dilepton resonances using 139 fb^{-1} of pp collision data collected at $\sqrt{s}$=13 TeV with the ATLAS detector. *Physics Letters B*, 796:68 – 87, 2019. `http://www.sciencedirect.com/science/article/pii/S0370269319304721`.

[121] Wouter Verkerke and David Kirkby. The RooFit toolkit for data modeling. *arXiv e-prints*, page physics/0306116, June 2003. `TheRooFittoolkitfordatamodeling`.

[122] L. Moneta, K. Cranmer, G. Schott, and W. Verkerke. The RooStats project. In *Proceedings of the 13th International Workshop on Advanced Computing and Analysis Techniques in Physics Research. February 22-27*, page 57, January 2010. `http://inspirehep.net/record/868303`.

[123] Tetiana Hryn'ova, Daniel Hayden, Peter Johannes Falke, Yosuke Takubo, Manuel Maria Perez-Victoria Moreno De Barreda, Ellis Kay, Uta Klein, Carl Gwilliam, and Wade Cameron Fisher. Combination of Z'→ ll and W'→ lnu in Heavy Vector Triplet model with 36fb-1 of 13TeV data. (ATL-COM-PHYS-2015-021), January 2015. Other Authors: Manuel Perez-Victoria and Javier Lizana `https://cds.cern.ch/record/1982245` ***Internal ATLAS note***.

[124] CMS Collaboration. Search for a narrow resonance in high-mass dilepton final states in proton-proton collisions using 140 fb^{-1} of data at $\sqrt{s} = 13$ TeV. 2019. `http://inspirehep.net/record/1747703`.

[125] The European Physical Society Conference on High Energy Physics 2015. `http://eps-hep2015.eu/`. 2013 Copyright by HEPHY - Institute of High Energy Physics of the Austrian Academy of Sciences.

[126] ATLAS VP1. `https://atlas-vp1.web.cern.ch/atlas-vp1/home/`. ATLAS VP1 Team - The ATLAS Experiment © 2019 CERN - all rights reserved.

[127] R M Bianchi, J Boudreau, N Konstantinidis, A C Martyniuk, E Moyse, J Thomas, B M Waugh, and D P Yallup. Event visualization in atlas. *Journal of Physics: Conference Series*, 898:072014, 10 2017. `https://iopscience.iop.org/article/10.1088/1742-6596/898/7/072014/pdf`.

[128] Giacomo Artoni, Tracey Berry, Marc Cano Bret, Raymond Brock, James Catmore, Mihail Chizhov, Tiesheng Dai, Frank Ellinghaus, Oleg Fedin, Woiciech Fedorko, Francesco Giuli, Daniel Hayden, Hannah Herde, Holger Herr, Noam Hod, Tetiana Hryn'ova, Uta Klein, Mikhail Levchenko, Yanlin Liu, Victor Maleev, Vanja Morisbak, Farid Ould-Saada, Sebastien Rettie, Graham Savage, Simon Schmitz, Gabriella Sciolla, Bernd Stelzer, Oliver Stelzer-Chilton, Heberth Torres, Knut Oddvar Hoie Vadla, Christopher Willis, Stephane Willocq, Yusheng Wu, Ivan Yeletskikh, Zhengguo Zhao, Bing Zhou, and Markus Zinser. Performance Plots: Exotics Z' $\rightarrow \ell\ell$ Search. (ATL-COM-PHYS-2015-726), July 2015. `https://cds.cern.ch/record/2034890` ***Internal ATLAS note***.

[129] The ATLAS Collaboration. Search for new phenomena in the dilepton final state using proton-proton collisions at $\sqrt{s}$ = 13 TeV with the ATLAS detector. 2015. `http://inspirehep.net/record/1410163`.

[130] ATLAS and CMS physics results from Run 2. `https://indico.cern.ch/event/442432/`. "December 15 2015".

[131] International masterclasses - hands on particle physics. `http://atlas.physicsmasterclasses.org/no/index.htm`.

[132] Farid Ould-Saada. LHC discoveries and particle physics concepts for education. *PoS*, EPS-HEP2015:359, 2015. `http://inspirehep.net/record/1430661`.

[133] The International Particle Physics Outreach Group (IPPOG). `http://ippog.org/`.

[134] Hypatia. `http://hypatia.phys.uoa.gr/`.

[135] M. Pedersen F. Ould-Saada, V. Morisbak. Oslo Plotting Tool (OPloT). `http://cernmasterclass.uio.no`.

[136] Preparing ATLAS for the future. `https://atlas.cern/updates/atlas-news/preparing-ATLAS-for-future`. "20 December, 2018 ".

[137] The New Small Wheels set ATLAS on track for high luminosity. `https://home.cern/news/news/experiments/new-small-wheels-set-atlas-track-high-luminosity`. "21 August, 2018 ".

[138] LHC prepares for new achievements. `https://home.cern/news/press-release/accelerators/lhc-prepares-new-achievements`. "3 December, 2018 ".

[139] LS2 Report: A new schedule. `https://home.cern/news/news/accelerators/ls2-report-new-schedule`. "24 June, 2020".

[140] A new schedule for the LHC and its successor. `https://home.cern/news/news/accelerators/new-schedule-lhc-and-its-successor`. "13 December, 2019".

[141] High-Luminosity LHC. `https://home.cern/science/accelerators/high-luminosity-lhc`. "Copyright ©2020 CERN".

[142] CERN updates LHC schedule. `CERNupdatesLHCschedule`. "10 January, 2020 ".

[143] Prospects for searches for heavy Z' and W' bosons in fermionic final states with the ATLAS experiment at the HL-LHC. "2018". `https://inspirehep.net/literature/1795252`.

[144] A. "Abada and others". HE-LHC: The High-Energy Large Hadron Collider: Future Circular Collider Conceptual Design Report Volume 4. *Eur. Phys. J. ST*, 228(5):1109–1382, 2019. `https://inspirehep.net/literature/1713703`.

[145] Michelangelo L. Mangano, Mauro Moretti, Fulvio Piccinini, Roberto Pittau, and Antonio D. Polosa. ALPGEN, a generator for hard multiparton processes in hadronic collisions. *JHEP*, 07:001, 2003. `http://inspirehep.net/record/589478`.

[146] V. Garonne et al. The ATLAS Distributed Data Management project: Past and Future. 2012. `http://inspirehep.net/record/1197024`.

[147] Andy Buckley, Jonathan Butterworth, Leif Lonnblad, David Grellscheid, Hendrik Hoeth, James Monk, Holger Schulz, and Frank Siegert. Rivet user manual. *Comput. Phys. Commun.*, 184:2803–2819, 2013. `http://inspirehep.net/record/847552`.

[148] Rivet analyses reference, MC_ZJETS. `https://rivet.hepforge.org/analyses/MC_ZJETS.html`. Monte Carlo ReleaseTests observables for Z[e+e-]+jets production.

[149] Rivet analyses reference, MC_ZINC. `https://rivet.hepforge.org/analyses/MC_ZINC.html`. MC validation analysis for Z events.

[150] H. L. Lai, J. Huston, S. Kuhlmann, J. Morfin, Fredrick I. Olness, J. F. Owens, J. Pumplin, and W. K. Tung. Global QCD analysis of parton structure of the nucleon: CTEQ5 parton distributions. *Eur. Phys. J.*, C12:375–392, 2000. `http://inspirehep.net/record/496368`.

[151] Rivet analyses reference, MC_JETS. `https://rivet.hepforge.org/analyses/MC_JETS.html`. Monte Carlo validation observables for jet production.

[152] Rivet analyses reference, MC_TTBAR. `https://rivet.hepforge.org/analyses/MC_TTBAR.html`. MC analysis for ttbar studies.

[153] Rivet analyses reference,M C_WJETS. `https://rivet.hepforge.org/analyses/MC_WJETS.html`. MC validation analysis for W + jets events.

[154] Rivet analyses reference, ATLAS_2012_I1094568. `https://rivet.hepforge.org/analyses/ATLAS_2012_I1094568.html`. Measurement of ttbar production with a veto on additional central jet activity.

[155] Georges Aad et al. Measurement of $t\bar{t}$ production with a veto on additional central jet activity in pp collisions at sqrt(s) = 7 TeV using the ATLAS detector. *Eur. Phys. J.*, C72:2043, 2012. `http://inspirehep.net/record/1094568/`.

List of Figures

List of Tables

Index